mathematical sciences publishers

A SINGULAR INTEGRAL EQUATION METHOD
FOR EXAMINING ASYMPTOTIC SOLUTIONS OF A KINKED CRACK
WITH INFINITESIMAL KINK LENGTH

Y. Z. CHEN, X. Y. LIN AND Z. X. WANG

This paper investigates the singular integral equation method for examining the stress intensity factor and the T-stress in the asymptotic solution of a kinked crack with an infinitesimal kink length. A numerical technique for the branch crack problem is introduced, which depends upon distribution of dislocation along the crack face. The technique reduces the branch crack problem to the solution of a singular integral equation. The kinked cracked problem can be considered as a particular case of the branch crack, and this problem can be solved by using the suggested technique. It is found from the computed results that the available asymptotic solution can give qualitatively correct results for stress intensity factors and the T-stress. In addition, the available asymptotic solution can only give sufficiently accurate results in a narrow range of the length of the kinked portion and the inclined kink angle.

1. Introduction

Williams [1957] investigated the stress distribution near a crack tip. In the notation of [Rice 1974], the nonsingular term in the Williams expansion is denoted as the T-stress and can be regarded as the stress acting parallel to the crack flanks. The T-stress evaluation may have engineering application in the following fields: determining the plastic zone near the crack tip in the case of small scale yielding [Larsson and Carlsson 1973; Betegón and Hancock 1991] and determining directional stability for the crack growth path [Rice 1974; Melin 2002].

The T-stress evaluation has attracted much attention from many investigators. Using the dislocation distribution method, Broberg [2005] solved several T-stress problems. Stress intensity factors and T-stress solutions for components containing cracks were computed by application of the boundary collocation method (BCM) with the fracture mechanics weight function for the stress intensity factor (SIF) and a Green's function for the T-stress [Fett 2001]. The obtained solutions were limited to a line crack in a circular plate.

Using the hybrid crack element (HCE), Karihaloo and Xiao [2001] evaluated the higher order terms in the stress distribution of a three-point bend beam. The coefficients of the first five terms of the crack tip asymptotic field are computed using a HCE. Those coefficients include the T-stress component. Xiao and Karihaloo [2002] studied the problem for an edge crack in a finite plate with a wedge force on the crack face. The problem was reduced to the problem of a traction free edge crack with loading on the outer boundary. The usage of the Williams expansion and the BCM gave the final solution. Yang and Ravi-Chandar [1999] developed a stress difference method to evaluate the T-stress in the crack problem.

Keywords: kinked crack, stress intensity factors, T-stress, asymptotic solution, singular integral equation.

It was proved that the limit of the difference of two normal stress components ahead of the crack tip would give the T-stress.

Evaluation of the SIFs and the T-stress in the slightly kinked crack was subject to much attention from many investigators [Lo 1978; Cotterell and Rice 1980; Melin 1986; Fett et al. 2006; Li and Xu 2007]. The Melin transform is used for the solution of a kinked crack [Melin 1994]. A solution was presented for the SIFs at the tip of a slightly curved or kinked crack. The solution is accurate to first order in the deviation of the crack face from a straight line [Cotterell and Rice 1980]. The influence of the T-stress on the stability of crack growth was investigated. The straight path is shown to be stable under mode I loading for $T < 0$ [Cotterell and Rice 1980].

Fett et al. [2006] studied the T-stress for a kinked crack and suggested a Green's function to solve the problem. The formulation was based on an edge crack in a rectangular plate. By using asymptotic analysis and the Westergaard stress function method, Li and Xu [2007] proposed approximate analytical formulas for the T-stress and the SIFs for a crack with an infinitesimal kink.

The mentioned studies depend on some assumptions. For example, normally we must investigate the SIFs and the T-stress at the kinked crack tip of the kinked crack. However, in asymptotic analysis the researcher generally obtains the SIFs and the T-stress from a semiinfinite crack with loading on some interval on the crack. All mentioned assumptions couldn't be proved theoretically. However, many researchers recognized that those formulations are true when the kinked crack length $d \to 0$ and the kinked angle θ keeps up a rather small value, for example $\theta \le 15°$.

In reality, only small crack kink angles were observed for isotropic materials. Large crack kink angles are almost impossible because of the crack branch possibility. Some researchers believe that the maximum crack branch angle is around 60 degrees so it is meaningful to study crack kink angles less than 30 degrees. In this paper, the assumed kink angle is up to 60 degrees. Clearly, the obtained computed results cover the case of a small kink angle.

Two singular point finite elements were developed for the analysis of kinked cracks [Dutta et al. 1991]. The suggested method could reflect the weaker stress singularity at the corner portion of a kinked crack.

In this paper, a numerical examination for the asymptotic solution of a kinked crack with an infinitesimal kink length is carried out. It is assumed that the main crack has a length b, and the kinked portion has a length d with an inclined angle θ. If d/b takes a very small value, for example if $d/b = 0.001$, and the usual singular integral equation method is used, the kinked portion will not share even one integration point after discretization of the integral equation. Since all the collocation points are placed on the main crack portion, the nature of the kinked portion cannot be reflected. Therefore, the technique suggested by Chen [2004] is no longer useful in the case of an infinitesimal kink length.

In this study, the kinked crack problem is considered as a particular case of the branch crack problem. The branch crack problem can be modeled by a continuous distribution of dislocations along the branches. In addition, a singular integral equation is obtained from this modeling. The number for integration divisions can be assumed for an individual branch even if the branch length is extremely short. Therefore, the kinked problem with an infinitesimal kinked length can be solved numerically. Finally, for the three loading case, $\sigma_x^\infty = p$, $\sigma_y^\infty = p$, or $\sigma_{xy}^\infty = -p$, the computed results are compared with those obtained from the asymptotic solution. Therefore, the asymptotic solution for the kinked problems with an infinitesimal kinked length is fully examined.

2. Asymptotic solution for a kinked crack with an infinitesimal kink length

Some basic equations for the singular stress field at the crack tip are introduced below. The stress distribution near a crack tip was investigated early by Williams [1957]. In polar coordinates (r, θ), the stress components σ_{ij} can be expressed by (see Figure 1a)

$$\begin{bmatrix} \sigma_x & \sigma_{xy} \\ \sigma_{xy} & \sigma_y \end{bmatrix} = \frac{K_1}{\sqrt{2\pi r}} \begin{bmatrix} f_{11}(\theta) & f_{12}(\theta) \\ f_{12}(\theta) & f_{22}(\theta) \end{bmatrix} + \frac{K_2}{\sqrt{2\pi r}} \begin{bmatrix} g_{11}(\theta) & g_{12}(\theta) \\ g_{12}(\theta) & g_{22}(\theta) \end{bmatrix} + \begin{bmatrix} T & 0 \\ 0 & 0 \end{bmatrix}, \tag{1}$$

where the first two terms in the expansion form are singular at the crack tip, K_1 and K_2 denote the mode I and II SIFs respectively, and the functions $f_{ij}(\theta)$ and $g_{ij}(\theta)$ represent the angular distributions of stresses near the crack tip. In addition, the third term is finite and bounded. In the notation of [Rice 1974], the third term is denoted as the T-stress.

In Equation (1), the term $O(r^{1/2})$ has been neglected for clarity. In addition, the angular distribution can be expressed as [Williams 1957]

$$\begin{Bmatrix} f_{11} \\ f_{12} \\ f_{22} \end{Bmatrix} = \cos\left(\frac{\theta}{2}\right) \begin{Bmatrix} 1 - \sin\left(\frac{\theta}{2}\right)\sin\left(3\frac{\theta}{2}\right) \\ \sin\left(\frac{\theta}{2}\right)\cos\left(3\frac{\theta}{2}\right) \\ 1 + \sin\left(\frac{\theta}{2}\right)\sin\left(3\frac{\theta}{2}\right) \end{Bmatrix}, \quad \begin{Bmatrix} g_{11} \\ g_{12} \\ g_{22} \end{Bmatrix} = \begin{Bmatrix} -\sin\left(\frac{\theta}{2}\right)\left[2 + \cos\left(\frac{\theta}{2}\right)\cos\left(3\frac{\theta}{2}\right)\right] \\ \cos\left(\frac{\theta}{2}\right)\left[1 - \sin\left(\frac{\theta}{2}\right)\sin\left(3\frac{\theta}{2}\right)\right] \\ \sin\left(\frac{\theta}{2}\right)\cos\left(\frac{\theta}{2}\right)\cos\left(3\frac{\theta}{2}\right) \end{Bmatrix}. \tag{2}$$

An asymptotic solution for a kinked crack with an infinitesimal kink length was suggested previously. The SIFs and the T-stress evaluation after crack kinking in two-dimensional elastic solids were studied [Cotterell and Rice 1980; Fett et al. 2006; Li and Xu 2007]. Contributions from the T-stress before crack kinking to the T-stress and SIFs of the kinked crack are clearly described. It is assumed that the main crack under remote loading, the SIFs, and the T-stress at the crack tip B are denoted by K_1^m, K_2^m, and T^m, respectively (see Figure 1b). After kinking, the SIFs and the T-stress at the kinked tip C are denoted by K_1^k, K_2^k, and T^k (see Figure 1c), respectively. After some manipulation, Li and Xu [2007] obtained the following results:

$$K_1^k = c_{11}(\theta)K_1^m + c_{12}(\theta)K_2^m + 2T^m\sqrt{\frac{2d}{\pi}}\sin^2\theta. \tag{3}$$

$$K_2^k = c_{21}(\theta)K_1^m + c_{22}(\theta)K_2^m - 2T^m\sqrt{\frac{2d}{\pi}}\sin\theta\cos\theta. \tag{4}$$

$$T^k = \sqrt{\frac{1}{2\pi d}}\left(N_1(\theta)K_1^m + N_2(\theta)K_2^m\right) + n(\theta)T^m, \tag{5}$$

where d denotes the length of kinked crack, θ the kinked angle (see Figure 1c), and

$$c_{11}(\theta) = \frac{(1+\cos\theta)\cos(\theta/2)}{2}, \qquad c_{22}(\theta) = \frac{(3\cos\theta - 1)\cos(\theta/2)}{2}, \tag{6}$$

$$c_{12}(\theta) = -\frac{3(1+\cos\theta)\sin(\theta/2)}{2}, \qquad c_{21}(\theta) = \frac{(1+\cos\theta)\sin(\theta/2)}{2}, \tag{7}$$

$$N_1(\theta) = \sin\theta\sin\left(\frac{\theta}{2}\right), \qquad N_2(\theta) = (1+3\cos\theta)\sin\left(\frac{\theta}{2}\right), \qquad n(\theta) = \cos 2\theta. \tag{8}$$
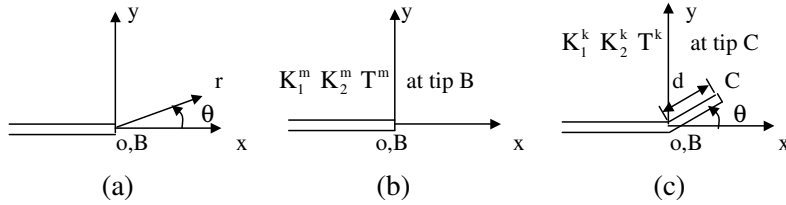
Figure 1. (a) A semiinfinite crack; (b) a main crack with loading K_1^m, K_2^m, and T^m; and (c) a kinked crack emanating from the main crack.

Note that the four functions $c_{11}(\theta)$, $c_{12}(\theta)$, $c_{21}(\theta)$, and $c_{22}(\theta)$ have also been suggested previously [Cotterell and Rice 1980]. It is expected that the suggested formulas are valid for the case of $d \to 0$, or if the length of the kinked portion is sufficient small.

Clearly, the asymptotic solution can only give an approximate solution for the kinked crack problem. This can be seen from the following analysis. It is assumed that the kinked crack with a small kink length d and an inclined angle θ is surrounded by a stress field defined by a mode I SIF, or $K_1^m \neq 0$, $K_2^m = 0$, and $T^m = 0$ (see Figure 2a). The original problem shown by Figure 2a can be considered as a superposition of the two problems shown by Figures 2b and 2c. In the problem shown by Figure 2b, the main crack has a loading $K_1^m \neq 0$, $K_2^m = 0$, and $T^m = 0$. However, in the problem shown by Figure 2c, the kinked crack has a loading on the kinked portion, or along the interval BC.

Clearly, from Equations (1) and (2), the stress singular distributions along the line BC in (r, θ) coordinates can be easily evaluated (see Figure 2b):

$$\sigma_r = \frac{K_1^m}{\sqrt{2\pi r}} c_{11}(\theta), \qquad \sigma_{r\theta} = \frac{K_1^m}{\sqrt{2\pi r}} c_{21}(\theta), \tag{9}$$

where $c_{11}(\theta)$ and $c_{21}(\theta)$ are defined in (6) and (7).

After making the substitution $r = d - s$, the loading on the kinked portion in Figure 2c will be

$$\sigma_{r*} = -\sigma_r = -\frac{K_1^m}{\sqrt{2\pi(d-s)}} c_{11}(\theta), \qquad \sigma_{r\theta*} = -\sigma_{r\theta} = -\frac{K_1^m}{\sqrt{2\pi(d-s)}} c_{21}(\theta). \tag{10}$$

An approximation was introduced as follows [Cotterell and Rice 1980; Li and Xu 2007]. The kinked crack shown by Figure 2c was approximated by a semiinfinite crack shown by Figure 2d with the loading applied on the interval $(0 < s < d)$. Therefore, the SIFs at the kinked tip C can be evaluated by

$$K_1^k = -\sqrt{\frac{2}{\pi}} \int_0^d \frac{\sigma_{r*}\, ds}{\sqrt{s}} = K_1^m c_{11}(\theta), \qquad K_2^k = -\sqrt{\frac{2}{\pi}} \int_0^d \frac{\sigma_{r\theta*}\, ds}{\sqrt{s}} = K_1^m c_{21}(\theta). \tag{11}$$

This result coincides with that obtained from Equations (3), (4), (6), and (7) in the case of $K_1^m \neq 0$, $K_2^m = 0$, and $T^m = 0$ [Cotterell and Rice 1980; Li and Xu 2007].

A similar approximation was suggested to consider the influence functions

$$2\sqrt{\frac{2d}{\pi}} \sin^2 \theta, \qquad -2\sqrt{\frac{2d}{\pi}} \sin\theta \cos\theta,$$

and $n(\theta)$ in (3)–(5), which represent the influence for K_1^k, K_2^k, and T^k caused by T^m.
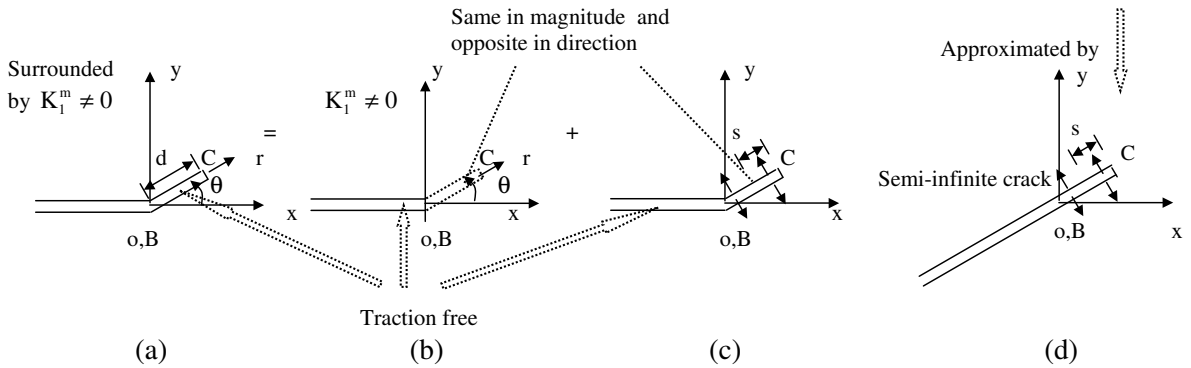
Figure 2. Superposition method in the kinked problem: (a) a kinked crack surrounded by the stress field defined by loading K_1^m, (b) a main crack with loading K_1^m, (c) a kinked crack with loading on the kinked portion BC, and (d) a semiinfinite crack with loading on the interval BC.

As mentioned above, the boundary value problem shown by Figure 2c was approximated by the problem shown by Figure 2d. Clearly, the most difficult point is to evaluate the deviation caused by this approximation. In addition, this difficult problem cannot be solved theoretically. A particular advantage of the asymptotic solution for kinked crack problem is it provides some equations for the SIFs and the T-stress in an explicit form. However, since many assumptions were used in the derivation, the accuracy of the asymptotic solution is generally not easy to judge. Naturally, it is necessary to propose a numerical examination for the asymptotic solution, particularly, for the case of an infinitesimal kink length.

3. Formulation for the solution of the branch crack problem

In the following, a numerical method for solving the branch crack problem is suggested. The problem is shown in Figure 3a, for example, a crack problem with three branches. It is assumed that the applied tractions are identical in magnitude and opposite in direction on the both sides of the crack face. The problem can be modeled by a dislocation distribution along the prospective site of the branches (see Figure 3b). In this case, even though some branches have smaller lengths, we can assume a suitable number of integration divisions for those branches. For example, in Figure 3, for two shorter branches, the branches BD and BC, we can assume $M_1 = 3$ and $M_2 = 5$ (the numbers of integration divisions), and we can take $M_3 = 15$ for longer branch. The kinked crack (with two branches) is a particular case of the branch crack problem. Therefore, the numerical solution based on the branch crack problem can be used for the kinked crack problem.

For evaluating the SIFs and the T-stress in the branch crack problem, a detailed formulation is introduced below. The complex variable function method plays an important role in plane elasticity. The fundamentals of this method are introduced. In the method, the stresses $(\sigma_x, \sigma_y, \sigma_{xy})$, the resultant forces (X, Y), and the displacements (u, v) are expressed in terms of complex potentials $\phi(z)$ and $\psi(z)$ such that [Muskhelishvili 1953]

$$\sigma_x + \sigma_y = 4 \operatorname{Re} \phi'(z),$$

$$\sigma_y - \sigma_x + 2i\sigma_{xy} = 2[\bar{z}\phi''(z) + \psi'(z)], \tag{12}$$

$$f = -Y + iX = \phi(z) + z\overline{\phi'(z)} + \overline{\psi(z)}, \qquad 2G(u+iv) = \kappa\phi(z) - z\overline{\phi'(z)} - \overline{\psi(z)}, \tag{13}$$

where a bar over a function denotes the conjugate of the function, G is the shear modulus of elasticity, $\kappa = (3-\nu)/(1+\nu)$ in the plane stress problem, $\kappa = 3 - 4\nu$ in the plane strain problem, ν is the Poisson's ratio, and $i = \sqrt{-1}$ denotes the unit imaginary value.

Except for the physical quantities mentioned above, from Equation (13) two derivatives in specified direction are introduced as follows: [Savruk 1981]

$$J_1(z) = \frac{d}{dz}\{-Y + iX\} = \Phi(z) + \overline{\Phi(z)} + \frac{d\bar{z}}{dz}\left(z\overline{\Phi'(z)} + \overline{\Psi(z)}\right) = \sigma_N + i\sigma_{NT}, \tag{14}$$

$$J_2(z) = 2G\frac{d}{dz}\{u+iv\} = \kappa\Phi(z) - \overline{\Phi(z)} - \frac{d\bar{z}}{dz}\left(z\overline{\Phi'(z)} + \overline{\Psi(z)}\right) = (\kappa+1)\Phi(z) - J_1. \tag{15}$$

It is easy to verify that $J_1 = \sigma_N + i\sigma_{NT}$ denotes the normal and shear tractions along the segment $\overline{z, z+dz}$. Secondly, the J_1 and J_2 values depend not only on the position of a point z, but also on the direction of the segment $d\bar{z}/dz$ (see Figure 4o).

For evaluating the T-stress at the branch tips with remote loading, it is suitable to use the superposition method. The original problem is shown in Figure 4o. The remote tractions are denoted as σ_x^∞, σ_y^∞, and σ_{xy}^∞. The original field can be considered as a superposition of a uniform field and a perturbation field, which are shown by Figures 4a and 4b, respectively. Here and after, the subscript (u) is used for the uniform field, and the subscript (p) for the perturbation field (see Figures 4a and 4b).

Clearly, the T-stress at the j-th branch tip A_j can be expressed as

$$T_j = T_{j(u)} + T_{j(p)}, \tag{16}$$

where $T_{j(u)}$ and $T_{j(p)}$ denote the T-stress at tip A_j from the uniform field and the perturbation field, respectively. It is seen that

$$T_{j(u)} = \sigma_{T(u)}(t_{A_j}), \tag{17}$$

where $\sigma_{T(u)}(t_{A_j})$ denote the σ_T component at the branch tip A_j in the uniform field (see Figure 4a).

Clearly, since the tractions on the crack face in the perturbation field are opposite to those tractions on the perspective site of crack in the uniform field, the boundary tractions applied on the j-th branch in
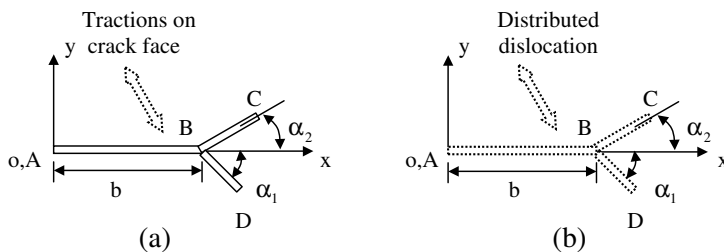
Figure 3. (a) A branch crack with loading on the crack face, and (b) a branch crack modeled by distributed dislocation.
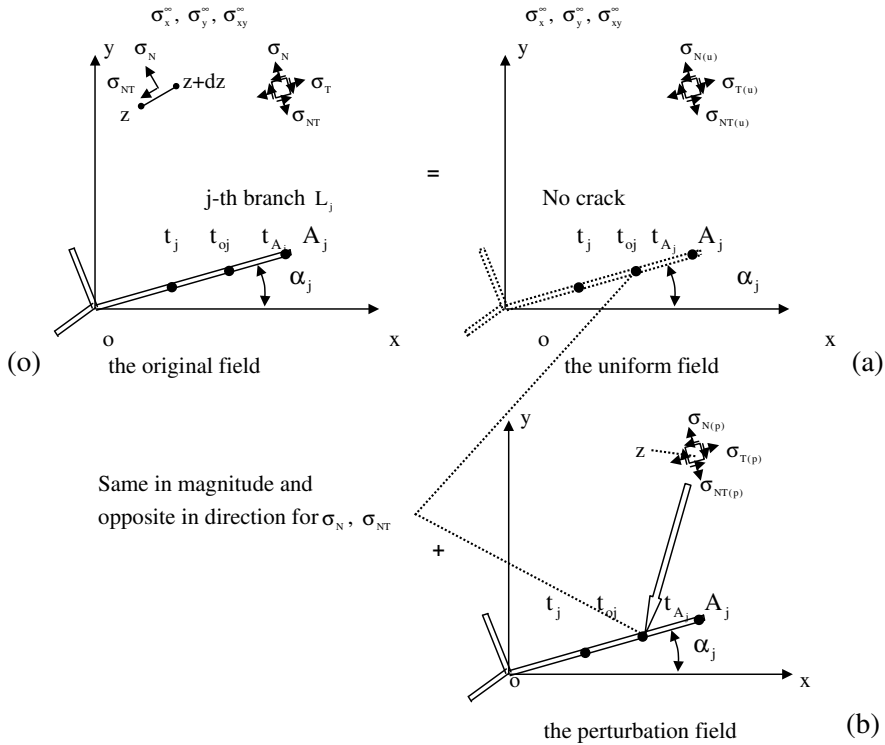
Figure 4. Superposition method for the branch crack problem: (*o*) a branch crack in an infinite plate, with *o* the original field; (*a*) a perfect plate with remote loading, with subscript (*u*) denoting the uniform stress field; and (*b*) a branch crack with loading on the crack face, with subscript (*p*) denoting the perturbation stress field.

the perturbation field will be

$$\sigma_{N(p)}(t_{oj}) + i\sigma_{NT(p)}(t_{oj}) = -\big(\sigma_{N(u)}(t_{oj}) + i\sigma_{NT(u)}(t_{oj})\big) \quad (t_{oj} \in L_j; j = 1, 2, \ldots, N). \tag{18}$$

In order to evaluate the T-stress in the branch crack problem, it is necessary to derive the relevant integral equation beforehand. In the perturbation field, the remote tractions are zero, and the applied tractions on branches are as follows (see Figure 4b):

$$\begin{aligned}
\sigma_N(t_{oj}) + i\sigma_{NT}(t_{oj}) &= \sigma_{N(p)}(t_{oj}) + i\sigma_{NT(p)}(t_{oj}) \\
&= -\big(\sigma_{N(u)}(t_{oj}) + i\sigma_{NT(u)}(t_{oj})\big) \quad (t_{oj} \in L_j; j = 1, 2, \ldots, N),
\end{aligned} \tag{19}$$

where $\sigma_N(t_{oj})$ and $\sigma_{NT}(t_{oj})$ denote the normal and shear tractions along the *j*-th branch or L_j, and $\sigma_{N(p)}(t_{oj})$ and $\sigma_{NT(p)}(t_{oj})$ denote the given normal and shear tractions along the *j*-th branch (see Figure 4b).

It was proved that the complex potentials for this field could be expressed as [Chen and Hasebe 1995]

$$\phi'(z) = \frac{H}{2\pi z} + \frac{1}{2\pi} \sum_{k=1}^{N} \int_{L_k} \frac{g_k'(t)\,dt}{t-z}, \qquad \phi''(z) = -\frac{H}{2\pi z^2} + \frac{1}{2\pi} \sum_{k=1}^{N} \int_{L_k} \frac{g_k'(t)\,dt}{(t-z)^2}, \tag{20}$$

$$\psi'(z) = \frac{\bar{H}}{2\pi z} + \frac{1}{2\pi} \sum_{k=1}^{N} \int_{L_k} \frac{\overline{g_k'(t)}\,d\bar{t}}{t-z} - \frac{1}{2\pi} \sum_{k=1}^{N} \int_{L_k} \frac{\bar{t}g_k'(t)\,dt}{(t-z)^2}, \tag{21}$$

where $g_k'(t)$ denotes the dislocation distribution along the k-th branch. Here, H ($H = H_1 + i H_2$) is a concentrated dislocation placed at the origin. The reason for assuming the complex potentials shown by Equations (20) and (21) will be expressed later.

Physically, the function $g_k'(t)$ represents the dislocation distribution along the k-th crack. Thus, integration to this function will give the crack opening displacement function, or the displacement discontinuity across the crack.

By substituting (20) and (21) into (14), letting the point z approach a point $t_{o_j} \in L_j$ on the j-th branch (see Figure 4b), and using the Plemelj formula for the Cauchy-type integral [Muskhelishvili 1953], one will find the following singular integral equation [Chen and Hasebe 1995]:

$$\frac{1}{\pi} \sum_{k=1}^{N} \int_{L_k} \frac{g_k'(t)\,dt}{t-t_{oj}} + M(t_{oj}) + \frac{H}{\pi t_{oj}} = \sigma_{N(p)}(t_{oj}) + i\sigma_{NT(p)}(t_{oj}) \quad (t_{oj} \in L_j; \; j = 1, 2, \dots, N), \tag{22}$$

where

$$M(t_{oj}) = \frac{1}{2\pi} \sum_{k=1}^{N}{}' \int_{L_k} K_1(t, t_{oj})g_k'(t)\,dt + \frac{1}{2\pi} \sum_{k=1}^{N}{}' \int_{L_k} K_2(t, t_{oj})\overline{g_k'(t)}\,d\bar{t}, \tag{23}$$

$$K_1(t, t_o) = \frac{d}{dt_o}\left\{\ln\frac{t-t_o}{\bar{t}-\bar{t}_o}\right\} = -\frac{1}{t-t_o} + \frac{1}{\bar{t}-\bar{t}_o}\frac{d\bar{t}_o}{dt_o}, \tag{24}$$

$$K_2(t, t_o) = -\frac{d}{dt_o}\left\{\frac{t-t_o}{\bar{t}-\bar{t}_o}\right\} = \frac{1}{\bar{t}-\bar{t}_o} - \frac{t-t_o}{(\bar{t}-\bar{t}_o)^2}\frac{d\bar{t}_o}{dt_o}. \tag{25}$$

In (23), $\sum_{k=1}^{N}{}'$ means that the term corresponding to $k = j$ should be excluded in the summation. This result can be easily seen from the following fact. In (24) and (25), if t, t_o, and dt_o are defined on the j-th branch, then $K_1(t, t_o) = 0$ and $K_2(t, t_o) = 0$.

In addition, the dislocation distribution $g_k'(t)$ should satisfy the following single-valued condition of displacements [Chen and Hasebe 1995]:

$$\sum_{k=1}^{N} \int_{L_k} g_k'(t)\,dt - H = 0. \tag{26}$$

Once the solution for the function $g_j'(t)$ is obtained from (22) and (26), the SIFs at the branch tip A_j can be evaluated by [Savruk 1981; Chen and Hasebe 1995]

$$(K_1 - iK_2)_j = -\sqrt{2\pi} \lim_{t \to t_{A_j}} \sqrt{|t - t_{A_j}|}\,g_j'(t). \tag{27}$$

On the other hand, from the invariant property for the sum of two normal stresses and (12), at any point we have

$$\sigma_{T(p)} = 4\,\mathrm{Re}\,\phi'(z) - \sigma_{N(p)}. \tag{28}$$

In addition, let the point z approach a point t_{oj} on the upper side of j-th branch and use the Plemelj formula (see Figure 4b), from (20) and we have

$$\phi'^{+}(t_{oj}) = \frac{H}{2\pi t_{oj}} + \frac{ig'_j(t_{oj})}{2} + \frac{1}{2\pi} \sum_{k=1}^{N} \int_{L_k} \frac{g'_k(t)dt}{t - t_{oj}} \quad (t_{oj} \in L_j; \, j = 1, 2, \ldots, N). \tag{29}$$

Under the same condition, or $z \to t_{oj}$, from (28) and (29), it follows

$$\sigma_{T(p)}(t_{oj}) = 2 \operatorname{Re}\big(ig'_j(t_{oj})\big) + 2 \operatorname{Re}\left(\frac{H}{\pi t_{oj}} + \frac{1}{\pi} \sum_{k=1}^{N} \int_{L_k} \frac{g'_k(t)\,dt}{t - t_{oj}}\right) - \sigma_{N(p)}(t_{oj}). \tag{30}$$

Substituting (22) into (30) yields

$$\sigma_{T(p)}(t_{oj}) = 2 \operatorname{Re}\big(ig'_j(t_{oj})\big) + \sigma_{N(p)}(t_{oj}) - 2 \operatorname{Re}\big(M(t_{oj})\big). \tag{31}$$

The T-stress at the branch tip A_j in the perturbation field can be defined by (see Figure 4b)

$$T_{j(p)} = \text{ Regular part of } \{\sigma_{T(p)}(t_{o_j})\}\big|_{t_{oj} \to t_{Aj}}. \tag{32}$$

It was proved that the term $2 \operatorname{Re}(ig'_j(t_{oj}))$ is singular when $t_{oj} \to t_{Aj}$ and makes no contribution to the regular part. Therefore, from (31) and (32), the T-stress at the j-th branch tip in the perturbation field can be evaluated by $T_{j(p)} = \sigma_{N(p)}(t_{A_j}) - 2 \operatorname{Re}(M(t_{A_j}))$. Here, $M(t_{Aj})$ means a value of the integral $M(t_{oj})$ defined by (23) when the point t_{oj} is at the branch crack tip point t_{A_j}.

Considering $\sigma_{N(p)}(t_{o_j}) = -\sigma_{N(u)}(t_{o_j})$ and using (16) and (17), the T-stress at the branch tip A_j in the original field is finally obtained as follows:

$$T_j = \sigma_{T(u)}(t_{A_j}) - \sigma_{N(u)}(t_{A_j}) - 2 \operatorname{Re}\big(M(t_{A_j})\big). \tag{33}$$

In the numerical solution, the dislocation functions $g'_j(t)$ $(j = 1, 2, \ldots, N)$ are generally expressed in the form

$$g'_j(t) = \sqrt{\frac{t}{a_j - t}} G_j(t) \quad (0 \le t < a_j). \tag{34}$$

Equation (34) can model the one-half singularity at the crack tip simply because $g'_j(t) = O(a_j - t)^{-1/2}$ as $t \to a_j$. In addition, from (34) we have $g'_j(t) = O(t^{1/2})$ as $t \to 0$. This property may not coincide with the nature of the dislocation distribution at the concave corner. However, it is expected that the influence caused by the assumption $g'_j(t) = O(t^{1/2})$ as $t \to 0$ is minor.

Since the modeling of $-1/2$ singularity at the crack tip is the main point in the analysis; it is a generally accepted assumption that the weaker singularity at the kinked corner has no significant influence on the solution of the SIFs and T-stress. Although, this assertion is not easy to prove theoretically. In the literature, many researchers use this assumption in the branch or kinked crack problems [Theocaris 1977; Savruk 1981; Chen and Hasebe 1995].

In addition, the following quadrature rules are useful in the numerical solution [Boiko and Karpenko 1981]:

$$\frac{1}{\pi} \int_0^a \frac{f(t)}{t - x_j} \sqrt{\frac{t}{a - t}} \, dt = \sum_{m=1}^{M} \frac{w_m f(t_m)}{t_m - x_j}, \tag{35}$$

$$\frac{1}{\pi} \int_0^a g(t) \sqrt{\frac{t}{a - t}} \, dt = \sum_{m=1}^{M} w_m g(t_m), \tag{36}$$

where

$$w_m = \frac{a}{M} \sin^2\left(\frac{m\pi}{2M}\right) \quad (m = 1, 2, \ldots, M - 1), \qquad w_M = \frac{a}{2M}, \tag{37}$$

$$t_m = a \sin^2\left(\frac{m\pi}{2M}\right) \quad (m = 1, 2, \ldots, M), \qquad x_j = a \sin^2\left(\frac{(j - 0.5)\pi}{2M}\right) \quad (j = 1, 2, \ldots, M). \tag{38}$$

Here and after, the value M in the quadrature rules (35) and (36) is called the number of integration divisions.

In fact, after the quadrature rule shown by (35) is used for the integral (22), the number of unknowns after discretization of the integral equation is equal to the number of algebraic equations. However, there is one more equation coming from the single-valuedness condition of the displacements. Under this situation, it is suitable to introduce one more unknown, which is shown by the term with H ($H = H_1 + i H_2$) in (20) and (21). It is seen that after introducing H, the balance of the numbers of unknowns and equations in the relevant algebraic equation is possible [Chen and Hasebe 1995].

Finally, for evaluating the SIFs, one needs to take the following steps: obtain the solution for the dislocation distributions $g_k'(t)$ ($k = 1, 2, \ldots, N$) from the singular integral equations composed of (22) and (26) and obtain the SIFs at branch tips from (27).

In addition, for evaluating T-stress, one needs to take the following steps: obtain the value of $M(t_{A_j})$ ($M(t_{A_j}) = M(t_{oj})|_{t_{oj} = t_{A_j}}$) from (23), evaluate the two stress components $\sigma_{T(u)}(t_{A_j})$ and $\sigma_{N(u)}(t_{A_j})$ in the uniform field, and use (33).

From the above analysis, we see that the whole computation depends on the choice of the numbers of integration divisions for the branches. Once the numbers of integration divisions for the branches are assumed, the solution is obtained.

4. Numerical examination

In the present case, a kinked crack with kink length d is emanated from the main crack with crack length $2a$ (see Figure 5). In this case, the two coefficients in (3) need to be revised as follows:

$$c_{11}(\theta) = \frac{(1 + \cos\theta)\cos(\theta/2)}{2}\sqrt{\frac{a + 0.5d\cos\theta}{a}}, \quad c_{22}(\theta) = \frac{(3\cos\theta - 1)\cos(\theta/2)}{2}\sqrt{\frac{a + 0.5d\cos\theta}{a}}. \tag{39}$$

The reason for the modification shown by Equation (39) is as follows. In the case of $\sigma_x^\infty = \sigma_y^\infty = p$, we have $K_1^m = p\sqrt{\pi a}$, $K_2^m = 0$, and $T^m = 0$. In addition, if $\theta = 0$, from (3) and (39), we have $K_1^k = p\sqrt{\pi(a + 0.5d)}$. In fact, if the half crack length is $a + 0.5d$, the SIF must take the value $K_1^k = p\sqrt{\pi(a + 0.5d)}$. Clearly, this result is self-consistent.
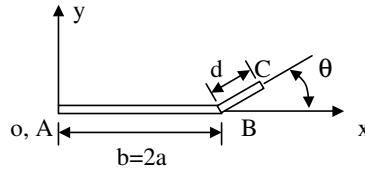
Figure 5. A kinked crack emanating from the main crack.

After substituting $\theta = 0$ in (6) and (7), we have $c_{12}(\theta) = 0$ and $c_{21}(\theta) = 0$. Therefore, the two coefficients $c_{12}(\theta)$, and $c_{12}(\theta)$ will not be affected.

In reality, only small crack kink angles were observed for isotropic materials, for example, a kinked angle of less than 30 degrees. For reference, the computed results up to 60 degrees are presented for the following three numerical examples.

The discretization for (22) and (26) is performed in the following manner. For a kinked crack with $d/b = 0.001$ (see Figure 5), we can assume the integration number $M_1 = 5$ (for $d/b = 0.001$) for the kinked portion, and $M_2 = 135$ for the main crack in (35) and (36). After discretization for (22), we can obtain $2 \times (M_1 + M_2)$ algebraic equations from (22), which are formulated on $M_1 + M_2$ observing points. Here, the factor of two is coming from the real and imaginary parts of equations. Similarly, after discretization for (26), we can obtain two algebraic equations. Therefore, there are a total of $2 \times (M_1 + M_2 + 1)$ equations obtained. In the meantime, there are a total of $2M_1$ unknowns from the kinked portion, or from the $g_1'(t)$ function at many discrete points. Similarly, there are a total of $2M_2$ unknowns from the main crack portion, or from the $g_2'(t)$ function at many discrete points. In addition, in (22) and (26), we have assumed two unknowns H_1 and H_2 (from $H = H_1 + i H_2$). Therefore, the are also a total of $2 \times (M_1 + M_2 + 1)$ unknowns.

4.1. *Numerical example 1.* In the first example, the following conditions are assumed:

$$\sigma_x^\infty = p; \qquad \theta = 0°, 10°, \ldots, 60°; \qquad d/b = 0.001, 0.01, 0.1, 0.25.$$

In computation, $M_1 = 5$ for $d/b = 0.001$, $M_1 = 15$ for $d/b = 0.01$, $M_1 = 35$ for $d/b = 0.1$, $M_1 = 55$ for $d/b = 0.25$ (the number of integration divisions in (35) and (36) is used for the kinked portion), and $M_2 = 135$ for the main crack portion. The computed results for the SIFs and the T-stress at the kinked crack tip C in Figure 5 are expressed as

$$K_1^k = F_1\left(\frac{d}{b}, \theta\right) p\sqrt{\pi(a + 0.5d\cos\theta)}, \tag{40}$$
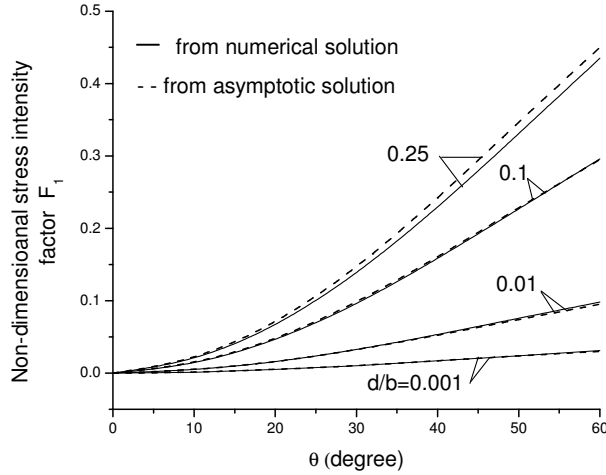
$$K_2^k = F_2\left(\frac{d}{b}, \theta\right) p\sqrt{\pi(a + 0.5d\cos\theta)}, \tag{41}$$

$$T^k = F_T\left(\frac{d}{b}, \theta\right) p. \tag{42}$$

The computed results for the SIFs and the T-stress are plotted in Figures 6–8, respectively.

In addition, for the main crack before kinking we have

$$K_1^m = 0, \qquad K_2^m = 0, \qquad T^m = p. \tag{43}$$

Figure 6. Nondimensional mode I SIF $F_1(d/b, \theta)$, from the numerical solution and from the asymptotic solution for a kinked crack under remote loading $\sigma_x^\infty = p$ (see Figure 5 and Equation (40)).

Further, by using (3)–(5), (7), (8), and (39), the relevant SIFs and the T-stress in the asymptotic solution can also be expressed by the same equations (40)–(42). Those results are also shown in Figures 6–8.

From the plotted results, the following properties have been found. Since $K_1^m = 0$ and $K_2^m = 0$ for the case of the main crack, the values of K_1^k and K_2^k are generally small. Secondly, the coincidence for the SIFs from the numerical and asymptotic solutions has been found.

For the values of K_1^k in the three cases $d/b = 0.001$, 0.01, and 0.1, the coincidence is good between the numerical and asymptotic solutions. However, in the case of $d/b = 0.25$, some deviations between the two solutions have been found. For the values of K_2^k in the two cases $d/b = 0.001$ and 0.01, the coincidence is good between the numerical and asymptotic solutions. However, in the cases $d/b = 0.1$ and 0.25, some deviations between the two solutions have been found, particularly for $\theta \geq 50°$. For the values of T^k in the four cases $d/b = 0.001$, 0.01, 0.1, and 0.25, the computed results from the numerical solutions merge into one curve, and the results deviate slightly from those from the asymptotic solution.

4.2. *Numerical example 2.* In the second example, the remote loading is $\sigma_y^\infty = p$ and the other computation conditions are same as in the first example. The computed results for the SIFs and the T-stress at the kinked crack tip C in Figure 5 are expressed by the same equations (40)–(42). The computed results for the SIFs and the T-stress are plotted in Figures 9–11, respectively.

In addition, for the main crack before kinking we have

$$K_1^m = p\sqrt{\pi a}, \qquad K_2^m = 0, \qquad T^m = -p. \tag{44}$$

Further, by using (3)–(5), (7), (8), and (39), the relevant SIFs and the T-stress in the asymptotic solution can also be expressed by the same equations (40)–(42). Those results are also shown in Figures 9–11.

For the values of K_1^k in the two cases $d/b = 0.001$, and 0.01, the coincidence is good between the numerical and asymptotic solutions. However, in the cases of $d/b = 0.1$ and 0.25, some deviations between the two solutions have been found. For the values of K_2^k in the four cases $d/b = 0.001$, 0.01,
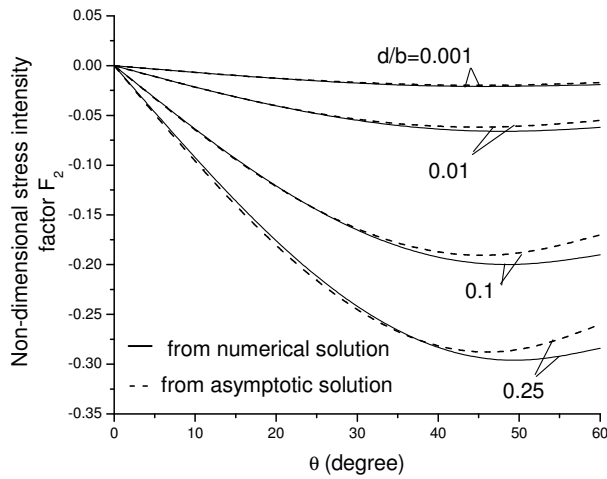
Figure 7. Nondimensional mode II SIF $F_2(d/b, \theta)$, from the numerical solution and from the asymptotic solution for a kinked crack under remote loading $\sigma_x^\infty = p$ (see Figure 5 and Equation (41)).
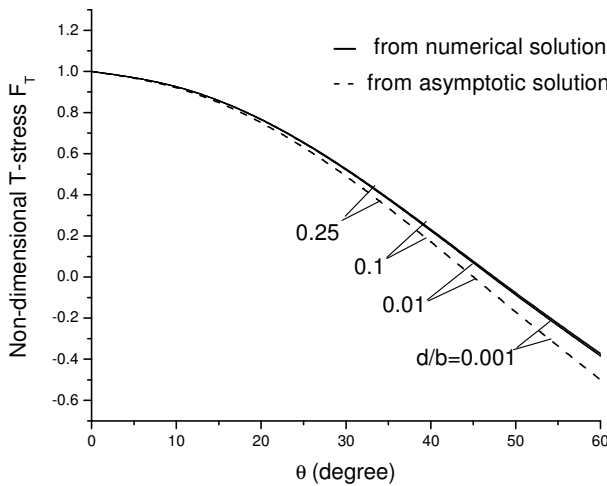
Figure 8. Nondimensional T-stress $F_T(d/b, \theta)$, from the numerical solution and from the asymptotic solution for a kinked crack under remote loading $\sigma_x^\infty = p$ (see Figure 5 and Equation (42)).

0.1, and 0.25, the coincidence is good between the numerical and asymptotic solutions. For the values of T^k in the two cases $d/b = 0.001$ and 0.01, the coincidence is good between the numerical and asymptotic solutions. However, in the cases of $d/b = 0.1$ and 0.25, some deviations between the two solutions have been found.

4.3. *Numerical example 3.* In the third example, the remote loading is $\sigma_{xy}^\infty = -p$ and the other computation conditions are same as in the first example. The computed results for the SIFs and the T-stress at

the kinked crack tip C in Figure 5 are expressed by the same equations (40)–(42). The computed results for the SIFs and the T-stress are plotted in Figures 12–14, respectively.

In addition, for the main crack before kinking we have

$$K_1^m = 0, \qquad K_2^m = -p\sqrt{\pi a}, \qquad T^m = 0. \tag{45}$$

Further, by using Equations (3)–(5), (7), (8), and (39), the relevant SIFs and the T-stress in the asymptotic solution can also be expressed by the same Equations (40)–(42). Those results are also shown in Figures 12–14.
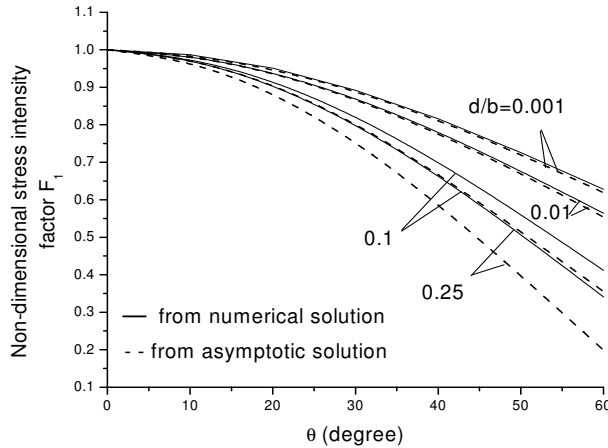
Figure 9. Nondimensional mode I SIF $F_1(d/b, \theta)$, from the numerical solution and from the asymptotic solution for a kinked crack under remote loading $\sigma_y^\infty = p$ (see Figure 5 and Equation (40)).
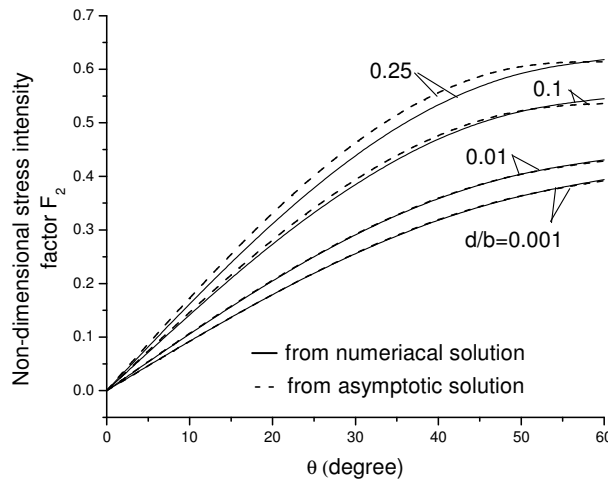
Figure 10. Nondimensional mode II SIF $F_2(d/b, \theta)$, from the numerical solution and from the asymptotic solution for a kinked crack under remote loading $\sigma_y^\infty = p$ (see Figure 5 and Equation (41)).

Figure 11. Nondimensional T-stress $F_T(d/b, \theta)$, from the numerical solution and from the asymptotic solution for a kinked crack under remote loading $\sigma_y^\infty = p$ (see Figure 5 and Equation (42)).

Figure 12. Nondimensional mode I SIF $F_1(d/b, \theta)$, from the numerical solution and from the asymptotic solution for a kinked crack under remote loading $\sigma_{xy}^\infty = -p$ (see Figure 5 and Equation (40)).

For the values of K_1^k in the four cases $d/b = 0.001$, 0.01, 0.1, and 0.25, the coincidence is good between the numerical and asymptotic solutions. For the values of K_2^k in the four cases $d/b = 0.001$, 0.01, 0.1, and 0.25, some deviations between the two solutions have been found. Particularly, the values of K_2^k in the asymptotic solution do not depend on the ratio d/b, and it is not reasonable. For the values of T^k in the two cases $d/b = 0.001$ and 0.01, some deviations between the two solutions have been found. However, in the cases of $d/b = 0.1$ and 0.25, the coincidence is good between the numerical and asymptotic solutions.
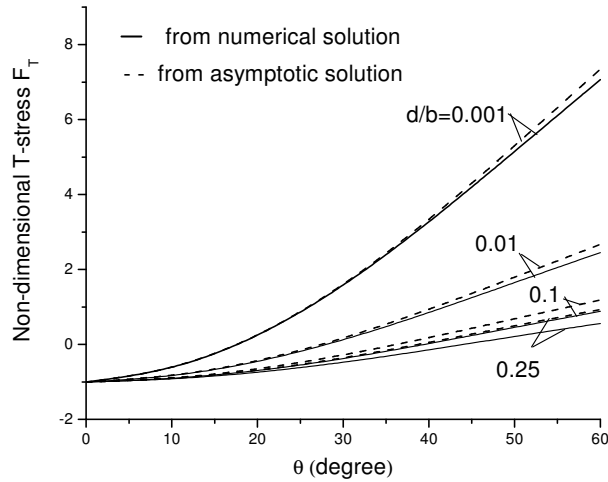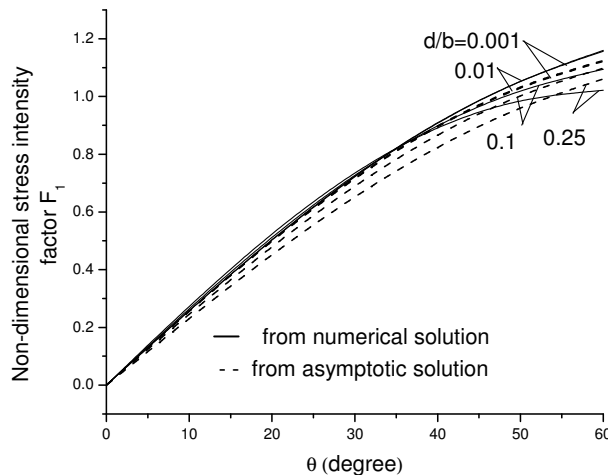
Figure 13. Nondimensional mode II SIF $F_2(d/b, \theta)$, from the numerical solution and from the asymptotic solution for a kinked crack under remote loading $\sigma_{xy}^{\infty} = -p$ (see Figure 5 and Equation (41)).
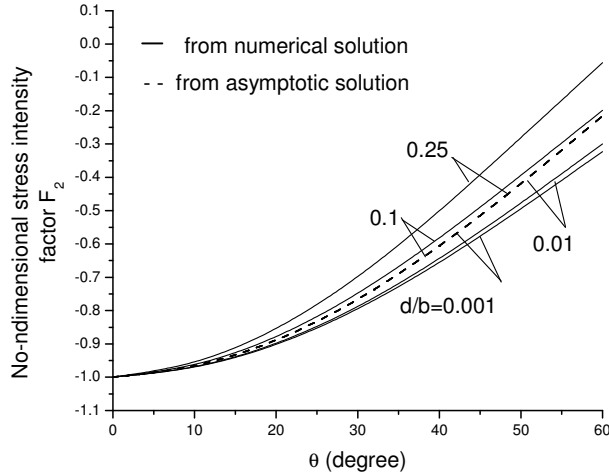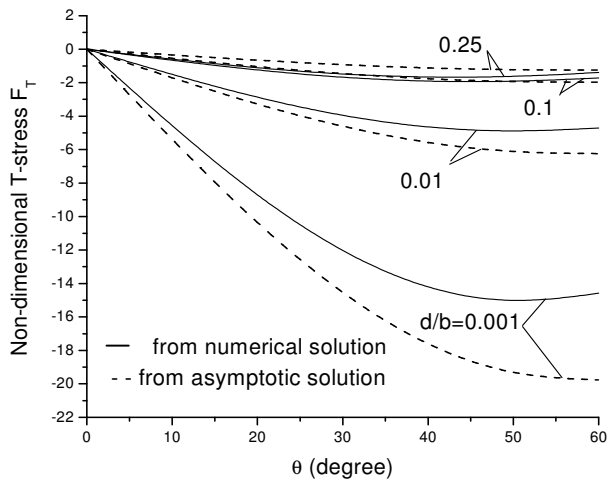

Figure 14. Nondimensional T-stress $F_T(d/b, \theta)$, from the numerical solution and from the asymptotic solution for a kinked crack under remote loading $\sigma_{xy}^{\infty} = -p$ (see Figure 5 and Equation (42)).

5. Conclusion

In this paper, an efficient numerical solution for a kinked crack with a finite kink has been developed. The aim of the present study is to examine the accuracy in the solutions for the stress intensity factors (SIFs) and T-stress from the asymptotic solution. A particular advantage of the asymptotic solution is that it provides an explicit form for the solutions. However, the asymptotic solution itself cannot examine the accuracy achieved in the solution. The suggested numerical solution will give a full examination of the results obtained in the asymptotic solution.

In this paper, the computed results for the SIFs and T-stress for the studied problem are given. From the computed results in the numerical solution and the results in the asymptotic solution, the following conclusion can be reached. For a configuration of the kinked crack within the ranges: $d/b = 0.001$, 0.01, 0.1 and 0.25 and $0° \leq \theta \leq 60°$ (see Figure 5); and for the remote loadings: $\sigma_x^\infty = p$, $\sigma_y^\infty = p$, or $\sigma_{xy}^\infty = -p$, the asymptotic solution can provide a qualitatively correct solution. This situation can be seen from Figures 6–14.

However, under some conditions, the asymptotic solution cannot provide quantitatively accurate results. For the SIFs, it is expected that the asymptotic solution can provide a reasonable results only for the following ranges: for a configuration of the kinked crack within the range: $d/b < 0.01$ and $0° \leq \theta \leq 20°$ (see Figure 5); and for the remote loadings: $\sigma_x^\infty = p$, $\sigma_y^\infty = p$, or $\sigma_{xy}^\infty = -p$. For the computed values of the T-stresses, the situation is not the same as in the case of the SIFs. For example, in the conditions $d/b < 0.01$, $\theta \geq 30°$, and $\sigma_{xy}^\infty = -p$, the asymptotic solutions for the T-stress shown in Figure 14 cannot provide accurate results.

References

[Betegón and Hancock 1991] C. Betegón and J. W. Hancock, "Two-parameter characterization of elastic-plastic crack-tip fields", *J. Appl. Mech. (ASME)* **58**:1 (1991), 104–110.

[Boiko and Karpenko 1981] A. V. Boiko and L. N. Karpenko, "On some numerical methods for the solution of the plane elasticity problem for bodies with cracks by means of singular integral equation", *Int. J. Fract.* **17**:4 (1981), 381–388.

[Broberg 2005] K. B. Broberg, "A note on *T*-stress determination using dislocation arrays", *Int. J. Fract.* **131**:1 (2005), 1–14.

[Chen 2004] Y. Z. Chen, "Solution of integral equation in curve crack problem by using curve length coordinate", *Eng. Anal. Bound. Elem.* **28**:8 (2004), 989–994.

[Chen and Hasebe 1995] Y. Z. Chen and N. Hasebe, "New integration scheme for the branch crack problem", *Eng. Fract. Mech.* **52**:5 (1995), 791–801.

[Cotterell and Rice 1980] B. Cotterell and J. R. Rice, "Slightly curved or kinked cracks", *Int. J. Fract.* **16**:2 (1980), 155–169.

[Dutta et al. 1991] B. K. Dutta, A. Kakodkar, and S. K. Maiti, "Two singular points finite elements in the analysis of kinked cracks", *Comput. Mech.* **7**:5–6 (1991), 329–339.

[Fett 2001] T. Fett, "Stress intensity factors and *T*-stress for internally cracked circular disks under various boundary conditions", *Eng. Fract. Mech.* **68**:9 (2001), 1119–1136.

[Fett et al. 2006] T. Fett, G. Rizzi, and H.-A. Bahr, "Green's functions for the *T*-stress of small kink and fork cracks", *Eng. Fract. Mech.* **73**:10 (2006), 1426–1435.

[Karihaloo and Xiao 2001] B. L. Karihaloo and Q. Z. Xiao, "Higher order terms of the crack tip asymptotic field for a notched three-point bend beam", *Int. J. Fract.* **112**:2 (2001), 111–128.

[Larsson and Carlsson 1973] S. G. Larsson and A. J. Carlsson, "Influence of non-singular stress terms and specimen geometry on small-scale yielding at crack tips in elastic-plastic materials", *J. Mech. Phys. Solids* **21**:4 (1973), 263–277.

[Li and Xu 2007] X.-F. Li and L. R. Xu, "*T*-stresses across static crack kinking", *J. Appl. Mech. (ASME)* **74**:2 (2007), 181–190.

[Lo 1978] K. K. Lo, "Analysis of branched cracks", *J. Appl. Mech. (ASME)* **45**:4 (1978), 797–802.

[Melin 1986] S. Melin, "On singular integral equations for kinked cracks", *Int. J. Fract.* **30**:1 (1986), 57–65.

[Melin 1994] S. Melin, "Accurate data for stress intensity factors at infinitesimal kinks", *J. Appl. Mech. (ASME)* **61**:2 (1994), 467–470.

[Melin 2002] S. Melin, "The influence of the *T*-stress on the directional stability of cracks", *Int. J. Fract.* **114**:3 (2002), 259–265.

[Muskhelishvili 1953] N. I. Muskhelishvili, *Some basic problems of the mathematical theory of elasticity*, Noordhoff, Groningen, 1953.

[Rice 1974] J. R. Rice, "Limitations to the small scale yielding approximation for crack tip plasticity", *J. Mech. Phys. Solids* **22**:1 (1974), 17–26.

[Savruk 1981] M. P. Savruk, *Two-dimensional problems of elasticity for body with crack*, Naukova Dumka, Kiev, 1981. In Russian.

[Theocaris 1977] P. S. Theocaris, "Asymmetric branching of cracks", *J. Appl. Mech.* (*ASME*) **44**:4 (1977), 611–618.

[Williams 1957] M. L. Williams, "On the stress distribution at the base of a stationary crack", *J. Appl. Mech.* (*ASME*) **24**:1 (1957), 109–114.

[Xiao and Karihaloo 2002] Q. Z. Xiao and B. L. Karihaloo, "Approximate Green's functions for singular and higher order terms of an edge crack in a finite plate", *Eng. Fract. Mech.* **69**:8 (2002), 959–981.

[Yang and Ravi-Chandar 1999] B. Yang and K. Ravi-Chandar, "Evaluation of elastic *T*-stress by the stress difference method", *Eng. Fract. Mech.* **64**:5 (1999), 589–605.

Y. Z. CHEN: chens@ujs.edu.cn
Division of Engineering Mechanics, Jiangsu University, Xue Fu Road 301, Zhenjiang, Jiangsu 212013, China

X. Y. LIN: xiaoyun39527@yahoo.com
Division of Engineering Mechanics, Jiangsu University, Xue Fu Road 301, Zhenjiang, Jiangsu 212013, China

Z. X. WANG: wzx-5566@163.com
Division of Engineering Mechanics, Jiangsu University, Xue Fu Road 301, Zhenjiang, Jiangsu 212013, China

NUMERICAL HOMOGENIZATION TECHNIQUES FOR THE EVALUATION OF MECHANICAL BEHAVIOR OF A COMPOSITE WITH SMA INCLUSIONS

VALERIO ALECCI, SILVIA BRICCOLI BATI AND GIOVANNA RANOCCHIAI

Numerical procedures are developed for the homogenization and evaluation of the stress field in a composite as a consequence of the presence of embedded SMA (shape-memory alloy) wires. In particular, the elastic field developed at the end of the SMA wire self-strain process is studied, knowledge of which is necessary to evaluate the feasibility of such a hybrid composite.

First, the numerical procedures are applied to the study of both a representative volume element (RVE) included in a theoretically infinite periodic medium and a RVE located near the medium free boundary, in order to evaluate the tangential stress field generated at the end of the fiber; then they are applied to the study of a plate able to bend after the effect of self-strain of the SMA wire.

Observations are reported about the obtained results and about the similarities and the differences between the two problems.

1. Introduction

In the early 1990s, as the exciting potential of hybrid composites [Ahmad et al. 1990] came to be understood, researchers investigated a range of problems, from the mechanical aspects of such materials [Boyd and Lagoudas 1994; Barrett and Gross 1996; Aboudi 1997] to their construction, characterization, and production [Wei et al. 1997]. More recently, significant attention has been given to polymeric matrix adaptive composites [Bidaux et al. 1994], cement matrix composites [Zheng et al. 2001], metal matrix (aluminum), and carbon or glass fiber-reinforced matrix composites [Wei et al. 1997]. Particularly, in [Baltá et al. 2002; Xu et al. 2002; Zheng et al. 2002; Murasawa et al. 2004; Tsoi et al. 2004], some specimens of composite material with integrated SMA (shape-memory alloy) wires are presented.

An interesting analysis of the interfacial quality in activated shape-memory alloy composites (CSMA) appeared in [Zheng et al. 2003]. Qualitative aspects were experimentally evaluated by differential scanning calorimeter, and quantitative results were obtained assuming that the behavior of the two phases, fiber and matrix, was linearly elastic. The radial and circumferential stress was calculated from the thermoelasticity solution provided by Hecker et al. [1970] to evaluate the residual stresses in composite cylinders originated during the cooling of the composite from fabrication temperatures.

Recently, works by Marfia and Sacco [2005] and Marfia [2005] were published, concerning micromechanical modeling of SMA-wire-reinforced materials. The authors proposed two homogenization procedures based on the following assumptions: the martensite volume fraction depends on the wire temperature and only on the normal stress acting in the fiber direction, and the inelastic strain occurs along the fiber direction. A finite element model in the two-dimensional setting for SMA hybrid composite plates was proposed by Daghia et al. [2006]. Finally, [Marfia and Sacco 2007] presents a nonlinear

Keywords: numerical homogenization, composite materials, shape-memory alloys.

laminate finite element able to reproduce both superelasticity and a memory effect for a laminated plate containing one or more ply made of SMA reinforced composite. These authors apply numerical homogenization procedures in order to develop the overall mechanical response of a CSMA, as a step of evolutive multiscale analysis.

The use of homogenization techniques seems quite apt to analyze the problem of the stress field induced by the self-strain of a portion of material, as the basic formulas of homogenization techniques were derived simulating the homogeneous deformation of an ellipsoidal region surrounded by elastic material [Eshelby 1957]. The development of numerical homogenization techniques for periodic media in the 80's [Duvaut 1984; Suquet 1985] produced the analytical solution for homogenization problems in which the shape of the periodic cell is by far dissimilar to ellipsoid, elliptic cylinders, or ribbons. In particular, several applications were developed in order to deduce at first in-plane elastic characteristics of masonry panels, characterized by two-directional periodicity under a plane stress assumption, generalized plane strain, and three-directional modeling [Anthoine 1995; 1997]; recently, out-of-plane characteristics of masonry walls were deduced via numerical homogenization [Cecchi et al. 2005; Milani et al. 2006].

In this paper the development of a numerical procedure for the homogenization and the evaluation of the stress field in a composite as a consequence of the shape-memory effect of embedded SMA wires are described. In particular, the elastic field developed at the end of the self-strain process of the SMA wire is studied, neglecting the intermediate stages. The stress state that is produced in the composite at the final stage is the most severe of the whole load history and knowledge of it is necessary to evaluate the feasibility of such a hybrid composite.

At first, the numerical homogenization procedure is applied to the study of an infinite medium, then to the study of a plate able to bend after the effect of self-strain of the SMA wire.

The paper is organized as follows: Section 2 is devoted to the homogenization procedure and to the evaluation of the elastic field produced by the activation of the SMA wires, for a three-dimensional solid; attention was focused on the boundary condition and on the possible load conditions; the derivation of the null condition for the average stress is reported in the Appendix; the results obtained for a case study are reported. Section 3 is devoted to the homogenization procedure and to the evaluation of the elastic field produced by the activation of the SMA wires embedded in a plate; the results for a case study are reported. Finally, conclusions are reported in Section 4.

2. Elastic field in a three-dimensional solid

2.1. *Homogenization.* The composite material subjected to analysis is a matrix-fiber composite made of resin and aligned SMA wires (150 μm in diameter) assumed to be in a regular array according with Figure 1. The span between the wires is 0.6 mm, and as a consequence, the volume fraction of the inclusion is about 5%. The two phases are assumed to be isotropic with the following elastic constants: $E = 70000$ MPa and $\nu = 0.33$ (fiber), and $E = 20000$ MPa and $\nu = 0.4$ (matrix). The values indicated for the SMA fiber represent the effective properties of a typical Ni-Ti alloy, while the Young's modulus and Poisson's ratio of the matrix might agree with those of a composite matrix made of epoxy resin with glass additives inside.

Homogenization techniques aim at describing the behavior of a heterogeneous material by means of the laws of a homogeneous material that is equivalent in some sense. The problem is not trivial when the
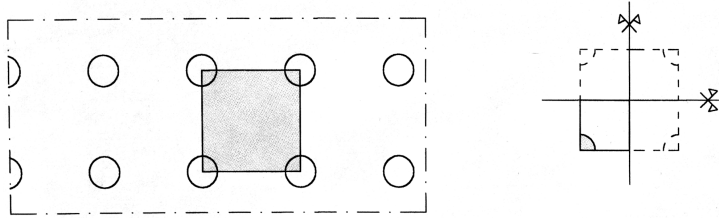
Figure 1. Left: schematic representation of the composite with embedded SMA fibers and localization of the unit cell. The plane shown is perpendicular to the fiber length. Right: region subjected to numerical analysis (continuous line).

parameters to be determined are not additive (extensive) quantities, as in the case of elasticity. Elastic coefficients in fact, like other intensive quantities, cannot be directly averaged in the volume of the body, as they take part in the functional laws among additive quantities.

We wish to produce a macroscopically homogeneous stress field in a heterogeneous body; that is, every representative volume element (RVE) is subjected to the same stress state.

The homogenized elastic tensor at a point x being $T(x) = K(x)D(x)$, the local constitutive relation the between the stress and strain tensors can be defined as

$$\langle T \rangle = K^{\text{hom}} \langle D \rangle, \tag{2-1}$$

where

$$\langle T \rangle = \frac{1}{V} \int_V T \, dV, \qquad \langle D \rangle = \frac{1}{V} \int_V D \, dV. \tag{2-2}$$

To calculate the components of K^{hom}, we must produce an elementary strain state, one of the form

$$D_1 = \begin{bmatrix} 1 & 0 & 0 \\ 0 & 0 & 0 \\ 0 & 0 & 0 \end{bmatrix}, \qquad D_2 = \begin{bmatrix} 0 & 0 & 0 \\ 0 & 1 & 0 \\ 0 & 0 & 0 \end{bmatrix}, \qquad \dots, \qquad D_6 = \begin{bmatrix} 0 & 0 & 0 \\ 0 & 0 & 1 \\ 0 & 1 & 0 \end{bmatrix}. \tag{2-3}$$

To do this, Hashin's lemmas are commonly used when dealing with nonperiodic heterogeneous materials, which guarantee that $\langle T \rangle = T$ if $Tn = \langle T \rangle n$ on ∂V and T is divergence free, and $\langle D \rangle = D$ if $u = Dx$ on ∂V.

When dealing with periodic heterogeneous materials the periodic cell represents the RVE; if the cell is sufficiently far from the boundary, stress and strain are periodic fields and periodicity conditions may be assumed on the border of the periodic cell, that is $t = Tn$ antiperiodic and $u = \langle D \rangle x + u^p$, where u^p is periodic, that is assumes the same value on the boundary of the cell.

The last equality can be written

$$D(u) = \langle D \rangle + D(u^p) \tag{2-4}$$

or

$$u_1 = d_{11}x_1 + d_{12}x_2 + d_{13}x_3 + u_1^{\text{per}}, \quad u_2 = d_{21}x_1 + d_{22}x_2 + d_{23}x_3 + u_2^{\text{per}}, \quad u_3 = d_{31}x_1 + d_{32}x_2 + d_{33}x_3 + u_3^{\text{per}}.$$

The field equations of elasticity, neglecting the body forces, are

$$\text{div}\big(K(x)D(u)\big) = 0 \tag{2-5}$$

and substituting the expression of displacement from (2-4):

$$\operatorname{div}\big(K(\boldsymbol{x})D(\boldsymbol{u}^p)\big) + \operatorname{div}\big(K(\boldsymbol{x})\langle D\rangle\big) = 0. \tag{2-6}$$

$K(\boldsymbol{x})$ is the local value of the elastic tensor and is constant within each phase and discontinuous on the border between the materials. For this reason the second term of (2-6) takes the form of a body force spread over the interface ∂S between the phases:

$$\boldsymbol{f} = (K_2 - K_1)\langle D\rangle \boldsymbol{n}\delta_{\partial S}, \tag{2-7}$$

where $\boldsymbol{n}$ is the unit vector normal to ∂S from phase 2 to phase 1 [Suquet 1985].

If we solve with FEM analysis the problem of (2-6) assigning $\boldsymbol{f}$ from (2-7) as produced by an elementary homogeneous strain tensor, the homogenized elasticity tensor can be calculated from (2-1), where $\langle D\rangle$ is the imposed elementary strain, $D(\boldsymbol{u}^p)$ is the result of the numerical analysis and, due to the linearity of the model, superposition of the elastic state applies:

$$\langle T\rangle = \frac{1}{V}\int_V K\big(D(\boldsymbol{u}^p) + \langle D\rangle\big)\,dV. \tag{2-8}$$

The elements of the homogenized elasticity tensor are calculated separately producing the different elementary strain tensors in the numerical model, by means of (2-7).

A solution of (2-6) by means of FEM analysis can be achieved with the proper boundary conditions on the cell chosen as the representative volume element of the homogenization problem; this choice is crucial. It is well known that several representative volume elements can be chosen to describe a periodic geometry, associated with the appropriate frame of reference and with appropriate integers representing the periods of the geometry [Anthoine 1995]. Usually the smallest one is thought to be the most useful, as the number of unknowns to be determined in the FEM calculation is fewer. On the contrary, as it will be shown, the use of a symmetric RVE may be preferable to a smaller one, because of the ease in imposing boundary conditions [Suquet 1985].

Assume for the periodic solid of Figure 1 a representative volume element characterized by two symmetry planes and an orthogonal frame of reference. Actually, the plane orthogonal to the fiber can be thought of as a symmetry plane as well. The volume subjected to numerical analysis (see Figure 2) is
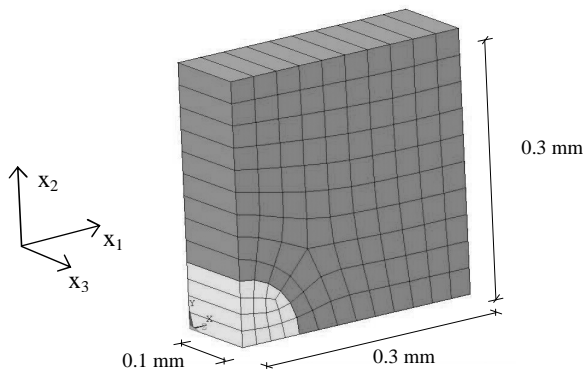
Figure 2. Element subjected to numerical analysis in the case of RVE far from the boundary.

one-quarter of the representative volume element. In this case, it is evident that the periodicity planes represent, also, symmetry planes with respect to the composite pattern.

The body forces applied to the interface between the two materials and deduced from (2-6) and from the elementary strain states, are in turn symmetric and skew symmetric. In particular, when unit strain tensors D_1, D_2, and D_3 are applied, the stress vector field in the interface is symmetric, and, due to the symmetry, the constraints prevent the boundary of the RVE from performing displacements normal to the boundary itself. This means that, on the boundary, $\boldsymbol{u}^p$ has no components out of the boundary planes. The final deformed RVE will display undistorted planes, which are not deformed with respect to the displacement component orthogonal to the plane itself. Figure 3 shows strain fluctuation, homogeneous strain, and total strain for the RVE chosen for the analysis of the composite under investigation,

When unit strain tensors D_4, D_5, and D_6 are applied, the stress vector field in the interface is skew symmetric, and, due to the symmetry, the constraints prevent the boundary of the RVE from performing displacements parallel to the boundary itself. This means that, on the boundary, $\boldsymbol{u}^p$ has no components on the boundary planes. The final deformed RVE will display planes not deformed with respect to the displacement components parallel to the planes.

According to several authors, the elementary strain can be otherwise imposed directly on the RVE with the so called displacement method [Lukkassen et al. 1995]. In this case the boundary conditions must be compatible with the periodicity but must impose, in turn, the desired boundary displacement; for example the homogeneous strain D_1 can be directly imposed substituting the boundary condition on the displacement $u_1 = D_1 x_1$ in place of the homogeneous boundary condition $u_1 = 0$. The other boundary conditions are not as easy to visualize as in the previous case and an accurate analysis of the displacement field and of the algebraic representation of the periodicity conditions is necessary.

As a comparison, the homogenization procedure was performed with the closed-form method described by Zhao and Weng [1990], which makes use of the elastic solution derived by Eshelby [1957] in the case of an infinitely extended matrix containing an ellipsoidal inhomogeneity. Here, the theory of Mori and Tanaka [1973] was not applied to extend Eshelby's solution in order to account for the reciprocal influence of inclusions, since the latter is not significant when the volume fraction is lower than 10%. Eshelby's solution was employed to determine stress and strain localization tensors in the inclusion and the average localization tensors in the matrix.
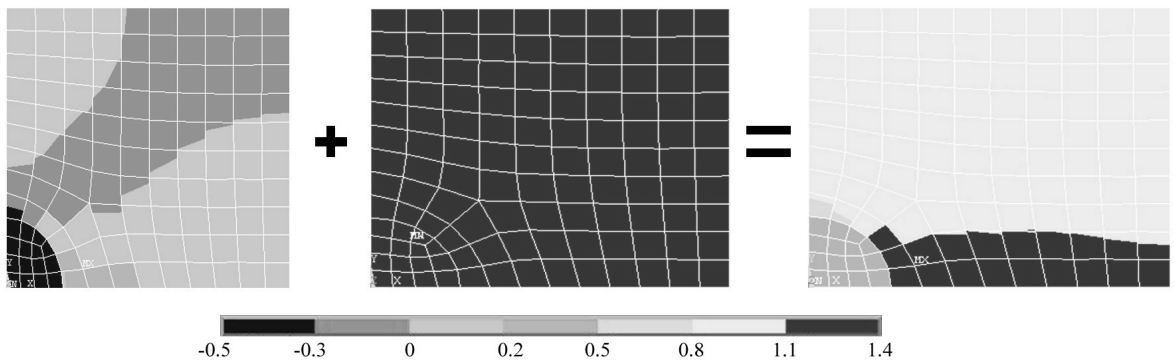
Figure 3. Fluctuation of strain, homogeneous strain, and total strain.

Model	$k_{11} = k_{22}$	k_{33}	$E_x = E_y$	E_z	$G_{yz} = G_{zx}$	G_{xy}
Closed-form	44298.6	45558.4	21264.1	22461.0	7717.5	7682.5
Numerical RVE far from body boundary	44320.8	45559.1	21302.7	22461.2	7021.2	6923.4
Numerical RVE near body boundary	44612.3	–	–	–	–	6927.2

Table 1. Main components of stiffness tensor, Young's modulus, and shear modulus for RVE determined by means of the closed-form procedure and numerical homogenization (in units of MPa).

According to the classical homogenization procedure [Suquet 1985], the homogenized stiffness tensor K^{hom} is obtained by the average of the stiffness tensors of the phases weighed with the strain localization tensors $B_i(\boldsymbol{x})$: $K^{\text{hom}} = c_1 K_1 \langle B_1(\boldsymbol{x}) \rangle + c_2 K_2 \langle B_2(\boldsymbol{x}) \rangle$, where c_1 and c_2 are the concentration factors, K_1 and K_2 the stiffness tensors, and $B_1(\boldsymbol{x})$ and $B_2(\boldsymbol{x})$ the localization tensors of the two phases.

Table 1 reports the homogenized elastic constants of the composite material determined with the numerical homogenization procedure described, along with those computed by means of the closed-form homogenization procedure.

2.2. Self-strain induced by SMA activation. In order to evaluate the strain state induced by the activation of the SMA wires, it is sufficient to apply on the boundary of the wire within the composite, the surface stress that would have produced the self-strain in the wire out of the composite; this approach follows the one proposed by Eshelby [1957]. In particular, the strain state produced by the activation of the SMA is purely deviatoric and can be represented by a strain tensor of the type

$$D' = r \begin{bmatrix} -\frac{1}{2} & 0 & 0 \\ 0 & -\frac{1}{2} & 0 \\ 0 & 0 & 1 \end{bmatrix}, \tag{2-9}$$

where r represents the axial self-strain capability of the wire. The stress vector field to be applied on the surface of the wire in the composite takes the form

$$\boldsymbol{f} = (K_2) D' \boldsymbol{n} \delta_{\partial S}, \tag{2-10}$$

where $\boldsymbol{n}$ is the outward unit normal vector. Owing to the geometric symmetry of the cylinder representing the SMA wire, the stress field is symmetric with respect to the planes that define the RVE. For this reason the boundary of the RVE in the final stage will be undistorted, as it is in the case of the homogenization of the strain tensors D_1, D_2, and D_3. It is necessary to produce a constraint system on the RVE that forces this kind of deformation; this can be achieved by imposing on the boundary of the RVE the same constraint as in the homogenization procedure, that is, preventing the boundary of the RVE from performing displacements normal to the boundary. When this is done, only the fluctuating part of the strain is computed, while the homogeneous part has to be determined subsequently.

The stress state corresponding to the fluctuating part of displacement can be computed from the elastic state obtained via the numerical analysis of the RVE, simply subtracting from the elements constituting the SMA inclusion the stress corresponding to the self-strain, so that equilibrium is reintroduced on the boundary of the SMA wire:

Model	$\langle \varepsilon_x \rangle = \langle \varepsilon_y \rangle$	$\langle \varepsilon_z \rangle$
Numerical RVE far from body boundary	0.003455	−0.007591
Numerical RVE near body boundary	0.001610	−

Table 2. Average strain of the composite material produced by a self-strain $r = 5\%$.

$$T = -(K_2)D' \quad \text{in } V_2. \tag{2-11}$$

In order to determine the homogeneous part of the strain field to be superimposed on the fluctuating part determined by the numerical analysis, the condition that the volume average of stress has to be zero in a body subjected to self-strain induced by internal causes is usually introduced:

$$\langle T \rangle = \sum_{j=1}^{6} \alpha_j \langle T(D_j) \rangle + \int_{\text{RVE}} T^{\text{num}} dV = 0. \tag{2-12}$$

This is formally a set of six equations in six unknowns, but the average stresses corresponding to D_4, D_5, and D_6 vanish because of the symmetry conditions, so the forth, fifth, and sixth equations are identities. The proof of this argument is given in the Appendix.

Table 2 reports the values of the average strain produced in the composite by the activation of the SMA wires, and also, on the last line, the results of the analysis of an RVE supposed to be near to the border of the body. The periodicity conditions are modified, as the x_3 axis is no longer a direction of periodicity. The analysis has been performed on a RVE long enough to represent, in correspondence with the mean plane, the behavior of the RVE analyzed before and supposed as far from the boundary. Figure 4 reports the tangential stress on transversal cross sections of the RVE in correspondence with a
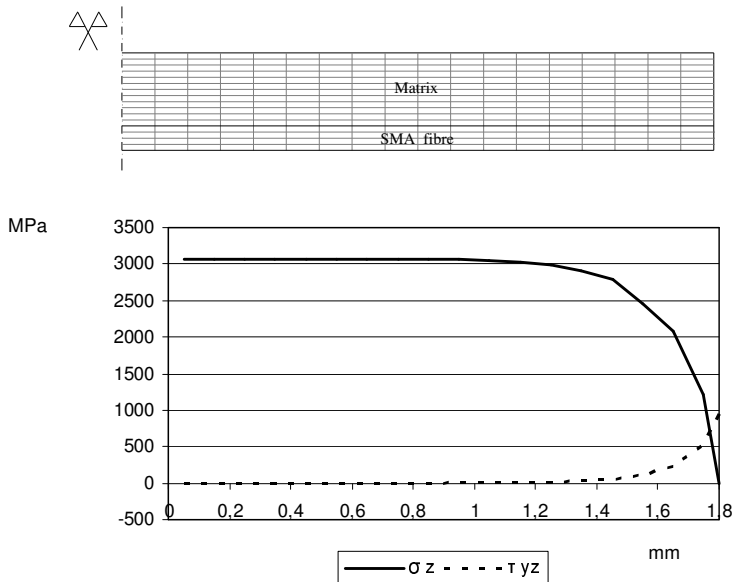
Figure 4. Normal and tangential stress (MPa) in the elements of inclusion corresponding with interface, as a function of the distance from the symmetry plane (mm).

progressively larger distance from the boundary of the body. These results can be employed to evaluate the tangential stresses that are generated at the end of the fiber and to check the feasibility of such a composite once the adhesion capability of the two phases is known.

3. Elastic field in a plate

In this paper attention is focused on the bending of a plate produced by the self-strain of an embedded SMA wire. The plate is supposed free from constraints and made of a resin characterized by low elastic modulus and high break deformation, which also supports the relatively large strain capability of the SMA wire. The polyester resin Distitron® 166 UV was selected for the analysis and tested in compression according to [ISO 604 1993]. The experimental campaign carried out on three different polymer materials is described in [Alecci and Ranocchiai 2007].

   The eccentricity of the wire with respect to the middle plane of the plate produces the bending of the plate, and is the cause of the coupling of the normal strain and moments, as well as the curvature and normal stress resultants.

3.1. *Homogenization.* The geometry of the medium is shown in Figure 5. The RVE and the coordinate system are shown in Figure 6. The SMA wire was 500 μm in diameter and, as a consequence, the volume fraction of the inclusion is about 2%. The two phases are assumed to be isotropic with the following elastic constants: $E = 70000$ MPa and $\nu = 0.33$ (fiber), and $E = 900$ MPa and $\nu = 0.4$ (matrix). The periodicity condition is valid along the x_1 and x_3 axes. The linear segments orthogonal to the middle plane are assumed to remain linear after the deformation and rotation is assumed small.

   The strain periodic displacement field that respects the periodicity conditions and guarantees the kind of deformation assumed previously is that proposed by Anthoine [1995]:

$$
\begin{aligned}
u_1 &= d_{11}x_1 + d_{13}x_3 + x_2(\chi_{11}x_1 + \chi_{13}x_3) + u_1^{\text{per}}, \\
u_2 &= -\tfrac{1}{2}\chi_{11}x_1^2 - \tfrac{1}{2}\chi_{33}x_3^2 - \chi_{13}x_1x_3 + u_2^{\text{per}}, \\
u_3 &= d_{31}x_1 + d_{33}x_3 + x_2(\chi_{31}x_1 + \chi_{33}x_3) + u_3^{\text{per}}.
\end{aligned}
\tag{3-1}
$$

Note that the coefficients representing the average strain components $(d_{11}, d_{13}, \ldots)$ have only indices 1 and 3, as the homogenization procedure according to the periodicity directions is significant; also the coefficients $\chi_{11}, \chi_{13}, \ldots$ have only indices 1 and 3, as they represent the average curvature components

(a)   (b)
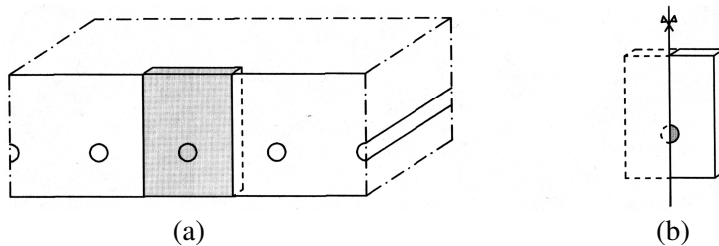
Figure 5. Left: schematic representation of the composite plate with embedded SMA fibers and localization of the unit cell. The plane shown is perpendicular to the fiber length. Right: region subjected to numerical analysis (continuous line).
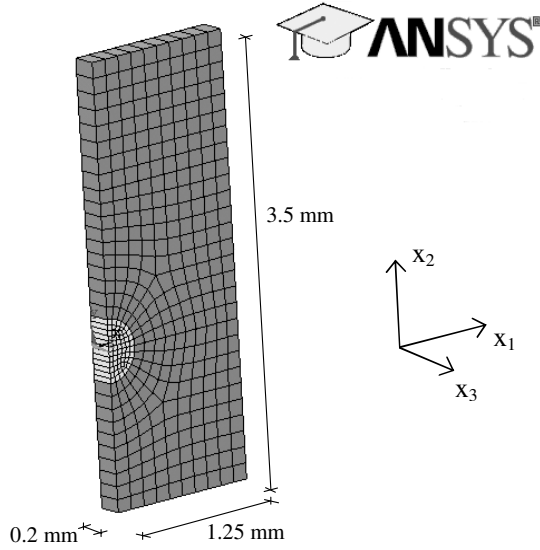
Figure 6. Plate element subjected to numerical analysis.

of the plate having extension in the $x_1 x_3$ plane. Also the periodic displacement components u_1^{per}, u_2^{per}, and u_3^{per} depend on the three variables x_1, x_2, and x_3, but they are periodic only in the axes x_1 and x_3.

It is convenient to perform the numerical homogenization in the framework of the displacement method, that is imposing one at a time the homogeneous strain components and average curvature components by means of the corresponding displacements on the boundary, as shown in (3-1) and with the proper boundary conditions. The values of normal stress components and of moment components resulting from the processing of the numerical analysis permits us to deduce the components of the constitutive matrix of the plate:

$$
\begin{Bmatrix} N_{11} \\ N_{33} \\ N_{13} \\ M_{11} \\ M_{33} \\ M_{13} \end{Bmatrix} = \begin{bmatrix} A_{11} & A_{13} & A_{14} & B_{11} & B_{13} & B_{14} \\ A_{13} & A_{33} & A_{34} & B_{13} & B_{33} & B_{34} \\ A_{14} & A_{34} & A_{44} & B_{14} & B_{34} & B_{44} \\ B_{11} & B_{13} & B_{14} & D_{11} & D_{13} & D_{14} \\ B_{13} & B_{33} & B_{34} & D_{13} & D_{33} & D_{34} \\ B_{14} & B_{34} & B_{44} & D_{14} & D_{34} & D_{44} \end{bmatrix} \begin{Bmatrix} d_{11} \\ d_{33} \\ 2d_{13} \\ \chi_{11} \\ \chi_{33} \\ 2\chi_{13} \end{Bmatrix}.
\tag{3-2}
$$

The stiffness matrix reported here is often represented partitioned into submatrices A, B, and D. Its symmetry and the symmetry of the submatrixes are a consequence of the symmetry of the elasticity tensor.

When imposing symmetric strain components, like d_{11}, d_{33}, χ_{11}, and χ_{33}, the displacement components u_1^{per} and u_3^{per} are zero respectively on the planes orthogonal to the $\boldsymbol{n}_1$ and $\boldsymbol{n}_3$ unit vectors belonging to the boundary of the RVE, representing symmetry planes; this means that the nodes on the boundary cannot move out of the planes. On the contrary, the displacement out of the plane u_2^{per} must be kept free from constraints also on the external boundary of RVE, normal to $\boldsymbol{n}_2$. The upper and lower surfaces of the plate have to be left free from constraints. This allows a symmetric deformation of the RVE.

When imposing *skew symmetric* strain components, like d_{13} and χ_{13}, the displacement component u_1^{per} is zero on the boundary plane orthogonal to the $\boldsymbol{n}_3$ unit vector and u_3^{per} is zero on the boundary plane orthogonal to the $\boldsymbol{n}_1$ unit vector. This allows a skew symmetric deformation of the RVE.

For this reason, coefficients A_{14}, A_{34}, B_{14}, B_{34}, D_{14}, and D_{34} are zero, as can be deduced observing that, from a macroscopic point of view, the plate is orthotropic and that axes 1 and 3 are orthotropy axes.

The results obtained by the homogenization procedure are reported in Table 3.

3.2. *Self-strain induced by SMA activation.* According to the method applied in Section 2.2, a surface stress vector field has to be applied on the boundary of the wire within the matrix of the RVE, which would have produced the self-strain if the wire was out of the matrix. The vector field is described in (2-10).

The stress system is again symmetric with respect to planes $x_1 = 0$ and $x_3 = 0$, so that the boundary constraints must be chosen as to prevent antisymmetric displacements. In this case, u_1 must be zeroed on the boundary planes of periodicity normal to the $\boldsymbol{n}_1$ unit vector, and u_3 must be zeroed on planes of periodicity normal to the $\boldsymbol{n}_3$ unit vector. Vertical displacements u_2 are allowed by the requirement for symmetry.

As in the previous case, the analysis reproduces the fluctuating part of strain, while the stress state can be computed by subtracting the stress corresponding with the self-strain from the elements constituting the SMA inclusion, according to (2-11), so that the equilibrium is reintroduced on the boundary of the SMA wire.

In order to determine the homogeneous part of the strain field to be superimposed on the fluctuating part determined by the numerical analysis, the condition that the volume average of the stress has to be zero in a body subjected to self-strain induced by internal causes is introduced. This time the plate normal stress and moments have to be zeroed by adding the plate strain components able to produce the opposite values of internal force; these can be computed by knowing the plate stiffness of (3-2) reported in Table 3.

Average strain and curvature produced by a self-strain of $r = 3\%$ are reported in Table 4. The stress distribution on the plane $x_3 = 0$ is reported in Figure 7.

A_{11} (N/mm)	A_{13} (N/mm)	A_{33} (N/mm)	A_{44} (N/mm)
3891.75	1549.29	9159.54	2335.13
B_{11} (N)	B_{13} (N)	B_{33} (N)	B_{44} (N)
70.85	24.65	2704.77	42.56
D_{11} (N mm)	D_{13} (N mm)	D_{33} (N mm)	D_{44} (N mm)
3866.28	1544.43	5264.49	2326

Table 3. Components of the constitutive matrix of the plate.

$\langle d_{11} \rangle$	$\langle d_{33} \rangle$	$\langle \chi_{11} \rangle$	$\langle \chi_{33} \rangle$
0.006231	−0.016608	0.003022	−0.007949

Table 4. Average strain and curvature produced by a self-strain of $r = 3\%$.
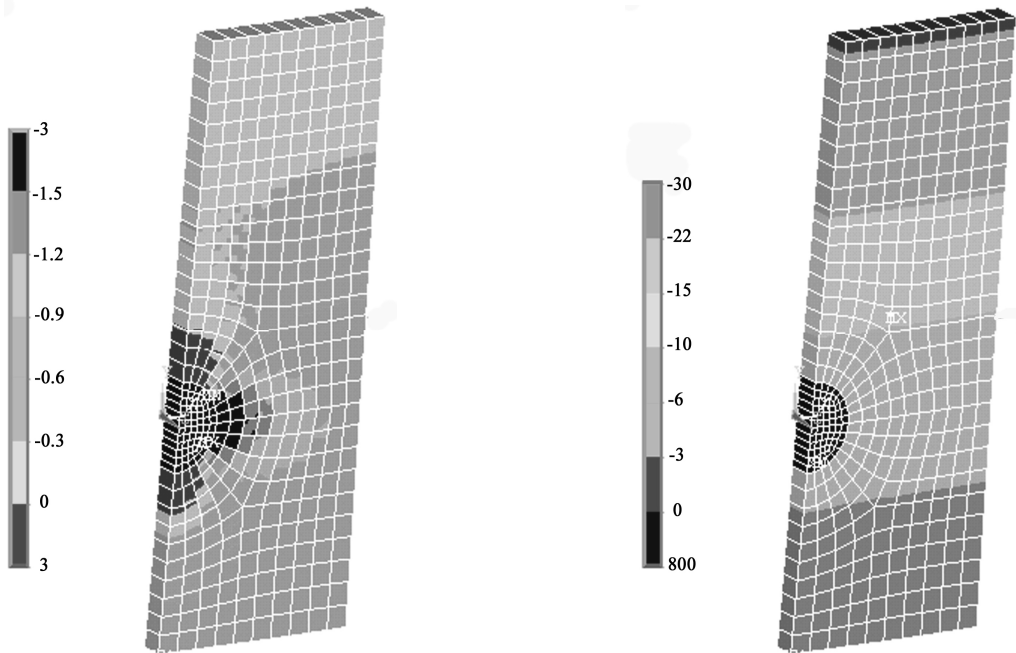
Figure 7. Normal stress (MPa) σ_x (left) and σ_z (right) in the plate element subjected to numerical analysis.

We note that the curvature tensor is negative definite at every point of the mean surface of the RVE, which is then a hyperbolic surface.

4. Conclusions

Numerical procedures have been described for the homogenization and the evaluation of the stress field in a composite as consequence of the shape-memory effect of embedded SMA wires. Such procedures proved suitable for the study of self-strain induced by SMA activation. In particular, it was shown that the individuation of the boundary conditions is strictly dependent on the choice of the RVE, and that it is simpler if the boundary constraints are individuated when the boundary of the RVE is also a symmetry plane for the composite.

As was expected, the stress state determined in the RVE, at the end of the SMA wire activation process, far from boundary is quite similar to the stress state in the symmetry plane of the RVE located near to the boundary. Nevertheless, this last case analysis is useful in order to evaluate the tangential stresses that are generated at the end of the fiber, the first step for the design of a real composite, once the adhesion properties of the constituents are experimentally investigated.

The analysis of a composite plate can produce the homogenized stiffness matrix of the plate, and the average main curvatures and strain of the composite plate, under the small rotation assumption.

Appendix: Derivation of the null average stress condition

The assumption of null average stress relies on the theory of dislocation. Volterra, in 1907, first used the term "distorsione", which Love [1927] translated as "dislocation"; nowadays the word dislocation is mainly used to indicate the defects of crystal lattices and the theory of dislocation explains the plasticity and work hardening of crystals.

When a body is not subjected to external forces, that is load and constraint forces, an eigenstrain produces an internal stress field. The body is free from constraints or it is constrained such as to be an isostatic system. This is the case of pretensioned, prestressed, reinforced concrete beams. The condition that average stress is null in the pretensioned, prestressed beam sections is usually employed and is a special case of (2-12), following simple equilibrium considerations. Equation (2-12) acquires particular interest when dealing with homogenization problems, because average stress is one of the basic quantities used in homogenization theory. Equation (2-12) can be easily proven by means of Signorini's theorem [Gurtin 1981].

In the case of no body forces acting on a finite region Ω and supposing that T is smooth, Signorini's theorem states that:

$$V(\Omega)\langle T\rangle = \int_{\partial\Omega} (Tn \otimes r)\,dA, \tag{A.1}$$

where $V(\Omega)$ is the volume of the body, T the stress tensor, n the unit vector normal to the boundary $\partial\Omega$, and r the position vector. If a portion Ω_1 of a body is subjected to an eigenstrain (see Figure 8), a surface stress state develops, opposite and equal on the two opposite sides of the boundary between Ω_1 and Ω_2, being Ω_2 its complementary part. We can write Signorini's formula for the two regions:

$$V(\Omega_1)\langle T_1\rangle = \int_{\partial\Omega_1} (T_1 n_1 \otimes r)\,dA, \qquad V(\Omega_2)\langle T_2\rangle = \int_{\partial\Omega_2} (T_2 n_2 \otimes r)\,dA.$$

Since $n_1 = -n_2$, $\partial\Omega_1 = \partial\Omega_2$, and $T_1 n_1 = -T_2 n_2$ (from the equilibrium condition), we have

$$V(\Omega_1)\langle T_1\rangle = \int_{\partial\Omega_1} (T_1 n_1 \otimes r)\,dA = \int_{\partial\Omega_2} -(T_2 n_2 \otimes r)\,dA = -V(\Omega_2)\langle T_2\rangle,$$

that is

$$V(\Omega_1)\langle T_1\rangle + V(\Omega_2)\langle T_2\rangle = 0, \tag{A.2}$$

which is equivalent to (2-12).
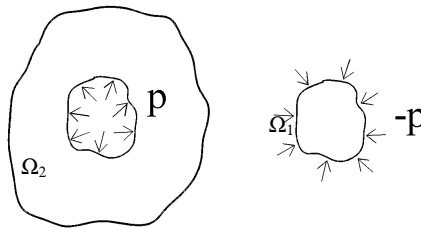
Figure 8. A region subjected to eigenstrain produces interfacial stress vector.

References

[Aboudi 1997] J. Aboudi, "The response of shape memory alloy composites", *Smart Mater. Struct.* **6**:1 (1997), 1–9.

[Ahmad et al. 1990] I. Ahmad, A. Crowson, C. A. Rogers, and M. Aizawa (editors), *US-Japan Workshop on Smart/Intelligent Materials and Systems* (Honolulu, HI, 1990), Technomic, Lancaster, PA, 1990.

[Alecci and Ranocchiai 2007] V. Alecci and G. Ranocchiai, "Caratterizzazione meccanica di materiali polimerici per la realizzazione di un composito attivo", pp. 782–791 in *Sperimentazione su materiali e strutture: convegno nazionale* (Venice, 2006), edited by S. Russo and E. Siviero, Università IUAV di Venezia, DCA, LabSCo, 2007.

[Anthoine 1995] A. Anthoine, "Derivation of the in-plane elastic characteristics of masonry through homogenization theory", *Int. J. Solids Struct.* **32**:2 (1995), 137–163.

[Anthoine 1997] A. Anthoine, "Homogenization of periodic masonry: plane stress, generalized plane strain or 3D modelling?", *Commun. Numer. Methods Eng.* **13**:5 (1997), 319–326.

[Baltá et al. 2002] J. A. Baltá, V. Michaud, J. Månson, M. Parlinska, and R. Gotthardt, "Adaptive composite materials processing", pp. 1–6 in *Composites for the future* (ECCM-10) (Brugge, 2002), edited by H. Sol and J. Degrieck, ESCM, Brugge, 2002.

[Barrett and Gross 1996] R. Barrett and R. S. Gross, "Super-active shape-memory alloy composites", *Smart Mater. Struct.* **5**:3 (1996), 255–260.

[Bidaux et al. 1994] J. E. Bidaux, J. A. E. Manson, and R. Gotthardt, "Dynamic mechanical behavior and phase transformation of polymer based shape memory alloys composites", pp. 37–42 in *Proceedings of SMST-94: the First International Conference on Shape Memory and Superelastic Technologies* (Pacific Grove, CA, 1994), edited by A. R. Pelton et al., Monterey Institute for Advanced Studies, Monterey, CA, 1994.

[Boyd and Lagoudas 1994] J. G. Boyd and D. C. Lagoudas, "Thermomechanical response of shape memory composites", *J. Intell. Mater. Syst. Struct.* **5**:3 (1994), 333–346.

[Cecchi et al. 2005] A. Cecchi, G. Milani, and A. Tralli, "Validation of analytical multiparameter homogenization models for out-of-plane loaded masonry walls by means of the finite element method", *J. Eng. Mech.* (*ASCE*) **131**:2 (2005), 185–198.

[Daghia et al. 2006] F. Daghia, F. Ubertini, E. Viola, and D. J. Inman, "A finite element model for SMA hybrid composite plates", in *Atti del XVI Convegno Italiano di Meccanica Computazionale* (Bologna, 2006), edited by F. Ubertini et al., Officine Grafiche Tecnoprint, Bologna, 2006.

[Duvaut 1984] C. Duvaut, "Homogénéisation et matériaux composites", pp. 35–62 in *Trends and applications of pure mathematics to mechanics* (Palaiseau, 1983), edited by P. G. Ciarlet and M. Roseau, Lecture Notes in Physics **195**, Springer, Berlin, 1984.

[Eshelby 1957] J. D. Eshelby, "The determination of the elastic field of an ellipsoidal inclusion, and related problems", *Proc. R. Soc. Lond. A* **241**:1226 (1957), 376–396.

[Gurtin 1981] M. E. Gurtin, *An introduction to continuum mechanics*, Academic Press, Boston, 1981.

[Hecker et al. 1970] S. S. Hecker, C. H. Hamilton, and L. J. Ebert, "Elastoplastic analysis of residual stresses and axial loading in composite cylinders", *J. Mater.* **5**:4 (1970), 868–900.

[ISO 604 1993] ISO 604, "Plastics: determination of compressive properties", 1993. Superseded by ISO 604:2002.

[Love 1927] A. E. H. Love, *A treatise on the mathematical theory of elasticity*, 4th ed., Cambridge Univ. Press, Cambridge, 1927.

[Lukkassen et al. 1995] D. Lukkassen, L.-E. Persson, and P. Wall, "Some engineering and mathematical aspects on the homogenization method", *Compos. Eng.* **5**:5 (1995), 519–531.

[Marfia 2005] S. Marfia, "Micro-macro analysis of shape memory alloy composites", *Int. J. Solids Struct.* **42**:13 (2005), 3677–3699.

[Marfia and Sacco 2005] S. Marfia and E. Sacco, "Micromechanics and homogenization of SMA-wire-reinforced materials", *J. Appl. Mech.* (*ASME*) **72**:2 (2005), 259–268.

[Marfia and Sacco 2007] S. Marfia and E. Sacco, "Analysis of SMA composite laminates using a multiscale modelling technique", *Int. J. Numer. Methods Eng.* **70**:10 (2007), 1182–1208.

[Milani et al. 2006] G. Milani, P. Laurenço, and A. Tralli, "Homogenization approach for the limit analysis of out-of-plane loaded masonry walls", *J. Struct. Eng.* (*ASCE*) **132**:10 (2006), 1650–1663.

[Mori and Tanaka 1973] T. Mori and K. Tanaka, "Average stress in matrix and average elastic energy of materials with misfitting inclusions", *Acta Metall.* **21**:5 (1973), 571–574.

[Murasawa et al. 2004] G. Murasawa, K. Tohgo, and H. Ishii, "Deformation behavior of NiTi/polymer shape memory alloy composites: experimental verifications", *J. Compos. Mater.* **38**:5 (2004), 399–416.

[Suquet 1985] P. M. Suquet, "Elements of homogenization for inelastic solid machanics", pp. 194–230 in *Homogenization techniques for composite media*, edited by E. Sanchez-Palencia and A. Zaoui, Springer, Berlin, 1985.

[Tsoi et al. 2004] K. A. Tsoi, J. Schrooten, Y. Zheng, and R. Stalmans, "II: Thermomechanical characteristics of shape memory alloy composites", *Mater. Sci. Eng. A* **368**:1–2 (2004), 299–310.

[Wei et al. 1997] Z. G. Wei, C. Y. Tang, and W. B. Lee, "Design and fabrication of intelligent composites based on shape memory alloys", *J. Mater. Process. Technol.* **69**:1–3 (1997), 68–74.

[Xu et al. 2002] Y. Xu, K. Otsuka, H. Yoshida, H. Nagai, R. Oishi, H. Horikawa, and T. Kishi, "A new method for fabricating SMA/CFRP smart hybrid composites", *Intermetallics* **10**:4 (2002), 361–369.

[Zhao and Weng 1990] Y. H. Zhao and G. J. Weng, "Effective elastic moduli of ribbon-reinforced composites", *J. Appl. Mech.* (*ASME*) **57**:1 (1990), 158–166.

[Zheng et al. 2001] Y. Zheng, L. Cui, Y. Li, and R. Stalmans, "Partial transformation behavior of prestrained TiNi fibers in composites", *Mater. Lett.* **51**:5 (2001), 425–428.

[Zheng et al. 2002] Y. J. Zheng, J. Schrooten, K. A. Tsoi, and R. Stalmans, "Thermal response of glass fibre/epoxy composites with embedded TiNiCu alloy wires", *Mater. Sci. Eng. A* **335**:1–2 (2002), 157–163.

[Zheng et al. 2003] Y. J. Zheng, J. Schrooten, K. A. Tsoi, and P. Šittner, "Qualitative and quantitative evaluation of the interface in activated shape memory alloy composites", *Exp. Mech.* **43**:2 (2003), 194–200.

VALERIO ALECCI: valerio.alecci@unifi.it
Dipartimento di Costruzioni, Università di Firenze, Piazza Brunelleschi 6, 50121 Firenze, Italy

SILVIA BRICCOLI BATI: silvia.briccolibati@unifi.it
Dipartimento di Costruzioni, Università di Firenze, Piazza Brunelleschi 6, 50121 Firenze, Italy

GIOVANNA RANOCCHIAI: giovanna.ranocchiai@unifi.it
Dipartimento di Costruzioni, Università di Firenze, Piazza Brunelleschi 6, 50121 Firenze, Italy

MOMENT LYAPUNOV EXPONENTS AND STOCHASTIC STABILITY FOR TWO COUPLED OSCILLATORS

PREDRAG KOZIĆ, GORAN JANEVSKI AND RATKO PAVLOVIĆ

The Lyapunov exponent and moment Lyapunov exponent of two degree-of-freedom linear systems subjected to white noise parametric excitation are investigated. Through a perturbation method we obtain the explicit asymptotic expressions for these exponents in the presence of low intensity noise. The Lyapunov exponent and moment Lyapunov exponents are important characteristics for determining the almost-sure and moment stability of a stochastic dynamical system. As an example, we study the almost-sure and moment stability of the flexural-torsion stability of a thin elastic beam subjected to a stochastically fluctuating follower force. The validity of the approximate results for moment Lyapunov exponents is checked by a numerical Monte Carlo simulation for these stochastic systems.

1. Introduction

In recent years there has been considerable interest in the study of the dynamic stability of nongyroscopic conservative elastic systems whose parameters fluctuate in a stochastic manner. To have a complete picture of the dynamic stability of a dynamic system, it is important to study both the almost-sure and the moment stability and to determine both the maximal Lyapunov exponent and the p-th moment Lyapunov exponent. The maximal Lyapunov exponent, defined by

$$\lambda_q = \lim_{t \to \infty} \frac{1}{t} \log \|\boldsymbol{q}(t; q_0)\|, \tag{1}$$

where $\boldsymbol{q}(t; q_0)$ is the solution process of a linear dynamical system. The almost-sure stability depends upon the sign of the maximal Lyapunov exponent, which is the exponential growth rate of the solution of the randomly perturbed dynamical system. A negative sign of the maximal Lyapunov exponent implies almost-sure stability, whereas a nonnegative value indicates instability. The exponential growth rate $E[\|\boldsymbol{q}(t; q_0, \dot{q}_0)\|^p]$ is provided by the moment Lyapunov exponent, defined as

$$\Lambda_q(p) = \lim_{t \to \infty} \frac{1}{t} \log E\big[\|\boldsymbol{q}(t; q_0)\|^p\big], \tag{2}$$

where $E[\ ]$ denotes an expectation. If $\Lambda_q(p) < 0$, then, by definition $E[\|\boldsymbol{q}(t; q_0, \dot{q}_0)\|^p] \to 0$ as $t \to \infty$. This is referred to as p-th moment stability. Although moment Lyapunov exponents are important in the study of the dynamic stability of stochastic systems, the actual evaluation of moment Lyapunov exponents is very difficult.

Arnold et al. [1997] constructed an approximation for the moment Lyapunov exponents of 2D linear systems driven by real or white noise. A perturbation approach was used to obtain explicit expressions for

these exponents in the presence of low intensity noise. Khasminskii and Moshchuk [1998] obtained an asymptotic expansion of the moment Lyapunov exponents of a 2D system under white noise parametric excitation in terms of the small fluctuation parameter ε, from which the stability index was obtained. Kozić et al. [2008] investigated the Lyapunov exponent and moment Lyapunov exponent of Hill's equation with frequency and damping coefficient fluctuated by white noise. A perturbation approach was used to obtain explicit expressions for these exponents in the presence of low intensity noise. Xie [2001] obtained weak noise expansions of the moment Lyapunov exponents of a 2D system under real noise excitation, an Ornstein–Uhlenbeck process. Xie [2002] determined small noise expansions of the moment Lyapunov exponents of a 2D viscoelastic system under bounded noise excitation. Sri Namachchivaya et al. [1994] used a perturbation approach to calculate the asymptotic growth rate of stochastically coupled 4D systems. The noise was assumed to be white and of low intensity in order to calculate the explicit asymptotic formulas for the maximum Lyapunov exponent. Sri Namachchivaya and Vedula [2000] obtained a general asymptotic approximation for the moment Lyapunov exponents and the Lyapunov exponent for 4D systems with one critical mode and another asymptotically stable mode driven by a small intensity process. Sri Namachchivaya and Van Roessel [2004] used a perturbation approach to obtain an approximation for the moment Lyapunov exponents of two coupled oscillators with commensurable frequencies driven by low intensity real noise with dissipation. The generator for the eigenvalue problem associated with the moment Lyapunov exponents was derived without any restrictions on the size of the p-th moment.

The aim of this paper is to determine a weak noise expansion for the moment Lyapunov exponents for stochastically coupled two-degree-of-freedom systems. The noise is assumed to be white noise of low intensity such that one can obtain an asymptotic growth rate. Here we apply the perturbation theoretic approach of [Khasminskii and Moshchuk 1998] to obtain weak noise expansions of the moment Lyapunov exponents and Lyapunov exponent. These results are applied to study the flexural-torsional stability of a narrow simply supported beam under a fluctuating stochastic follower force. The approximate analytical results of the moment Lyapunov exponents are compared with the numerical values obtained by Monte Carlo simulation for these exponents of two-degree-of freedom stochastic systems.

2. Theoretical formulation

Consider the linear oscillatory systems described by equations of motion of the form

$$\ddot{q}_i + \omega_i^2 q_i + 2\varepsilon\zeta_i\omega_i\dot{q}_i + \varepsilon^{1/2}\sum_{j=1}^{2} k_{ij}q_j\xi(t) = 0, \qquad i, j = 1, 2, \tag{3}$$

where q_i is a generalized coordinate, ω_i is the i-th natural frequency, and $\varepsilon\zeta_i$ represents the i-th small viscous damping coefficient. It is assumed that the natural frequency is not commensurable. The stochastic term, $\varepsilon^{1/2}\xi(t)$, is a white-noise process with low intensity. The almost-sure and moment stability of the equilibrium state $q = \dot{q} = 0$ of (3) is to be investigated. Using the transformation

$$q_1 = x_1, \quad \dot{q}_1 = \omega_1 x_2, \quad q_2 = x_3, \quad \dot{q}_2 = \omega_2 x_4,$$

we can represent (3) in first-order form by the Stratonovich differential equations (4) on the next page — which is also the form of the Itô equations:

$$\frac{d}{dt}\begin{Bmatrix} x_1 \\ x_2 \\ x_3 \\ x_4 \end{Bmatrix} = \begin{bmatrix} 0 & \omega_1 & 0 & 0 \\ -\omega_1 & -2\varepsilon\zeta_1\omega_1 & 0 & 0 \\ 0 & 0 & 0 & \omega_2 \\ 0 & 0 & -\omega_2 & -2\varepsilon\zeta_2\omega_2 \end{bmatrix}\begin{Bmatrix} x_1 \\ x_2 \\ x_3 \\ x_4 \end{Bmatrix} + \sqrt{\varepsilon}\begin{bmatrix} 0 & 0 & 0 & 0 \\ -k_{11}/\omega_1 & 0 & -k_{12}/\omega_1 & 0 \\ 0 & 0 & 0 & 0 \\ -k_{21}/\omega_2 & 0 & -k_{22}/\omega_2 & 0 \end{bmatrix}\begin{Bmatrix} x_1 \\ x_2 \\ x_3 \\ x_4 \end{Bmatrix} \circ \xi(t),$$

$$(4)$$

where $\xi(t)$ is the white noise process with zero mean and autocorrelation function

$$R_{\xi\xi}(t_1, t_2) = E[\xi(t_1)\xi(t_2)] = \sigma^2 \min(t_2, t_1). \tag{5}$$

Here σ is the intensity of the random process $\xi(t)$ and δ is the Dirac delta function.

We next apply the transformation

$$x_1 = a\cos\phi_1\cos\theta, \quad x_2 = -a\sin\phi_1\cos\theta, \quad x_3 = a\cos\phi_2\sin\theta, \quad x_4 = -a\sin\phi_2\sin\theta, \tag{6}$$

where ϕ_1 and ϕ_2 the angles of the first and second oscillators, and θ the coupling or energy exchange between the two oscillators. Introducing also

$$P = a^p = (x_1^2 + x_2^2 + x_3^2 + x_4^2)^{p/2}, \quad -\infty < p < \infty,$$

the p-th power of the norm of the response, we obtain a set of Itô equations for P the and phase variables ϕ_1, ϕ_2, θ (where we omit from the notation the dependence of the m_i and σ_{i1} on ϕ_1, ϕ_2, θ):

$$\begin{aligned} d\phi_1 &= m_1\, dt + \sigma_{11}\, dW(t), & d\theta &= m_3\, dt + \sigma_{31}\, dW(t), \\ d\phi_2 &= m_2\, dt + \sigma_{21}\, dW(t), & dP &= Pm_4\, dt + P\sigma_{41}\, dW(t). \end{aligned} \tag{7}$$

Here

$$\sigma_{11} = \frac{\sigma}{\omega_1}\sqrt{\frac{\varepsilon}{2}}(k_{11}\cos\phi_1 + k_{12}\cos\phi_2\tan\theta)\cos\phi_1, \quad \sigma_{21} = \frac{\sigma}{\omega_2}\sqrt{\frac{\varepsilon}{2}}(k_{21}\cos\phi_1\cot\theta + k_{22}\cos\phi_2)\cos\phi_2,$$

$$\sigma_{31} = \frac{\sigma}{4}\sqrt{\frac{\varepsilon}{2}}\left[\left(\frac{k_{22}}{\omega_2}\sin 2\phi_2 - \frac{k_{11}}{\omega_1}\sin 2\phi_1\right)\sin 2\theta + 4\frac{k_{21}}{\omega_2}\sin\phi_2\cos\phi_1\cos^2\theta - 4\frac{k_{12}}{\omega_1}\sin\phi_1\cos\phi_2\sin^2\theta\right],$$

$$\sigma_{41} = \frac{p\sigma}{2}\sqrt{\frac{\varepsilon}{2}}\left[\left(\frac{k_{12}}{\omega_1}\sin\phi_1\cos\phi_2 + \frac{k_{21}}{\omega_2}\sin\phi_2\cos\phi_1\right)\sin 2\theta + \frac{k_{11}}{\omega_1}\sin 2\phi_1\cos^2\theta + \frac{k_{22}}{\omega_2}\sin 2\phi_2\sin^2\theta\right],$$

$$m_1 = \omega_1 - \varepsilon\left(\zeta_1\omega_1 + \frac{\sigma^2}{4\omega_1^2}(k_{11}\cos\phi_1 + k_{12}\cos\phi_2\tan\theta)^2\right)\sin 2\phi_1,$$

$$m_2 = \omega_2 - \varepsilon\left(\zeta_1\omega_2 + \frac{\sigma^2}{4\omega_2^2}(k_{21}\cos\phi_1\cot\theta + k_{22}\cos\phi_2)^2\right)\sin 2\phi_2,$$

$$\begin{aligned} m_3 = &\frac{\varepsilon}{2}\left(\zeta_1\omega_1(1 - \cos 2\phi_1) - \zeta_2\omega_2(1 - \cos 2\phi_2)\right)\sin 2\theta \\ &+ \frac{\varepsilon\sigma^2}{4}\left[\frac{-\cos^2\phi_1\tan\theta + \sin^2\phi_1\sin 2\theta}{\omega_1^2}(k_{11}\cos\phi_1\cos\theta + k_{12}\cos\phi_2\sin\theta)^2\right. \\ &\quad - \frac{2\sin\phi_1\sin\phi_2\cos 2\theta}{\omega_1\omega_2}(k_{11}\cos\phi_1\cos\theta + k_{12}\cos\phi_2\sin\theta)(k_{21}\cos\phi_1\cos\theta + k_{22}\cos\phi_2\sin\theta) \\ &\quad \left. + \frac{\cos^2\phi_2\cot\theta - \sin^2\phi_2\sin 2\theta}{\omega_2^2}(k_{21}\cos\phi_1\cos\theta + k_{22}\cos\phi_2\sin\theta)^2\right], \end{aligned}$$

$$m_4 = -\varepsilon p\big(\zeta_1\omega_1(1-\cos 2\phi_1)\cos^2\theta + \zeta_2\omega_2(1-\cos 2\phi_2)\sin^2\theta\big)$$

$$+ \frac{\varepsilon p\sigma^2}{4}\bigg[\frac{1+(p-2)\sin^2\phi_1\cos^2\theta}{\omega_1^2}(k_{11}\cos\phi_1\cos\theta + k_{12}\cos\phi_2\sin\theta)^2$$

$$+ \frac{(p-2)\sin\phi_1\sin\phi_2\sin 2\theta}{\omega_1\omega_2}(k_{11}\cos\phi_1\cos\theta + k_{12}\cos\phi_2\sin\theta)(k_{21}\cos\phi_1\cos\theta + k_{22}\cos\phi_2\sin\theta)$$

$$+ \frac{1+(p-2)\sin^2\phi_2\sin^2\theta}{\omega_2^2}(k_{21}\cos\phi_1\cos\theta + k_{22}\cos\phi_2\sin\theta)^2\bigg],$$

Following [Wedig 1988], we perform the stochastic linear transformation

$$S = T(\phi_1,\phi_2,\theta)P, \qquad P = T^{-1}(\phi_1,\phi_2,\theta)S. \tag{8}$$

We introduce the new norm process S by means of the scalar function $T(\phi_1,\phi_2,\theta)$ which is defined on the stationary phase processes ϕ_1, ϕ_2, and θ in the range $0 \le \phi_1 \le 2\pi$, $0 \le \phi_2 \le 2\pi$, $0 \le \theta \le \pi/2$, as

$$dS = P\big[\tfrac{1}{2}T_{\phi_1\phi_1}\sigma_{11}^2 + T_{\phi_1\phi_2}\sigma_{11}\sigma_{21} + T_{\phi_1\theta}\sigma_{11}\sigma_{31} + \tfrac{1}{2}T_{\phi_2\phi_2}\sigma_{21}^2 + T_{\phi_2\theta}\sigma_{21}\sigma_{31}$$

$$+ \tfrac{1}{2}T_{\theta\theta}\sigma_{31}^2 + (m_1+\sigma_{11}\sigma_{41})T_{\phi_1} + (m_2+\sigma_{21}\sigma_{41})T_{\phi_2} + (m_3+\sigma_{31}\sigma_{41})T_\theta + m_4 T\big]\,dt$$

$$+ P(T_{\phi_1}\sigma_{11} + T_{\phi_2}\sigma_{21} + T_\theta\sigma_{31} + T\sigma_{41})\,dW(t). \tag{9}$$

If the transformation function $T(\phi_1,\phi_2,\theta)$ is bounded and nonsingular, both processes P and S possess the same stability behavior. Therefore, $T(\phi_1,\phi_2,\theta)$ is chosen so that the drift term, of the Itô differential (9), does not depend on the phase processes ϕ_1, ϕ_2, and θ, so that

$$dS = \Lambda(p)S\,dt + ST^{-1}(T_{\phi_1}\sigma_{11} + T_{\phi_2}\sigma_{21} + T_\theta\sigma_{31} + T\sigma_{41})\,dW(t). \tag{10}$$

By comparing (9) and (10), we see that such a $T(\phi_1,\phi_2,\theta)$ is given by the following equation:

$$\tfrac{1}{2}T_{\phi_1\phi_1}\sigma_{11}^2 + T_{\phi_1\phi_2}\sigma_{11}\sigma_{21} + T_{\phi_1\theta}\sigma_{11}\sigma_{31} + \tfrac{1}{2}T_{\phi_2\phi_2}\sigma_{21}^2 + T_{\phi_2\theta}\sigma_{21}\sigma_{31} + \tfrac{1}{2}T_{\theta\theta}\sigma_{31}^2$$

$$+ (m_1+\sigma_{11}\sigma_{41})T_{\phi_1} + (m_2+\sigma_{21}\sigma_{41})T_{\phi_2} + (m_3+\sigma_{31}\sigma_{41})T_\theta + m_4 T = \Lambda(p)T. \tag{11}$$

To avoid lengthy calculations, the analysis presented in this section considers the special case where $k_{11} = k_{22} = 0$, so that

$$[L_1 + \varepsilon L_2]\,T(\phi_1,\phi_2,\theta) = \Lambda(p)T(\phi_1,\phi_2,\theta). \tag{12}$$

Here L_1 and L_2 are the following first- and second-order differential operators (again we suppress the dependence of the coefficients on ϕ_1,ϕ_2,θ):

$$L_1 = \omega_1\frac{\partial}{\partial\phi_1} + \omega_2\frac{\partial}{\partial\phi_2},$$

$$L_2 = a_1\frac{\partial^2}{\partial\phi_1^2} + a_2\frac{\partial^2}{\partial\phi_1\partial\phi_2} + a_3\frac{\partial^2}{\partial\phi_1\partial\theta} + a_4\frac{\partial^2}{\partial\phi_2^2} + a_5\frac{\partial^2}{\partial\phi_2\partial\theta} + a_6\frac{\partial^2}{\partial\theta^2} + b_1\frac{\partial}{\partial\phi_1} + b_2\frac{\partial}{\partial\phi_2} + b_3\frac{\partial}{\partial\theta} + c,$$

where

$$a_1 = \frac{k_{12}^2 \sigma^2}{4\omega_1^2} \cos^2 \phi_1 \cos^2 \phi_2 \tan^2 \theta, \qquad a_2 = \frac{k_{12}k_{21}\sigma^2}{2\omega_1\omega_2} \cos^2 \phi_1 \cos^2 \phi_2,$$

$$a_3 = \frac{\sigma^2}{4}\left(-\frac{k_{12}^2}{\omega_1^2} \sin 2\phi_1 \cos^2 \phi_2 \sin^2 \theta + \frac{k_{12}k_{21}}{\omega_1\omega_2} \sin 2\phi_2 \cos^2 \phi_1 \cos^2 \theta\right) \tan \theta,$$

$$a_4 = \frac{k_{21}^2 \sigma^2}{4\omega_2^2} \cos^2 \phi_1 \cos^2 \phi_2 \cot^2 \theta, \qquad a_6 = \frac{\sigma^2}{4}\left(-\frac{k_{12}}{\omega_1} \sin \phi_1 \cos \phi_2 \sin^2 \theta + \frac{k_{21}}{\omega_2} \sin \phi_2 \cos \phi_1 \cos^2 \theta\right)^2,$$

$$a_5 = \frac{\sigma^2}{4}\left(-\frac{k_{12}k_{21}}{\omega_1\omega_2} \sin 2\phi_1 \cos^2 \phi_2 \sin^2 \theta + \frac{k_{21}^2}{\omega_2^2} \sin 2\phi_2 \cos^2 \phi_1 \cos^2 \theta\right) \cot \theta,$$

$$b_1 = -\left(\zeta_1\omega_1 + \frac{k_{12}^2\sigma^2}{4\omega_1^2}(\tan^2 \theta - p \sin^2 \theta) \cos^2 \phi_2\right) \sin 2\phi_1 + \frac{k_{12}k_{21}\sigma^2}{4\omega_1\omega_2} p \cos^2 \phi_1 \sin^2 \theta \sin 2\phi_2,$$

$$b_2 = -\left(\zeta_2\omega_2 + \frac{k_{21}^2\sigma^2}{4\omega_2^2}(\cot^2 \theta - p \cos^2 \theta) \cos^2 \phi_1\right) \sin 2\phi_2 + \frac{k_{12}k_{21}\sigma^2}{4\omega_1\omega_2} p \cos^2 \phi_2 \cos^2 \theta \sin 2\phi_1,$$

$$b_3 = (\zeta_1\omega_1 \sin^2 \phi_1 - \zeta_2\omega_2 \sin^2 \phi_2) \sin 2\theta + \frac{\sigma^2}{4}\left(\frac{k_{12}^2}{\omega_1^2}\left(-\cos^2 \phi_1 \tan \theta - (p-1) \sin^2 \phi_1 \sin 2\theta\right) \cos^2 \phi_2 \sin^2 \theta\right.$$
$$\left. + \frac{k_{21}^2}{\omega_2^2}\left(\cos^2 \phi_2 \cot \theta + (p-1) \sin^2 \phi_2 \sin 2\theta\right) \cos^2 \phi_1 \cos^2 \theta + \frac{k_{12}k_{21}}{4\omega_1\omega_2}(p-1) \sin 2\phi_1 \sin 2\phi_2 \cos 2\theta \sin 2\theta\right),$$

$$c = -2p(\zeta_1\omega_1 \sin^2 \phi_1 \cos^2 \theta + \zeta_2\omega_2 \sin^2 \phi_2 \sin^2 \theta) + \frac{p\sigma^2}{4}\left(\frac{k_{12}^2}{\omega_1^2}\left(1 + (p-2) \sin^2 \phi_1 \cos^2 \theta\right) \cos^2 \phi_2 \sin^2 \theta\right.$$
$$\left. + \frac{k_{21}^2}{\omega_2^2}\left(1 + (p-2) \sin^2 \phi_2 \sin^2 \theta\right) \cos^2 \phi_1 \cos^2 \theta + (p-2) \frac{k_{12}k_{21}}{2\omega_1\omega_2} \sin 2\phi_1 \sin 2\phi_2 \sin^2 \theta \cos^2 \theta\right).$$

Either (11) or (12) defines a second-order eigenvalue problem for the determination of the unknown transformation function $T(\phi_1, \phi_2, \theta)$ and the associated eigenvalue $\Lambda(p)$ or Lyapunov exponent of the p-th mean. From (10) the eigenvalue $\Lambda(p)$ is seen to be the p-th moment Lyapunov exponent of the system (4). This approach was first applied by Wedig [1988] to derive the eigenvalue problem for the moment Lyapunov exponent of a 2D linear Itô stochastic system. In the following section, the method of regular perturbation is applied to the eigenvalue problem (11) to obtain a weak noise expansion of the moment Lyapunov exponent for the system (4).

3. Weak noise expansion of the moment Lyapunov exponent

Applying the method of regular perturbation, both the moment Lyapunov exponent $\Lambda(p)$ and the eigenfunction $T(\phi_1, \phi_2, \theta)$ are expanded in power series of ε as

$$\Lambda(p) = \Lambda_0(p) + \varepsilon\Lambda_1(p) + \varepsilon^2\Lambda_2(p) + \ldots + \varepsilon^n\Lambda_n(p) + \ldots,$$
$$T(\phi_1, \phi_2, \theta) = T_0(\phi_1, \phi_2, \theta) + \varepsilon T_1(\phi_1, \phi_2, \theta) + \varepsilon^2 T_2(\phi_1, \phi_2, \theta) + \ldots + \varepsilon^n T_n(\phi_1, \phi_2, \theta) + \ldots.$$

(13)

Substituting the perturbation series (13) into the eigenvalue problem (12) and equating terms with equal powers of ε leads to the following equations:

$$
\begin{aligned}
\varepsilon^0 &: L_1 T_0(\phi_1, \phi_2, \theta) = \Lambda_0(p) T_0(\phi_1, \phi_2, \theta), \\
\varepsilon^1 &: L_1 T_1(\phi_1, \phi_2, \theta) + L_2 T_0(\phi_1, \phi_2, \theta) = \Lambda_0(p) T_1(\phi_1, \phi_2, \theta) + \Lambda_1(p) T_0(\phi_1, \phi_2, \theta), \\
\varepsilon^2 &: L_1 T_2(\phi_1, \phi_2, \theta) + L_2 T_1(\phi_1, \phi_2, \theta) = \Lambda_0(p) T_2(\phi_1, \phi_2, \theta) \\
&\qquad\qquad\qquad\qquad\qquad\qquad + \Lambda_1(p) T_1(\phi_1, \phi_2, \theta) + \Lambda_2(p) T_0(\phi_1, \phi_2, \theta), \\
\varepsilon^3 &: L_1 T_3(\phi_1, \phi_2, \theta) + L_2 T_2(\phi_1, \phi_2, \theta) = \Lambda_0(p) T_3(\phi_1, \phi_2, \theta) + \Lambda_1(p) T_2(\phi_1, \phi_2, \theta) \\
&\qquad\qquad\qquad\qquad\qquad\qquad + \Lambda_2(p) T_1(\phi_1, \phi_2, \theta) + \Lambda_3(p) T_0(\phi_1, \phi_2, \theta), \\
&\qquad\vdots \\
\varepsilon^n &: L_1 T_n(\phi_1, \phi_2, \theta) + L_2 T_{n-1}(\phi_1, \phi_2, \theta) = \Lambda_0(p) T_n(\phi_1, \phi_2, \theta) + \Lambda_1(p) T_{n-1}(\phi_1, \phi_2, \theta) \\
&\qquad\qquad\qquad\qquad\qquad\qquad\qquad\qquad\qquad + \ldots + \Lambda_n(p) T_0(\phi_1, \phi_2, \theta),
\end{aligned}
\tag{14}
$$

where each function $T_i(\phi_1, \phi_2, \theta)$, $i = 0, 1, 2, \ldots$, must be positive and periodic in the range $0 \le \phi_1 \le 2\pi$, $0 \le \phi_2 \le 2\pi$, $0 \le \theta \le \pi/2$.

3.1. *Zeroth-order perturbation.* The zeroth-order perturbation equation is $L_1 T_0 = \Lambda_0(p) T_0$ or

$$
\omega_1 \frac{\partial T_0(\phi_1, \phi_2, \theta)}{d\phi_1} + \omega_2 \frac{\partial T_0(\phi_1, \phi_2, \theta)}{d\phi_2} = \Lambda_0(p) T_0(\phi_1, \phi_2, \theta).
\tag{15}
$$

From the properties of the moment Lyapunov exponent, it is known that

$$
\Lambda(0) = \Lambda_0(0) + \varepsilon \Lambda_1(0) + \varepsilon^2 \Lambda_2(0) + \cdots + \varepsilon^n \Lambda_n(0) = 0,
\tag{16}
$$

which results in $\Lambda_n(0) = 0$ for $n = 0, 1, 2, 3, \ldots$. Since the eigenvalue problem (15) does not contain p, the eigenvalue $\Lambda_0(p)$ is independent of p. Hence, $\Lambda_0(0) = 0$ leads to $\Lambda_0(p) = 0$. Then (15) has a periodic solution if and only if

$$
\Lambda_0(p) = 0, \qquad T_0(\phi_1, \phi_2, \theta) = 1.
\tag{17}
$$

3.2. *First-order perturbation.* The first-order perturbation equation is

$$
L_1 T_1(\phi_1, \phi_2, \theta) + L_2 T_0(\phi_1, \phi_2, \theta) = \Lambda_0(p) T_1(\phi_1, \phi_2, \theta) + \Lambda_1(p) T_0(\phi_1, \phi_2, \theta).
\tag{18}
$$

This has a periodic solution if and only if

$$
\int_0^{2\pi} \int_0^{2\pi} \int_0^{\pi/2} [L_2 \cdot 1 - \Lambda_1(p)] \, d\phi_1 d\phi_2 d\theta = 0,
\tag{19}
$$

so we have

$$
\begin{aligned}
\Lambda_1(p) &= \frac{1}{2\pi^3} \int_0^{2\pi} \int_0^{2\pi} \int_0^{\pi/2} c(\phi_1, \phi_2, \theta) \, d\phi_1 \, d\phi_2 \, d\theta \\
&= p \left[\frac{3\sigma^2}{64} \left(\frac{k_{12}^2}{\omega_1^2} + \frac{k_{21}^2}{\omega_2^2} \right) - \frac{1}{2} (\zeta_1 \omega_1 + \zeta_2 \omega_2) \right] + p^2 \frac{\sigma^2}{128} \left(\frac{k_{12}^2}{\omega_1^2} + \frac{k_{21}^2}{\omega_2^2} \right).
\end{aligned}
\tag{20}
$$

Now the first-order perturbation equation reduces to

$$\omega_1 \frac{\partial T_1(\phi_1, \phi_2, \theta)}{d\phi_1} + \omega_2 \frac{\partial T_1(\phi_1, \phi_2, \theta)}{d\phi_2} + c(\phi_1, \phi_2, \theta) = \Lambda_1(p). \tag{21}$$

Since it is assumed that the frequencies ω_1 and ω_2 are not commensurable, the general periodic solution (21) cannot be obtained explicitly for the eigenfunction $T_1(\phi_1, \phi_2, \theta)$. Therefore it is possible to obtain the moment Lyapunov exponent only in the first-order perturbation.

3.3. *Moment Lyapunov exponent, Lyapunov exponent, and stability conditions.* We next obtain the weak noise expansion of the moment Lyapunov exponent in the first-order perturbation for the system (4):

$$\Lambda(p) = \varepsilon \Lambda_1(p) + O(\varepsilon^2)$$
$$= \varepsilon p \left[\frac{3\sigma^2}{64} \left(\frac{k_{12}^2}{\omega_1^2} + \frac{k_{21}^2}{\omega_2^2} \right) - \frac{1}{2}(\zeta_1 \omega_1 + \zeta_2 \omega_2) \right] + \varepsilon p^2 \frac{\sigma^2}{128} \left(\frac{k_{12}^2}{\omega_1^2} + \frac{k_{21}^2}{\omega_2^2} \right) + O(\varepsilon^2). \tag{22}$$

The Lyapunov exponent for system (4) can be obtained from (22) by using a property of the moment Lyapunov exponent

$$\lambda = \frac{d\Lambda(p)}{dp} \bigg|_{p=0} = \varepsilon \lambda_1 + O(\varepsilon^2) = \varepsilon \left[\frac{3\sigma^2}{64} \left(\frac{k_{12}^2}{\omega_1^2} + \frac{k_{21}^2}{\omega_2^2} \right) - \frac{1}{2}(\zeta_1 \omega_1 + \zeta_2 \omega_2) \right] + O(\varepsilon^2). \tag{23}$$

Using the result above for the moment Lyapunov exponent, with the definition of the moment stability $\Lambda_{q(t)} < 0$, we determine analytically the p-th moment stability boundary in the first-order perturbation for various values of $p = 1, 2, 4$, respectively, as

$$\zeta_1 \omega_1 + \zeta_2 \omega_2 > \frac{7\sigma^2}{64} \left(\frac{k_{12}^2}{\omega_1^2} + \frac{k_{21}^2}{\omega_2^2} \right), \quad \zeta_1 \omega_1 + \zeta_2 \omega_2 > \frac{\sigma^2}{8} \left(\frac{k_{12}^2}{\omega_1^2} + \frac{k_{21}^2}{\omega_2^2} \right), \quad \zeta_1 \omega_1 + \zeta_2 \omega_2 > \frac{5\sigma^2}{32} \left(\frac{k_{12}^2}{\omega_1^2} + \frac{k_{21}^2}{\omega_2^2} \right).$$

It is known that the system is asymptotically stable only if the Lyapunov exponent $\lambda_{q(t)}$ is negative. Then, (32) is employed to determine the almost-sure stability boundary of the system (4)

$$\zeta_1 \omega_1 + \zeta_2 \omega_2 > \frac{3\sigma^2}{32} \left(\frac{k_{12}^2}{\omega_1^2} + \frac{k_{21}^2}{\omega_2^2} \right). \tag{24}$$

4. Application to a beam under stochastic load

The results obtained in the previous section in the context of real engineering applications show how these results can be applied to physical problems. To this end, we consider the flexural torsional instability of a thin rectangular beam of length L subjected to a stochastically fluctuating follower force (Figure 1). It is assumed that the simply supported beam is bent by a stochastically varying central load $P(t)$. The
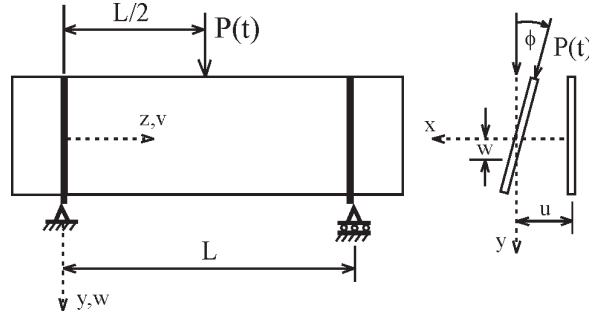
Figure 1. Thin rectangular beam subjected to stochastic excitation.

motion of the beam is governed by the partial differential equations [Bolotin 1964]

$$m\frac{\partial^2 w}{\partial t^2} + d_w\frac{\partial w}{\partial t} + EI_x\frac{\partial^4 w}{\partial z^4} = 0, \tag{25}$$

$$m\frac{\partial^2 u}{\partial t^2} + d_u\frac{\partial u}{\partial t} + EI_y\frac{\partial^4 u}{\partial z^4} + \frac{\partial^2 (M(z,t)\phi)}{\partial z^2} + P(t)\delta\left(\frac{L}{2} - z\right)\phi = 0, \tag{26}$$

$$m\rho^2\frac{\partial^2 \phi}{\partial t^2} + d_\phi\frac{\partial \phi}{\partial t} - GJ\frac{\partial^4 \phi}{\partial z^4} + M(z,t)\frac{\partial^2 u}{\partial z^2} = 0, \tag{27}$$

where $u(z,t)$ and $w(z,t)$ denote the x and y components of the deflection of the beam center line and ϕ is the angle of twist of the cross-section. The quantities EI_x, EI_y, and GJ are the flexural and torsional rigidities of the cross-section and d_w, d_u, and d_ϕ are the viscous damping coefficients. In addition, m denotes the mass per unit length, and ρ is the polar radius of gyration of the cross-section. The function $M(z,t)$ can be expressed in terms of the applied stochastic load as

$$M(z,t) = \begin{cases} \frac{1}{2}P(t)\cdot z, & 0 \le z \le \frac{1}{2}L, \\ \frac{1}{2}P(t)\cdot(L-z), & \frac{1}{2}L \le z \le L. \end{cases} \tag{28}$$

It is obvious that (25) is uncoupled from the other two equations and describes the ordinary random vibration of the beam in the plane of its largest rigidity with the inhomogeneous boundary conditions given by

$$EI_x\frac{\partial^2 w}{\partial z^2}(0,t) = -M(0,t) = EI_x\frac{\partial^2 w}{\partial z^2}(L,t) = -M(L,t). \tag{29}$$

The other two equations form a pair of coupled partial differential equations with stochastic coefficients subjected to homogeneous boundary conditions given by

$$u(0,t) = u(L,t) = \frac{\partial^2 u}{\partial z^2}(0,t) = \frac{\partial^2 u}{\partial z^2}(L,t), \qquad \phi(0,t) = \phi(L,t) = 0. \tag{30}$$

Consider the shape function $\sin(\pi z/L)$, which satisfies the boundary conditions for the first mode vibration. The displacement $u(z,t)$ and twist $\phi(z,t)$ can be described by

$$u(z,t) = \rho q_1(t)\sin\left(\frac{\pi z}{L}\right), \qquad \phi(z,t) = q_2(t)\sin\left(\frac{\pi z}{L}\right). \tag{31}$$

Substituting these into the partial differential equations (26) and (27) yields

$$\ddot{q}_1 + \omega_1^2 q_1 + 2\varepsilon\zeta_1\omega_1\dot{q}_1 + \sqrt{\varepsilon}k_{12}q_2\xi(t) = 0,$$
$$\ddot{q}_2 + \omega_2^2 q_2 + 2\varepsilon\zeta_2\omega_2\dot{q}_2 + \sqrt{\varepsilon}k_{21}q_1\xi(t) = 0,$$

(32)

where

$$\omega_1^2 = \frac{\pi^4}{mL^4}EI_y, \quad \omega_2^2 = \frac{\pi^2}{m\rho^2 L^2}GJ, \quad 2\varepsilon\zeta_1\omega_1 = \frac{d_u}{m}, \quad 2\varepsilon\zeta_2\omega_2 = \frac{d_\phi}{\rho^2 m},$$

$$k_{12} = \frac{1}{2mL\rho}\left(7 - \frac{\pi^2}{4}\right), \quad k_{12} = -\frac{1}{2mL\rho}\left(1 + \frac{\pi^2}{4}\right), \quad \xi(t) = \frac{P(t)}{P_{cr}}, \quad P_{cr} = \frac{4|\omega_1^2 - \omega_2^2|mL\rho}{\sqrt{(28-\pi^2)(4+\pi^2)}}.$$

Here, $\xi(t)$ is assumed to be a stationary stochastic process.

5. Numerical determination of the p-th moment Lyapunov exponent and conclusions

The numerical determination of the p-th moment Lyapunov exponents is important in assessing the validity and the ranges of applicability of the approximate analytical results. For systems of large dimensions, it is very difficult, if is not impossible, to obtain analytical results. In many engineering applications, the amplitude of noise excitation is not small and approximate analytical methods, such as the method of perturbation or the method of stochastic averaging, cannot be applied. Therefore, numerical approaches have to be employed to evaluate the moment Lyapunov exponents. The numerical approach is based on expanding the exact solution of the system of Itô stochastic differential equations, (33), in powers of the time increment h and the small parameter ε, as proposed in [Milstein and Tret'yakov 1997]. The state vector of the system (4) is to be rewritten as a system of Itô stochastic differential equations with low noise in the form

$$dx_1 = \omega_1 x_2\, dt = [\tilde{a}_1(t, X) + \varepsilon\tilde{b}_1(t, X)]\, dt + \sqrt{\varepsilon}\sigma_{11}(t, X)\, dw(t),$$

$$dx_2 = -\omega_1(x_1 + 2\varepsilon\zeta_1 x_2)\, dt - \sqrt{\varepsilon}\sigma\left(\frac{k_{11}}{\omega_1}x_1 + \frac{k_{12}}{\omega_1}x_3\right)dw(t)$$
$$= [\tilde{a}_2(t, X) + \varepsilon\tilde{b}_2(t, X)]\, dt + \sqrt{\varepsilon}\sigma_{21}(t, X)\, dw(t),$$

$$dx_3 = \omega_2 x_4\, dt = [\tilde{a}_3(t, X) + \varepsilon\tilde{b}_3(t, X)]\, dt + \sqrt{\varepsilon}\sigma_{31}(t, X)\, dw(t),$$

$$dx_4 = -\omega_2(x_3 + 2\varepsilon\zeta_2 x_4)\, dt - \sqrt{\varepsilon}\sigma\left(\frac{k_{21}}{\omega_2}x_1 + \frac{k_{22}}{\omega_2}x_3\right)dw(t)$$
$$= [\tilde{a}_4(t, X) + \varepsilon\tilde{b}_4(t, X)]\, dt + \sqrt{\varepsilon}\sigma_{41}(t, X)\, dw(t).$$

(33)

For numerical solutions of the stochastic differential (33) the weak Runge–Kutta method with error $R = O(h^4 + \varepsilon^4 h)$ may be applied to evaluate numerically the p-th moment $E[\|X\|^p]$. A total of N samples of the solutions of (33) are generated. The weak Runge–Kutta scheme of the s-th realization of (33) at the $(k+1)$-th iteration with $t^{(k+1)} - t^{(k)} = h$, where h is the time step of integration, is given by

[Milstein and Tret'yakov 1997]:

$$X_j^{(k+1)} = X_j^{(k)} + \frac{\varepsilon^{1/2}h^{1/2}}{6}\Big[\sigma_{j1}(t^{(k)}, X^{(k)})(\xi^{(k)} + 6\eta^{(k)}) + 4\sigma_{j1}\Big(t^{(k+1/2)}, X^{(k)} + \frac{K_2}{2}\Big)\cdot\xi^{(k)}$$
$$+ \sigma_{j1}(t^{(k+1)}, X^{(k)} + K_1)\cdot(\xi^{(k)} - 6\eta^{(k)})\Big]$$
$$+ \frac{h}{2}\Big[\tilde{a}_j\Big(t^{(k)}, X^{(k)} + \varepsilon^{1/2}h^{1/2}\sigma_{j1}(t^{(k)}, X^{(k)})\eta^{(k)}\Big) - \tilde{a}_j\Big(t^{(k)}, X^{(k)} - \varepsilon^{1/2}h^{1/2}\sigma_{j1}(t^{(k)}, X^{(k)})\eta^{(k)}\Big)\Big]$$
$$+ \frac{1}{6}(K_1 + 2K_2 + 2K_3 + K_4) + \frac{\varepsilon}{4}(l_1 + 3l_2), \qquad j = 1, 2, 3, 4, \quad (34)$$

where

$$\boldsymbol{\sigma}_1 = (\sigma_{11}(t, X), \sigma_{21}(t, X), \sigma_{31}(t, X), \sigma_{41}(t, X)),$$
$$X = (x_1, x_2, x_3, x_4),$$
$$\boldsymbol{a} = (\tilde{a}_1(t, X), \tilde{a}_2(t, X), \tilde{a}_3(t, X), \tilde{a}_4(t, X)),$$
$$\boldsymbol{b} = (\tilde{b}_1(t, X), \tilde{b}_2(t, X), \tilde{b}_3(t, X), \tilde{b}_4(t, X)),$$
$$K_1 = (K_{11}, K_{12}, K_{13}, K_{14}) = h \cdot \tilde{\boldsymbol{a}}(t^{(k)}, X^{(k)}),$$
$$K_2 = (K_{21}, K_{22}, K_{23}, K_{24}) = h \cdot \tilde{\boldsymbol{a}}\Big(t^{(k+1/2)}, X^{(k)} + \frac{K_1}{2}\Big),$$
$$K_3 = (K_{31}, K_{32}, K_{33}, K_{34}) = h \cdot \tilde{\boldsymbol{a}}\Big(t^{(k+1/2)}, X^{(k)} + \varepsilon^{1/2}h^{1/2}\boldsymbol{\sigma}_1(t^{(k)}, X^{(k)})\xi^{(k)} + \frac{K_2}{2} + \varepsilon\frac{l_1}{4} + \varepsilon\frac{3}{4}l_2\Big),$$
$$K_4 = (K_{41}, K_{42}, K_{43}, K_{44}) = h \cdot \tilde{\boldsymbol{a}}\Big(t^{(k+1)}, X^{(k)} + \varepsilon^{1/2}h^{1/2}\boldsymbol{\sigma}_1(t^{(k+1)}, X^{(k)} + K_1)\xi^{(k)} + K_3 + \varepsilon l_1\Big),$$
$$l_1 = (l_{11}, l_{12}, l_{13}, l_{14}) = h \cdot \tilde{\boldsymbol{b}}(t^{(k)}, X^{(k)}),$$
$$l_2 = (l_{21}, l_{22}, l_{23}, l_{24}) = h \cdot \tilde{\boldsymbol{b}}\Big(t^{(k+2/3)}, X^{(k)} + \frac{2}{9}K_1 + \frac{4}{9}K_2\Big),$$

and ξ and η are random variables simulated using the two-point distribution

$$P(\xi = -1) = P(\xi = 1) = \frac{1}{2}, \qquad P\Big(\eta = -\frac{1}{\sqrt{12}}\Big) = P\Big(\eta = \frac{1}{\sqrt{12}}\Big) = \frac{1}{2}.$$

Having obtained N samples of the solutions of the stochastic differential equations (33) the p-th moment can be determined as follows:

$$E\big[\|X^{(k+1)}\|^p\big] = \frac{1}{N}\sum_{s=1}^{N}\|X_s^{(k+1)}\|^p, \qquad \|X_s^{(k+1)}\| = \sqrt{(X_s^{(k+1)})^T(X_s^{(k+1)})}. \quad (35)$$

By the Monte Carlo technique we numerically calculate the p-th moment Lyapunov exponent for all the values of p of interest, defined as

$$\Lambda(p) = \frac{1}{T}\ln E\big[\|X_{(T)}\|^p\big]. \quad (36)$$

The function $\Lambda(p)$ in the limit of large time ($T \to \infty$) tends to the moment Lyapunov exponent $\Lambda(p)$. In this paper, a singular perturbation method is applied to obtain first-order low noise expansions of the moment Lyapunov exponent of a coupled white noise driven, two-degree-of-freedom system. The
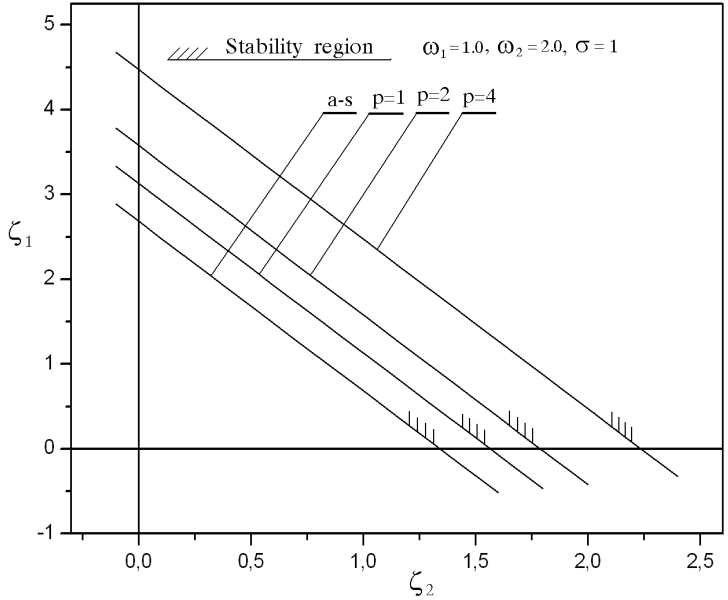
Figure 2. Stability regions for almost-sure (a-s) and p-th moment stability for $k_{12} = 5$, $k_{21} = -3.82$.

Lyapunov exponent is determined by using the relationship between the moment Lyapunov exponent and the Lyapunov exponent. The slope of the moment Lyapunov exponent curve at $p = 0$ is the Lyapunov exponent. When the Lyapunov exponent is negative, the system (3) is almost-sure stable with probability 1; otherwise it is unstable. The results obtained above can be directly applied to analyze the flexural-torsional stability of a thin rectangular elastic beam of length L subjected to a stochastic follower force. For the purpose of illustration, in the numerical study we consider set system parameters $k_{12} = 5$, $k_{21} = -3.82$, $\omega_1 = 1$, $\omega_2 = 2$, and $\sigma = 1$. Figure 2 shows the almost-sure and p-th moment stability boundaries with respect to the damping coefficients ζ_1 and ζ_2. Note that the moment stability boundaries are more conservative than the almost-sure boundary. These boundaries become increasingly conservative as p increases. Numerical determination of the p-th moment Lyapunov exponent is important in assessing the validity and the range of applicability of the approximate analytical results obtained for stochastic systems. The Monte Carlo simulation methods are usually more versatile, especially when the noise excitations cannot be described in a form that can be treated easily using analytical tools. From the central limit theorem, it is well known that the estimated p-th moment Lyapunov exponent is a random number, with the mean being the true value of the p-th moment Lyapunov exponent and the standard deviation $n_p/\sqrt{N}$, where n_p is the sample standard deviation determined from the N samples. The standard deviation of the estimated p-th moment Lyapunov exponent can be reduced by increasing the number of samples, $N = 2000, 4000, 8000$. The total time of simulation is 5 and $h = 0.0005$ is the time step of integration. Numerical results of the p-th moment Lyapunov exponent $\Lambda(p)$ from the Monte Carlo simulation, along with Equation (22) (the solid line), are plotted in Figure 3 for $\omega_1 = 1.0$, $\omega_2 = 2.0$, $\sigma = 1$, $\zeta_1 = 4.5$, $\zeta_2 = 0.2$ and $\varepsilon = 0.025, 0.05, 0.1$. It is observed that the discrepancies between the approximate analytical results (the solid line) and the numerical results (the dotted line) increase for large values of ε.
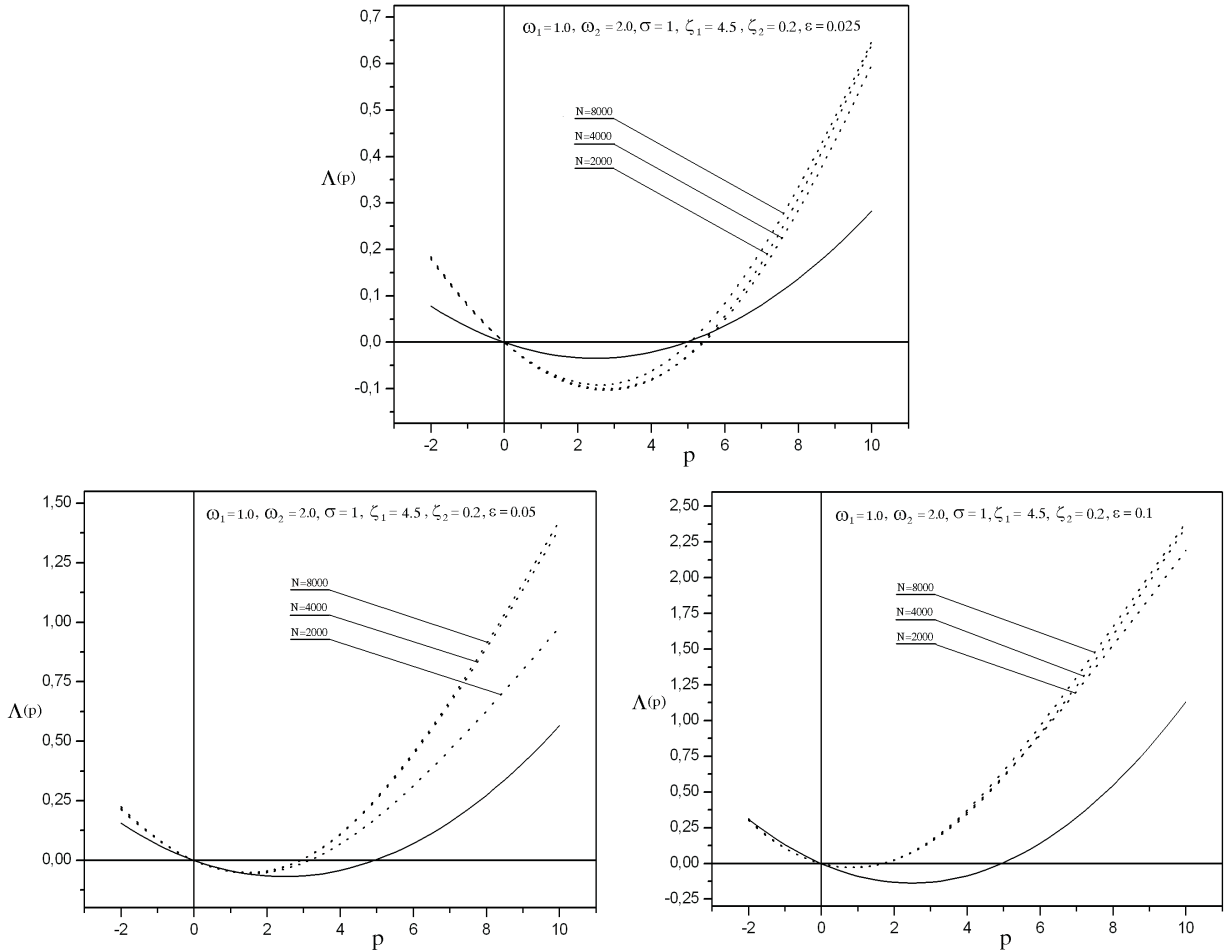
Figure 3. Variation of the moment Lyapunov exponent $\Lambda(p)$ with p for $k_{12} = 5$, $k_{21} = -3.82$ and different value ε.

References

[Arnold et al. 1997] L. Arnold, M. M. Doyle, and N. Sri Namachchivaya, "Small noise expansion of moment Lyapunov exponents for two-dimensional systems", *Dyn. Stab. Syst.* **12**:3 (1997), 187–211.

[Bolotin 1964] V. Bolotin, *The dynamic stability of elastic systems*, Holden-Day, San Francisco, 1964.

[Khasminskii and Moshchuk 1998] R. Khasminskii and N. Moshchuk, "Moment Lyapunov exponent and stability index for linear conservative system with small random perturbation", *SIAM J. Appl. Math.* **58**:1 (1998), 245–256.

[Kozić et al. 2008] P. Kozić, R. Pavlović, and G. Janevski, "Moment Lyapunov exponents of the stochastic parametrical Hill's equation", *Int. J. Solids Struct.* **45**:24 (2008), 6056–6066.

[Milstein and Tret'yakov 1997] G. N. Milstein and M. V. Tret'yakov, "Numerical methods in the weak sense for stochastic differential equations with small noise", *SIAM J. Numer. Anal.* **34**:6 (1997), 2142–2167.

[Sri Namachchivaya and Van Roessel 2004] N. Sri Namachchivaya and H. J. Van Roessel, "Stochastic stability of coupled oscillators in resonance: a perturbation approach", *J. Appl. Mech.* (*ASME*) **71**:6 (2004), 759–767.

[Sri Namachchivaya and Vedula 2000] N. Sri Namachchivaya and L. Vedula, "Stabilization of linear systems by noise: application to flow induced oscillations", *Dyn. Stab. Syst.* **15**:2 (2000), 185–208.

[Sri Namachchivaya et al. 1994] N. Sri Namachchivaya, H. J. Van Roessel, and S. Talwar, "Maximal Lyapunov exponent and almost-sure stability for coupled two-degree-of-freedom stochastic systems", *J. Appl. Mech.* (*ASME*) **61**:2 (1994), 446–452.

[Wedig 1988] W. Wedig, "Lyapunov exponent of stochastic systems and related bifurcation problem", pp. 315–327 in *Stochastic structural dynamics: progress in theory and applications*, edited by S. T. Ariaratnam et al., Elsevier, London, 1988.

[Xie 2001] W.-C. Xie, "Moment Lyapunov exponents of a two-dimensional system under real-noise excitation", *J. Sound Vib.* **239**:1 (2001), 139–155.

[Xie 2002] W.-C. Xie, "Moment Lyapunov exponents of a two-dimensional viscoelastic system under bounded noise excitation", *J. Appl. Mech.* (*ASME*) **69**:3 (2002), 346–357.

PREDRAG KOZIĆ: kozip@yahoo.com
Department of Mechanical Engineering, University of Niš, Medvedeva 14, 18000 Niš, Serbia

GORAN JANEVSKI: gocky.jane@gmail.com
Department of Mechanical Engineering, University of Niš, Medvedeva 14, 18000 Niš, Serbia

RATKO PAVLOVIĆ: ratpav@yahoo.com
Department of Mechanical Engineering, University of Niš, Medvedeva 14, 18000 Niš, Serbia

EVALUATION OF FILM-SUBSTRATE ADHESION VIA IMPACT USING COATED BULLETS

CHEN-WU WU, ZHI-LIN WU, KUN ZHANG AND GUANG-NAN CHEN

A method was devised to evaluate the adhesion between a film and a substrate. A front-end coated bullet is accelerated by a gas gun and hits the substrate of the specimen under test. The impact generates a compressive stress pulse that propagates toward the film. After transmission through the interface, part of the pulse is reflected on the free surface of the film, and tensile stress arises at the film-substrate interface, possibly inducing debonding of the film.

This dynamic process was demonstrated analytically and simulated numerically by the finite element method. The results validate the initial concept and lay the foundation for further optimization of this method.

1. Introduction

Films and coatings with resistance to wear, corrosion, thermal degradation, and other important functions have been adopted in a great many fields [Freund and Suresh 2003]. However, their prospective applications are restricted because of premature debonding. Numerous ways have been tried to evaluate the adhesion between the film and the substrate [Hsueh 2002]. The key step in these experiments is to exert a simple loading directly at the interface and separate the film from the substrate. This is hard to accomplish, especially when the film is strongly bonded. Although some methods, such as scratching and indenting, have been adopted in some situations, the severe deformation around the interface makes it difficult to quantify the adhesion.

The method of laser spallation was developed to overcome this problem [Vossen 1978; Gupta et al. 1990; Gupta and Yuan 1993]. By irradiating the substrate with a laser beam, a compressive stress pulse of short duration is generated. Tensile stress arises after the compressive stress pulse is reflected on the free surface of the film being tested. This tensile stress can peel the film from the substrate if the pulse is strong enough.

It is recognized that the method of laser spallation can exert pulse loadings of short duration directly on the interface and obtain a high strain rate to restrain the effect of plasticity of the materials. At the same time, this dynamic method may reveal some dynamic behaviors of the film-substrate interface that are not attainable by quasistatic methods. However, the laser spallation inevitably involves complicated phenomena such as rapid melting and ablation of the materials, which brings about great difficulties in analysis and modeling.
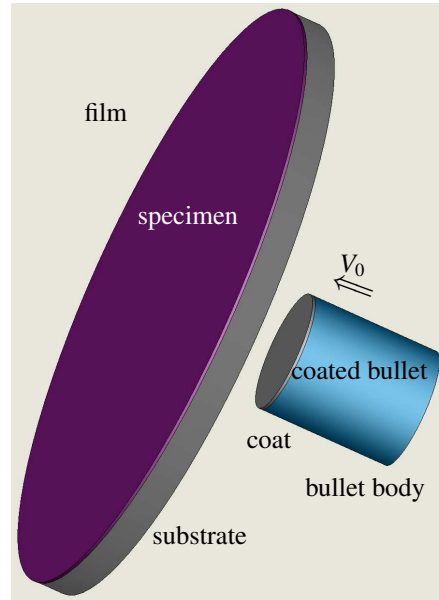
Figure 1. Sketch of the coated bullet and the specimen.

In this study, a method of impact with coated bullets was devised in order to evaluate the interface adhesion between film and substrate. Finite element simulation was then carried out to compute the profiles of the interface stresses as well as the surface stresses of the specimen under impact.

2. Theoretical formulation of the impact method

As shown in Figure 1, a cylindrical bullet with a coated front-end is accelerated by a gas gun and hits the substrate of the test specimen, with initial velocity V_0. Under the impact, a compressive stress pulse is generated and propagate toward the film. Tensile stress then arises after the compressive stress pulse is reflected on the free surface of the film.

For convenience, the coating material for the front-end of the bullet body is chosen to have the same acoustic impedance as the substrate of the specimen. The acoustic impedance of the bullet body is denoted by $\rho_1 c_1$, the acoustic impedance of both the bullet coating and the test substrate is denoted by $\rho_2 c_2$, and the acoustic impedance of the test film is denoted by $\rho_3 c_3$.

To produce an appropriate stress pulse, $\rho_1 c_1$ should be much less than $\rho_2 c_2$, so as to significantly reduce the transmission of the initial compressive stress pulse into the bullet body. In the following, r indicates the radius of the bullet, l is its length, t_c the thickness of the coating on the bullet body, r_s the radius of the specimen, t_s the thickness of the substrate, and t_f that of the film. If the equation $t_c c_3 = t_f c_2$ is satisfied, the spatial width of the stress pulse running through the tested film is $2t_f$. This ensures that the tensile stress arises mainly around the interface in the test.

The propagation and evolution of the stress wave are sketched in Figure 2. At $t = t_1$, the coated end of the bullet collides with the substrate and compressive stress waves arise within both the bullet coat and the substrate. At $t = t_2$, the compressive stress wave propagating into the bullet impinges on the interface

of the bullet coat and the bullet body. This wave is partly transmitted into the bullet body and partly reflected, as depicted under $t = t_3$. Thus, a compressive stress pulse with a tail develops and propagates toward the specimen, as depicted under $t = t_4, t_5, t_6$.

If l is large enough, the compressive stress pulse σ imported into the specimen can be roughly predicted by one-dimensional stress wave theory. The shape of this pulse is seen in Figure 2, right, before the influences of the far rear of the bullet body can be sensed. This prediction is rather accurate, especially in the initial stage after impact; see [Wang 2005, pp. 29–47] for details.

The intensity of the tail of the compressive stress pulse (the plateau in Figure 2, right) is given by $2\rho_1 c_1 \sigma_0/(\rho_1 c_1 + \rho_2 c_2)$. This is the stress transmitted into the bullet body. This tail can be decreased to a very small value if $\rho_1 c_1$ is much less than $\rho_2 c_2$. When the input compressive stress pulse impinges on the interface between the film and the substrate in the test ($t = t_7$), it is, again, partly reflected and partly transmitted into the specimen film [Wang 2005, pp. 29–47]. The reflected and transmitted pulses have intensities, respectively,

$$\sigma_{r1} = \frac{\rho_3 c_3 - \rho_2 c_2}{\rho_2 c_2 + \rho_3 c_3}\sigma \qquad \text{and} \qquad \sigma_t = \frac{2\rho_3 c_3}{\rho_2 c_2 + \rho_3 c_3}\sigma.$$
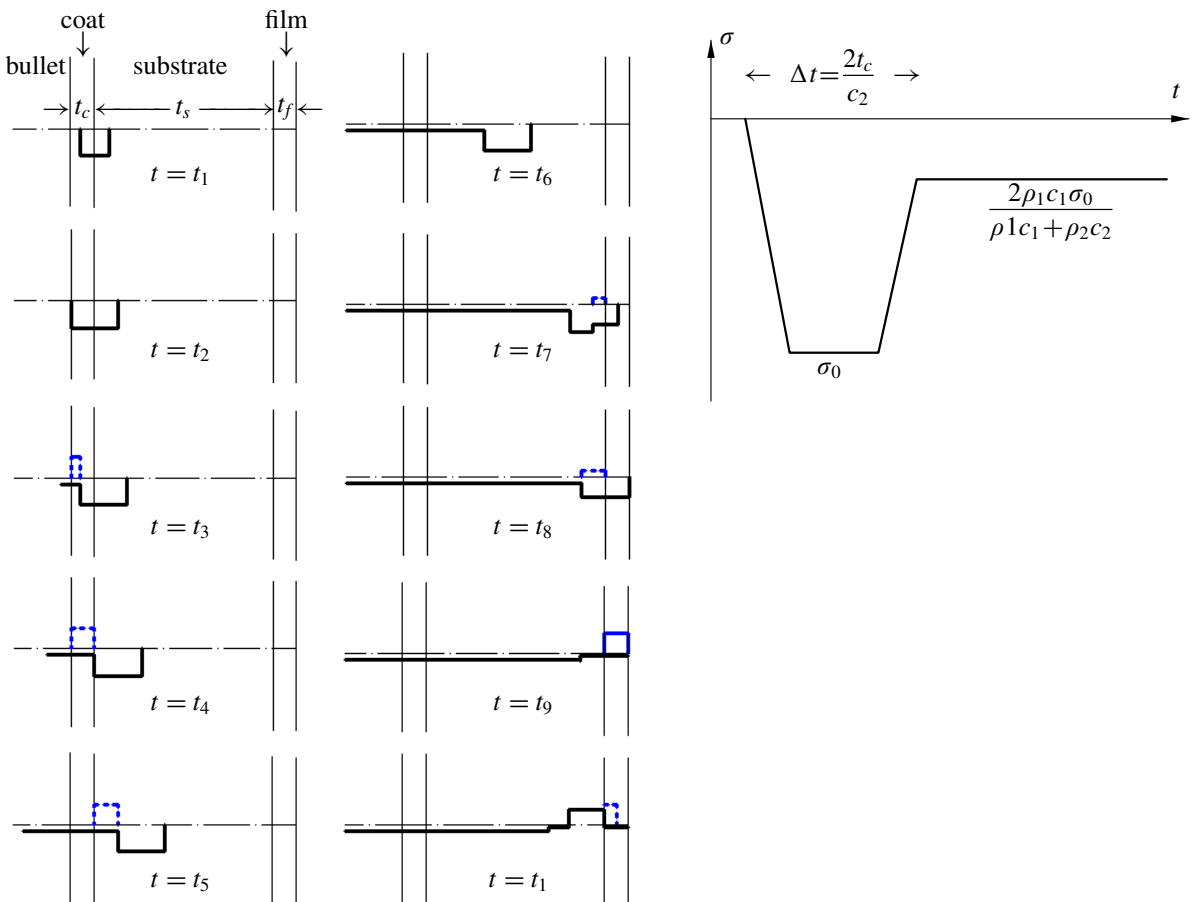

Figure 2. Evolution of the stress wave under impact.

A tensile stress pulse $\sigma_{r2} = -\sigma_t$ arises after the transmission pulse σ_t is reflected from the free surface of the film ($t = t_8, t_9$ in Figure 2, left). By taking the algebraic sum of this tensile stress with that of the local tail of the input compressive stress pulse, a resultant tensile stress is obtained around the interface ($t = t_{10}$ in Figure 2). If the resulting tensile stress exceeds the bonding strength of the interface, debonding occurs. By measuring the initial velocity of the bullet, for which classical methods of high accuracy can be applied, the interface stress history can be very accurately predicted with the finite element method. Combined with the fracture features of the interface through the experimental observation, the relationship between the interface stress history and the adhesion between the film and the substrate can be established.

3. Numerical analysis of the stress

To describe the stress profiles more accurately, an axisymmetric finite element model was set up as shown in Figure 3, and the impact was simulated with the finite element code LS-DYNA. The materials are assumed to be ideally elastic and the parameters chosen are listed in Table 1. Item 1 represents the material of the bullet body, item 2 represents the coating on the bullet and the substrate of the specimen in the test, and item 3 represents the film of the specimen. The geometric parameters are $l = 5$ mm, $r = 2.5$ mm, $t_s = 1$ mm, and $r_s = 10$ mm. A thickness of $t_c = t_f = 0.1$ mm was adopted considering that the acoustic impedance of the coating on the bullet was very near to that of the tested film. The initial velocity of the bullet was $V_0 = 250$ m/s.

We consider the stress component σ_{yy} (*normal stress*) acting on the surface of the substrate and the stress component σ_{yy} acting on the interface between the film and the substrate. Figure 4 shows the mean value of σ_{yy} over the circular region of radius r around the symmetry axis. It can be seen that the
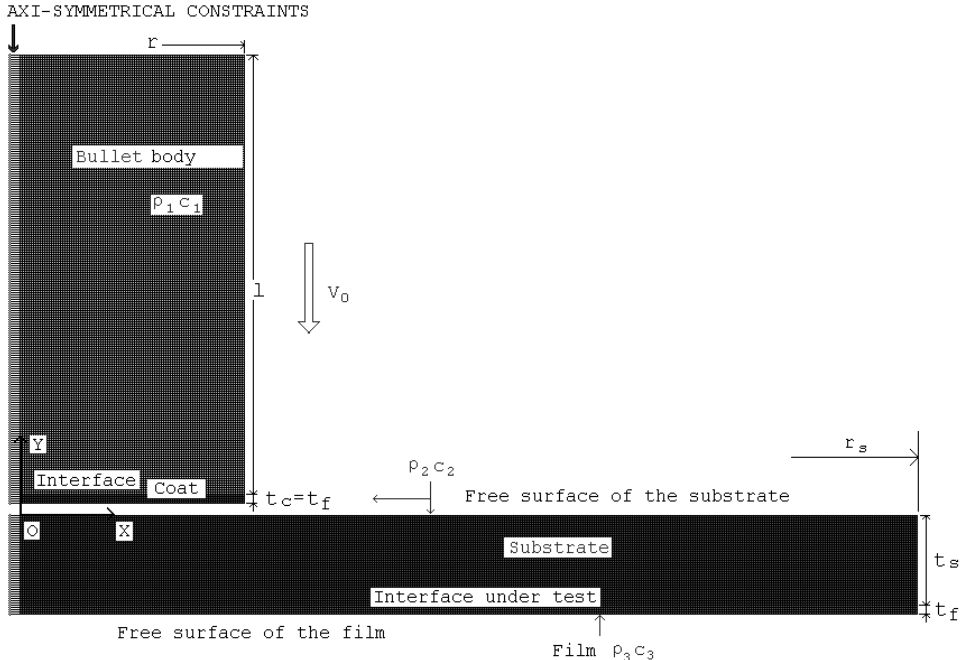

Figure 3. Finite element model of the coated bullet and specimen.

	ρ (kg/m^3)	E (GPa)	ν
1 = bullet body	1050	3.38	0.35
2 = bullet coating, specimen substrate	7850	209	0.30
3 = film	7190	242	0.15

Table 1. Mechanical parameters of the material. ρ = density, E = elastic modulus, ν = Poisson's ratio.

input compressive stress pulse (black line in Figure 4) oscillates around the theoretical trend line drawn in Figure 2, right (here represented by the red dots). At the interface, there is a compressive stress pulse and subsequently a tensile stress pulse, both with duration of approximately t_f/c_3. The maximum interface normal stress appears at the instant $t \approx 0.268\,\mu$s. The stress component σ_{yy} within the specimen for this instant is shown in Figure 5, in which a thin strip area, close to r in length and adjacent to the interface, is shaded according to the tensile stress.
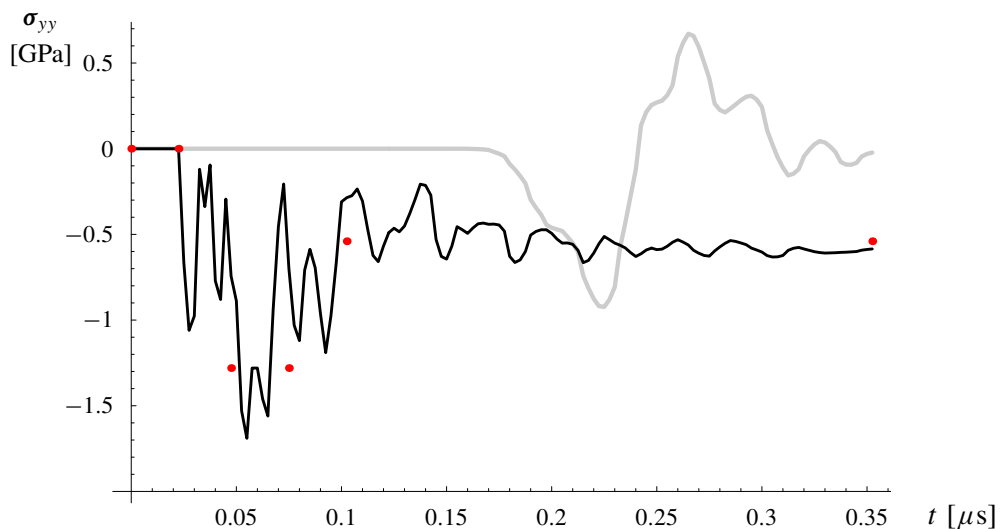
Figure 4. Average normal stress at the surface of the substrate (black line) and at the interface (gray line) as a function of time. The red dots indicate the trend line (pulse shape in Figure 2, right).
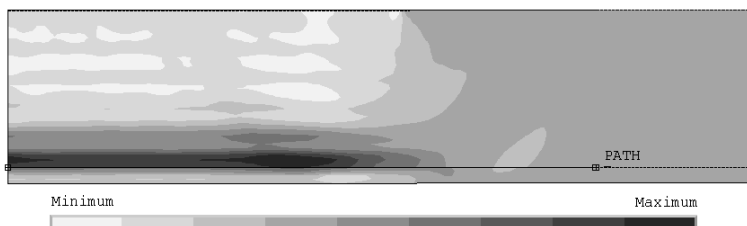
Figure 5. Stress component σ_{yy} at $t \approx 0.268\,\mu$s.
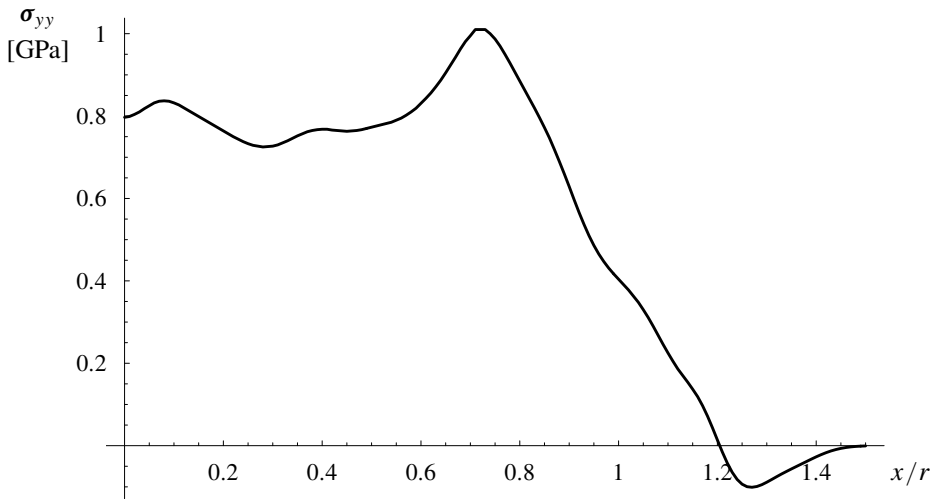
Figure 6. Interfacial normal stress at $t \approx 0.268 \, \mu$s.

The interface normal stresses are further mapped at a path of length $1.5r$ along the interface as shown in Figure 6, of which the origin is located at the symmetrical axis. This figure suggests that the tensile stress is mainly confined to the circular region of radius r and roughly uniform within that region. It is this tensile stress that can induce the debonding of the film from the substrate.

As mentioned above, the matching of the acoustic impedance of the materials for the bullet body and the bullet coating significantly influences the input compressive pulse. Moreover, the bullet might penetrate the specimen once its kinetic energy exceeds some magnitude [Wang 2005, pp. 29–47]; this is to be avoided in the test. Therefore, in order to produce the expected interface stress and separate the film from the substrate without the bullet penetrating into specimen, an analysis and numerical simulation should be conducted to decide the appropriate range of the initial velocity for specific material pairs.

4. Conclusions

In this study, a method of impact with a front-end coated bullet was devised to evaluate the adhesion between a film and a substrate. The evolution of the stress wave during the impact was investigated theoretically. The stresses were calculated numerically. The results showed that a compressive stress pulse with a tail develops on the surface of the substrate. After the compressive stress pulse is reflected on the free surface of the film, tensile stress arises around the interface in the test. This model can be used directly for further optimization of the impact method.

References

[Freund and Suresh 2003] L. B. Freund and S. Suresh, *Thin film materials*, Cambridge University Press, Cambridge, 2003.

[Gupta and Yuan 1993] V. Gupta and J. Yuan, "Measurement of interface strength by the modified laser spallation technique, II: Applications to metal/ceramic interfaces", *J. Appl. Phys.* **74** (1993), 2397–2404.

[Gupta et al. 1990] V. Gupta, A. S. Argon, J. A. Cornie, and D. M. Parks, "Measurement of interface strength by laser-pulse-induced spallation", *Mater. Sci. Eng. A* **126** (1990), 105.

[Hsueh 2002] C. H. Hsueh, "Devising a method to measure film adhesion through modeling", *Appl. Phys. Lett.* **81**:9 (2002), 1615–1617.

[Vossen 1978] J. L. Vossen, "Measurement of film-substrate bond strength by laser spallation", pp. 122–133 in *Adhesion measurement of thin films, thick films, and bulk coatings*, edited by K. L. Mittal, ASTM Special Technical Publication **640**, American Society for Testing and Materials, Philadelphia, 1978.

[Wang 2005] L. L. Wang, *Foundations of stress waves*, 2nd ed. ed., National Defense Industry Press, Beijing, 2005. In Chinese.

CHEN-WU WU: wcw_on@yahoo.com.cn
Institute of Mechanics, Chinese Academy of Sciences, 15 Beisihuanxi Road, Beijing 100190, China

ZHI-LIN WU: wuruinan-1994@mail.njust.edu.cn
School of Mechanical Engineering, Nanjing University of Science and Technology, Nanjing 210094, China

KUN ZHANG: kzhang@imech.ac.cn
Institute of Mechanics, Chinese Academy of Sciences, 15 Beisihuanxi Road, Beijing 100190, China

GUANG-NAN CHEN: gnchen@imech.ac.cn
Institute of Mechanics, Chinese Academy of Sciences, 15 Beisihuanxi Road, Beijing 100190, China

THE EFFECTS OF WARPING CONSTRAINTS ON THE BUCKLING OF THIN-WALLED STRUCTURES

MARCELLO PIGNATARO, NICOLA RIZZI, GIUSEPPE RUTA AND VALERIO VARANO

We present two applications of a direct one-dimensional beam model suitable for describing the buckling of thin-walled structures. The first application considers the buckling of a compressed beam with an intermediate stiffener under various warping constraints. The second describes the buckling of a two-bar frame, known as a Roorda frame, loaded by a dead force at the joint. Various warping constraints at the bar ends are considered and the relevant buckling modes and loads are numerically evaluated. Numerical results are presented for both cases; some of these appear to be new.

1. Introduction: a direct one-dimensional model for thin-walled beams

A very interesting problem in the elastic stability of structural elements is the flexural-torsional buckling of thin-walled beams. A short description of the origins of the problem with references to related existing literature may be found in [Ruta et al. 2006; 2008].

In [Ruta et al. 2006] the direct model introduced in [Tatone and Rizzi 1991; Rizzi and Tatone 1996] was refined in order to describe the flexural-torsional buckling of beams with nonsymmetric cross-sections. Strain measures are described with respect to both the centroidal and the shear center axes of the beam (as a first step, it is immaterial which of the shear centers presented in the literature is chosen). The power expended by inner actions is decomposed so as to distinguish between forces and moments at the centroid or the shear center. Nonlinear hyperelastic constitutive relations and standard inner constraints [Rizzi and Tatone 1996; Pignataro and Ruta 2003; Pignataro et al. 2006] imply reactive terms in addition to the active parts of some contact actions, accounting for the geometry of nonsymmetric cross-sections. The obtained field equations for the bifurcation in terms of the displacement components are more general than those in [Rizzi and Tatone 1996; Pignataro and Ruta 2003; Pignataro et al. 2006].

In [Ruta et al. 2006] some simple examples of flexural-torsional buckling and postbuckling phenomena have been investigated, showing the coincidence of the results with those in the literature, for instance in [Timoshenko and Gere 1961; Grimaldi and Pignataro 1979]. Further applications of the refined model are found in [Ruta et al. 2008] where, for a simply supported compressed beam, the effect of warping constraints at the beam ends has been examined and the relevant critical loads have been presented.

A natural development of the studies performed in [Ruta et al. 2006; 2008] appears to be the analysis of the buckling of more complex structures by means of the refined model. In this paper, the authors present two cases of interest in applications. The first is a compressed beam reinforced by an intermediate stiffener acting as a warping constraint. The second is a simple frame loaded by a dead force, known

as a Roorda frame in the literature. We first summarize the key notes of the refined model (details are found in [Ruta et al. 2006; 2008]); then, we present the field equations for the considered problems and some numerical results.

The beam reference shape consists of a series of plane cross-sections orthogonally attached to the straight centroidal axis, or to the parallel shear center axis. We fix orthogonal cartesian coordinates with x_1 parallel to the beam axes and a consistent orthonormal right-handed vector basis (i_1, i_2, i_3). Suitable strain measures are

$$
\begin{aligned}
\boldsymbol{E} &= \boldsymbol{R}^\top \boldsymbol{R}' = \chi_1 \boldsymbol{i}_2 \wedge \boldsymbol{i}_3 + \chi_2 \boldsymbol{i}_3 \wedge \boldsymbol{i}_1 + \chi_3 \boldsymbol{i}_1 \wedge \boldsymbol{i}_2, \\
\boldsymbol{e}_o &= \boldsymbol{R}^\top \boldsymbol{p}'_o - \boldsymbol{q}'_o = \varepsilon_1 \boldsymbol{i}_1 + \varepsilon_2 \boldsymbol{i}_2 + \varepsilon_3 \boldsymbol{i}_3, \\
\boldsymbol{e}_c &= \boldsymbol{R}^\top \boldsymbol{p}'_c - \boldsymbol{q}'_c = \boldsymbol{e}_o + \boldsymbol{E}\boldsymbol{c} = \varepsilon_{1c} \boldsymbol{i}_1 + \varepsilon_{2c} \boldsymbol{i}_2 + \varepsilon_{3c} \boldsymbol{i}_3 \\
&= (\varepsilon_1 + \chi_2 c_3 - \chi_3 c_2) \boldsymbol{i}_1 + (\varepsilon_2 - \chi_1 c_3) \boldsymbol{i}_2 + (\varepsilon_3 + \chi_1 c_2) \boldsymbol{i}_3, \qquad \alpha, \qquad \eta = \alpha',
\end{aligned}
\tag{1-1}
$$

where o is the centroid, c is the shear center, and $\boldsymbol{c} = c_2 \boldsymbol{i}_2 + c_3 \boldsymbol{i}_3 = c - o$; $\boldsymbol{p}_o(x_1, t)$ and $\boldsymbol{p}_c(x_1, t)$ are the vector-valued present placements of the axes, given by $\boldsymbol{q}_o(x_1)$ and $\boldsymbol{q}_c(x_1)$ in the reference shape; $\boldsymbol{R}(x_1, t)$ is the proper orthogonal tensor-valued cross-sectional rotation from the reference to the present shape; and $\alpha(x_1, t)$ is the scalar-valued coarse descriptor of warping. The skew tensor $\boldsymbol{E}$ provides the curvature of the beam axes, and the vectors $\boldsymbol{e}_o$ and $\boldsymbol{e}_c$ measure the differences between the tangent to the axes in the present and reference shape. We have defined χ_1 as the torsion curvature (twist); χ_2 and χ_3 as the bending curvatures; the wedge product $\wedge$ between vectors provides skew tensors; ε_1 is the elongation of the centroidal axis; and ε_2 and ε_3 are the shearing strains between this axis and the cross-sections. We decompose the displacement of the centroidal axis and the rotation:

$$
\boldsymbol{u} = \boldsymbol{p}_o - \boldsymbol{q}_o = u_1 \boldsymbol{i}_1 + u_2 \boldsymbol{i}_2 + u_3 \boldsymbol{i}_3, \qquad \boldsymbol{R} = \boldsymbol{R}_3 \boldsymbol{R}_2 \boldsymbol{R}_1,
\tag{1-2}
$$

where $\boldsymbol{R}_1$ is a rotation of amplitude φ_1 around $\boldsymbol{i}_1$; $\boldsymbol{R}_2$ is a rotation of amplitude φ_2 around $\boldsymbol{R}_1 \boldsymbol{i}_2$; $\boldsymbol{R}_3$ is a rotation of amplitude φ_3 around $\boldsymbol{R}_2 \boldsymbol{R}_1 \boldsymbol{i}_3$.

The power P^e expended by external actions is a linear functional of the velocities with respect to the shear center, while the power P^i expended by the interactions among different parts of the beam is a linear functional of the velocities with respect to the shear center and of their first derivatives with respect to x_1 (grade one theory, see, for example, [DiCarlo 1996]). Standard arguments on the balance of power and a pull-back procedure [Ruta et al. 2006; 2008] yield the local balance of force and torque in the reference shape with respect to c, the auxiliary equations for bishear and bimoment and the internal power:

$$
\begin{aligned}
\boldsymbol{s}' + \boldsymbol{E}\boldsymbol{s} + \boldsymbol{a} = \boldsymbol{0}, \qquad \boldsymbol{S}' + \boldsymbol{E}\boldsymbol{S} - \boldsymbol{S}\boldsymbol{E} + (\boldsymbol{q}'_c + \boldsymbol{e}_c) \wedge \boldsymbol{s} + \boldsymbol{A} = \boldsymbol{0}, \\
\tau = \beta + \mu', \qquad P^i = \int_0^l (\boldsymbol{s} \cdot \dot{\boldsymbol{e}}_c + \boldsymbol{S} \cdot \dot{\boldsymbol{E}} + \tau \omega + \mu \omega').
\end{aligned}
\tag{1-3}
$$

The vectors $\boldsymbol{a}$ and $\boldsymbol{s}$ are the bulk and contact forces; the skew tensors $\boldsymbol{A}$ and $\boldsymbol{S}$ are the bulk and contact couples; the scalar β is the bulk action spending power on warping; the scalars μ and τ are the bimoment and bishear [Vlasov 1961], respectively, all in the reference shape. We pose:

$$
\boldsymbol{s} = Q_1 \boldsymbol{i}_1 + Q_2 \boldsymbol{i}_2 + Q_3 \boldsymbol{i}_3, \qquad \boldsymbol{S} = S_1 \boldsymbol{i}_2 \wedge \boldsymbol{i}_3 + S_2 \boldsymbol{i}_3 \wedge \boldsymbol{i}_1 + S_3 \boldsymbol{i}_1 \wedge \boldsymbol{i}_2.
\tag{1-4}
$$

By introducing equations (1-1) and (1-4) into (1-3)$_4$, the internal power reads

$$\int_0^l \left[Q_1 \dot{\varepsilon}_1 + Q_2 \dot{\varepsilon}_{2c} + Q_3 \dot{\varepsilon}_{3c} + S_1 \dot{\chi}_1 + (S_2 + c_3 Q_1)\dot{\chi}_2 + (S_3 - c_2 Q_1)\dot{\chi}_3 + \tau \omega + \mu \omega' \right], \tag{1-5}$$

that is, the normal force Q_1 spends power on the centroidal straining, while the shearing forces Q_2 and Q_3 are applied at the shear center; S_1 is the twisting couple, while $M_2 = S_2 + c_3 Q_1$ and $M_3 = S_3 - c_2 Q_1$ are the bending torques, evaluated with respect to the centroid.

If ξ is a constant, we postulate the inner constraints [Vlasov 1961; Reissner 1983; Simo and Vu-Quoc 1991; Tatone and Rizzi 1991; Rizzi and Tatone 1996]

$$\alpha = \xi \chi_1, \quad \xi \in \mathbb{R}, \quad \eta = \xi \chi_1', \quad e_o = \varepsilon_1 q_o' = \varepsilon_1 e_1, \quad \varepsilon_2 = \varepsilon_3 = 0. \tag{1-6}$$

The cross-sections and shear axis do not remain normal ($\varepsilon_{2c} \neq 0$, $\varepsilon_{3c} \neq 0$; see (1-1)).

If the beam is homogeneous and elastic, the material response depends on e, E, α, and η and inner constraints make the contact actions consist of an active and a reactive part [Truesdell and Noll 1965]. The former (subscript a) is determined by a constitutive relation; the latter (subscript r) spends no power on the velocities compatible with the constraints [Truesdell and Noll 1965]. In our refined model, the normal force, the bending torques, and the bimoment are entirely active, while the shearing forces and the bishear have a reactive part [Ruta et al. 2006; 2008]; the reactive twisting torque S_{1r} contains the bishear, in accord with the literature [Vlasov 1961]. As is customary, we suppose that the shearing force and the bishear depend only on the shearing strain, which makes them purely constraint reactions. Thus, some actions are entirely active, others reactive, and only the twisting torque has both components [Ruta et al. 2006; 2008].

We adopt nonlinear hyperelastic constitutive relations in order to apply Koiter's theory [1945] and a static perturbation technique [Budiansky 1974]:

$$\begin{aligned}
Q_{1a} = Q_1 &= a\varepsilon_1 + \tfrac{1}{2}d\chi_1^2, & S_{1a} &= (k + d\varepsilon_1 + f_2\chi_2 + f_3\chi_3 + g\eta)\chi_1, \\
M_{2a} = M_2 &= b_2\chi_2 + \tfrac{1}{2}f_2\chi_1^2, & M_{3a} = M_3 &= b_3\chi_3 + \tfrac{1}{2}f_3\chi_1^2, & \mu_a = \mu = h\eta + \tfrac{1}{2}g\chi_1^2.
\end{aligned} \tag{1-7}$$

The coefficients a, b_j ($j = 2, 3$), k, and h are the rigidities in extension, bending, torsion, and warping, respectively; d, f_j ($j = 2, 3$), and g take into account the couplings between extension and torsion, bending and torsion, and warping and torsion, respectively [Truesdell and Noll 1965; Møllmann 1986]. If, as is standard, the bulk action β vanishes, we obtain [Ruta et al. 2006; 2008]

$$\tau = h\xi\chi_1'' + g\chi_1\chi_1', \qquad S_1 = (k + d\varepsilon_1 + f_2\chi_2 + f_3\chi_3)\chi_1 - h\xi^2\chi_1'' + c_3 Q_2 - c_2 Q_3. \tag{1-8}$$

Comparing [Vlasov 1961, equation (V.1.10)$_3$] with ours we obtain

$$\begin{aligned}
a &= EA, & b_j &= EI_j \quad (j = 2, 3), & k &= GI_c, \\
d &= EI_d, & f_j &= EI_{f_j} \quad (j = 2, 3), & h\xi^2 &= EI_\omega;
\end{aligned} \tag{1-9}$$

E and G are the moduli in extension and shear; A is the cross-sectional area; I_j ($j = 2, 3$) are the centroidal principal moments of inertia; I_c is the torsion factor; I_d is the polar inertia with respect to c; I_ω is the warping inertia (second moment of the sectorial coordinate with respect to the area); $I_{f_2} = \int_A x_3 r^2$; and $I_{f_3} = \int_A x_2 r^2$, with x_j ($j = 2, 3$) the coordinates of a point with respect to the centroid and r its distance from the shear center.

2. Buckling of a compressed beam with a warping stiffener

For a beam compressed by a dead centroidal load of magnitude λ, one solution of the elastic static problem, called the *fundamental* path and denoted by the superscript f, is:

$$
\begin{aligned}
\boldsymbol{u}^{\mathrm{f}} &= -\frac{\lambda}{a}x_1\boldsymbol{i}_1, & \boldsymbol{R}^{\mathrm{f}} &= \boldsymbol{I}, & \alpha^{\mathrm{f}} &= 0, \\
\boldsymbol{e}^{\mathrm{f}} &= -\frac{\lambda}{a}\boldsymbol{i}_1, & \boldsymbol{E}^{\mathrm{f}} &= \boldsymbol{0}, & \eta^{\mathrm{f}} &= 0, \\
\boldsymbol{s}^{\mathrm{f}} &= -\lambda\boldsymbol{i}_1, & \boldsymbol{S}^{\mathrm{f}} &= \boldsymbol{0}, & \tau^{\mathrm{f}} &= 0, & \mu^{\mathrm{f}} &= 0.
\end{aligned}
\tag{2-1}
$$

A different solution, called the *bifurcated* path and denoted by the superscript b, is

$$
\begin{aligned}
\boldsymbol{u}^{\mathrm{b}} &= \boldsymbol{u} - \frac{\lambda}{a}x_1\boldsymbol{i}_1, & \boldsymbol{R}^{\mathrm{b}} &= \boldsymbol{R}+\boldsymbol{I}, & \alpha^{\mathrm{b}} &= \alpha, \\
\boldsymbol{e}^{\mathrm{b}} &= \boldsymbol{e} - \frac{\lambda}{a}\boldsymbol{i}_1, & \boldsymbol{E}^{\mathrm{b}} &= \boldsymbol{E}, & \eta^{\mathrm{b}} &= \eta, \\
\boldsymbol{s}^{\mathrm{b}} &= \boldsymbol{s} - \lambda\boldsymbol{i}_1, & \boldsymbol{S}^{\mathrm{b}} &= \boldsymbol{S}, & \tau^{\mathrm{b}} &= \tau, & \mu^{\mathrm{b}} &= \mu.
\end{aligned}
\tag{2-2}
$$

The differences of quantities evaluated along the bifurcated and the fundamental paths are expressed without superscripts, that is, $(\cdot) := (\cdot)^{\mathrm{b}} - (\cdot)^{\mathrm{f}}$. Strain measures, balance, and auxiliary equations, as well as constitutive relations, are written in terms of differences. The latter are supposed to regularly depend on a parameter σ:

$$
(\cdot) = (\cdot)(\sigma), \quad \sigma \in [0, 1], \qquad (\cdot)\big|_{\sigma=0} = 0.
\tag{2-3}
$$

A formal σ-power series expansion of the quantities of interest in a neighborhood of $\sigma = 0$ provides the first-order equations of interest for the buckling,

$$
\begin{aligned}
\bar{u}_1'' = 0, \quad b_3\bar{u}_2'''' + \lambda\frac{a-\lambda}{a}(\bar{u}_2'' - c_3\bar{\varphi}_1'') = 0, \quad b_2\bar{u}_3'''' + \lambda\frac{a-\lambda}{a}(\bar{u}_3'' + c_2\bar{\varphi}_1'') = 0, \\
h\xi^2\bar{\varphi}_1'''' + \frac{d\lambda-ak}{a}\bar{\varphi}_1'' + \lambda\frac{a}{a-\lambda}(c_2\bar{u}_3'' - c_3\bar{u}_2'') = 0,
\end{aligned}
\tag{2-4}
$$

with the overbar standing for increments of first order in σ.

We have considered the case of a beam with an intermediate stiffener, preventing warping in a section $x_1 = m$, $m \in (0, l)$. A number of values of m and of the boundary conditions have been considered. Each problem has been solved numerically using the COMSOL Multiphysics FEM code, available at the Dipartimento di Strutture of the Università Roma Tre. For this purpose, (2-4) has been written in weak form on the two regular subdomains $x_1 \in (0, m)$ and $x_1 \in (m, l)$. Then, giving the appropriate boundary conditions, the eigenvalue problems providing the critical values λ_c of the load multiplier and the mode shapes $\bar{u}_{2c}$, $\bar{u}_{3c}$, and $\bar{\varphi}_{1c}$, have been solved using the COMSOL PDE application.

Consider a beam channel with length $l = 2000$ mm, outer dimensions 100 mm (web), 60 mm (flanges), and uniform thickness of 3 mm [Ruta et al. 2008]. Let the x_3-axis of the chosen cartesian system coincide with the symmetry axis of the cross-section. The geometric and inertial quantities have been derived by means of standard calculations and well-known tables, such as those in [Timoshenko and Gere 1961]. Let the material of the beam be elastic and isotropic and characterized by $E = 206$ GPa, $G = 79$ GPa.

The constitutive coefficients (1-9) are

$$a = 642 \, \text{mm}^2 E, \quad b_3 = 1054726 \, \text{mm}^4 E, \quad h\xi^2 = 446086956 \, \text{mm}^6 E, \quad k = 1875 \, \text{mm}^4 G,$$
$$d = 2370581 \, \text{mm}^4 E, \quad b_2 = 236653 \, \text{mm}^4 E, \quad c_3 = -41 \, \text{mm}, \quad c_2 = 0 \, \text{mm}.$$

(2-5)

We assume that the beam is simply supported, with torsional rotation prevented at both ends. The corresponding boundary conditions in terms of first-order quantities are

$$\bar{\varphi}_1 = \bar{u}_2 = \bar{u}_3 = \bar{u}_2'' = \bar{u}_3'' = 0, \qquad \text{in } x_1 = 0, \ x_1 = l. \tag{2-6}$$

Continuity conditions must be imposed in the section $x_1 = m$, where the stiffener is present. We will consider the following three cases:

(1) warping is free in both $x_1 = 0$ and $x_1 = l$;

(2) warping is prevented in $x_1 = 0$ and free in $x_1 = l$;

(3) warping is prevented in both $x_1 = 0$ and $x_1 = l$.

For each case, we study how the buckling is affected when the warping is prevented by the stiffener. Then, in addition to the continuity conditions, the warping constraint at $x_1 = m$ must be taken into account. In the following, we present the critical loads and the corresponding buckling modes. For the sake of simplicity, overbars and subscript c are omitted.

Figure 1 shows the flexural-torsional critical mode associated with boundary condition (1) and with the stiffener located at $m = 400$ mm. The first plot in the figure shows the flexural component of the buckling mode, while the second graph illustrates the torsional component. It is apparent, as it was to be expected, that the flexural mode is exactly the same as in Euler buckling (a half sine wave), while the torsional component has a stationary point by correspondence with the stiffener (where $\alpha = \varphi_1' = 0$).
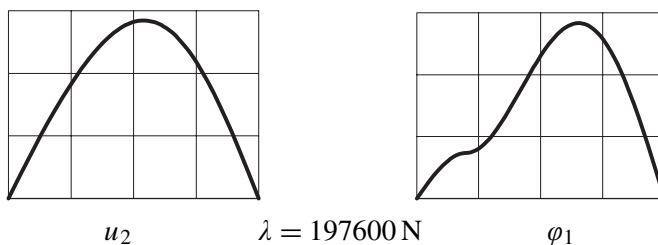

u_2 $\lambda = 197600 \, \text{N}$ φ_1

Figure 1. Beam warping-free at the ends, with stiffener at $m = 400$ mm.

u_2 $\lambda = 92699 \, \text{N}$ φ_1
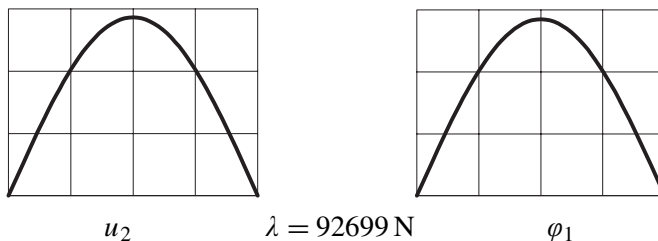
Figure 2. Beam warping-free at the ends, without stiffener.

This mode is compared with that for the beam without the stiffener, shown in Figure 2, where the corresponding critical load is also indicated. The difference, as was to be expected, is in the torsional component which in absence of the stiffener remains a half sine wave. Moreover, the critical load is significantly lower than the previous one.

In Figure 3 the flexural-torsional critical mode associated with case (2) and with the stiffener located at $m = 1600$ mm is shown. The first plot shows the flexural component of the buckling mode, while the second graph illustrates the torsional component. It is apparent, as expected, that the flexural component corresponds to Euler buckling (a half sine wave) while the torsional component has a stationary point by correspondence with the stiffener (where $\alpha = \varphi_1' = 0$). Notice also that the restrained warping at one end (for instance, $x_1 = 0$ in this case) is represented by a horizontal tangent in the graph for the torsional component, φ_1, of the buckling mode. The critical load is significantly higher than that shown in Figure 1, confirming that the system is globally stiffer.

The two components of this buckled shape are compared with the corresponding ones for the beam without a stiffener shown in Figure 4. Here it emerges that the two components of the mixed buckling mode are still a half-sine wave for the flexural part and a curve with initial zero slope, due to the restrained warping at the origin, for the torsional part. The critical load is significantly lower than the previous one.

In Figure 5 the flexural-torsional critical mode associated with case (3) and with the stiffener located at $m = 400$ mm is shown. The first plot shows the flexural component of the buckling mode, and the second graph illustrates the torsional component. Once again, as was to be expected, the flexural mode corresponds to Euler buckling (a half sine wave) since it remains unaltered by the constraints on the torsional rotation and on the warping. The torsional component has a stationary point by correspondence with the stiffener (where $\alpha = \varphi_1' = 0$) and the restrained warping at both ends is represented by horizontal tangents in the graph for the torsional component φ_1 of the buckling mode. The critical load attains the maximum value among those seen so far.
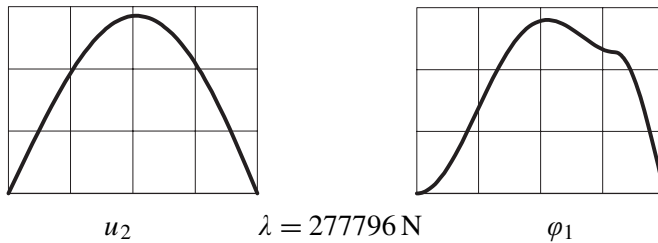

u_2 \qquad $\lambda = 277796$ N \qquad φ_1

Figure 3. Beam with warping restrained at one end and stiffener at $m = 1600$ mm.

u_2 \qquad $\lambda = 145737$ N \qquad φ_1
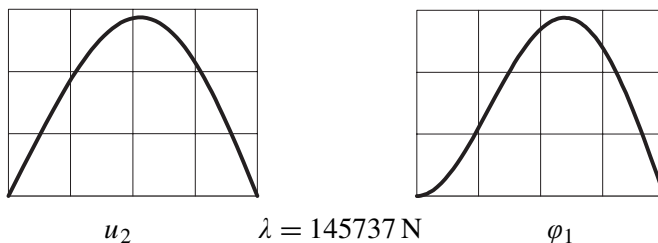
Figure 4. Beam with warping restrained at one end, without stiffener.

u_2 $\lambda = 322416\,\mathrm{N}$ φ_1
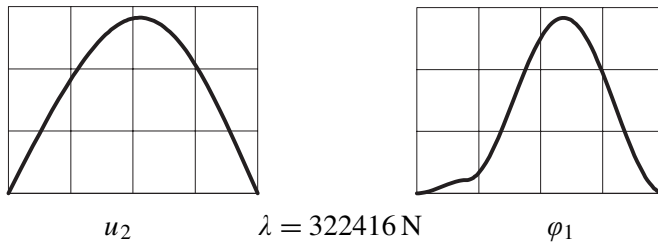
Figure 5. Beam with warping restrained at both ends and stiffener at $m = 400\,\mathrm{mm}$.

u_2 $\lambda = 228256\,\mathrm{N}$ φ_1
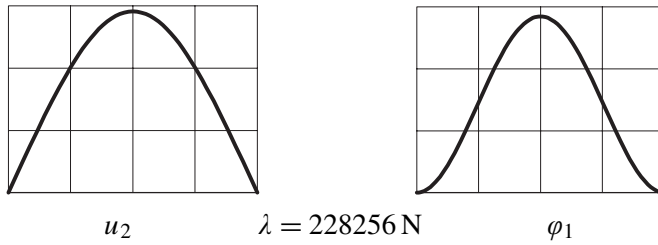
Figure 6. Beam with warping restrained at both ends, without stiffener.

The components of the mixed buckling are compared with the corresponding ones for the beam without a stiffener, shown in Figure 6, where it turns out that the mixed buckling in the absence of the stiffener is composed of two modes symmetric with respect to the midspan. The transverse displacement is a half sine wave, while the horizontal tangents at the ends of the torsional rotation point out the presence of the warping constraints.

Figure 7 shows the values of the critical load versus the position of the stiffener. The horizontal line shows the value of the Euler critical load, which is not affected by the warping restrictions at the beam ends and at the stiffener, when flexural buckling occurs around the axis of smaller inertia (x_2 for the cross-section considered). The other curves show the values of the critical load for flexural-torsional buckling.

We note that when a stiffener is located at $m = \frac{1}{2}$ and the boundary conditions are those of case (1), the Euler buckling load around the axis of smaller inertia is higher than the flexural-torsional one.
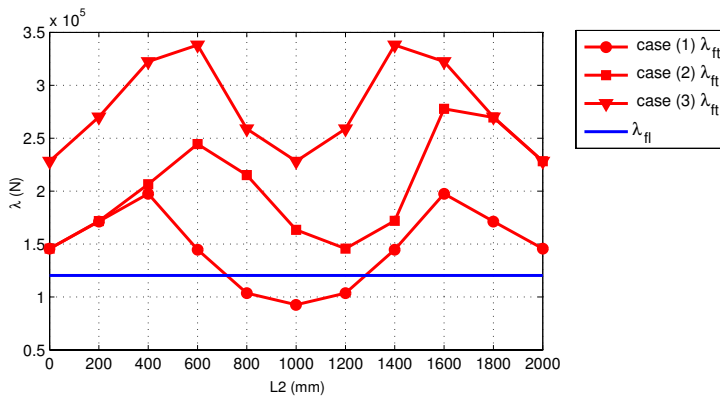
Figure 7. Numerical results.

This happens also when both ends are free to warp and no stiffener is present, as shown in [Ruta et al. 2008]. In fact, due to the symmetry of the torsional rotation (see Figure 2) the warping vanishes at midspan. By inserting a stiffener in a different section the flexural-torsional critical load in general varies nonmonotonically.

With reference to Figure 7, when both ends are free to warp, as in case (1), for $m \in [0, 700)$ or $m \in (1300, 2000]$ the flexural-torsional critical load is higher than the Euler one while for $m \in (700, 1300)$ the opposite happens (all lengths are here expressed in millimeters). The maximum value of the critical load is attained at $m = 400$ or $m = 1600$, since the dependence of the flexural-torsional critical load on the location of the stiffener is in this case symmetric with respect to the midspan. On the other hand, as it was already pointed out, the symmetry of both the components of the mixed buckling mode fails, see Figure 1.

When warping is prevented at both ends, case (3), the flexural-torsional critical load is higher than the Euler buckling load in the plane of smaller inertia, irrespective of the stiffener location. This is of importance in applications, since in practice design against buckling could be restricted to Euler buckling in the plane of smaller inertia simply by preventing warping at the ends and inserting an intermediate stiffener at will. The maximum effect of the increase of the critical load, however, is attained when the stiffener is located at $m = 600$ or $m = 1400$. Indeed, here also the dependence of the flexural-torsional critical load on the location of the stiffener is symmetric with respect to the midspan.

If warping is restrained at one end, described by case (2), the curve representing the effect of the intermediate stiffener coincides at $m = 0$ with the curve representing case (1). By increasing m, the flexural-torsional critical load increases in a nonmonotonic way, and the curve tends to the one representing case (3). In particular, the two curves coincide at $m = 2000$. In this case, as well as in the previous one, the entire curve lies above the straight horizontal line representing the Euler buckling load in the plane of smaller inertia. This is again of some importance in applications.

It must be stressed that the curves in the preceding figures change dramatically if the beam length is changed, fixing all the other parameters. In particular, as shown in [Ruta et al. 2008], the flexural-torsional critical load for case (1) coincides with the Euler one in the plane of smaller inertia when $l = 2731$ mm. It may be shown that when $l > 2731$ mm the curves describing the dependence of the flexural-torsional critical load on the stiffener location always lie above the straight horizontal line representing the Euler buckling load in the plane of smaller inertia, irrespective of the stiffener location.

3. Bifurcations in a two-bar frame

We now consider a two-bar frame, called a Roorda frame in the literature on stability of structures [Bažant and Cedolin 1991] and exhibiting interesting interactions between flexural and torsional modes occurring out of the frame plane. Results for the buckling of a frame made of I-beams are in [Pignataro et al. 2006]: two buckling modes are possible, one in-plane flexural (Euler-like) and another flexural-torsional, where one of the bars undergoes torsion while the other bends out of the plane. These results are of limited applicability, since the beam model in [Pignataro et al. 2006] cannot describe thin-walled elements with generic cross-sections as pointed out in Section 1.

It is thus interesting to study the buckling of a Roorda frame composed of thin-walled beams with nonsymmetric cross-sections, which are widely used in many structures (a standard example being the
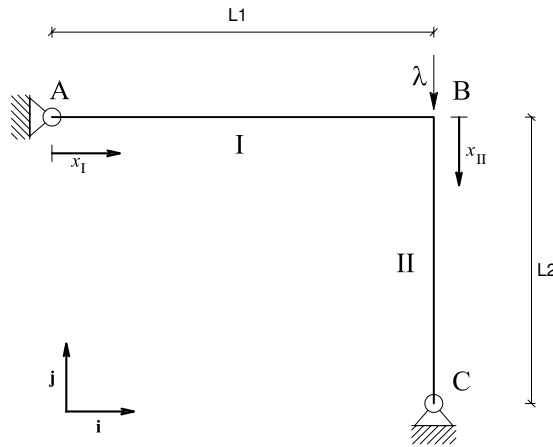
Figure 8. Two-bar frame.

so-called rack structures). In the literature there are numerical results obtained via refined finite element codes and experimental studies on the subject. Some of these, regarding a frame shaped spatial beam, are in [Kim and Kim 2000; Kim et al. 2001; Gu and Chan 2005; Teh 2005]. Still, to the authors' knowledge, an analytical study derived from a geometrically exact model is not available and the results obtained here could be of importance in applications.

Despite the fact that the model in [Ruta et al. 2006; 2008] considers generic cross-sections, we limit our study to a frame with beams exhibiting one axis of symmetry. This does not limit the generality of the results for two reasons: on one hand, the coupling between flexural and torsional buckling, so important in these structures, is clearly put into evidence; on the other hand, beams with one axis of symmetry such as channels are of widespread use.

Consider the frame in Figure 8: the bars AB (the beam) and BC (the column) are hinged to the ground in A and C and clamped at the common joint B. The frame is loaded at B by a dead load of magnitude λ in order to apply standard techniques [Koiter 1945; Budiansky 1974]. A global basis and local abscissas are indicated in the figure; the subscripts I and II distinguish quantities referring to the beam and the column, respectively. We take into account the possibility of various warping constraints at the beam ends A, B, and C.

The fundamental equilibrium path is

$$
\begin{aligned}
&\boldsymbol{u}_{\mathrm{I}}^{\mathrm{f}} = \boldsymbol{0}, && \boldsymbol{R}_{\mathrm{I}}^{\mathrm{f}} = \boldsymbol{I}, && \alpha_{\mathrm{I}}^{\mathrm{f}} = 0, \\
&\boldsymbol{e}_{\mathrm{I}}^{\mathrm{f}} = \boldsymbol{0}, && \boldsymbol{E}_{\mathrm{I}}^{\mathrm{f}} = \boldsymbol{0}, && \eta_{\mathrm{I}}^{\mathrm{f}} = 0, \\
&\boldsymbol{s}_{\mathrm{I}}^{\mathrm{f}} = \boldsymbol{0}, && \boldsymbol{S}_{\mathrm{I}}^{\mathrm{f}} = \boldsymbol{0}, && \tau_{\mathrm{I}}^{\mathrm{f}} = 0, && \mu_{\mathrm{I}}^{\mathrm{f}} = 0, \\
&\boldsymbol{u}_{\mathrm{II}}^{\mathrm{f}} = -\frac{\lambda}{a}x_1\boldsymbol{i}_1, && \boldsymbol{R}_{\mathrm{II}}^{\mathrm{f}} = \boldsymbol{I}, && \alpha_{\mathrm{II}}^{\mathrm{f}} = 0, \\
&\boldsymbol{e}_{\mathrm{II}}^{\mathrm{f}} = -\frac{\lambda}{a}\boldsymbol{i}_1, && \boldsymbol{E}_{\mathrm{II}}^{\mathrm{f}} = \boldsymbol{0}, && \eta_{\mathrm{II}}^{\mathrm{f}} = 0, \\
&\boldsymbol{s}_{\mathrm{II}}^{\mathrm{f}} = -\lambda\boldsymbol{i}_1, && \boldsymbol{S}_{\mathrm{II}}^{\mathrm{f}} = \boldsymbol{0}, && \tau_{\mathrm{II}}^{\mathrm{f}} = 0, && \mu_{\mathrm{II}}^{\mathrm{f}} = 0.
\end{aligned}
\tag{3-1}
$$

The bifurcated path is written in terms of the differences

$$
\begin{aligned}
&\boldsymbol{u}_\mathrm{I}^\mathrm{b} = \boldsymbol{u}, &&\boldsymbol{R}_\mathrm{I}^\mathrm{b} = \boldsymbol{R} + \boldsymbol{I}, &&\alpha_\mathrm{I}^\mathrm{b} = \alpha, \\
&\boldsymbol{e}_\mathrm{I}^\mathrm{b} = \boldsymbol{e}, &&\boldsymbol{E}_\mathrm{I}^\mathrm{b} = \boldsymbol{E}, &&\eta_\mathrm{I}^\mathrm{b} = \eta, \\
&\boldsymbol{s}_\mathrm{I}^\mathrm{b} = \boldsymbol{s}, &&\boldsymbol{S}_\mathrm{I}^\mathrm{b} = \boldsymbol{S}, &&\tau_\mathrm{I}^\mathrm{b} = \tau, &&\mu_\mathrm{I}^\mathrm{b} = \mu, \\
&\boldsymbol{u}_\mathrm{II}^\mathrm{b} = \boldsymbol{u} - \frac{\lambda}{a} x_1 \boldsymbol{i}_1, &&\boldsymbol{R}_\mathrm{II}^\mathrm{b} = \boldsymbol{R} + \boldsymbol{I}, &&\alpha_\mathrm{II}^\mathrm{b} = \alpha, \\
&\boldsymbol{e}_\mathrm{II}^\mathrm{b} = \boldsymbol{e} - \frac{\lambda}{a} \boldsymbol{i}_1, &&\boldsymbol{E}_\mathrm{II}^\mathrm{b} = \boldsymbol{E}, &&\eta_\mathrm{II}^\mathrm{b} = \eta, \\
&\boldsymbol{s}_\mathrm{II}^\mathrm{b} = \boldsymbol{s} - \lambda \boldsymbol{i}_1, &&\boldsymbol{S}_\mathrm{II}^\mathrm{b} = \boldsymbol{S}, &&\tau_\mathrm{II}^\mathrm{b} = \tau, &&\mu_\mathrm{II}^\mathrm{b} = \mu.
\end{aligned}
\tag{3-2}
$$

Operating as in Section 2, some steps provide the first-order equations for the buckling in terms of the displacement components

$$
\bar{u}_1'' = 0, \qquad b_3 \bar{u}_2'''' = 0, \qquad b_2 \bar{u}_3'''' = 0, \qquad h\xi^2 \bar{\varphi}_1'''' - k\bar{\varphi}_1'' = 0 \qquad \text{on } AB,
$$

$$
\left.
\begin{aligned}
&\bar{u}_1'' = 0, \quad b_3 \bar{u}_2'''' + \lambda \frac{a-\lambda}{a}(\bar{u}_2'' - c_3 \bar{\varphi}_1'') = 0, \quad b_2 \bar{u}_3'''' + \lambda \frac{a-\lambda}{a}(\bar{u}_3'' + c_2 \bar{\varphi}_1'') = 0, \\
&h\xi^2 \bar{\varphi}_1'''' + \frac{d\lambda - ak}{a}\bar{\varphi}_1'' + \lambda \frac{a}{a-\lambda}(c_2 \bar{u}_3'' - c_3 \bar{u}_2'') = 0
\end{aligned}
\right\}
\quad \text{on } BC.
\tag{3-3}
$$

Equations (3-3) plus boundary conditions constitute an eigenvalue problem providing the critical values λ_c and the mode shapes $\bar{u}_{2c}$, $\bar{u}_{3c}$, and $\bar{\varphi}_{1c}$. For simplicity of notation, the overbars indicating first-order quantities have been dropped in the following, as has subscript c. The effect of different warping constraints at the ends of the beams composing the frame on the critical loads has been studied numerically by means of the COMSOL code.

3A. *Geometrical and material data.* Two benchmark cases have been considered, characterized by two different cross sections exhibiting two and one axes of symmetry, respectively: a wide flange HEA240 and a channel (U-shape) with outer dimensions 100 mm (web) and 60 mm (flanges) and a uniform thickness of 3 mm. By assuming the local coordinate systems as in Figure 9, the geometric and inertial quantities of the cross-section are obtained by standard calculations and well-known tables [Timoshenko and Gere 1961; Pignataro et al. 1991]:
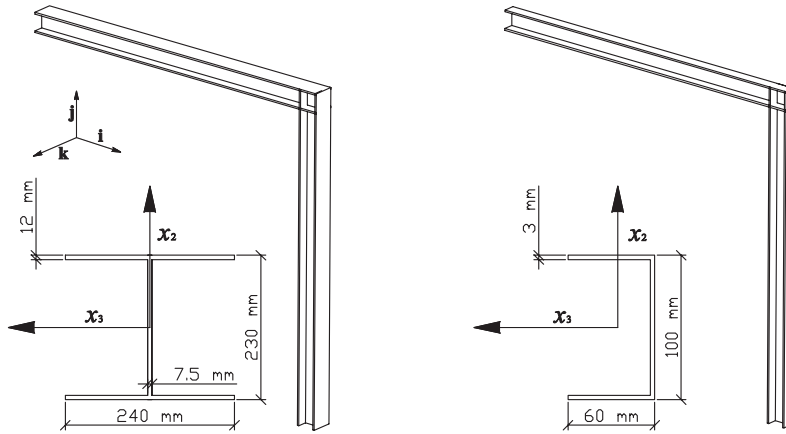
- U100:

$$
a = 642\,\mathrm{mm}^2 E, \qquad b_3 = 1054726\,\mathrm{mm}^4 E, \qquad h\xi^2 = 446086956\,\mathrm{mm}^6 E, \qquad k = 1875\,\mathrm{mm}^4 G,
$$

$$
d = 2370581\,\mathrm{mm}^4 E, \quad b_2 = 236653\,\mathrm{mm}^4 E, \qquad c_3 = -41\,\mathrm{mm}, \qquad c_2 = 0\,\mathrm{mm};
$$

- HEA240:

$$
a = 7.68 \times 10^3\,\mathrm{mm}^2 E, \quad b_2 = 2.769 \times 10^7\,\mathrm{mm}^4 E, \quad h\xi^2 = 3.65 \times 10^{11}\,\mathrm{mm}^6 E,
$$

$$
k = 3.1 \times 10^5\,\mathrm{mm}^4 G, \qquad d = 1.05 \times 10^8\,\mathrm{mm}^4 E, \qquad b_3 = 7.763 \times 10^7\,\mathrm{mm}^4 E, \quad c_3 = c_2 = 0\,\mathrm{mm}.
$$

We assume the Young's modulus is $E = 206\,\mathrm{GPa}$ and the shear modulus $G = 79\,\mathrm{GPa}$ as in Section 2.

Figure 9. Three-dimensional view.

3B. *Boundary conditions.* In [Pignataro et al. 2006] a two-bar frame such as that in Figure 8 was analyzed. At the ends A and C the rotations φ_2 and φ_3 were assumed to be free while it was supposed $\varphi_1 = 0$. In addition, the joint B was allowed to move out of the plane of the frame: this resulted in a very low critical load. This case, however, is hardly of any technical interest due to the fact that in 3D frames actual hinges are cylindrical and the out-of-plane movement of nodes like B is controlled by the presence of braces.

In this section, therefore, we consider the case in which node B is prevented from moving along the unit vector $\boldsymbol{k}$ and the hinges in A and C allow the sole rotation along $\boldsymbol{k}$. This results in the following boundary conditions:

$$\boldsymbol{u} = \boldsymbol{0}, \qquad \varphi_1 = 0, \qquad \varphi_2 = 0, \qquad M_3 = 0, \qquad\qquad\qquad \text{in A and C;}$$

$$\boldsymbol{u}_{\mathrm{I}} = \boldsymbol{u}_{\mathrm{II}}, \quad \boldsymbol{R}_{\mathrm{I}} = \boldsymbol{R}_{\mathrm{II}}, \quad S_{\mathrm{I}} = S_{\mathrm{II}}, \quad \boldsymbol{u}_{\mathrm{I}} \cdot \boldsymbol{k} = 0, \quad (\boldsymbol{I} - \boldsymbol{k} \otimes \boldsymbol{k})(\boldsymbol{s}_{\mathrm{I}} - \boldsymbol{s}_{\mathrm{II}}) = \boldsymbol{0}, \qquad \text{in B.}$$

In order to investigate the influence of warping on buckling, some additional boundary conditions on the warping are assumed, as follows:

case	node A	node B	node C
a	free	free	free
b	free	prevented	free
c	prevented	free	prevented
d	prevented	prevented	prevented

Here "prevented" stands for warping prevented and "free" stands for no constraint on warping which implies vanishing bimoment at the indicated beam ends. Details of the boundary conditions at node B are shown in Figure 10.

This results in four cases:

Case a: $\mu = 0$ in A, B and C;   Case b: $\mu = 0$ in A and C, and $\alpha = 0$ in B;

Case c: $\mu = 0$ in B, and $\alpha = 0$ in A and C;   Case d: $\alpha = 0$ in A, B and C.
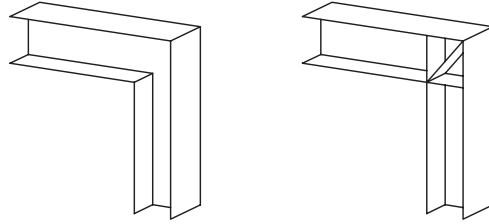
**Figure 10.** Detail of frame joint B, warping free (left) and warping restrained (right).

3C. *Numerical examples.* In this section we consider a set of frames in which the length of the beam (say L1) is fixed to 2000 mm, while the length of the column (say L2) has been varied in the range 3000 mm–8000 mm.

Results have been obtained for each of the boundary cases a–d.

3C.1. *Modes.* Figures 11 and 12 refer to the frame with HEA240 beams and show the buckling modes and the corresponding critical value of the load multiplier. It is apparent that the considered frame may buckle in three different ways:

Mode 1 is purely flexural (Euler-like) in the plane of the frame and involves both beam and column (see Figure 11, mode u_2);
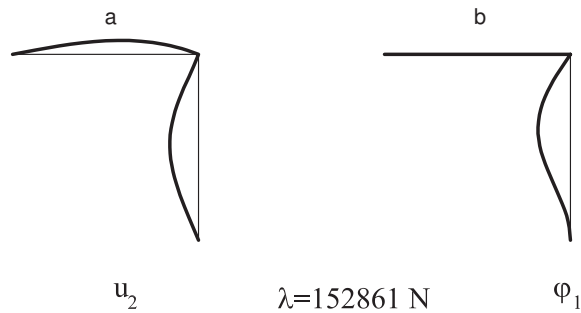
Mode 2 is purely torsional and involves the sole column (see Figure 11, mode φ_1) which buckles in the shape of a half-sine wave while the beam remains straight;
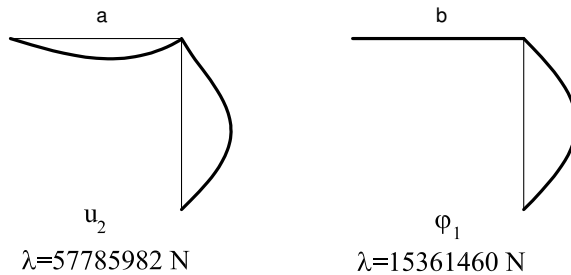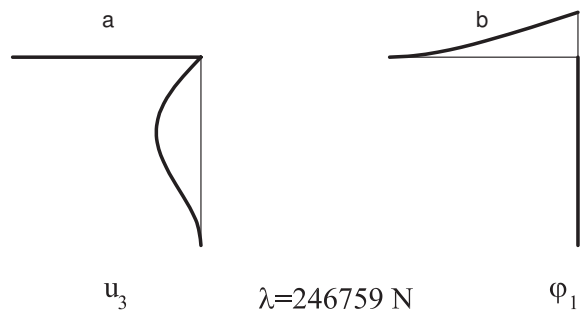

Figure 11. HEA240: In-plane flexural mode and torsional mode.
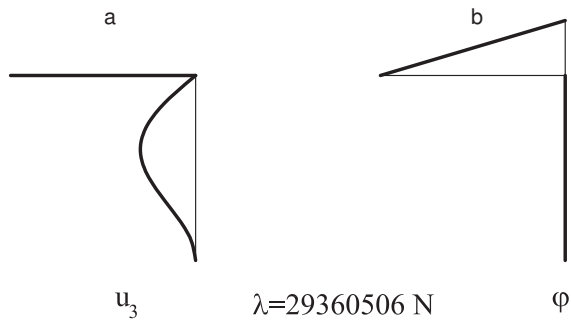
Figure 12. HEA240: Out-of-plane flexural mode.

Figure 13. U100 flexural-torsional mode.

Figure 14. U100 flexural mode out of plane.

Mode 3 is such that the column bends out of the plane of the frame while the beam twists, acting only as a flexural constraint in B (see Figure 12). On the other hand, the torsional rotation is different from zero only in the beam where it has the linear behavior characteristic of the Saint-Venant uniform torsion.

This result, apart from the different constraint on the out-of-plane displacement of the joint B, corresponds to that in [Pignataro et al. 2006]: when the centroid coincides with the shear center of the cross-sections no coupling exists between the buckling modes which are either flexural or torsional and may be different for the two bars simply for geometrical reasons (in section B a torsional rotation of the beam is a bending rotation of the column).

When the frame bars have cross-sections with one symmetry axis only the frame may buckle in two ways only as shown in Figures 13 and 14:

Mode 4 is such that the beam is subjected only to flexure in the plane of the frame, while the column undergoes flexure and torsion (see Figure 13). Note that the torsional mode has zero initial slope due to the warping constraint in C;

the other mode (see Figure 14) corresponds to the buckling mode 3 before except for the initial zero slope of the torsional mode due to the warping constraint.

3C.2. *Critical loads.* Figures 15 and 16 show the values of the critical load (expressed in N) versus the length L2 of the column for each of the warping constraints in cases a–d for the HEA240 and U100
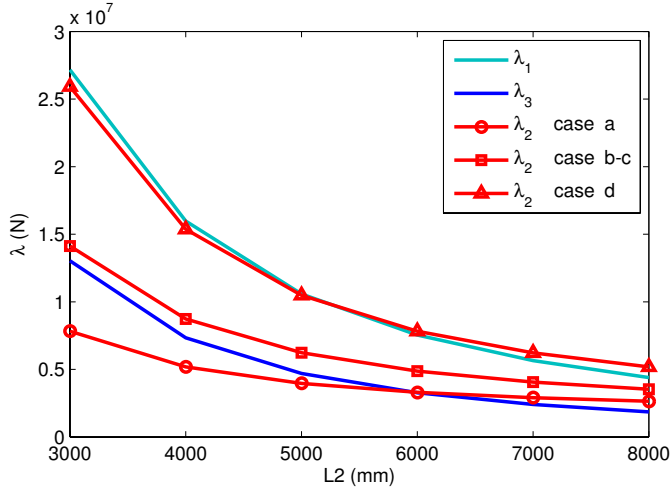
Figure 15. Critical loads versus column length for HEA240 bars.
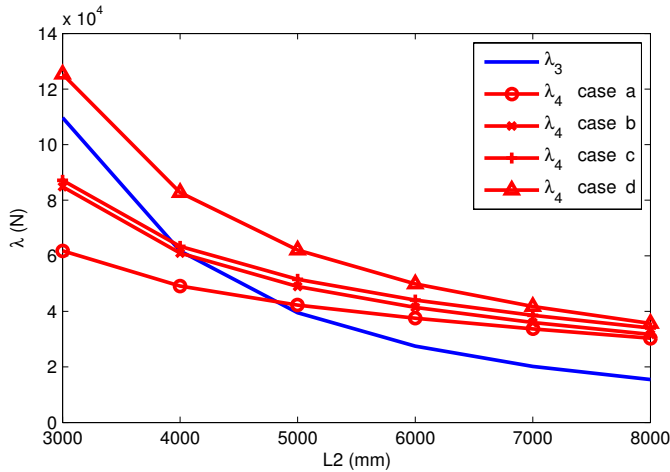
Figure 16. Critical loads versus column length for U100 bars.

cross-sections, respectively. The critical loads corresponding to modes 1 and 3 above are drawn in light blue and dark blue, respectively. The critical loads corresponding to modes 2 and 4 are drawn in red.

It is apparent that the flexural critical loads are not influenced by the constraints on warping as was to be expected. It also appears that the torsional mode has a significant effect on the critical load when the column is short.

In addition, Figure 15 shows that for the boundary conditions of case a $\lambda_2 < \lambda_3$ when L2 < 6000 mm, that is, the purely torsional critical load is attained before the one corresponding to the buckling mode 3. Moreover, $\lambda_3 < \lambda_1$ for all L2; this means that the critical load of the out-of-plane buckling mode is always lower than the one associated with the purely in-plane flexural, Euler-like, buckling mode. This sounds adequate, because in mode 3 the column bends around the lower inertia axis, while in the purely flexural mode 1 both the beam and the column bend around the axis of higher inertia which is twice the inertia

around the other axis. All the results show that when warping constraints are introduced at the ends of the bars, the flexural-torsional critical loads show a remarkable increase due to a globally stiffer system.

The analysis carried out after the introduction of the additional warping constraints labeled as cases b and c gives more or less the same results and one finds that $\lambda_3 < \lambda_2 < \lambda_1$. Finally, for the warping constraints of case d the critical load corresponding to the purely torsional mode attains the highest values and $\lambda_3 < \lambda_2 < \lambda_1$; only when L2 > 5200 mm, that is, for very slender columns, the effect of the warping constraint is less significant and the out-of-plane mode 3 prevails on the purely torsional mode 2.

The dependence of the critical loads on the length L2 of the column when the frame is composed of U100 bars is shown in Figure 16. It is first to be remarked that in this case only two buckling modes (modes 3 and 4) are possible, thus only two buckling loads henceforth denoted by λ_3 and λ_4 shall be calculated for the warping constraint cases a–d. From Figure 16 we deduce that we face the following different situations:

- L2 < 4000 mm $\Rightarrow \lambda_4 < \lambda_3$ for cases a, b, and c. This is reasonable, since mode 4 is dominated by the very modest torsional stiffness of the channel. Moreover, the additional constraints for the warping do not seem to add enough stiffness to the system;

- 4000 mm < L2 < 4800 mm $\Rightarrow \lambda_4 < \lambda_3$ for case a and $\lambda_3 < \lambda_4$ for cases b and c. That is, if the column becomes appreciably slender the mixed flexural-torsional mode for the column is attained at a lower critical load than the corresponding out-of-plane flexural mode when the warping constraints are not present. Even a modest set of additional warping constraints makes the opposite hold. This is reasonable since for slender bars the Euler flexural buckling load sensibly decreases, while even a modest increase in the torsional stiffness can make the mixed flexural-torsional buckling load increase over the purely flexural one;

- L2 > 4800 mm $\Rightarrow \lambda_3 < \lambda_4$ for cases a, b, and c. This sounds again adequate since for very slender columns the Euler buckling load is so low that it is attained before any possible flexural-torsional buckling load even when modest additional warping constraints are introduced;

- In case d, that is when the stiffest system with respect to torsion and warping is considered, $\lambda_4 > \lambda_3$ ∀L2. That is, when the frame has the highest possible stiffness against torsion, the Euler-like buckling load is the lowest critical load and hence the most important in applications, irrespective of the length of the column.

It has to be remarked that these results may be of importance in applications since design against Euler buckling is a well-known subject in engineers' education while design against flexural-torsional buckling of thin-walled structures is still a debated topic.

4. Final remarks

The direct one-dimensional beam model suitable for the description of the flexural-torsional buckling introduced in [Ruta et al. 2006] has been used to study two cases of interest in applications, namely a compressed beam with an intermediate stiffener and the Roorda frame. The direct formulation has made it possible to use standard static perturbation techniques of well-known reliability and to limit the use of numerical codes to the parametric solutions of the field equations for the buckling. Some very interesting results have been found which may have some importance in applications: the introduction

of an intermediate stiffener globally increases the stiffness of the beam against warping and torsion and makes the Euler buckling mode the most meaningful one. In the Roorda frame, the warping constraints and the length of the column play a very important role and the first critical load may sometimes not be the one corresponding to the Euler-like buckling mode. This fact of course is of interest in applications because of the well-known low torsion rigidity of thin-walled open sections. These results, to the authors' knowledge, are new and subject to further improvement. As a matter of fact, it appears that a further step in this study is the analysis of more complex 3D frames.

References

[Bažant and Cedolin 1991] Z. P. Bažant and L. Cedolin, *Stability of structures: elastic, inelastic, fracture, and damage theories*, Oxford Engineering Science Series **26**, Oxford University Press, New York, 1991.

[Budiansky 1974] B. Budiansky, "Theory of buckling and post-buckling behavior of elastic structures", *Adv. Appl. Mech.* **14** (1974), 1–65.

[DiCarlo 1996] A. DiCarlo, "A non-standard format for continuum mechanics", pp. 263–268 in *Contemporary research in the mechanics and mathematics of materials: Symposium on Recent Developments in Elasticity, ASME Mechanics and Materials Conference* (Baltimore, MD, 1996), edited by R. C. Batra and M. F. Beatty, CIMNE, Barcelona, 1996.

[Grimaldi and Pignataro 1979] A. Grimaldi and M. Pignataro, "Postbuckling behavior of thin-walled open cross-section compression members", *Mech. Based Des. Struct. Mach.* **7**:2 (1979), 143–159.

[Gu and Chan 2005] J.-X. Gu and S.-L. Chan, "A refined finite element formulation for flexural and torsional buckling of beam-columns with finite rotations", *Eng. Struct.* **27**:5 (2005), 749–759.

[Kim and Kim 2000] S.-B. Kim and M.-Y. Kim, "Improved formulation for spatial stability and free vibration of thin-walled tapered beams and space frames", *Eng. Struct.* **22**:5 (2000), 446–458.

[Kim et al. 2001] M.-Y. Kim, S.-P. Chang, and H.-G. Park, "Spatial postbuckling analysis of nonsymmetric thin-walled frames, I: Theoretical considerations based on semitangential property", *J. Eng. Mech.* (*ASCE*) **127**:8 (2001), 769–778.

[Koiter 1945] W. T. Koiter, *Over de stabiliteit van het elastisch evenwicht*, Ph.D. thesis, Delft, 1945. Translated in NASA TT F-10 vol. 833 (1967) and AFFDL Report TR 70-25 (1970).

[Møllmann 1986] H. Møllmann, "Theory of thin-walled beams with finite displacements", pp. 195–209 in *Finite rotations in structural mechanics: proceedings of the Euromech Colloquium 197* (Jabłonna, 1985), edited by W. Pietraszkiewicz, Lecture Notes in Engineering **19**, Springer, New York, 1986.

[Pignataro and Ruta 2003] M. Pignataro and G. C. Ruta, "Coupled instabilities in thin-walled beams: a qualitative approach", *Eur. J. Mech. A Solids* **22**:1 (2003), 139–149.

[Pignataro et al. 1991] M. Pignataro, N. L. Rizzi, and A. Luongo, *Stability, bifurcation and postcritical behaviour of elastic structures*, Elsevier, Amsterdam, 1991.

[Pignataro et al. 2006] M. Pignataro, N. L. Rizzi, and G. C. Ruta, "Buckling and post-buckling in a two-bar frame: a qualitative approach", pp. 337–346 in *4th International Conference on Coupled Instabilities in Metal Structures* (*CIMS 2004*) (Rome, 2004), edited by M. Pignataro et al., Tipografia Esagrafica, Rome, 2006.

[Reissner 1983] E. Reissner, "On a simple variational analysis of small finite deformations of prismatical beams", *Z. Angew. Math. Phys.* **34**:5 (1983), 642–648.

[Rizzi and Tatone 1996] N. Rizzi and A. Tatone, "Nonstandard models for thin-walled beams with a view to applications", *J. Appl. Mech.* (*ASME*) **63**:2 (1996), 399–403.

[Ruta et al. 2006] G. Ruta, M. Pignataro, and N. Rizzi, "A direct one-dimensional beam model for the flexural-torsional buckling of thin-walled beams", *J. Mech. Mater. Struct.* **1**:8 (2006), 1479–1496.

[Ruta et al. 2008] G. C. Ruta, V. Varano, M. Pignataro, and N. L. Rizzi, "A beam model for the flexural-torsional buckling of thin-walled members with some applications", *Thin-Walled Struct.* **46**:7–9 (2008), 816–822.

[Simo and Vu-Quoc 1991] J. C. Simo and L. Vu-Quoc, "A geometrically-exact rod model incorporating shear and torsion-warping deformation", *Int. J. Solids Struct.* **27**:3 (1991), 371–393.

[Tatone and Rizzi 1991] A. Tatone and N. Rizzi, "A one-dimensional model for thin-walled beams", pp. 312–320 in *Trends in applications of mathematics to mechanics* (Hollabrunn, 1989), edited by W. Schneider et al., Longman, Harlow, 1991.

[Teh 2005] L. H. Teh, "Spatial rotation kinematics and flexural-torsional buckling", *J. Eng. Mech.* (*ASCE*) **131**:6 (2005), 598–605.

[Timoshenko and Gere 1961] S. P. Timoshenko and J. M. Gere, *Theory of elastic stability*, McGraw-Hill, New York, 1961.

[Truesdell and Noll 1965] C. Truesdell and W. Noll, *The non-linear field theories of mechanics*, Handbuch der Physik **III/3**, Springer, Berlin, 1965.

[Vlasov 1961] V. Z. Vlasov, *Thin-walled elastic beams*, Monson, Jerusalem, 1961.

MARCELLO PIGNATARO: marcello.pignataro@uniroma1.it
Dipartimento di Ingegneria Strutturale e Geotecnica, Università degli Studi di Roma 'La Sapienza', via Eudossiana 18, 00184 Roma, Italy

NICOLA RIZZI: nlr@uniroma3.it
Dipartimento di Strutture, Università degli Studi Roma Tre, via Corrado Segre 6,   00146 Roma, Italy

GIUSEPPE RUTA: giuseppe.ruta@uniroma1.it
Dipartimento di Ingegneria Strutturale e Geotecnica, Università degli Studi di Roma 'La Sapienza', via Eudossiana 18, 00184 Roma, Italy

VALERIO VARANO: v.varano@uniroma3.it
Dipartimento di Strutture, Università degli Studi Roma Tre, via Corrado Segre 6,   00146 Roma, Italy

NONLINEAR BUCKLING FORMULATIONS AND IMPERFECTION MODELS FOR SHEAR DEFORMABLE PLATES BY THE BOUNDARY ELEMENT METHOD

JUDHA PURBOLAKSONO AND M. H. (FERRI) ALIABADI

This paper presents a nonlinear buckling analysis of shear deformable plates. Two models of imperfections are introduced: small uniform transverse loads and distributed transverse loads, according to the number of half-waves indicated by the eigenvectors from linear elastic buckling analysis. A simple numerical algorithm is presented to analyze the problems. Numerical examples with different geometries, loading and boundary conditions are presented to demonstrate the accuracy of the formulation.

1. Introduction

Plate buckling behavior has been investigated analytically and experimentally since the first experimental observation, almost 150 years ago; see [Walker 1984] for a review. Analytical solutions of linear buckling of plates based on classical plate theory can be found in [Brush and Almroth 1975; Timoshenko and Gere 1961]. Numerical methods have also been used [Bao et al. 1997; Liu 2001; Manolis et al. 1986; Purbolaksono and Aliabadi 2005b]. Liu [1987] and Syngellakis [1998] applied the boundary element method (BEM) to the stability analysis of thin plates. In [Purbolaksono and Aliabadi 2005a] we developed a boundary element method for analyzing linear buckling problems of shear deformable plates.

The boundary element method has also been applied to the analysis of nonlinear plate problems. Early works on geometrically nonlinear shear deformable plates by boundary element method include [Lei et al. 1990; He and Qin 1993], while Marczak and de Barcellos [1998] reported on a nonlinear stability analysis in shear deformable plates by the BEM. Other works contributing to BEM analysis of nonlinear buckling of thin plates have been made [Kamiya et al. 1984; Qin and Huang 1990; Tanaka et al. 1999].

Here we perform a nonlinear buckling analysis of shear deformable Mindlin plates. Two models of imperfections are introduced, one involving small uniform transverse loads and one involving distributed transverse loads corresponding to the number of half-waves indicated by the eigenvectors obtained from linear elastic buckling analysis. A simple numerical algorithm is presented to analyze the problems. Numerical examples with different geometries, loading and boundary conditions are used to demonstrate the accuracy of the formulations.
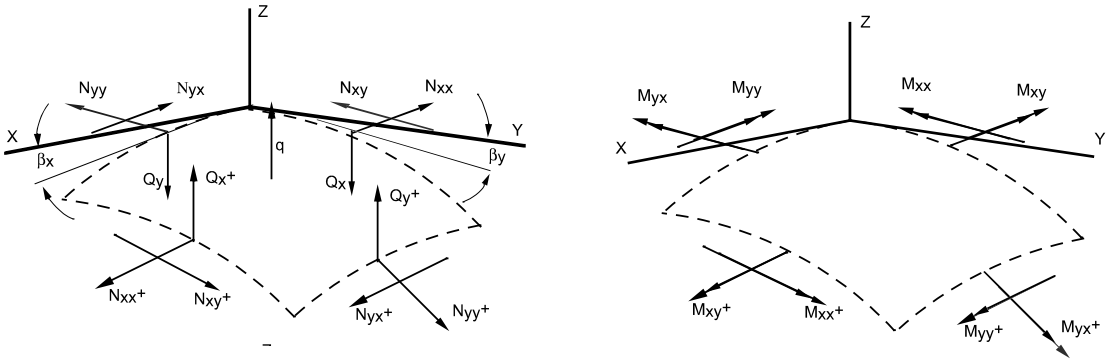
2. Governing equations

Figure 1 shows a geometrically nonlinear Mindlin plate. With the notation there, and with Greek indices varying from 1 to 2 and Roman indices from 1 to 3, the plate's governing equations can be written as

$$M_{\alpha\beta,\beta} + Q_\alpha = 0, \quad Q_{\alpha,\alpha} + (N_{\alpha\beta}w_{3,\beta})_{,\alpha} + q = 0 \quad N_{\alpha\beta,\beta} = 0, \tag{1}$$

Keywords: boundary element method, shear deformable plates, nonlinear buckling, imperfections.

Figure 1. Stress resultant equilibrium in geometrically nonlinear plate element.

where u_α and w_3 are displacements in the x_α (in-plane) and x_3 (out-of-plane) directions; w_α are rotations in the x_α directions; δ is the Kronecker delta function; $Q_\alpha = C(w_\alpha + w_{3,\alpha})$ and

$$M_{\alpha\beta} = \frac{1-\nu}{2}D\left(w_{\alpha,\beta} + w_{\beta,\alpha} + \frac{2\nu}{1-\nu}w_{\gamma,\gamma}\delta_{\alpha\beta}\right) + \frac{\nu}{(1-\nu^2)\lambda^2}q\delta_{\alpha\beta}$$

are the stress resultants in plate bending problems, while $N_{\alpha\beta} = N_{\alpha\beta}^{\text{lin}} + N_{\alpha\beta}^{\text{nonlin}}$, with

$$N_{\alpha\beta}^{\text{lin}} = \frac{1-\nu}{2}B\left(u_{\alpha,\beta} + u_{\beta,\alpha} + \frac{2\nu}{1-\nu}u_{\gamma,\gamma}\delta_{\alpha\beta}\right), \quad N_{\alpha\beta}^{\text{nonlin}} = \frac{1-\nu}{2}B\left(w_{3,\beta}w_{3,\alpha} + \frac{2\nu}{1-\nu}w_{3,\gamma}w_{3,\gamma}\delta_{\alpha\beta}\right),$$

are the stress resultants for two-dimensional plane stress elasticity. The parameters are $B = Eh/(1-\nu^2)$, the membrane stiffness; $D = Eh^3/(12(1-\nu^2))$, the bending stiffness of the plate; q, the transverse load; $C = D(1-\nu)\lambda^2/2$, the shear stiffness; E, the modulus of elasticity; $\lambda = \sqrt{10}/h$, the shear factor; h, the thickness of the plate; ν, the Poisson's ratio.

Extensive discussion on bending solutions of shear deformable plate theories can be found in [Wang et al. 2001].

3. Boundary integral equations

The boundary integral equation for the nonlinear buckling analysis of a plate bending can be written as

$$C_{ij}w_i(x') + \int_\Gamma P_{ij}^*(x', x)w_j(x)d\Gamma = \int_\Gamma W_{ij}^*(x', x)p_j^{\text{lin}}(x)d\Gamma + \int_\Omega W_{ij}^*(x', X)q(X)d\Omega(X)$$
$$+ \int_\Omega W_{i3}^*(x', X)(N_{\alpha\beta}w_{3,\chi})_{,\alpha}(X)d\Omega(X). \quad (2)$$

The kernel solutions P_{ij} and W_{ij} can be found in [Aliabadi 2002]. The boundary integral equation for two-dimensional plane stress is expressed as

$$C_{\theta\alpha}(x')u_\alpha(x') + \int_\Gamma T_{\theta\alpha}^*(x', x)u(x)d\Gamma = \int_\Gamma U_{\theta\alpha}^*(x', x)t^{\text{lin}}(x)d\Gamma + \int_\Omega U_{\theta\alpha}^*(x', X)N_{\alpha\gamma,\gamma}^{\text{nonlin}}(X)d\Omega(X). \quad (3)$$

Using the divergence theorem, the domain integral on the right-hand side of (3) can be expressed as

$$C_{\theta\alpha}(x')u_\alpha(x') + \int_\Gamma T_{\theta\alpha}^*(x',x)u(x)d\Gamma = \int_\Gamma U_{\theta\alpha}^*(x',x)t^{\lin}(x)d\Gamma + n_\gamma(x)\int_\Gamma U_{\theta\alpha}^*(x',x)N_{\alpha\gamma}^{\nonlin}(x)d\Gamma$$

$$- \int_\Omega U_{\theta\alpha,\gamma}^*(x',X)N_{\alpha\gamma}^{\nonlin}(X)d\Omega(X). \quad (4)$$

In a similar way, (4) can be simplified and written as

$$C_{\theta\alpha}(x')u_\alpha(x') + \int_\Gamma T_{\theta\alpha}^*(x',x)u(x)d\Gamma = \int_\Gamma U_{\theta\alpha}^*(x',x)t(x)d\Gamma - n_\gamma(x)\int_\Gamma U_{\theta\alpha}^*(x',x)N_{\alpha\gamma}^{\nonlin}(x)d\Gamma$$

$$+ \int_\Omega U_{\theta\alpha}^*(x',X)N_{\alpha\gamma,\gamma}^{\nonlin}(X)d\Omega(X), \quad (5)$$

where $t_\alpha = t_\alpha^{\lin} + t_\alpha^{\nonlin}$ and $t_\alpha^{\nonlin} = N_{\alpha\gamma}^{\nonlin}n_\gamma$. The fundamental solutions $U_{\theta\alpha}$ and $T_{\theta\alpha}$ are can be found in [Aliabadi 2002].

To calculate the nonlinear terms, two additional integral equations of the deflection w_3 and the in-plane stress resultants $N_{\alpha\beta}^{\lin}$ at domain points are required:

$$w_i(X') + \int_\Gamma P_{ij}^*(X',x)w_j(x)d\Gamma = \int_\Gamma W_{ij}^*(X',x)p_j^{\lin}(x)d\Gamma + \int_\Omega W_{ij}^*(X',X)q(X)d\Omega(X)$$

$$+ \int_\Omega W_{i3}^*(X',X)(N_{\alpha\beta}w_{3,\chi})_{,\alpha}(X)d\Omega(X), \quad (6)$$

$$N_{\alpha\beta}^{\lin}(X') = \int_\Gamma U_{\Delta\alpha\beta}^*(X',x)t_\Delta(x)d\Gamma - \int_\Gamma T_{\Delta\alpha\beta}^*(X',x)u_\Delta(x)d\Gamma$$

$$- n_\gamma(x)\int_\Gamma U_{\Delta\alpha\beta}^*(X',x)N_{\alpha\gamma}^{\nonlin}(x)d\Gamma + \int_\Omega U_{\Delta\alpha\beta}^*(X',X)N_{\alpha\gamma,\gamma}^{\nonlin}(X)d\Omega(X), \quad (7)$$

where the fundamental solutions $U_{\Delta\alpha\beta}^*$ and $T_{\Delta\alpha\beta}^*$ can be found in [Aliabadi 2002].

The domain integrals appearing in (2), (5), (6), and (7) are evaluated by using the dual reciprocity technique as described in [Wen et al. 2000]. The particular solutions for plate bending and two-dimensional plane stress can also be found in the same reference.

4. Evaluation of derivative terms

The derivatives of deflection $w_{3,\gamma}$ on the boundary and in the domain can be approximated using a radial basis function $f(r) = \sqrt{c^2 + r^2}$, where $r = \sqrt{(x_1 - x_1^m)^2 + (x_2 - x_2^m)^2}$:

$$w_3(x_1 + x_2) = \sum_{m=1}^{M+N} f(r)^m \Psi^m, \quad (8)$$

where N and M are respectively the number of selected points x_1 and x_2 on the boundary and in the domain. The Ψ^m are coefficients which are determined by values at the selected points as follows:

$$\Psi = F^{-1}\{w_3\}. \quad (9)$$

The derivatives of the deflection values may be expressed by

$$w_{3,\gamma}(x_1 + x_2) = f(r),_{\gamma} F^{-1}\{w_3\}. \tag{10}$$

The nonlinear terms $N_{\alpha\gamma,\gamma}^{\mathrm{nonlin}}$ which appear in (5) and (7) can be evaluated in a similar way as well. Using this approach, there is no need to evaluate the derivatives of the transverse displacement $w_{3,\gamma}$ through the integral equations. The integral equations usually have complicated mathematical terms and may have singularities of higher order.

A relaxation procedure is used to improve the numerical results. As the nonlinear terms are calculated in each step (k) of increments, the deflection w_3 can be modified as

$$w_3^{k+1} = \frac{w_3^{k+1} + w_3^k}{2}. \tag{11}$$

Note that the relaxation procedure shown in (11) works well for moderately low load levels. If higher load levels are applied, the use of (11) is not recommended.

5. Imperfection models

The initial imperfections of the transverse loads are introduced to trigger buckling modes. Figure 2 shows the two imperfection models used:

(i) uniform distribution of the transverse loads q_0 in the domain Ω;

(ii) distributed transverse loads q_0 in the domain Ω, corresponding to a number of half-waves indicated by the eigenvectors from the linear elastic buckling analysis [Purbolaksono and Aliabadi 2005a].

The first model only allows few nonlinear buckling problems to be accurately analyzed such as the geometries of square and circular models. The second model is generally recommended, since the imperfections can be modeled based on the eigenvectors that are related to the buckling modes. Hence, the second model may represent the initial imperfections that should be distributed in the domain.
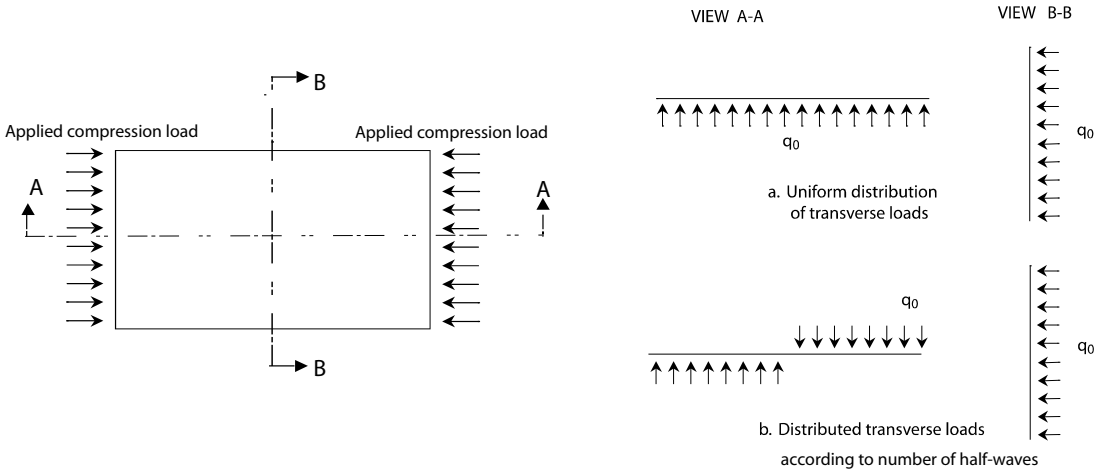
Figure 2. Initial imperfection models.

The following equations are used to define the magnitudes of the load increment $\Delta\sigma$ and transverse loads q_0 throughout this work. The magnitudes are empirically maintained to be small enough. The relation between the load increment $\Delta\sigma$ and modulus of elasticity may be proposed as

$$\frac{\Delta\sigma}{E} \approx X, \tag{12}$$

where X is in the range of 10^{-7} to 5×10^{-7}. Next, the relation between the load increment $\Delta\sigma$ and transverse loads q_0 is proposed as

$$q_0 = \frac{\Delta\sigma_h}{5b}, \tag{13}$$

where b is the width or diameter of plates.

The transverse loads q_0 are used to introduce the initial imperfection loads in the plates according to the models shown in Figure 2.

6. Numerical algorithms

A simple numerical algorithm, requiring no iterations, is used to analyze nonlinear buckling problems. It can be summarized as follows:

Step 1: After introducing initial imperfection by uniform distribution q_0 or distributed transverse loads $q_0 = q_0^1$ (see Figure 2) and a load increment $\Delta\sigma$, let the first step $k = 1$ and the final step k^{final} and initial values of $N_{\alpha\beta}^{\text{lin}} = 0$ and $w_{,\alpha} = 0$.

Step 2: Compute the coefficient matrices related to fundamental solutions. They can be stored in the core and used in each increment without any change.

Step 3: If $k \neq 1$ then $q_0^{k+1} = q_0^k + q_0^1$. Solve the linear system equation of the boundary integral equations to obtain boundary values. Then calculate the in-plane stress resultants $N_{\alpha\beta}^{\text{lin}}$ and derivative of deflection $w_{,\alpha}$ in the domain.

Step 4: Apply the relaxation procedure given in (11). Then calculate the nonlinear terms $(N_{\alpha\gamma,\gamma}^{\text{nonlin}})^{(k)}$ and $[(N_{\alpha\beta}w_{3,\beta})_{,\alpha}]^{(k)}$ using approximation function as described in (6)–(8). The nonlinear terms will be used for the evaluation in the next step $k + 1$.

*Step 5*: Calculate the nonlinear membrane traction t_α^{nonlin} on the boundary.

Step 6: Print results.

Step 7: If $k = k^{\text{final}}$, terminate; otherwise let step $k = k + 1$ and go to Step 3.

By introducing cumulative transverse loads q_0^k at each step k, the equilibrium of (4) could be maintained. The transverse loads q_0 as the imperfection loads however might provide potential biasing of the results if they are arbitrarily defined.

7. Numerical examples

Several numerical examples with different geometries, loadings, and boundary conditions are presented to demonstrate the ability of the proposed method. Equations (12) and (13) are used to define the magnitudes of the load increment $\Delta\sigma$ and transverse loads q_0.
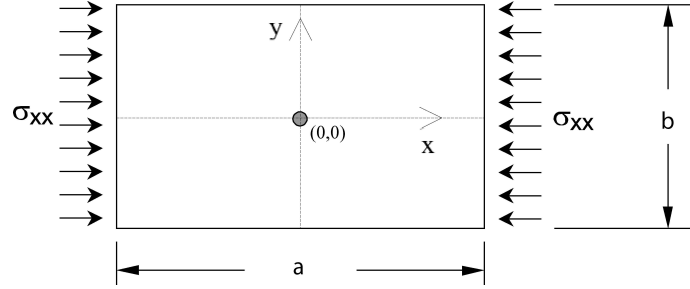
Figure 3. Nonlinear buckling model.

The nonlinear buckling model is shown in Figure 3. In the following examples, the normalized critical compression stress K_{nl} is defined by
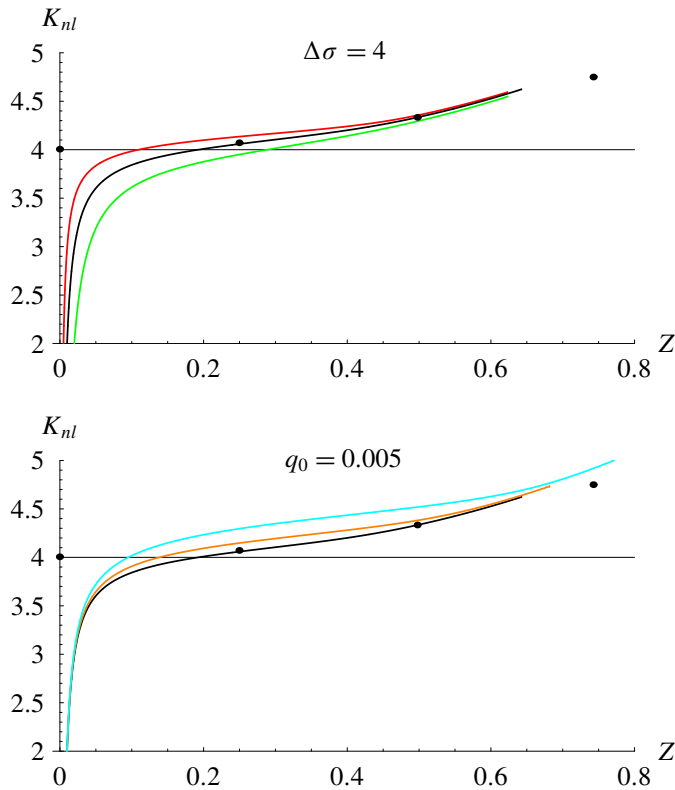
$$K_{nl} = \frac{b^2 h}{\pi^2 D} \sigma, \tag{14}$$

where σ is compression stress.

7.1. *Convergence study of simply supported square plate subjected to uniaxial compression loads.* In this example, a square plate subjected to compression loads at its ends as shown in Figure 3 is analyzed. Five different distributions of domain points are used for the dual reciprocity calculation. The initial imperfection is introduced by uniform transverse load $q_0 = 0.005$ units and in the case of $\Delta\sigma = 4$ units. A convergence study of the simply supported square plate is performed and the normalized compression stresses K_{nl} and the normalized deflection Z ($= w_3/h$) are plotted in Figure 4. The results given in [Levy 1942] are also plotted in Figure 4. It can be seen that the convergence of the results can be achieved with 49 domain points. The normalized compression stress is in agreement with the critical value $K_{nl} \approx 4$ of the analytical result [Timoshenko and Gere 1961]. The BEM results are also in good agreement with Levy's solution [Levy 1942].
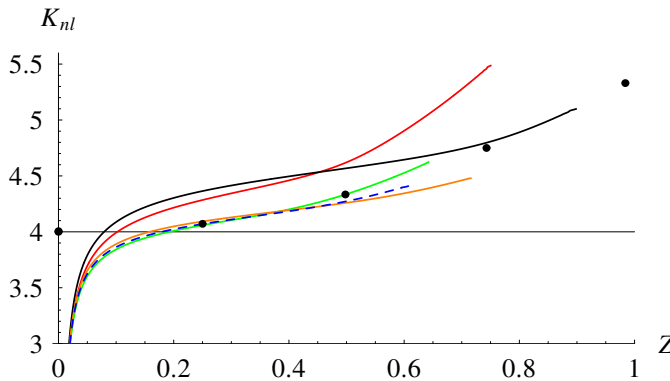
Figure 4. Normalized compression stresses K_{nl} and deflection Z for different numbers of domain points: from top to bottom at rightmost point, 5×5, 6×6, 7×7, and 8×8 (dashed curve). The black dots are values from [Levy 1942]. The thin horizontal line marks the critical value [Timoshenko and Gere 1961].

Figure 5. Normalized compression stresses K_{nl} and deflection Z for various transverse loads (top diagram; curves from top to bottom, $q_0 = 0.0025, 0.005, 0.01$) and for various increments of the compression load (bottom diagram: curves from from top to bottom, $\Delta\sigma = 16, 8, 4$). Black dots and horizontal line as in Figure 4.

7.2. Simply supported square plate subjected to uniaxial compression loads with different initial imperfections and increments of load.

In this example, a simply supported square plate subjected to uniaxial compression load is analyzed with different imperfections and increments of the load. BEM meshing with 20 quadratic boundary elements and 49 domain points are used. The normalized compression stresses K_{nl} and deflection Z for different initial imperfections and in the case of $\Delta\sigma = 4$ unit of compression loads are plotted in Figure 5, top.

The normalized compression stresses K_{nl} and deflection Z for different increment of compression loads and in the case of $q_0 = 0.005$ units of uniform transverse loads are plotted in Figure 5, bottom. It can be seen that the bigger value of initial imperfection provides a lower critical buckling load. The same graph also shows that the bigger value of compression load increment provides a bigger critical buckling load.
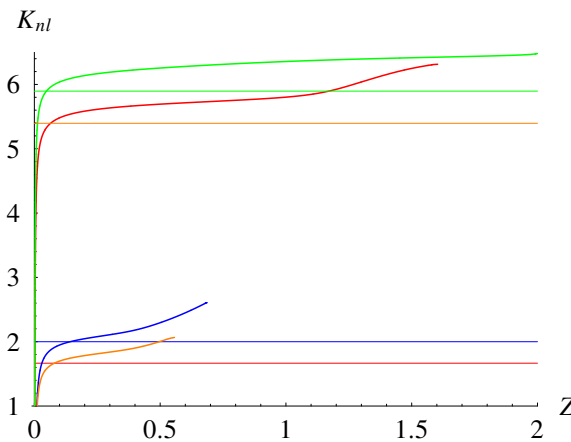
7.3. Circular and square plates subjected to a uniform normal compression loads.

We performed the nonlinear buckling analysis of circular and square plates subjected to uniform normal compression loads (Figure 6). Two boundary conditions, simply supported and clamped, are applied. The BEM meshes used had 16 quadratic boundary elements and 33 domain points for the circular plate, and 20 quadratic
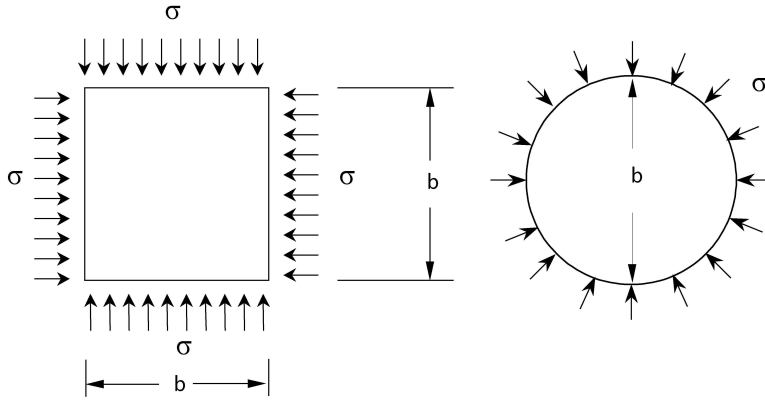
Figure 6. Circular and square plates subjected to uniform normal compression loads.

boundary elements and 25 domain points for the square plate. The compression load increments were chosen as $\Delta\sigma = 4$ units and the initial imperfection as $q_0 = 0.005$ units. Figure 7 shows the normalized compression stresses K_{nl} and the normalized deflection Z together the with critical value of each model for linear elastic buckling analysis [Timoshenko and Gere 1961]. The results are seen to be agreement with the critical values.

7.4. *Analysis of two imperfection models on simply supported rectangular plates.* In this example, two imperfection models, namely uniform distribution and distributed transverse loads, are evaluated. A simply supported rectangular plate as shown in Figure 3 is used to investigate the proposed imperfection models. The origin is at the center of the plate. In the case of uniform distribution, the increments of compression loads as $\Delta\sigma = 4$ units and initial imperfection as $q_0 = 0.005$ units are applied.

Figure 7. Normalized stresses K_{nl} of circular and square plates subjected to uniform normal compression loads. Curves from top to bottom correspond to clamped circle, clamped square, simply supported square, and simply supported circle configuration. The horizontal lines show the critical values in the same order.
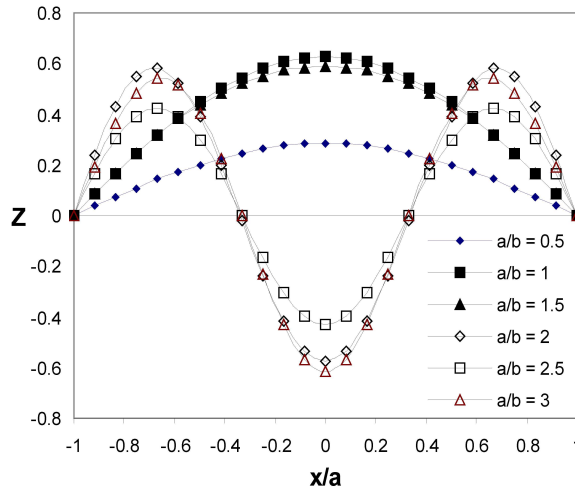
Figure 8. Half-wave modes for rectangular plates with different aspect ratio a/b due to uniform imperfections.

The normalized deflections Z for the points along x-axis due to uniform imperfections are plotted in Figure 8. It can be seen that the plates will buckle in odd number of half-waves for different aspect ratios a/b.

For the distributed transverse load model, imperfections are introduced according to the buckling modes defined by the eigenvectors from linear elastic buckling analysis for the corresponding geometry. For the rectangular plate, the distribution of imperfections is shown in Figure 9.
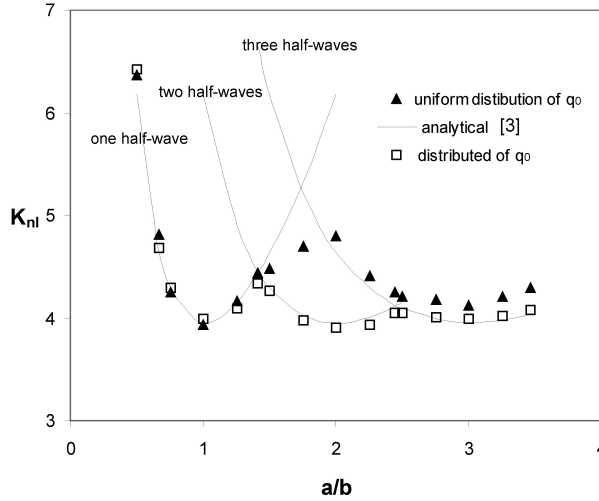
The estimated normalized compression stresses K_{nl} for different aspect ratio of the plates are plotted in Figure 10. It can be seen that the uniform imperfection of transverse loads provides inaccurate results with the increasing of aspect ratios. Moreover, for aspect ratios a/b between 1.4 and 2.5, the buckling deformations of the plate do not form two half-wave modes as expected. The results obtained with the distributed loads according to the buckling modes are in good agreements with the published results.

7.5. *Nonlinear buckling analysis of rectangular plates with different boundary conditions.* We next turn to a nonlinear buckling analysis of rectangular plates as shown in Figure 3 subjected to a uniform
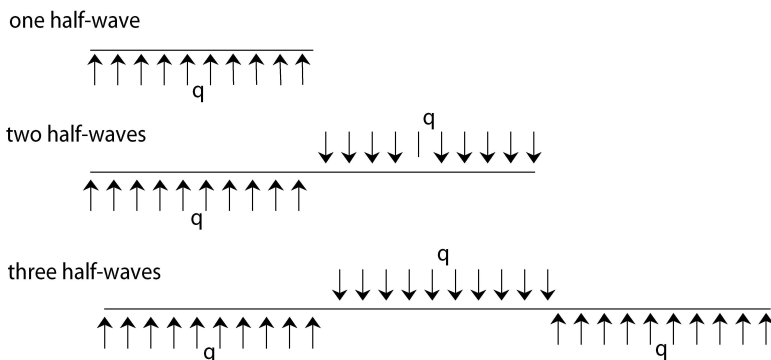
**Figure 9.** Simplified imperfections for rectangular plates.

Figure 10. The normalized compression stresses K_{nl} for different aspect ratio of the simply supported rectangular plates.

normal compression loads. Three boundary conditions are applied: all sides clamped (cccc), two opposite loaded side clamped and two others simply supported (cscs), and three sides simply supported and one unloaded side free (sssf). The deformations for rectangular plates with the these boundary conditions are shown in Figure 11.

The normalized compression stresses K_{nl} and the normalized deflection Z together with the critical value of each the three models above are plotted in Figure 12.
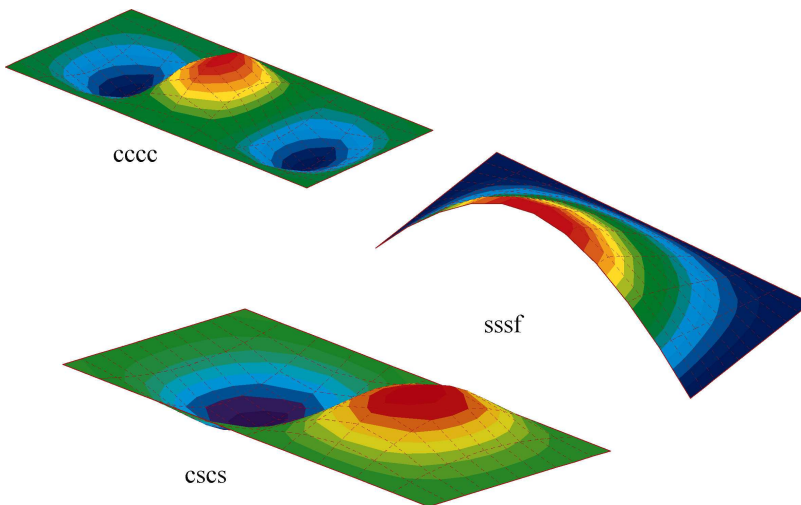
Figure 11. Nonlinear buckling deformations for rectangular plates with different boundary conditions. See text immediately above for abbreviations.
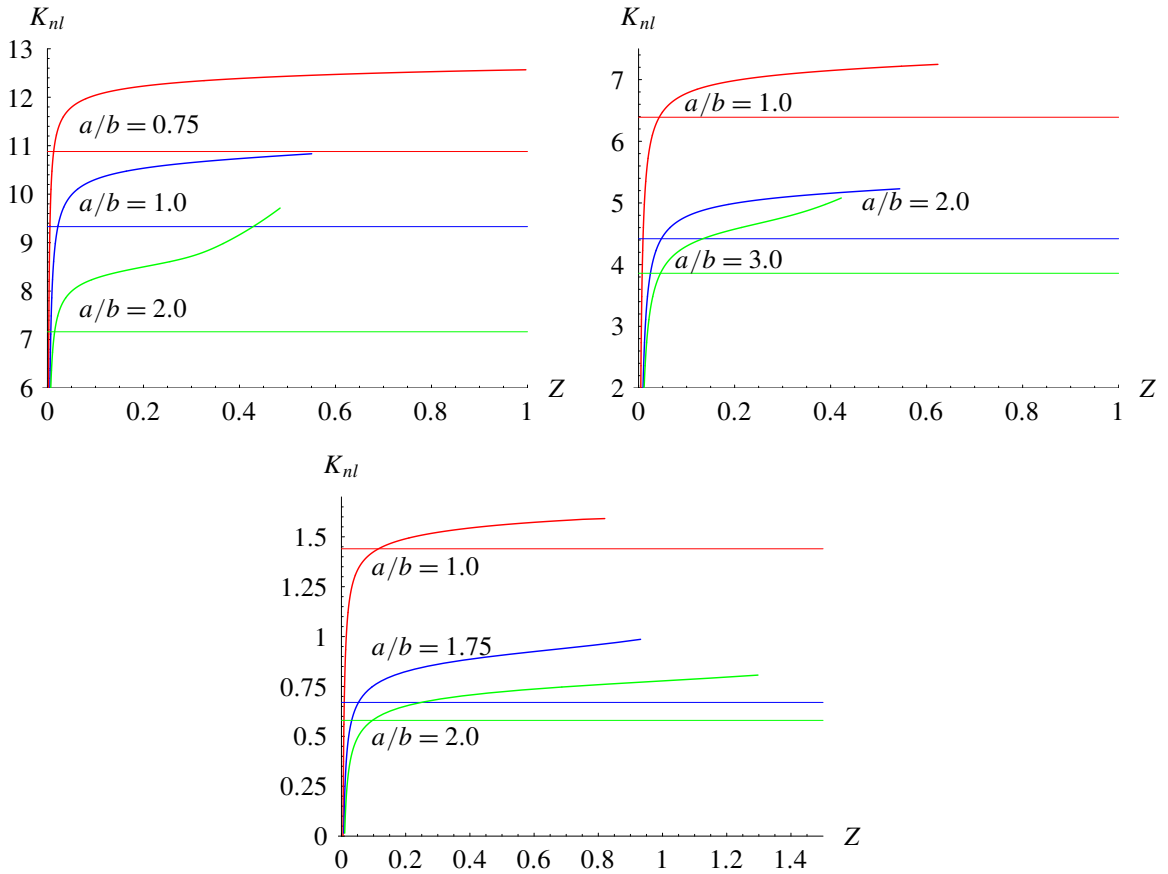
Figure 12. Normalized compression stresses K_{nl} of rectangular plates, for different values of a/b (given next to the curves to which they apply). Top left: all sides clamped. Top right: two opposite loaded sides clamped and two others simply supported. Bottom: three sides simply supported and one unloaded side free. The critical values (horizontal lines) are taken from [Purbolaksono and Aliabadi 2005a].

8. Conclusions

The BEM results obtained by using imperfections of the distributed transverse loads corresponding to the expected buckling modes were in good agreement with the published results and the theoretical critical buckling strengths. The proposed equations for defining the magnitudes of the load increment $\Delta\sigma$ and transverse loads q_0 reasonably also demonstrated the accuracy of the results for the analyses.

Acknowledgments

References

[Aliabadi 2002] M. H. Aliabadi, *The boundary element method, applications in solids and structures*, vol. 2, Wiley, Chichester, 2002.

[Bao et al. 1997] G. Bao, W. Jiang, and J. C. Roberts, "Analytic and finite element solutions for bending and buckling of orthotropic rectangular plates", *Int. J. Solids Struct.* **34**:14 (1997), 1797–1822.

[Brush and Almroth 1975] D. O. Brush and B. Almroth, *Buckling of bars, plates, and shells*, McGraw-Hill, New York, 1975.

[He and Qin 1993] X. Q. He and Q. H. Qin, "Nonlinear analysis of Reissner's plate by the variational approaches and boundary element methods", *Appl. Math. Model.* **17**:3 (1993), 149–155.

[Kamiya et al. 1984] N. Kamiya, Y. Sawaki, and Y. Nakamura, "Postbuckling analysis by the boundary element method", *Eng. Anal.* **1**:3 (1984), 40–44.

[Lei et al. 1990] X. Y. Lei, M. K. Huang, and X. X. Wang, "Geometrically nonlinear analysis of a Reissner type plate by the boundary element method", *Comput. Struct.* **37**:6 (1990), 911–916.

[Levy 1942] S. Levy, *Bending of rectangular plates with large deflections*, National Advisory Committee for Aeronautics, 1942, Available at http://naca.central.cranfield.ac.uk/reports/1942/naca-report-737.pdf. TN-737.

[Liu 1987] Y. Liu, "Elastic stability analysis of thin plate by the boundary element method - new formulation", *Eng. Anal.* **4**:3 (1987), 160–164.

[Liu 2001] F. L. Liu, "Differential quadrature element method for buckling analysis of rectangular Mindlin plates having discontinuities", *Int. J. Solids Struct.* **38**:14 (2001), 2305–2321.

[Manolis et al. 1986] G. D. Manolis, D. E. Besko, and M. F. Pineros, "Beam and plate stability by boundary elements", *Comput. Struct.* **22**:6 (1986), 917–923.

[Marczak and de Barcellos 1998] R. J. Marczak and C. S. de Barcellos, "A boundary element formulation for linear and nonlinear bending of plates", in *Proc. Fourth World Congress of Computational Mechanics, IACM*, 1998.

[Purbolaksono and Aliabadi 2005a] J. Purbolaksono and M. H. Aliabadi, "Buckling analysis of shear deformable plates by boundary element method", *Int. J. Numer. Methods Eng.* **62**:4 (2005), 537–563.

[Purbolaksono and Aliabadi 2005b] J. Purbolaksono and M. H. Aliabadi, "Dual boundary element method for instability analysis of cracked plates", *Comput. Model. Eng. Sci.* **8**:1 (2005), 73–90.

[Qin and Huang 1990] Q. Qin and Y. Huang, "BEM of postbuckling analysis of thin plates", *Appl. Math. Model.* **14**:10 (1990), 544–548.

[Syngellakis 1998] S. Syngellakis, *Stability plate bending analysis with boundary elements*, edited by M. H. Aliabadi, Computational Mechanics Publications, Southampton and Boston, 1998.

[Tanaka et al. 1999] M. Tanaka, T. Matsumoto, and Z. Zheng, "Application of the boundary-domain element method to the pre/post-buckling problem of von Karman plates", *Eng. Anal. Bound. Elem.* **23**:5-6 (1999), 399–404.

[Timoshenko and Gere 1961] S. P. Timoshenko and J. M. Gere, *Theory of elastic stability*, 2nd ed., McGraw-Hill, New York, 1961.

[Walker 1984] A. C. Walker, "A brief review of plate buckling research", in *Behaviour of thin-walled structures*, edited by J. Rhodes and J. Spence, Elsevier, London, 1984.

[Wang et al. 2001] C. M. Wang, G. T. Lim, J. N. Reddy, and K. H. Lee, "Relationships between bending solutions of Reissner and Mindlin plate theories", *Eng. Struct.* **23**:7 (2001), 838–849.

[Wen et al. 2000] P. H. Wen, M. H. Aliabadi, and A. Young, "Application of dual reciprocity method to plates and shells", *Eng. Anal. Bound. Elem.* **24**:7-8 (2000), 583–590.

JUDHA PURBOLAKSONO: judha@uniten.edu.my
Department of Mechanical Engineering, Universiti Tenaga Nasional, Km 7 Jalan Kajang–Puchong, Kajang 43009, Selangor, Malaysia

M. H. (FERRI) ALIABADI: m.h.aliabadi@imperial.ac.uk
Department of Aeronautics, Faculty of Engineering, Imperial College London, Prince Consort Road, London SW7 2BY, United Kingdom

A NEW ANALYTIC SYMPLECTIC ELASTICITY APPROACH FOR BEAMS RESTING ON PASTERNAK ELASTIC FOUNDATIONS

C. F. Lü, C. W. Lim AND W. A. Yao

Analytic solutions describing the stresses and displacements of beams on a Pasternak elastic foundation are presented using a symplectic method based on classical two-dimensional elasticity theory. Hamilton's principle with a Legendre transformation is employed to derive the Hamiltonian dual equation, and separation of variables reduces the dual equation to an eigenequation that differs from the conventional eigenvalue problems involved in vibration and buckling analysis. Using adjoint symplectic orthonormality, a group of eigensolutions of zero eigenvalue, corresponding to the Saint-Venant problem, are derived. This approach differs from the traditional semi-inverse analysis, which requires stress or deformation trial functions in the Lagrangian system. The final solutions, which account for the effects of an elastic foundation and applied lateral loads, are approximated by an eigenfunction expansion. Comparisons with existing numerical solutions are conducted to validate the efficiency of this new approach.

1. Introduction

Isotropic beams and plates on elastic foundations are widely used to model civil engineering structures, including building footings designed in the form of plates or planar framed structures, bases of artificial navigable waterways, the pavement of highways and runways, and rails, to name a few. Much of the existing literature on structure-foundation systems is based on classical thin beam/plate theory [Leissa 1973; Franciosi and Masi 1993; De Rosa and Maurizi 1998], which relies on the assumption that a foundation's reaction forces act on the midplane of the modeled beam/plate. This assumption, however, may be unrealistic for thicker structures in which shear deformations may be significant. In addition, the effects of the foundation on deformation and stress fields in the vicinity of the two lateral surfaces become important for larger beam and plate aspect ratios.

A variety of first-order shear deformation theories [Timoshenko 1921; Shirima and Giger 1992; Wang et al. 1998; Lee et al. 2003] and refined higher-order theories [Reddy 1984; Frostig et al. 1992; Matsunaga 2000], which account for shear deformations and/or rotary inertia, have been proposed to improve the accuracy of thick beam/plate models. However, they suffer from the shortcoming that transverse normal stress is neglected [Lim 1999].

A number of studies have attempted to present two-dimensional elasticity solutions for isotropic and anisotropic beams. Whitney [1985] performed a stress analysis on orthotropic beams subjected to concentrated loads within the framework of the classical theory of elasticity. Stresses that developed during interlaminar beam tests were examined in detail, and observations showed considerable deviation from

classical beam theory over large portions of the beam. Sullivan and Vanoene [1986] derived an elasticity solution for centrally loaded orthotropic beams by virtue of a stress function and the Fourier series. The symmetric properties of the stress field in the beams were investigated and compared to those predicted by beam theory. Regions in which the beam theory predictions coincided with the theory of elasticity were identified. Sankar [2001] reported an exact elasticity solution for a simply supported functionally graded beam with the aid of the Fourier series. Although no assumptions concerning the stress and deformation fields were adopted in these papers, and, hence, the solution formulations were applicable to beams of arbitrary thickness, such exact solutions are only available for fully simply supported beams. Ding et al. [2005] proposed analytic elasticity solutions for the stress and displacement fields of an isotropic fixed-fixed beam produced by uniform loading. They constructed biharmonic stress functions using the Airy stress function method, and investigated the differences between the two types of fixed ends described in [Timoshenko and Goodier 1970]. Their analysis employed the semi-inverse method, which is the approach of choice for dealing with a higher-order partial differential equation with a single variable. Such single-variable solution procedures rely on the Lagrangian method, for which many effective methods of mathematical physics, such as separation of variables and expansion of eigenfunctions, are not applicable.

We have not been able to find in the literature analytic solutions for generally supported beams resting on elastic foundations using classical two-dimensional theory of elasticity. In this paper, a rational derivation based on that theory is presented to determine the mechanical behavior of such beams. The solution involves the *symplectic group*, which was introduced by Weyl [1939] and has found applications in many areas of physics, including quantum mechanics, relativity, gravitation, astrophysics, classical mechanics, Hamiltonian mechanics, and elasticity. Details regarding the development and applications of the symplectic approach can be found in [Lim et al. 2007].

In the Hamiltonian framework, separation of variables and eigenfunction expansions can be applied to derive exact analytic solutions for some basic elasticity problems, although solutions are still unavailable and have long been a bottleneck for the development of the theory of elasticity. In [Lim et al. 2008] we proposed a new symplectic approach to analyze the bending behavior of corner-supported thin plates subjected to uniform transverse pressures, for which an exact explicit solution for deflection is derived here for the first time. The zero bending moment and shear forces at the free edges are exactly satisfied, and the twisting moment conditions at the support corners are exactly predicted. These quantities have long eluded both analytic and numerical analysis, including application of the finite element method.

For beams in a plane state without body forces, a Legendre transformation may be applied to derive the conservative Hamiltonian variational principle, from which a Hamiltonian dual equation, i.e., the symplectic dual system, is formulated. With homogeneous side boundary conditions, the method of separation of variables is employed to obtain the eigenequation for the transverse cross section. The present work emphasizes eigensolutions of zero eigenvalue, because they correspond to the basic solutions of Saint-Venant problems [Yao et al. 2009].

The effect of an elastic foundation on the mechanical behavior of a beam arises from the interaction between the foundation and the beam surface, which are unlike those modeled in classical beam theory. Hence, an elastic foundation is treated with side boundary conditions, similar to those of an applied load, and the contributions of these boundary conditions to the solutions for beams are approximated by a linear expansion of all eigensolutions of zero eigenvalue. A comparison of numerical examples with other methods is presented to illustrate the accuracy of the present symplectic approach.

2. Hamilton's variational principle and symplectic formulation

Consider an isotropic beam of length l, depth $2h$, and unit width. The Cartesian coordinate system is defined such that $-h \leq z \leq h$ and $0 \leq x \leq l$ ($l \gg 2h$), as shown in Figure 1. Suppose that all loads (including the boundary conditions) are applied in the xOz plane and remain constant along the width. These conditions define a plane stress problem involving a beam.

Here, the top surface of the beam is subjected to the following applied loads:

$$\sigma_z = \bar{F}_{z1}(x), \quad \tau_{xz} = \bar{F}_{x1}(x), \quad \text{at } z = -h, \tag{1}$$

and the bottom surface is attached to an elastic foundation (see Figure 1). We assume that the foundation experiences only vertical displacements without horizontal movement, and that only the compatibility of normal displacements at the foundation-beam interface is considered. Hence, the beam is subjected to normal reaction forces by the foundation, which is modeled as a two-parameter foundation. The displacement–reaction force relation [Pasternak 1954] is

$$\sigma_z = \bar{F}_{z2}(x) = k_p \frac{\partial^2 w}{\partial x^2} - k_w w, \quad \tau_{xz} = \bar{F}_{x2}(x) = 0, \quad \text{at } z = h, \tag{2}$$

where k_w is the normal stiffness (modulus of the Winkler foundation) and k_p the shear stiffness of the foundation.

For an isotropic beam in a plane stress state as described above, the constitutive equations are

$$\begin{Bmatrix} \sigma_x \\ \sigma_z \\ \tau_{xz} \end{Bmatrix} = \frac{E}{1-v^2} \begin{bmatrix} 1 & v & 0 \\ v & 1 & 0 \\ 0 & 0 & \frac{1}{2}(1-v) \end{bmatrix} \begin{Bmatrix} \dfrac{\partial u}{\partial x} \\ \dfrac{\partial w}{\partial z} \\ \dfrac{\partial w}{\partial x} + \dfrac{\partial u}{\partial z} \end{Bmatrix}, \tag{3}$$

where σ_x and σ_z are the normal stresses, τ_{xz} is the shear stress, u and w are the displacement components, respectively, in the x- and z-directions, E and v are the Young's modulus and Poisson's ratio, respectively. In the absence of body forces, the governing differential equations of the beam in equilibrium are

$$\frac{\partial \sigma_x}{\partial x} + \frac{\partial \tau_{xz}}{\partial z} = 0, \quad \frac{\partial \tau_{xz}}{\partial x} + \frac{\partial \sigma_z}{\partial z} = 0. \tag{4}$$
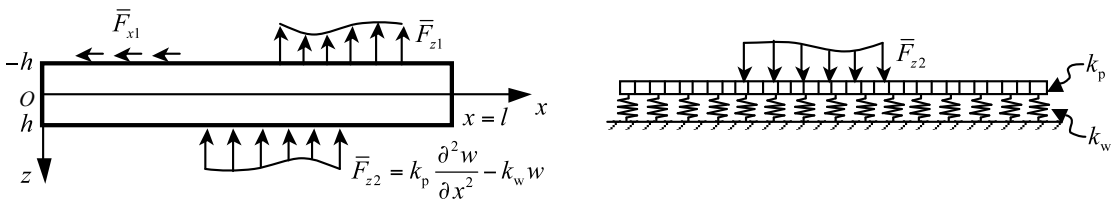
Figure 1. Left: geometry, coordinate system and loading condition of a beam resting on elastic foundations. Right: Pasternak foundation and beam foundation.

In the following Hamiltonian formulation, the time variable is designated as the x coordinate, and a dot indicates partial differentiation with respect to x. Following the routine transformation of the Lagrangian system into the Hamiltonian system, via the Legendre transformation, we arrive at the Hamiltonian variational principle,

$$\delta\left(\int_0^l \int_{-h}^h \left[\boldsymbol{p}^T\dot{\boldsymbol{q}} - \mathcal{H}(\boldsymbol{q},\boldsymbol{p})\right]dxdz + \int_0^l (\bar{\boldsymbol{F}}_1^T\boldsymbol{q})_{z=-h}\,dx + \frac{1}{2}\int_0^l (k_w w^2 + k_p \dot{w}^2)_{z=h}\,dx\right) = 0, \quad (5)$$

where $\mathcal{H}(\boldsymbol{q},\boldsymbol{p})$ is the Hamiltonian energy density, as given in [Yao et al. 2009], $\boldsymbol{q} = [u\ w]^T$ and $\boldsymbol{p} = [\sigma\ \tau]^T$ (with $\sigma = \sigma_x$ and $\tau = \tau_{xz}$) are a pair of dual vectors, and $\bar{\boldsymbol{F}}_1^T = [\bar{F}_{x1}\ \bar{F}_{z1}]$. Based on (5), the Hamiltonian dual equation is derived as

$$\dot{\boldsymbol{v}} = \boldsymbol{H}\boldsymbol{v}, \qquad (6)$$

where $\boldsymbol{v} = [u\ w\ \sigma\ \tau]^T$ is called the state vector, and $\boldsymbol{H}$ is the Hamiltonian operator matrix [Yao et al. 2009]. From (3), the induced variable σ_z is obtained as

$$\sigma_z = E\frac{\partial w}{\partial z} + \nu\sigma. \qquad (7)$$

For the present Hamiltonian dual equation (6), the method of variable separation is applicable, i.e., the solution to (6) is assumed to be of the form

$$\boldsymbol{v}(x,z) = \xi(x)\boldsymbol{\psi}(z). \qquad (8)$$

Substitution of (8) into (6) yields

$$\xi(x) = e^{\mu x}, \qquad (9)$$

where μ is the eigenvalue in the x-direction, and the eigenvalue equation

$$\boldsymbol{H}\boldsymbol{\psi}(z) = \mu\boldsymbol{\psi}(z), \qquad (10)$$

where $\boldsymbol{\psi}(z)$ is the eigenvector, which fulfills the homogeneous boundary conditions

$$E\frac{\partial w}{\partial z} + \nu\sigma = 0, \quad \tau = 0, \quad \text{at } z = \pm h. \qquad (11)$$

3. Basic solutions to the Saint-Venant problem

Basic solutions. According to the Saint-Venant principle, forces in equilibrium pose local influences, i.e., local effects decay dramatically with the distance. The solution to the Saint-Venant problem is inherent in the eigensolutions with nonzero eigenvalues. Meanwhile, (8) implies that the zero eigenvalue solutions are not sensitive to the equilibrium system of forces, because no exponential functions are present. Hence, for the slender beam ($l \gg 2h$), the effects of the equilibrium system of forces at the two ends are negligible, that is, the eigensolutions of nonzero eigenvalues can be excluded. As a result, only eigensolutions for the repeated zero-valued eigenvalue $\mu = 0$ will be used to construct the basic solution to the beam in the Saint-Venant problem [Yao et al. 2009], i.e.,

$$\boldsymbol{v} = a_1\boldsymbol{\psi}_f^{(0)} + a_2\boldsymbol{\psi}_f^{(1)} + a_3\boldsymbol{\psi}_s^{(0)} + a_4\boldsymbol{\psi}_s^{(1)} + a_5\boldsymbol{\psi}_s^{(2)} + a_6\boldsymbol{\psi}_s^{(3)}, \qquad (12)$$

where $\boldsymbol{\psi}_f^{(n)}$ and $\boldsymbol{\psi}_s^{(n)}$ are, respectively, the Jordan form eigensolutions of the first and second chains, for which explicit expressions have been derived in [Yao et al. 2009]. Equation (12) can be expanded to

$$u = a_1 - a_4 z + a_6 \left(-\frac{6+5\nu}{10} h^2 z + \frac{2+\nu}{6} z^3 \right), \quad \sigma = a_2 E - a_5 E z,$$

$$w = -a_2 \nu z + a_3 - a_5 \left(\frac{4+5\nu}{10} z^2 - \frac{\nu}{2} z^2 \right), \quad \tau = \tfrac{1}{2} a_6 E(z^2 - h^2), \tag{13}$$

where the a_i are x-dependent parameters to be determined using the constraints at $x = 0, l$. The basic solution in (13) is applicable to the Hamiltonian dual equation (6) with the homogeneous side boundary conditions given in (11). When the beam is subjected to external loading and elastic foundations, a_i should be determined from the Hamiltonian variational principle in (5).

Determination of the a_i. Because each basic eigensolution in (12) is related to a special deformation, the a_i should be related to particular physical quantities. Here, a_1, a_3, a_4 correspond to axial deformation, transverse deformation, and rotation angle, respectively, and a_2, a_5, a_6 correspond to axial force, bending moment, and shear force, respectively. Note that a_1 and a_2 are related to symmetric deformations, whereas a_3–a_6 are related to antisymmetric deformations.

In the present analysis, only the bending behavior of the beam on an elastic foundation is considered. The symmetric deformations described by a_1 and a_2 are therefore excluded. Substituting the antisymmetric portion of (13) into (5) leads to

$$\dot{a}_3 = a_4 + \frac{4+5\nu}{10E} \bar{F}_{x1}, \quad \dot{a}_4 = a_5 - 0.4 h^2 \dot{a}_6, \quad \dot{a}_5 = a_6 + \frac{1}{EI} \bar{F}_{x1},$$

$$\dot{a}_6 = -\frac{1}{EI} \left(k_w (a_3 - 0.4 h^2 a_5) - k_p (\ddot{a}_3 - 0.4 h^2 \ddot{a}_5) + \bar{F}_{z1} \right), \tag{14}$$

where $I = \frac{2}{3} h^3$ is the second moment of the area. The set of coupled differential equations above can be reduced to a fourth-order differential equation with respect to a_3, i.e.,

$$\bar{E} a_3^{(4)} - \bar{k}_p a_3^{(2)} + k_w a_3 = f(x), \tag{15}$$

where $f(x) = \left((EI + 0.4 k_p h^2)g - 0.4 h^3 \right) \dddot{\bar{F}}_{x1} + (h - 0.4 g k_w h^2) \dot{\bar{F}}_{x1} + 0.4 h^2 \ddot{\bar{F}}_{z1} - \bar{F}_{z1}$, $\bar{E} = EI + 0.8 k_p h^2$, $\bar{k}_p = k_p + 0.8 k_w h^2$, and $g = (2+\nu)/(2E)$. The eigenvalues of (15) are

$$\pm r_1 = \sqrt{\frac{\bar{k}_p + \sqrt{\bar{k}_p^2 - 4\bar{E} k_w}}{2\bar{E}}}, \qquad \pm r_2 = \sqrt{\frac{\bar{k}_p - \sqrt{\bar{k}_p^2 - 4\bar{E} k_w}}{2\bar{E}}}. \tag{16}$$

We find that $r_2 = 0$ when $k_w = 0$, and $r_1 = r_2 = 0$ when $k_w = k_p = 0$. Hence, the general solution, a_3, depends on whether k_w and k_p vanish:

<u>Case 1: $k_w \neq 0$</u>	$a_3 = c_1 e^{r_1 x} + c_2 e^{-r_1 x} + c_3 e^{r_2 x} + c_4 e^{-r_2 x} + \tilde{a}_3$;
<u>Case 2: $k_w = 0$, $k_p \neq 0$</u>	$a_3 = c_1 e^{r_1 x} + c_2 e^{-r_1 x} + c_3 + c_4 x + \tilde{a}_3$;
<u>Case 3: $k_w = 0$, $k_p = 0$</u>	$a_3 = c_1 + c_2 x + c_3 x^2 + c_4 x^3 + \tilde{a}_3$.

$$\tag{17}$$

Here, the c_i are constants of integration and $\tilde{a}_3$ is the particular solution to (15) for the inhomogeneous term $f(x)$ for the applied loads.

Knowing the values for a_3, all remaining parameters a_4–a_6 can be determined, based on (14):

$$a_4 = \dot{a}_3 - \frac{4+5\nu}{10E}\bar{F}_{x1}, \tag{18}$$

$$a_5 = \frac{1}{\tilde{E}}\left(\bar{E}\ddot{a}_3 - 0.4k_w h^2 a_3 + g_1\dot{\bar{F}}_{x1} - 0.4h^2\bar{F}_{z1}\right), \tag{19}$$

$$a_6 = \frac{1}{\tilde{E}}\left(\bar{E}\dddot{a}_3 - 0.4k_w h^2\dot{a}_3 + g_1\ddot{\bar{F}}_{x1} - 0.4h^2\dot{\bar{F}}_{z1}\right) - \frac{h}{EI}\bar{F}_{x1}, \tag{20}$$

where $\tilde{E} = EI + 0.4h^2(k_p - 0.4k_w h^2)$ and $g_1 = 0.4h^3 - g(EI + 0.4k_p h^2)$.

In practice, the constants in Equations (17) should be determined according to the support conditions at the two ends. Considering the energy related to the end constraints in accordance with the Hamiltonian variational principle in (5), the following three typical constraint conditions at $x = 0$ and $x = l$, for clamped (C), simple supports (S), and free (F) supports, are derived, where $\lambda = 0.4(1+\nu)h^2$:

$$\text{F}: \quad a_5 = a_6 = 0 \tag{21}$$

$$\text{S}: \quad a_3 = a_5 = 0 \tag{22}$$

$$\text{C}: \quad a_3 - \lambda a_5 = 0, \quad a_4 + \lambda a_6 = 0 \tag{23}$$

According to the previously described interpretations of the a_i, the expression in (21) can be interpreted physically as a case of zero axial force, zero bending moment, and zero shear force, while the expression in (22) can be interpreted as zero axial force, zero transverse displacement, and zero bending moment. Similarly, in (23), the first condition represents an axial displacement of zero for the clamped end, but the remaining two expressions indicate a zero equivalent transverse displacement and zero equivalent rotation angle, respectively [Yao et al. 2009].

4. Bending of beams due to uniform pressure

To illustrate applications of the present symplectic approach, a beam subjected to a uniform pressure on the top surface is considered. The applied loading conditions in (1) are expressed as

$$\bar{F}_{x1} = 0, \quad \bar{F}_{z1} = -q_0, \quad \text{at } z = -h, \tag{24}$$

where p_0 is a constant independent of x. Substituting these conditions into (15) yields

$$(EI + 0.8k_p h^2)a_3^{(4)} - (k_p + 0.8k_w h^2)a_3^{(2)} + k_w a_3 = q_0, \tag{25}$$

for which a particular solution should be sought according to the foundation parameters. Combining (17)–(21) with (25) leads to the general solutions for a_3–a_6:

$$\underline{\text{Case 1}: k_w \neq 0} \quad \begin{cases} a_3 = c_1 e^{r_1 x} + c_2 e^{-r_1 x} + c_3 e^{r_2 x} + c_4 e^{-r_2 x} + q_0/k_w, \\ a_4 = c_1 r_1 e^{r_1 x} - c_2 r_1 e^{-r_1 x} + c_3 r_2 e^{r_2 x} - c_4 r_2 e^{-r_2 x}, \\ a_5 = \frac{1}{\tilde{E}}\left(c_1 M_1 e^{r_1 x} + c_2 M_1 e^{-r_1 x} + c_3 M_2 e^{r_2 x} + c_4 M_2 e^{-r_2 x}\right), \\ a_6 = \frac{1}{\tilde{E}}\left(c_1 M_1 r_1 e^{x} - c_2 M_1 r_1 e^{-r_1 x} + c_3 M_2 r_2 e^{r_2 x} - c_4 M_2 r_2 e^{-r_2 x}\right); \end{cases} \tag{26}$$

$$\underline{\text{Case 2: } k_w = 0, \, k_p \neq 0} \quad \begin{cases} a_3 = c_1 e^{r_1 x} + c_2 e^{-r_1 x} + c_3 + c_4 x - q_0 x^2 / 2k_p, \\ a_4 = c_1 r_1 e^{r_1 x} - c_2 r_1 e^{-r_1 x} + c_4 - q_0 x / k_p, \\ a_5 = \frac{1}{\bar{E}} M_1 (c_1 e^{r_1 x} + c_2 e^{-r_1 x}) + \frac{q_0}{\bar{E}} (0.4 h^2 - \bar{E}/k_p), \\ a_6 = \frac{1}{\bar{E}} M_1 r_1 (c_1 e^{r_1 x} - c_2 e^{-r_1 x}); \end{cases} \tag{27}$$

$$\underline{\text{Case 2: } k_w = 0, \, k_p = 0} \quad \begin{cases} a_3 = c_1 + c_2 x + c_3 x^2 + c_4 x^3 + \frac{q_0}{24EI} x^4. \\ a_4 = c_2 + 2c_3 x + 3c_4 x^2 + \frac{q_0}{6EI} x^3, \\ a_5 = 2c_3 + 6c_4 x + \frac{q_0}{2EI} x^2 + \frac{6q_0}{5EA}, \\ a_6 = 6c_4 + \frac{q_0}{EI} x; \end{cases} \tag{28}$$

where $M_1 = \bar{E} r_1^2 - 0.4 k_w h^2$ and $M_2 = \bar{E} r_2^2 - 0.4 k_w h^2$.

In this paper, three combinations of the typical end constraints in (21)–(23) are considered: clamped-clamped (CC), simply supported at both ends (SS), and clamped-free (CF). Incorporating these constraints into the three cases describing elastic foundations gives rise to an algebraic matrix equation governing the integral constants c_i:

$$\boldsymbol{D} \boldsymbol{c} = \boldsymbol{p}, \tag{29}$$

where $\boldsymbol{c} = [c_1 \ c_2 \ c_3 \ c_4]^T$. The explicit expressions of the coefficient matrix $\boldsymbol{D}$ and vector $\boldsymbol{p}$ for each beam in Cases 1 and 2 are given in the Appendix. Case 3 is exactly the case without an elastic foundation, for which the coefficients are simple and can be expressed explicitly. Hence the parameters a_3–a_6 are directly presented in the Appendix. From (29), the c_i are obtained as

$$c_i = \sum_{k=1}^{4} \frac{d_{ki}}{D} p_i, \tag{30}$$

where $d_{ki} = (-1)^{k+i} |\bar{\boldsymbol{D}}_{ki}|$ ($i = 1, 2, 3, 4$) is the algebraic complement of the element D_{ki}, $\bar{\boldsymbol{D}}_{ki}$ is obtained by eliminating the kth row and ith column of $\boldsymbol{D}$, and p_i is the element of $\boldsymbol{p}$.

5. Numerical comparisons and discussions

To validate the rationality, accuracy, and effectiveness of this symplectic elasticity approach, comparisons are presented for slender beams $l \gg 2h$ on an elastic foundation. For generality and brevity, the following nondimensional parameters and variables are introduced:

$$(U, W) = \frac{(u, w) EI}{q_0 l^4}, \quad X = \frac{\sigma_x}{q_0}, \quad K_w = \frac{k_w l^4}{EI}, \quad K_p = \frac{k_p l^2}{EI}.$$

In all examples, the Poisson's ratio is taken as $\nu = 0.3$.

Bending of beams without elastic foundation. As a first attempt, the bending behavior of beams without elastic foundations ($K_w = K_p = 0$) is considered, and the solutions are compared with results from other methods. Figure 2 shows the longitudinal distributions of nondimensional transverse displacements $W(x, 0)$ at the neutral line and the axial normal stress $X(x, h)$ at the lower surface of CC beams with different aspect ratios. The figures show that the present results (solid lines) agree well with the results obtained using the semianalytic method (dashed lines) in [Chen et al. 2004] based on two-dimensional
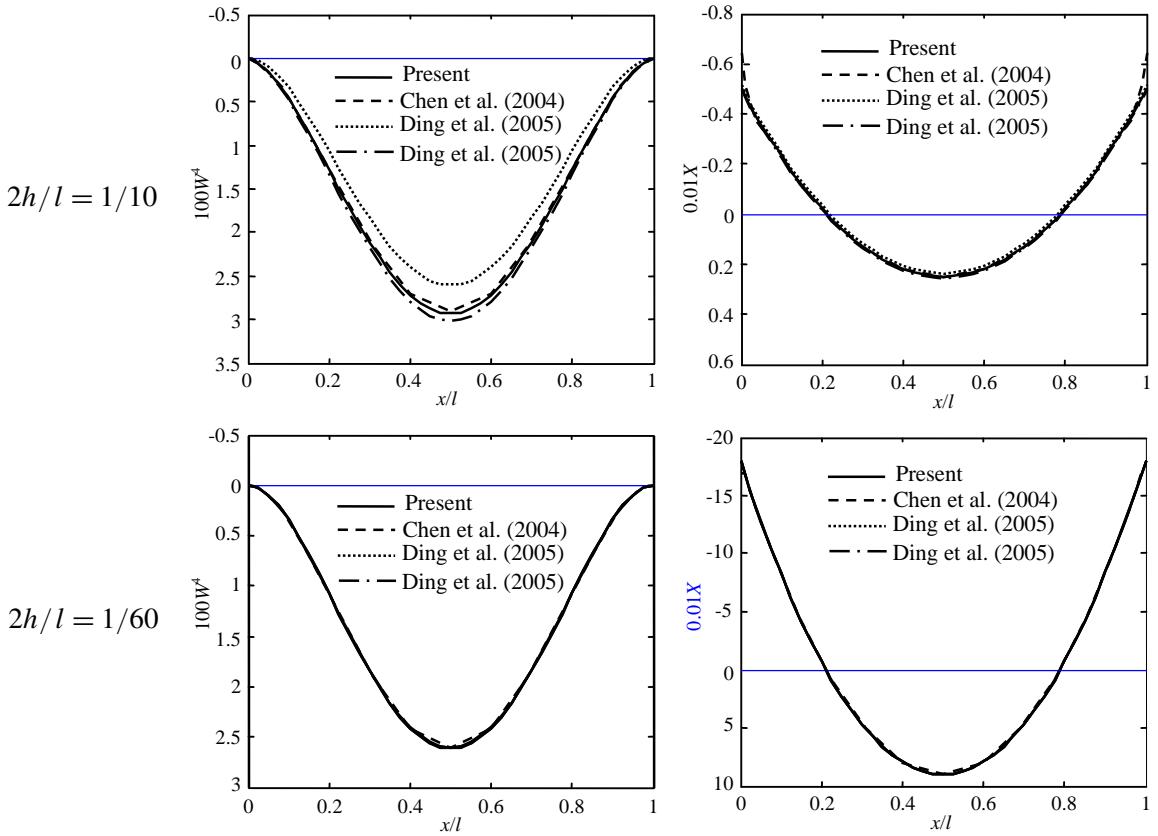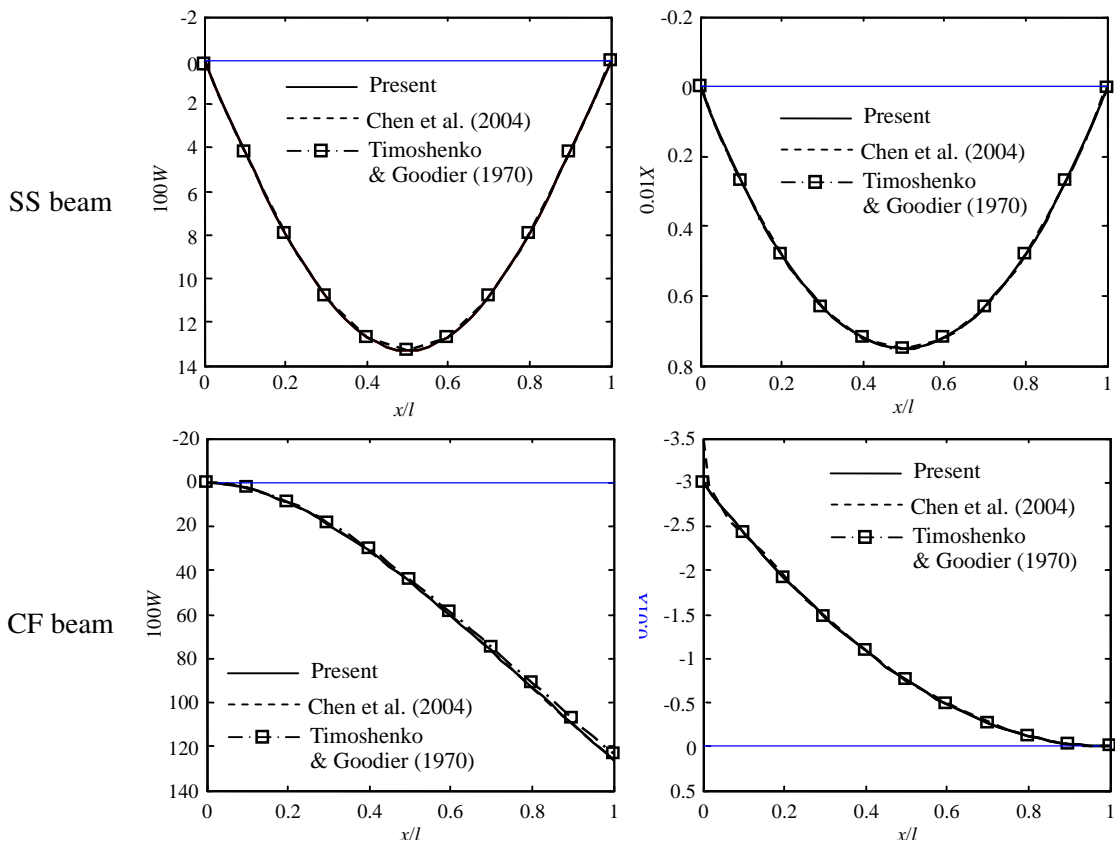
Figure 2. Deflection curves $W(x, 0)$ and longitudinal axial normal stresses $X(x, h)$ for CC beams without elastic foundations ($K_w = K_p = 0$).

elasticity theory without invoking assumptions regarding the deformations and stresses. We emphasize a comparison of these results with those of Ding et al. [2005], who used the Airy stress function based on two-dimensional elasticity theory. They considered two kinds of constraint conditions for clamped ends, as described in [Timoshenko and Goodier 1970]:

$$\frac{\partial w}{\partial x} = 0 \quad \text{and} \quad \frac{\partial u}{\partial z} = 0.$$

Figure 2 illustrates the results corresponding to these two end conditions, with dotted lines for the first condition and dash-dot lines for the second. For the case $2h/l = 1/10$, the present result is significantly larger than the analytic solution for the first type of clamped end, but is somewhat smaller than the analytic solution for the second type. This indicates that the present constraints of zero equivalent transverse displacement and rotation angle for a clamped end in (25) are looser than the first type of clamped end in [Timoshenko and Goodier 1970] but a little stiffer that the second type. For more slender beams, the differences between the three types of end constraints for clamped ends are small, and, hence, the results are almost identical, as can be seen in Figure 2, bottom.

Figure 3. Deflection curves $W(x, 0)$ and longitudinal axial normal stresses $X(x, h)$ for SS and CF slender beams ($2h/l = 1/10$) without elastic foundations ($K_w = K_p = 0$).
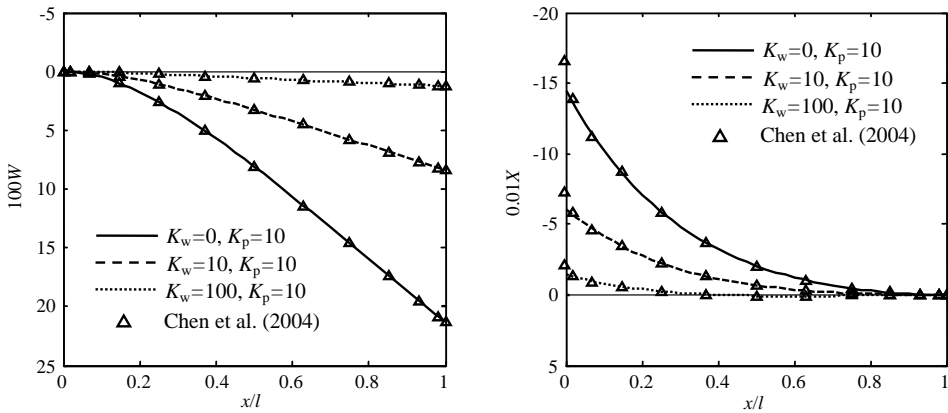
Figure 3 shows the longitudinal distributions of the transverse displacement $W(x, 0)$ at the neutral line and axial normal stress $X(x, h)$ at the lower surface of the SS and CF beams ($2h/l = 10$). The Saint-Venant solutions of [Timoshenko and Goodier 1970] and the semianalytic elasticity solutions of [Chen et al. 2004] are also shown for comparison. As can be seen, the accuracy of the present method is again validated for slender beams.

Bending of beams on elastic foundations. We now assess the correctness of the symplectic formulation for beams resting on elastic foundations by comparison with the numerical results from the literature. Table 1 presents the nondimensional midspan deflection $W(0.5l, 0)$ for uniformly loaded SS and CC beams on an elastic foundation with different values of K_w and K_p. The semianalytic and exact solutions of [Chen et al. 2004], based on two-dimensional elasticity theory, are also listed for comparison. The results presented here, for all beams in consideration, compare well to the semianalytic results. A careful comparison shows that, for a moderately thick SS beam ($2h/l = 1/5$), the present results agree better with the exact solutions than with the semianalytic solutions.

Figure 4 plots the deflection $W(x, 0)$ at the midplane and the axial normal stresses $X(x, h)$ at the bottom surface of a cantilever (CF) beam on an elastic foundation with different values of K_w ($K_p = 10$).

	K_w	K_p	simply supported			clamped-clamped	
			present	semiana.	exact	present	semiana.
$2h/l = 1/15$	0	0	1.31528	1.315277	1.315271	0.27500	0.27493
		10	0.64831	0.648347	0.648299	0.21902	0.21893
		25	0.36736	0.367416	0.367353	0.16820	0.16811
	10	0	1.19135	1.191402	1.191335	0.26925	0.26921
		10	0.61650	0.616562	0.616485	0.21533	0.21526
		25	0.35685	0.356923	0.356843	0.16600	0.16593
	100	0	0.64344	0.643767	0.643428	0.22653	0.22662
		10	0.42717	0.427409	0.427156	0.18697	0.18701
		25	0.28361	0.283799	0.283603	0.14851	0.14853
$2h/l = 1/5$	0	0	1.42083	1.420261	1.420243	0.39170	0.38814
		10	0.67565	0.678202	0.674505	0.29722	0.29426
		25	0.37711	0.381703	0.376671	0.21910	0.21760
	10	0	1.27829	1.282598	1.277311	0.38014	0.37817
		10	0.64134	0.646391	0.640247	0.29045	0.28874
		25	0.36608	0.372064	0.365680	0.21536	0.21478
	100	0	0.66969	0.696100	0.668478	0.29999	0.30908
		10	0.43944	0.459267	0.438808	0.24086	0.24823
		25	0.28957	0.305161	0.289436	0.18662	0.19299

Table 1. Midspan deflection $W(0.5l, 0)$ of uniformly loaded SS and CC beams.

Figure 4. Longitudinal distributions of the deflection $W(x, 0)$ and axial normal stress $X(x, h)$ of a cantilever (CF) beam on an elastic foundation ($2h/l = 1/15$).

For numerical comparison, the semianalytic method in [Chen et al. 2004], based on two-dimensional elasticity theory, is applied here to calculate the semianalytic solutions, as denoted by the upward triangle markers in Figure 4. Excellent agreement is once again observed, further demonstrating the rationality and accuracy of the present symplectic method.

6. Conclusions

The symplectic elasticity approach, which has been widely used in theoretical physics, is applied in this paper to derive analytic elasticity solutions for beams resting on Pasternak foundations. The Legendre transformation is adopted to transform the Lagrangian system, based on the minimum potential energy principle, to the Hamiltonian symplectic dual system. An eigenvalue problem with respect to the transverse cross section is, then, solved using the method of separation of variables. Saint-Venant solutions to the problem are obtained by considering the eigensolutions of zero eigenvalue. The effects of applied loading conditions and elastic foundations are treated as the boundary conditions. Together with the end constraints, the problem is formulated using the Hamiltonian variational principle.

Analytic Saint-Venant solutions for beams with different end constraints and on Pasternak foundations are presented. A comparison of the present results with those available in the literature are conducted, and, hence, the applicability and efficiency of the present symplectic approach for slender beams on elastic foundations are validated. It should be emphasized that the symplectic approach can be applied to study arbitrarily thick beams if nonzero eigenvalues are considered in the solution expansion, which will be a subject to be explored in the future.

Appendix: Expressions of the matrix D and vectors p and c

(Recall that $Dc = p$. See page 1747 for discussion. Except for the case $k_w = k_p = 0$, we give D and p, from which c can be derived.)

<u>Case 1</u>: $k_w \neq 0$

CC beams:

$$D = \begin{bmatrix} \tilde{E}-\lambda M_1 & \tilde{E}-\lambda M_1 & \tilde{E}-\lambda M_2 & \tilde{E}-\lambda M_2 \\ (\tilde{E}+\lambda M_1)r_1 & -(\tilde{E}+\lambda M_1)r_1 & (\tilde{E}+\lambda M_2)r_2 & -(\tilde{E}+\lambda M_2)r_2 \\ (\tilde{E}-\lambda M_1)e^{r_1 l} & (\tilde{E}-\lambda M_1)e^{-r_1 l} & (\tilde{E}-\lambda M_2)e^{r_2 l} & (\tilde{E}-\lambda M_2)e^{-r_2 l} \\ (\tilde{E}+\lambda M_1)r_1 e^{r_1 l} & -(\tilde{E}+\lambda M_1)r_1 e^{-r_1 l} & (\tilde{E}+\lambda M_2)r_2 e^{r_2 l} & -(\tilde{E}+\lambda M_2)r_2 e^{-r_2 l} \end{bmatrix}, \quad p = -\frac{\tilde{E} q_0}{k_w} \begin{Bmatrix} 1 \\ 0 \\ 1 \\ 0 \end{Bmatrix}.$$

SS beams:

$$D = \begin{bmatrix} 1 & 1 & 1 & 1 \\ M_1 & M_1 & M_2 & M_2 \\ e^{r_1 l} & e^{-r_1 l} & e^{r_2 l} & e^{-r_2 l} \\ M_1 e^{r_1 l} & M_1 e^{-r_1 l} & M_2 e^{r_2 l} & M_2 e^{-r_2 l} \end{bmatrix}, \quad p = -\frac{q_0}{k_w} \begin{Bmatrix} 1 \\ 0 \\ 1 \\ 0 \end{Bmatrix}.$$

CF beams:

$$D = \begin{bmatrix} \tilde{E}-\lambda M_1 & \tilde{E}-\lambda M_1 & \tilde{E}-\lambda M_2 & \tilde{E}-\lambda M_2 \\ (\tilde{E}+\lambda M_1)r_1 & -(\tilde{E}+\lambda M_1)r_1 & (\tilde{E}+\lambda M_2)r_2 & -(\tilde{E}+\lambda M_2)r_2 \\ M_1 e^{r_1 l} & M_1 e^{-r_1 l} & M_2 e^{r_2 l} & M_2 e^{-r_2 l} \\ M_1 r_1 e^{r_1 l} & -M_1 r_1 e^{-r_1 l} & M_2 r_2 e^{r_2 l} & -M_2 r_2 e^{-r_2 l} \end{bmatrix}, \quad p = -\frac{\tilde{E} q_0}{k_w} \begin{Bmatrix} 1 \\ 0 \\ 0 \\ 0 \end{Bmatrix}.$$

Case 2: $k_w = 0$, $k_p \neq 0$

CC beams:

$$\boldsymbol{D} = \begin{bmatrix} \tilde{E} - \lambda M_1 & \tilde{E} - \lambda M_1 & \tilde{E} & 0 \\ (\tilde{E} + \lambda M_1)r_1 & -(\tilde{E} + \lambda M_1)r_1 & 0 & \tilde{E} \\ (\tilde{E} - \lambda M_1)e^{r_1 l} & (\tilde{E} - \lambda M_1)e^{-r_1 l} & \tilde{E} & \tilde{E}l \\ (\tilde{E} + \lambda M_1)r_1 e^{r_1 l} & -(\tilde{E} + \lambda M_1)r_1 e^{-r_1 l} & 0 & \tilde{E} \end{bmatrix}, \qquad \boldsymbol{p} = \frac{q_0}{k_p} \begin{Bmatrix} -\lambda \hat{E} \\ 0 \\ \frac{1}{2}\tilde{E}l^2 - \lambda \hat{E} \\ \tilde{E}l \end{Bmatrix},$$

where $\hat{E} = \bar{E} - 0.4 k_p h^2$.

SS beams:

$$\boldsymbol{D} = \begin{bmatrix} 1 & 1 & 1 & 0 \\ M_1 & M_1 & 0 & 0 \\ e^{r_1 l} & e^{-r_1 l} & 1 & l \\ M_1 e^{r_1 l} & M_1 e^{-r_1 l} & 0 & 0 \end{bmatrix}, \qquad \boldsymbol{p} = \frac{q_0}{k_p} \begin{Bmatrix} 0 \\ \hat{E} \\ l^2/2 \\ \hat{E} \end{Bmatrix}.$$

CF beams:

$$\boldsymbol{D} = \begin{bmatrix} \tilde{E} - \lambda M_1 & \tilde{E} - \lambda M_1 & \tilde{E} & 0 \\ (\tilde{E} + \lambda M_1)r_1 & -(\tilde{E} + \lambda M_1)r_1 & 0 & \tilde{E} \\ M_1 e^{r_1 l} & M_1 e^{-r_1 l} & 0 & 0 \\ M_1 r_1 e^{r_1 l} & -M_1 r_1 e^{-r_1 l} & 0 & 0 \end{bmatrix}, \qquad \boldsymbol{p} = \frac{q_0}{k_p} \begin{Bmatrix} -\lambda \hat{E} \\ 0 \\ \hat{E} \\ 0 \end{Bmatrix}.$$

Case 3: $k_w = 0$ and $k_p = 0$

CC beams:

$$a_3 = \frac{q_0}{24EI}(x - l)^2 x^2 - \frac{(1 + v)q_0}{10EA}(6x^2 - 6lx - l^2) - \frac{6v(1 + v)\lambda q_0}{5EA},$$

$$a_4 = \frac{3(1 + v)q_0}{5EA}(l - 2x) + \frac{q_0}{12EI}(2x - l)(x - l)x,$$

$$a_5 = -\frac{6v(1 + v)q_0}{5EA} + \frac{q_0}{12EI}(6x^2 - 6lx + l^2),$$

$$a_6 = \frac{q_0}{2EI}(2x - l),$$

SS beams:

$$a_3 = \frac{3q_0}{5EA}(l - x)x + \frac{q_0}{24EI}[(l + x)l - x^2](l - x)x,$$

$$a_4 = \frac{3q_0}{5EA}(l - 2x) + \frac{q_0}{24EI}(l^3 - 6lx^2 + 4x^3),$$

$$a_5 = \frac{q_0}{2EI}(x - l)x,$$

$$a_6 = \frac{q_0}{2EI}(2x - l).$$

CF beams:

$$a_3 = \frac{3q_0}{5EA}[(1+\nu)(l+2x)l-x^2] + \frac{q_0}{24EI}(x^2-4lx+6l^2)x^2,$$

$$a_4 = \frac{6q_0}{5EA}[(1+\nu)l-x] + \frac{q_0}{6EI}(x^2-3lx+3l^2)x,$$

$$a_5 = \frac{q_0}{2EI}(x-l)^2,$$

$$a_6 = \frac{q_0}{EI}(x-l).$$

References

[Chen et al. 2004] W. Q. Chen, C. F. Lü, and Z. G. Bian, "A mixed method for bending and free vibration of beams resting on a Pasternak elastic foundation", *Appl. Math. Model.* **28**:10 (2004), 877–890.

[De Rosa and Maurizi 1998] M. A. De Rosa and M. J. Maurizi, "The influence of concentrated mass and Pasternak soil on the free vibrations of Euler beams – Exact solution", *J. Sound Vib.* **212**:4 (1998), 573–581.

[Ding et al. 2005] H. J. Ding, D. J. Huang, and W. Q. Chen, "Analytical solution for fixed-fixed beam subjected to uniform load", *J. Zhejiang Univ. SCI.* **6A**:8 (2005), 779–783.

[Franciosi and Masi 1993] C. Franciosi and A. Masi, "Free vibrations of foundation beams on 2-parameter elastic soil", *Comput. Struct.* **47**:3 (1993), 419–426.

[Frostig et al. 1992] Y. Frostig, M. Baruch, O. Vilnay, and I. Sheinman, "Higher-order theory for sandwich-beam behavior with transversely flexible core", *ASCE J. Eng. Mech.* **118**:5 (1992), 1026–1043.

[Lee et al. 2003] Y. Y. Lee, C. M. Wang, and S. Kitipornchai, "Vibration of Timoshenko beams with internal hinge", *J. Eng. Mech.* **129**:3 (2003), 293–301.

[Leissa 1973] A. W. Leissa, "The free vibration of plates", *J. Sound Vib.* **31**:3 (1973), 257–293.

[Lim 1999] C. W. Lim, "Three-dimensional vibration analysis of a cantilevered parallelepiped: exact and approximate solutions", *J. Acoust. Soc. Am.* **106**:6 (1999), 3375–3381.

[Lim et al. 2007] C. W. Lim, S. Cui, and W. A. Yao, "On new symplectic elasticity approach for exact bending solutions of rectangular thin plates with two opposite sides simply supported", *Int. J. Solids Struct.* **44**:16 (2007), 5369–5411.

[Lim et al. 2008] C. W. Lim, W. A. Yao, and S. Cui, "Benchmarks of analytical symplectic solutions for bending of corner-supported rectangular thin plates", *IES J. Part A* **1**:3 (2008), 106–115.

[Matsunaga 2000] H. Matsunaga, "Vibration and stability of thick plates on elastic foundations", *ASCE J. Eng. Mech.* **126**:1 (2000), 27–34.

[Pasternak 1954] P. L. Pasternak, *On a new method of analysis of an elastic foundation by means of two foundation constants* (in Russian), Gosudarstrennoe Izdatelstvu Literaturi po Stroitelstvu I Arkhitekture, Moscow, 1954.

[Reddy 1984] J. N. Reddy, "A simple higher-order theory for laminated composite plates", *ASME J. Appl. Mech.* **51**:4 (1984), 745–752.

[Sankar 2001] B. V. Sankar, "An elasticity solution for functionally graded beams", *Compos. Sci. Technol.* **61**:5 (2001), 689–696.

[Shirima and Giger 1992] L. M. Shirima and M. W. Giger, "Timoshenko beam element resting on two-parameter elastic foundation", *ASCE J. Eng. Mech.* **118**:3 (1992), 280–295.

[Sullivan and Vanoene 1986] J. L. Sullivan and H. Vanoene, "An elasticity analysis for the generally and specially orthotropic beams subjected to concentrated loads", *Compos. Sci. Technol.* **27**:3 (1986), 133–155.

[Timoshenko 1921] S. P. Timoshenko, "On the correction for shear of the differential equation for transverse vibrations of prismatic bars", *Philos. Mag.* **41**:6 (1921), 744–746.

[Timoshenko and Goodier 1970] S. P. Timoshenko and J. N. Goodier, *Theory of elasticity*, McGraw-Hill, London, 1970.

[Wang et al. 1998] C. M. Wang, K. Y. Lam, and X. Q. He, "Exact solutions for Timoshenko beams on elastic foundations using Green's functions", *Mech. Struct. Mach.* **26**:1 (1998), 101–113.

[Weyl 1939] H. Weyl, *The classical groups, their invariants and representations*, Princeton University Press, 1939.

[Whitney 1985] J. M. Whitney, "Elasticity analysis of orthotropic beams under concentrated loads", *Compos. Sci. Technol.* **22**:3 (1985), 167–184.

[Yao et al. 2009] W. A. Yao, W. X. Zhong, and C. W. Lim, *Symplectic elasticity*, World Scientific, Singapore, 2009.

C. F. LÜ: lucf@zju.edu.cn
Department of Civil Engineering, Zhejiang University, Hangzhou 310058, China

C. W. LIM: bccwlim@cityu.edu.hk
Department of Building and Construction, City University of Hong Kong, Tat Chee Avenue, Kowloon, Hong Kong

W. A. YAO: ywa@dlut.edu.cn
State Key Laboratory of Structural Analysis for Industrial Equipment and Department of Engineering Mechanics, Dalian University of Technology, Dalian 116024, China

NUMERICAL SIMULATION OF RAM EXTRUSION IN SHORT-FIBER-REINFORCED FRESH CEMENTITIOUS COMPOSITES

XIANGMING ZHOU AND ZONGJIN LI

A series of ram extrusion tests was carried out on a short-fiber-reinforced, semisolid, fresh cementitious composite. An elastoviscoplastic constitutive model is proposed for the extrudable fresh cementitious composite. It features the associative flow rule, a nonlinear strain rate-hardening law, and the von Mises yield criterion. The model is then implemented in ANSYS/LS-DYNA explicit finite element code.

Various ram extrusion processes of the fresh cementitious composite were simulated. It has been found that the extrusion load versus imposed displacement predictions agree well with the experimental results. The fresh paste flow, through the die entry and the die-land, is then interpreted in light of the evolution of the deformation and distribution of state variables, mainly based on numerical results and the ram extrusion mechanism.

The effects of extrusion ratio and extrusion velocity on extrusion load are also investigated, based on the mechanical properties of the fresh cementitious composite. The study indicates that the numerical procedure established, together with the constitutive model proposed, is applicable for describing ram extrusion of short-fiber-reinforced fresh cementitious composites, which might provide a numerical rheometric tool from which ram extrusion of elastoviscoplastic paste-like materials can be examined and quantified.

1. Introduction

Extrusion is a material processing technology for manufacturing semisolid paste-like products used in the mechanical, chemical, ceramic, food, and pharmaceutical industries. In the last two decades, it has been applied in the concrete industry as an economical, efficient, and environmentally friendly manufacturing method for short-fiber-reinforced cement-based construction materials and products [Shao et al. 1995; Shao and Shah 1997; Aldea et al. 1998; Li and Mu 1998; Li et al. 1999; 2001; 2004; Peled and Shah 2003]. Compared with the traditional concrete casting method, extrusion techniques can significantly improve the mechanical properties of the final products through the high shear and high compression processing environment within an extruder [Shao et al. 1995; Peled and Shah 2003].

There are two main extrusion methods: the continuous screw-driven method (screw extrusion) and the intermittent piston-driven method (ram extrusion). The screw-driven method allows continuous production. However, it is not generally suitable for small batch runs because of difficulties in cleaning the extruder [Aydin et al. 2000]. It may not even be possible for some materials, such as metal alloys, due to limitations in rheology. On the other hand, ram extrusion is favored for short runs and accurate
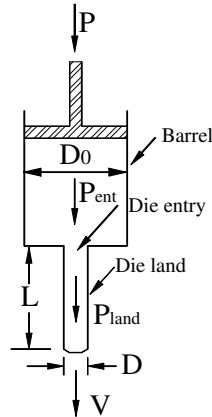
Figure 1. Schematic diagram of Benbow–Bridgwater ram extrusion mechanism.

dimensional control [Aydin et al. 2000]. In this method, a piston drives the highly viscous, semisolid fresh paste to flow through a die entry and then a die-land, thereby reducing the cross-sectional area of the paste and shaping it as desired.

Axisymmetric ram extrusion with a circular die entry, as shown in Figure 1, is a simple but effective method for tailoring mix proportions for an extrudable fiber-reinforced cementitious composite [Srinivasan et al. 1999; Zhou and Li 2005a]. The most widely used model for analyzing this type of ram extrusion data is based on a relationship known as the Benbow–Bridgwater equation [1993]:

$$P = P_{\text{ent}} + P_{\text{land}} = 2\ln\left(\frac{D_0}{D}\right)(\sigma_0' + \alpha V_p^j) + \frac{4L}{D}(\tau_0' + \beta V_p^q), \tag{1-1}$$

where, as shown in Figure 1, P is the overall pressure drop; the first term on the right in (1-1) is the die entry pressure drop, P_{ent}, representing that a plastic flow dominates at the die entry; the second term, P_{land}, is the die-land pressure drop, representing a slip flow in the die-land; D_0 is the barrel diameter; D is the die-land diameter; L is the die-land length; V_p is the mean paste flow velocity in the die-land; σ_0' is the initial die entry yield stress when the paste velocity approaches zero; α is the die entry yield stress velocity factor; j is an exponent that accounts for the nonlinear velocity dependence of the plastic flow in the die entry; τ_0' is the initial die-land wall shear stress as the paste velocity approaches zero; β is the die-land shear stress velocity factor, which accounts for the increase of the die-land wall shear stress with increasing paste flow velocity; and q is an exponent that accounts for the nonlinear velocity dependence of the shear flow in the die-land. Note that σ_0', α, j, τ_0', β, and q are not necessarily material parameters of the paste itself.

Though the Benbow–Bridgwater equation provides reasonably satisfactory ram extrusion predictions — mainly the relationship between the overall extrusion pressure drop and the mean paste flow velocity — for many paste-like materials, such as ceramics and clays [Benbow et al. 1991; Benbow and Bridgwater 1993; Blackburn and Böhm 1994; Chou et al. 2003], it is basically a phenomenological model rather than a constitutive model for the ram extrusion process. It can only give an overall description of paste flow in a ram extruder with simple symmetrical geometry, based on the assumption of simple rigid plastic or rigid-viscoplastic material behavior for the paste. The ram extrusion process of paste-like materials with

elastoviscoplastic constitutive behavior, in a nonaxisymmetric geometry, is difficult to directly describe with the Benbow–Bridgwater model. In this case, only numerical methods can give a full description of the ram extrusion process of materials exhibiting complicated elastoviscoplastic behavior.

In this study, a ram extrusion process using a short-fiber-reinforced, semisolid, fresh cementitious composite, with a circular die entry and die-land, is investigated through experimental as well as numerical analysis. The extrusion load versus the imposed ram displacement data, the evolution of the deformation, and the distribution of state variables within the paste flow are obtained through numerical simulation based on the ANSYS/LS-DYNA explicit finite element code, combined with an elastoviscoplastic constitutive model for the highly concentrated, short-fiber-reinforced fresh cementitious composite. Explicit analysis has been regarded as a more efficient solution than implicit analysis for large-deformation problems, such as material forming processes like extrusion [Antúnez 2000]. The numerical procedure and the constitutive model are mainly verified quantitatively by comparing numerical and experimental results with the extrusion load versus imposed ram displacement data. Then, the evolution of the deformation and state variables within the composite during the ram extrusion process is interpreted based on the numerical results and the ram extrusion mechanism. The effects of the extrusion ratio, the ratio between the area of the barrel and that of the die-land, and the extrusion velocity, the ram driving velocity, on the extrusion load are investigated based on the experimental and numerical results. The aim of this research is to test the applicability of the numerical procedure, combined with the elastoviscoplastic constitutive model, for describing the ram extrusion process of a short-fiber-reinforced, semisolid, fresh cementitious composite. The verified numerical procedure might also be used for modeling the forming processes of other paste-like materials, exhibiting elastoviscoplastic behavior, as well as for design and optimization of materials processing equipment.

2. Experimental

The experimental program within the scope of this study is essentially divided into two parts. The first part involves rheological measurements to establish an appropriate constitutive model for the extrudable fresh cementitious composite, through orifice and capillary extrusion [Zhou 2004; Zhou and Li 2005b] and upsetting tests [Zhou and Li 2006]. The second part involves ram extrusion tests of the fresh cementitious composite under various extrusion conditions, that is, extrusion ratios and/or extrusion velocities, that may appear in practice, from which the applied extrusion load with respect to the imposed ram displacement data are obtained. Both parts of the experimental program are carried out on the short-fiber-reinforced fresh cementitious composite with mix formulation shown in Table 1. The basic constitutive compositions include ordinary Portland cement and slag with a weight ratio of 1:1 as the cementitious

Cement	Slag	SS1	SS2	PVA	Methocel	ADVA	W/B
0.5	0.5	0.2	0.125	2%	1%	0.375%	0.27

Table 1. Mix formulation for the short-fiber-reinforced fresh cementitious composite used for extrusion (see text at the top of the next page for abbreviations). SS1, SS2, Methocel, and ADVA are presented in the weight ratio of the binder. PVA fiber is presented in the volume ratio of the paste.

binder; 6 mm long polyvinyl alcohol (PVA) fiber with an average diameter of 14 μm; two types of silica sands (denoted SS1 and SS2, with a nominal diameter of 300–600 μm and 90–150 μm, respectively) from David Ball Comp. Ltd with a weight ratio of 8:5 as aggregates; Methocel powder, produced by Dow Chemical Comp. Ltd, as a rheology enhancer; and ADVA solution, made by W. R. Grace (HK) Ltd, as a superplasticizer. The water-to-binder weight ratio is 0.27 while the silica sands-to-binder weight ratio is 0.325. The dosage of ADVA solid powder is 0.375% of the weight of the binder and it is incorporated into the composite in the form of an aqueous solution with a concentration of 30% by weight as supplied by the manufacturer. The total volume of PVA fibers incorporated is 2% of that of the readily mixed composite.

The mix formulation shown in Table 1 is a typical recipe for an extrudable shore fiber-reinforced cementitious composite [Srinivasan et al. 1999; Zhou and Li 2005a; 2005b]. To prepare the fresh cementitious composite for extrusion, cementitious binders (cement and slag), fibers, and Methocel powder are first mixed for 3 minutes in a dry state at a low speed by a Hobart planetary mixer. Then water, with ADVA superplasticizer solution, is added into the mixture and mixed for another 3 minutes. Once the dry powders are moistened, a higher speed is adjusted to for 3 minutes high shear mixing till a dough-like paste is produced. This dough-like paste is then used for various experiments, including orifice extrusion, capillary extrusion, ram extrusion, and upsetting tests as referred to in this study.

Note that short-fiber-reinforced fresh cementitious composites for extrusion purposes are largely different from traditional cement paste, mortar, suspension, slurry, fresh self-compacting concrete, and other fresh concretes which normally have larger water-to-binder ratios and better fluidity. Fresh cementitious composites for extrusion purposes are dough-like, have almost no fluidity, and exhibit high cohesion and pseudoplastic behavior under normal conditions [Srinivasan et al. 1999; Zhou and Li 2005a; Li and Li 2007]. Though a number of extrusion practices have been successfully performed, little research has been carried out on the rheological behavior of extrudable fresh cementitious composites and the extrusion process itself.

Material tests and rheological measurements. The experimental setup and procedures for orifice and capillary extrusion have been presented in [Zhou 2004; Zhou and Li 2005b] while those for upsetting tests have been reported in detail in [Zhou and Li 2006]. Based on these studies, the steady-state postyield constitutive behavior of an extrudable short-fiber-reinforced fresh cementitious composite has been formulated from which the shear flow stress, τ, is plotted as a function of the plastic shear strain rate, $\dot{\gamma}^{\mathrm{vp}}$. The postyield shear flow behavior of the extrudable fresh cementitious composite has been found to be satisfactorily described by the Herschel–Bulkley model [Zhou and Li 2005b] in the form

$$\tau = \tau_0 + k_{\mathrm{sc}}(\dot{\gamma}^{\mathrm{vp}})^m, \tag{2-1}$$

where τ_0 is the static shear yield stress, and k_{sc} and m are the shear plastic flow consistency and the shear flow index, respectively. The values of the material parameters in (2-1) have been obtained through orifice and capillary extrusion tests as $\tau_0 = 2.15$ kPa, $k_{\mathrm{sc}} = 4.17$ kPa·s^m, and $m = 0.38$ [Zhou 2004; Zhou and Li 2005b]. Prior to yielding, the fresh cementitious composite exhibits elastic behavior with a constant Young's modulus of $E = 8$ kPa, which is obtained from its true stress versus true strain curve through upsetting tests presented in [Zhou and Li 2006].

Ram extrusion.   The experimental setup and procedure for ram extrusion are similar to those described in [Zhou and Li 2005a], but different extrusion conditions are investigated in this research. The results of these tests are utilized to evaluate the applicability of the numerical procedure presented in this paper, combined with the elastoviscoplastic constitutive model, for describing the ram extrusion process for fresh cementitious composite.

The experimental setup for ram extrusion is shown in Figure 2, where a homemade ram extruder, with smooth-surface stainless steel barrel and die, is mounted in a servohydraulic materials test system machine. Before extrusion, a certain amount of readily prepared, highly concentrated, dough-like fresh cementitious composite is fed into the barrel, with an inner diameter of 80 mm, of the extruder up to its brim. After this, the ram extrusion test starts, and the paste inside the barrel is driven by the ram with a constant velocity till it flows out of the die exit in a steady state.

Three sets of dies, with diameters of 8 mm, 12 mm, and 15 mm, are used in the experiment, resulting in extrusion ratios of 100, 44.4, and 28.4, respectively. The die-land lengths are truncated to obtain die-land length-to-diameter ratios, L/D, of 0.83 and 4.79 for each set of dies. A series of tests with various extrusion velocities are conducted, representing a broad range of apparent strain rates imposed on the fresh composite. During extrusion, the data acquisition system records ram displacement, time, and extrusion load. Each test is repeated three times and the average values are taken as representative results.

A typical experimental output on the variation of extrusion load with imposed ram displacement is shown in Figure 3 on the next page. In the initial stage when the ram pushes the fresh cementitious composite against the die-land, the composite undergoes upsetting, which leads to a rapid increase in
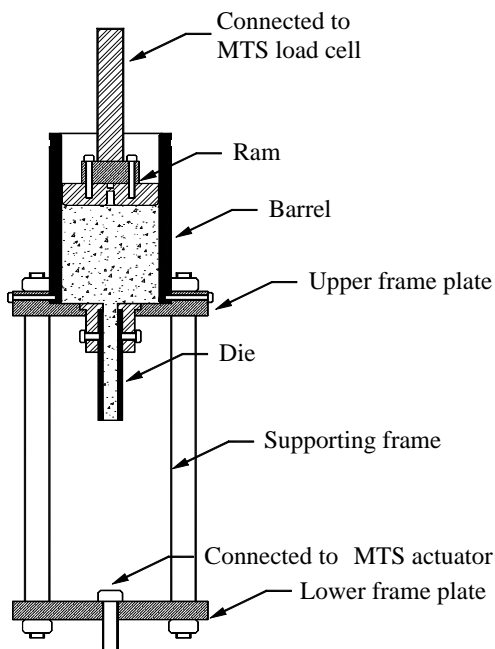
Figure 2. Experimental setup of the ram extrusion test: schematic diagram and laboratory apparatus.
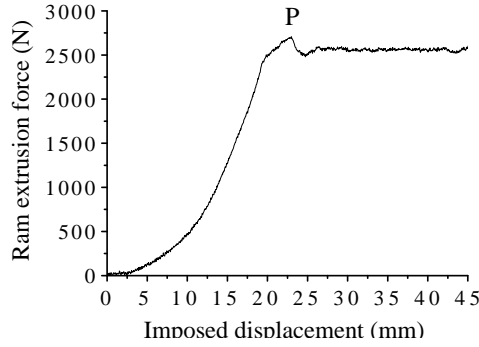
Figure 3. A typical ram extrusion load versus imposed displacement curve from the experiment.

extrusion load until it attains a peak value (point P in Figure 3), where the paste breaks through the die exit. After this breakthrough, the extrusion load decreases, which is due to the reduction of the contact area, and thus friction, between the composite and the barrel. The experimental data, after the breakthrough, clearly demonstrates the attainment of a steady state extrusion (stable plateau value of the extrusion load).

3. Numerical simulation

Constitutive model and associated material parameters. A time-continuous model normally forms the basis for the constitutive equations in numerical simulations of elastoviscoplastic material behavior [Lof and van den Boogaard 2001]. In the time-continuous model, the relation between stress and strain, in both the elastic and the plastic domains, is usually defined in a rate formulation. Based on infinitesimal deformation theory, it is reasonable to assume that the rate of deformation can be additively decomposed into an elastic (reversible) part and an inelastic (irreversible) part, so that the total strain rate, $\dot{\varepsilon}$, can be expressed as $\dot{\varepsilon} = \dot{\varepsilon}^{\text{el}} + \dot{\varepsilon}^{\text{vp}}$, where $\dot{\varepsilon}^{\text{el}}$ and $\dot{\varepsilon}^{\text{vp}}$ represent the elastic and viscoplastic strain rates, respectively. By assuming isotropic material behavior, the elastic part is treated as linear and is expressed in Cartesian index notation as

$$\dot{\varepsilon}_{ij}^{\text{el}} = \frac{1+\nu}{E}\dot{S}_{ij} + \frac{1-2\nu}{3E}\dot{\sigma}_{kk}\delta_{ij}, \tag{3-1}$$

where E is the Young's modulus, ν is the Poisson's ratio, $\dot{\sigma}$ is the rate of change of stress, and $\dot{S}$ is the rate of change of deviatoric stress. A constant Poisson's ratio, $\nu = 0.465$, which is somewhat arbitrary, is incorporated in the constitutive model to represent nearly incompressible material behavior, which has been found to be a reasonable assumption for this highly viscous paste-like material for extrusion purposes [Zhou 2004; Zhou and Li 2006].

It has been found that the constitutive behavior of highly concentrated short-fiber-reinforced fresh cementitious paste for extrusion purposes is dominated by rheological (strain rate-dependent) effects once it deforms inelastically [Srinivasan et al. 1999; Zhou and Li 2005a; 2006; Li and Li 2007]. For simplicity, it is further assumed that the isotropic strain rate-hardening law is sufficient to describe the evolution of the flow stress of the extrudable fresh cementitious composite during plastic deformation. The strain rate-hardening law is formulated in terms of the equivalent viscoplastic strain rate, $\bar{\dot{\varepsilon}}^{\text{vp}}$. Assuming an associative J_2 plastic flow where J_2 is the second invariant of the deviatoric stress tensor, the von Mises

yield criterion is used to define the equivalent flow stress, $\bar{\sigma}$. Extending the notion of associative plasticity to viscoplasticity, the viscoplastic strain rate is assumed to be in the direction of the deviatoric stress, S, and is defined as

$$\dot{\varepsilon}^{\mathrm{vp}} = \frac{3}{2} \bar{\dot{\varepsilon}}^{\mathrm{vp}} \frac{S}{\bar{\sigma}}, \tag{3-2}$$

where the equivalent viscoplastic strain rate, $\bar{\dot{\varepsilon}}^{\mathrm{vp}}$, is defined as

$$\bar{\dot{\varepsilon}}^{\mathrm{vp}} = \sqrt{\tfrac{2}{3} \dot{\varepsilon}^{\mathrm{vp}} : \dot{\varepsilon}^{\mathrm{vp}}}, \tag{3-3}$$

and the equivalent flow stress, $\bar{\sigma}$, is calculated according to the von Mises yield criterion as

$$\bar{\sigma} = \sqrt{3J_2} = \sqrt{\tfrac{3}{2} S : S}. \tag{3-4}$$

On the other hand, rate-dependent plasticity is often introduced by so-called overstress models, such as the Perzyna model [Perzyna 1966; 1971; Wang et al. 1997; Lof and van den Boogaard 2001; Ponthot 2002] or the Duvaut–Lions model [Simo and Hughes 1998]. Contrary to the case of rate independent plasticity, in these models the equivalent flow stress, $\bar{\sigma}$, is no longer constrained to remain less than or equal to the static yield stress, σ_0, but could be greater than it. The part of the stress that is outside the static yield surface, which is called the overstress, determines the viscoplastic strain rate [Ponthot 2002]. Clearly, an inelastic process can take place if, and only if, the overstress, $d = \langle \bar{\sigma} - \sigma_0 \rangle$, is not less than zero, that is if $d \geq 0$, where $\langle x \rangle$ denotes the MacAuley brackets defined by $\langle x \rangle = 1/2(x + |x|)$. The classical viscoplastic models of Perzyna type [1966; 1971] may be formulated as

$$\bar{\dot{\varepsilon}}^{\mathrm{vp}} = D_{\mathrm{vp}} \left(\frac{\bar{\sigma} - \sigma_0}{\sigma_0} \right)^{1/r}, \tag{3-5}$$

where D_{vp} and r are the viscoplastic material parameters. This mathematical relationship describes the evolution of the equivalent viscoplastic strain rate, $\bar{\dot{\varepsilon}}^{\mathrm{vp}}$, as a function of the overstress, $\bar{\sigma} - \sigma_0$, in the plastic domain. The material parameters in (3-5), namely D_{vp} and r, can be obtained for the extrudable fresh cementitious composite through the following procedure.

First, the shear-form Herschel–Bulkley equation, (2-1), is transformed into its pertinent uniaxial formulation following the theoretical procedure proposed in [Stouffer and Dame 1996] as

$$\bar{\sigma} = \sigma_0 + k(\bar{\dot{\varepsilon}}^{\mathrm{vp}})^n, \tag{3-6}$$

where the material parameters σ_0, k, and n are the uniaxial yield stress, the uniaxial plastic flow consistency, and the uniaxial plastic flow index, respectively. On the other hand, for a material that obeys the von Mises yield criterion, the uniaxial form of the Herschel–Bulkley equation may be obtained from the graph of shear stress against shear strain rate by plotting $\tau = \sigma/\sqrt{3}$ as a function of ... $\gamma^{\mathrm{vp}} = \sqrt{3}\dot{\varepsilon}^{\mathrm{vp}}$ from its shear-form equation [Adams et al. 1997; Aydin et al. 2000]. Substituting these relationships into (2-1) yields

$$\sigma = \sqrt{3}\tau_0 + (\sqrt{3})^{1+m} k_{\mathrm{sc}} (\dot{\varepsilon}^{\mathrm{vp}})^m. \tag{3-7}$$

It has been found that the uniaxial bulk flow index, n, in (3-6) is approximately equal to the shear flow index, m, in (2-1), that is, $n = m$, for the extrudable short-fiber-reinforced fresh cementitious composite investigated in this study [Zhou 2004]. In the case of uniaxial bulk flow, $\bar{\sigma} = \sigma$ and $\bar{\dot{\varepsilon}}^{\mathrm{vp}} = \dot{\varepsilon}^{\mathrm{vp}}$. Therefore,

by comparing (3-6) and (3-7), the material parameters in (3-6) can be obtained as $\sigma_0 = \sqrt{3}\tau_0$ and $k = \sqrt{3}^{1+m} k_{\text{sc}}$ for the extrudable fresh cementitious composite. Rewriting (3-5) in the form of (3-6) gives

$$\bar{\sigma} = \sigma_0 + \frac{\sigma_0}{D_{\text{vp}}^r}(\bar{\dot{\varepsilon}}^{\text{vp}})^r. \tag{3-8}$$

Thus, the interrelationships between the parameters in (3-6) and (3-8) are obtained as $r = m$ and $D_{\text{vp}} = (\sigma_0/k)^{1/m}$. Therefore, the associated material parameters in (3-8) are derived as $\bar{\sigma}_0 = 3.72$ kPa, $D_{\text{vp}} = 0.101\,\text{s}^{-1}$, and $r = 0.38$, by referring to the material test results for orifice extrusion and capillary extrusion presented in [Zhou 2004; Zhou and Li 2005b].

As seen above, our elastoviscoplastic constitutive model features the strain rate-dependent von Mises yield criterion, an associative flow rule, and an nonlinear strain rate-hardening law. The rate-form constitutive model has been integrated into an incremental formulation and implemented into a numerical procedure based on the ANSYS/LS-DYNA explicit finite element code [Zhou 2004]. In this paper, various ram extrusion processes are simulated by this numerical procedure, combined with the constitutive model for the short-fiber-reinforced fresh cementitious composite for extrusion purposes.

Geometries and the finite element model. In numerical analysis, the ram and the extruder, which is composed of the barrel and the die-land, are modeled as rigid objects. Due to axisymmetry, the deformation of the paste in the radial direction at the center of the extruder is zero. Thus, only a single azimuthal slice of the ram extruder and the cementitious composite inside of the center line is modeled in the numerical analysis with a two-dimensional (2D) finite element model composed of a set of four-node isoparametric 2D solid elements, which makes remeshing easier.

Figure 4 shows a typical initial mesh, generated by the ANSYS/LS-DYNA finite element code, for the ram extrusion experimental setup investigated in this study (Figure 2). No contact element is available in explicit analysis based on the LS-DYNA finite element code; contact is achieved using a penalty

Figure 4. Initial finite element mesh for simulating the ram extrusion process with a die diameter of 15 mm.

approach in the LS-DYNA code, in which the fresh cementitious paste is defined as the slave surface while the walls of the extruder and the ram are assigned as the master surfaces. A Coulomb friction criterion, with a constant friction coefficient of $\mu = 0.195$ obtained through upsetting tests [Zhou and Li 2006], is adopted to model boundary interaction whenever the paste contacts the walls of the extruder. A reduced kinematic value is used as the dynamic friction coefficient to simulate reduced boundary friction during dynamic loading. The fresh paste within the ram extruder is modeled by an arbitrary Lagrangian–Eulerian (ALE) mesh as it travels through the die entry into the die-land, while the ram, the barrel, and the die-land are modeled by a much coarser Lagrangian mesh to reduce computation time. The ALE mesh is very effective for simulating large deformation and large strain problems, and allows smoothing of a distorted mesh without requiring a complete remeshing. Thus, it can largely avoid mesh distortion.

A typical initial mesh for the highly concentrated fresh cementitious paste body in the barrel contains 1200–2000 elements, the smallest element size being about 10% of the radius of the die-land. In numerical simulation, an incremental analysis is performed, in which the imposed ram displacement during each analytical step, before remeshing, is between 0.01 and 0.02% of the initial height of the fresh cementitious paste body in the barrel. A very small time step is adopted in numerical analysis to ensure stability in the fine mesh near the die entry, resulting in much longer computation time than for the simulation of the upsetting process presented in [Zhou and Li 2007]. The computation time is longer for cases with larger extrusion ratios than for those with smaller extrusion ratios. In general, remeshing is required to achieve a successful complete numerical simulation, resulting in the element number increasing during analysis.

A series of ram extrusion processes of the fresh cementitious composite, under various extrusion velocities, die-land lengths, and diameters, were simulated with the numerical procedure described above, combined with an elastoviscoplastic constitutive model proposed for the fresh cementitious composite tailored for extrusion purposes. The extrusion load can be obtained at any time during numerical analysis by integrating the longitudinal stress component, $\sigma_y(r)$, over the area of the ram. For an axisymmetric problem, the extrusion load, F_{ext}, is given by

$$F_{\text{ext}} = \int_0^{D_0/2} 2\pi r \sigma_y(r) \, dr, \qquad (3\text{-}9)$$

where $\sigma_y(r)$ is the longitudinal stress of the elements contacting the ram. The extrusion load predicted at each deformation stage is then plotted against the imposed ram displacement to produce an extrusion load versus imposed displacement curve, to which the predicted extrusion load versus imposed displacement curve is referred in this paper. It is then compared with its experimental counterpart to test the applicability of the numerical procedure, combined with the constitutive model, to simulate the ram extrusion process of the fresh cementitious composite.

Comparison of numerical and experimental results. For every extrusion process, the numerical prediction is conducted from the start of extrusion until a steady state is reached. The relationship between the extrusion load and the imposed ram displacement offers a channel for comparing the numerical and experimental results quantitatively. The numerical procedure, as well as the elastoviscoplastic constitutive model for the fresh cementitious composite, presented in this study, is thus mainly verified by this comparison. Figure 5, top left, shows the predicted and experimental extrusion load versus imposed
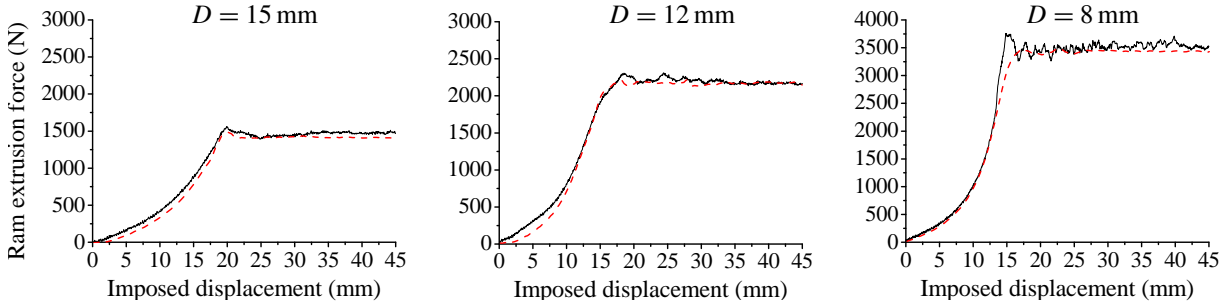
Figure 5. Curves of experimental (solid) and predicted (dashed) extrusion load versus imposed displacement, for $L/D = 0.83$, $V = 0.1$ mm/s, and various values of D.
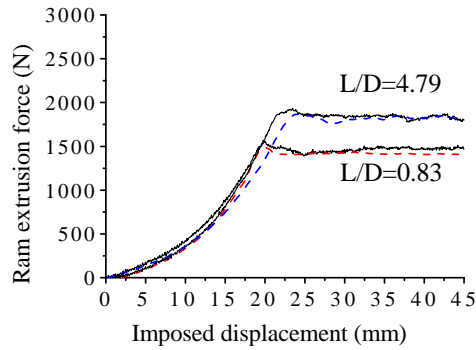
Figure 6. Curves of experimental (solid) and predicted (dashed) extrusion load versus imposed displacement, for $D = 15$ mm, $V = 0.1$ mm/s, and two values of L/D.

displacement curves for the ram extrusion process through a 15 mm diameter die, with a die-land length-to-diameter ratio of 0.83, at an extrusion velocity of 0.1 mm/s. It can be seen that the agreement between the numerical and experimental results is good during the upsetting stage and is within 5% difference under higher loads at steady-state extrusion. The predicted and experimental peak extrusion loads are 1485 N and 1562 N, respectively. Reviewing the uncertainty in the dynamic boundary interaction, the agreement between the predicted and experimental extrusion loads should be considered satisfactory. Besides, the numerical prediction also indicates a decrease in extrusion load after the breakthrough, which is similar to that observed experimentally (as shown in Figure 3).

More results of the predicted and experimental extrusion load versus imposed ram displacement curves are shown in the rest of Figure 5 and in Figure 6 for other parameter values. The results from numerical simulation are generally seen to be in good accordance with the pertinent experimental results and the difference between the predicted and measured steady-state extrusion loads is relatively low, which further verifies that the numerical procedure and the constitutive model presented in this paper can be used with confidence for the prescribed ram extrusion conditions.

Interpretation of the paste flow in ram extrusion. Based on the verified numerical procedure, the evolution of the deformation and distribution of the state variables, such as extrusion pressure, within the paste flow are also predicted throughout the extrusion process. The paste flow in ram extrusion is thus

interpreted based on these numerical results, which also helps in validating the numerical procedure and the constitutive model for the fresh cementitious composite qualitatively and in understanding the ram extrusion mechanism for the short-fiber-reinforced fresh cementitious composite.

Evolution of deformation. At the start of the ram extrusion process, when the ram pushes the fresh cementitious composite in the barrel, the composite paste commences upsetting. As the process continues, the paste flows towards the die-land, where the velocity is the highest within the extruder. A breakthrough extrusion load (indicated by the peak point P in the extrusion load versus imposed displacement curve shown in Figure 3) is necessary for the paste to be extruded out of the die exit. Past this peak, the steady-state extrusion process starts, although the extrusion load decreases due to the drop in friction between the paste and the walls of the barrel. As seen in Figures 5 and 6, the extrusion load reaches its peak value when the paste fills the die-land and starts to emerge, and then it decreases.

The deformation U_y of the composite along the extrusion direction is shown in Figure 7, for a ram extrusion process with a 30 mm diameter die under a ram velocity of 0.1 mm/s, at ram imposed displacements of 1 mm and 4.2 mm. It can be seen that the deformation of the composite in the die-land is significantly higher than that in the barrel, because of the high extrusion ratio. In the corner between the die-land and the barrel, which is referred as the static zone (Figure 7), the deformation of the composite is close to zero. The outline of the static zone, however, is not so obvious. When the composite travels in the die-land, a nonuniform displacement field occurs. It can be seen that the composite near the walls of the barrel and the die-land flows more slowly than the paste in the inner region, due to the boundary friction existing between the composite paste and the walls of the extruder.
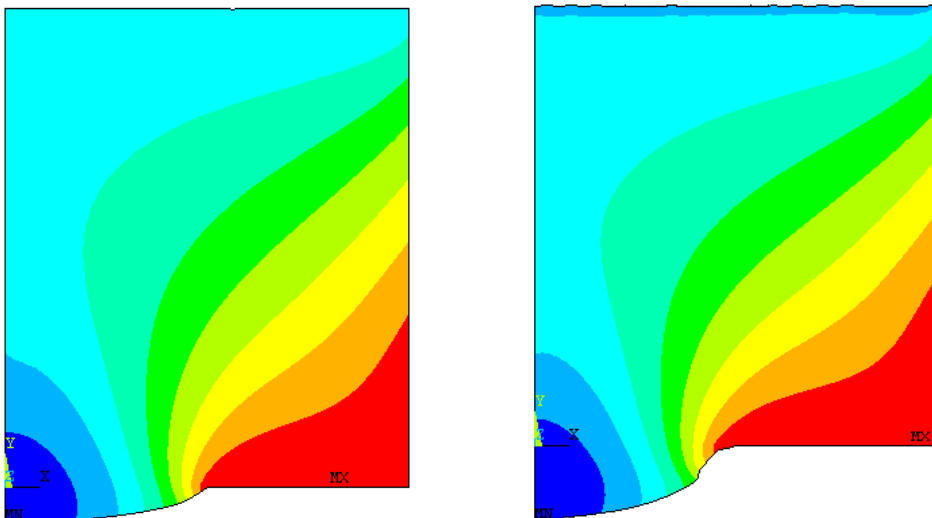
Figure 7. Deformation U_y (average) of the fresh paste flow along the extrusion direction, at an imposed ram displacement of 1 mm (left) and 4.2 mm (right). Color bands range in equal increments from the minimum value, represented by blue and achieved at the bottom left of each diagram, to the maximum, represented by red at the bottom right. The intervals are $[-1.290, -0.001]$ for the left diagram and $[-5.292, 0.017]$ for the right diagram (in mm).
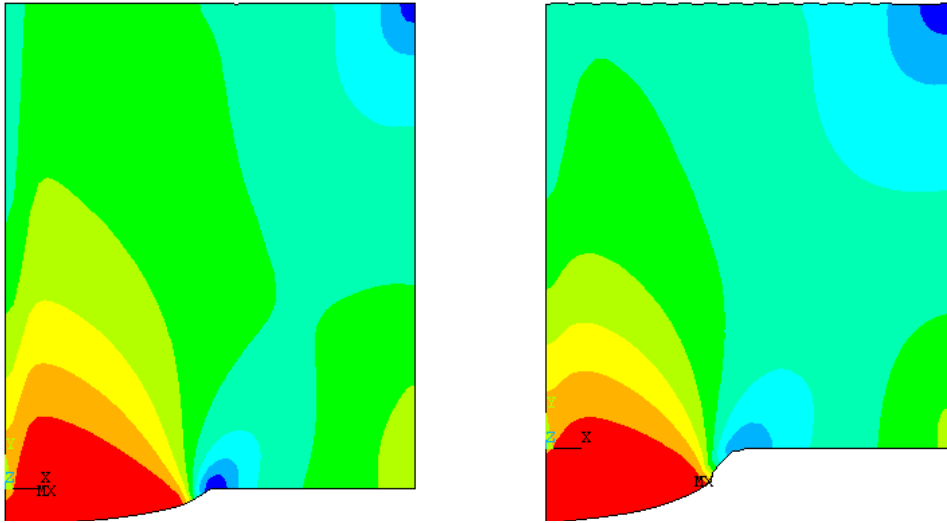
Figure 8. Extrusion pressure S_y (average) within the paste flow along the extrusion direction, at an imposed ram displacement of 1 mm (left) and 4.2 mm (right). Color bands range in equal increments from the minimum value, represented by blue and achieved at the top right (and nearly so at the concave corner) of each diagram, to the maximum, represented by red at the bottom left. The intervals are $[-915, 5]$ for the left diagram and $[-3670, 43]$ for the right diagram (in kPa).

Distribution of state variables within the paste flow. The distribution of the extrusion pressure S_y along the extrusion direction is shown in Figure 8 at imposed ram displacements of 1 mm and 4.2 mm for a ram extrusion process with a 30 mm diameter die under a ram velocity of 0.1 mm/s. In general, negative stress is found from these figures, which is representative of an essential compression-dominant state. However, tensile stress exists in the front surface of the paste flow, owing to the surface friction at the die-land wall, which restricts the paste flow. As a result, the front surface of the paste flow is mainly subjected to tension (see Figure 8). Tensile stress in the front surface of the paste flow is mainly due to two factors: first, the material in the inner region flows faster than that near the die-land wall; and second, the friction between the composite paste and the die-land wall restricts the paste flow. It could also be ascribed to gravity as well.

Effects of extrusion ratio and extrusion velocity. The effect of the extrusion ratio on the extrusion load is demonstrated in Figure 9 for extrusion processes with a 12 mm diameter die and a 15 mm diameter die at a ram velocity of 0.2 mm/s. An increase in the extrusion ratio, that is, a decrease in die diameter, corresponds to an increase in the apparent strain rate. Since the fresh cementitious composite is a strain rate-hardening material, its flow stress increases with the strain rate. Thus more work is required to extrude the composite out of the die-land with a smaller diameter than that with a larger diameter, resulting in an increase in extrusion load. It can also be seen from Figure 9 that the extrusion load increases more rapidly till reaching the steady-state value for the extrusion process with a higher extrusion ratio.

The effect of the extrusion velocity on the extrusion load can be seen in Figure 10, where the numerical and experimental results are shown for the extrusion processes at velocities of 0.1 mm/s and 0.2 mm/s
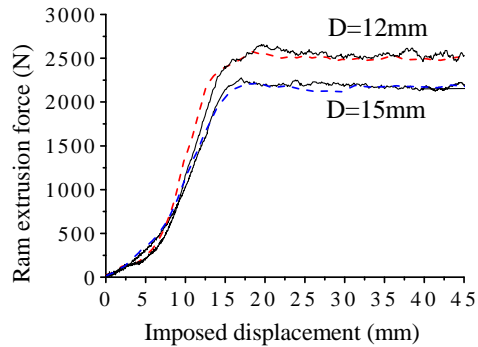
Figure 9. Curves of experimental (solid) and predicted (dashed) extrusion load versus imposed displacement ($L/D = 0.83$ and $V = 0.2$ mm/s).

with a die diameter of 12 mm and a die-land length-to-diameter ratio of 0.83. Again, since the fresh cementitious composite is a strain rate-hardening material, its flow stress increases as its strain rate increases. An increase of extrusion velocity results in an increase of apparent strain rate, and thus equivalent flow stress and, consequently, extrusion load as can be seen from Figure 10 in which the extrusion load for the process under the extrusion velocity 0.2 mm/s is much higher than under the extrusion velocity 0.1 mm/s. Again, the extrusion load in the former extrusion process increases more rapidly to a steady-state value than for the latter.
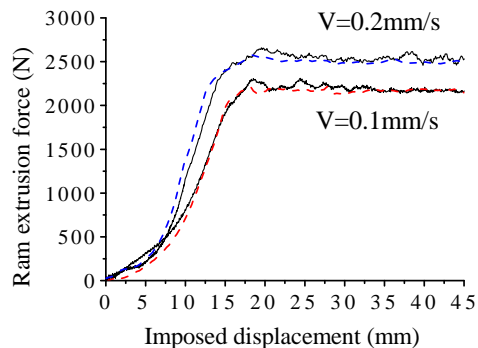
Figure 10. Curves of experimental (solid) and predicted (dashed) extrusion load versus imposed displacement ($L/D = 0.83$ and $L = 12$ mm).

4. Conclusions

A numerical procedure based on the explicit ANSYS/LS-DYNA finite element code, combined with an elastoviscoplastic constitutive model for the extrudable fresh cementitious composite, has been established to simulate a series of ram extrusion processes. The predictions of extrusion load versus imposed displacement are compared with experimental results. The evolution of deformation and the distribution of state variables within the composite paste flow in the ram extrusion process are then interpreted based on numerical results and the ram extrusion mechanism. The effects of the extrusion ratio and extrusion

velocity on extrusion load are discussed. Based on experimental and numerical investigations, the main conclusions that can be drawn are the following:

- The extrusion load versus imposed displacement predictions agree well with the experimental results for various extrusion processes, suggesting that the numerical procedure established and the constitutive model proposed for the fresh cementitious composite can be used with confidence for the prescribed ram extrusion processes. The extrusion load increases more rapidly to a steady-state value in cases of greater extrusion ratio and/or higher ram velocity. In these processes, the steady-state extrusion loads are also greater.

- The evolution of deformation, as well as the distribution of state variables within the paste flow, predicted by numerical analyses, gives a promising interpretation of the fresh cementitious composite paste flow in various ram extrusion processes. Due to surface friction existing between the paste flow and the walls of the extruder, the paste in the central region moves faster than that along the walls of the extruder, resulting in the composite at the front surface being mainly under tension, while the composite in other regions is mainly subjected to compression.

- The numerical procedure presented in this paper shows the potential for improving the understanding of the flow behavior of paste-like materials in extrusion, which might be applied to forming processes for other concentrated paste-like semisolid elastoviscoplastic materials.

References

[Adams et al. 1997] M. J. Adams, I. Aydin, B. J. Briscoe, and S. K. Sinha, "A finite element analysis of the squeeze flow of an elasto-viscoplastic paste material", *J. Non-Newton. Fluid Mech.* **71**:1–2 (1997), 41–57.

[Aldea et al. 1998] C. Aldea, S. Marikunte, and S. P. Shah, "Extruded fiber reinforced cement pressure pipes", *Adv. Cem. Based Mater.* **8**:2 (1998), 47–55.

[Antúnez 2000] H. J. Antúnez, "Linear elements for metal-forming problems within the flow approach", *Comput. Methods Appl. Mech. Eng.* **190**:5–7 (2000), 783–801.

[Aydin et al. 2000] I. Aydin, F. R. Biglari, B. J. Briscoe, C. J. Lawrence, and M. J. Adams, "Physical and numerical modelling of ram extrusion of paste materials: conical die entry case", *Comput. Mater. Sci.* **18**:2 (2000), 141–155.

[Benbow and Bridgwater 1993] J. J. Benbow and J. Bridgwater, *Paste flow and extrusion*, Clarendon, Oxford, 1993.

[Benbow et al. 1991] J. J. Benbow, S. H. Jazayeri, and J. Bridgwater, "The flow of pastes through dies of complicated geometry", *Powder Technol.* **65**:1–3 (1991), 393–401.

[Blackburn and Böhm 1994] S. Blackburn and H. Böhm, "The influence of powder packing on the rheology of fibre-loaded pastes", *J. Mater. Sci.* **29**:16 (1994), 4157–4166.

[Chou et al. 2003] S. Chou, K. Sydow, P. J. Martin, J. Bridgwater, and D. I. Wilson, "Stress relaxation in the extrusion of pastes", *J. Eur. Ceram. Soc.* **23**:5 (2003), 637–646.

[Li and Li 2007] Z. Li and X. Li, "Squeeze flow of viscoplastic cement-based extrudate", *J. Eng. Mech.* (*ASCE*) **133**:9 (2007), 1003–1008.

[Li and Mu 1998] Z. Li and B. Mu, "Application of extrusion for manufacture of short fiber reinforced cementitious composite", *J. Mater. Civ. Eng.* (*ASCE*) **10**:1 (1998), 2–4.

[Li et al. 1999] Z. Li, B. Mu, and S. N. C. Chui, "Systematic study of properties of extrudates with incorporated metakaolin or silica fume", *ACI Mater. J.* **96**:5 (1999), 574–580.

[Li et al. 2001] Z. Li, B. Mu, and S. N. C. Chui, "Static and dynamic behavior of extruded sheets with short fibers", *J. Mater. Civ. Eng.* (*ASCE*) **13**:4 (2001), 248–254.

[Li et al. 2004] Z. Li, X. Zhou, and B. Shen, "Fiber-cement extrudates with perlite subjected to high temperatures", *J. Mater. Civ. Eng.* (*ASCE*) **16**:3 (2004), 221–229.

[Lof and van den Boogaard 2001] J. Lof and A. H. van den Boogaard, "Adaptive return mapping algorithms for J_2 elasto-viscoplastic flow", *Int. J. Numer. Methods Eng.* **51**:11 (2001), 1283–1298.

[Peled and Shah 2003] A. Peled and S. P. Shah, "Processing effects in cementitious composites: extrusion and casting", *J. Mater. Civ. Eng.* (*ASCE*) **15**:2 (2003), 192–199.

[Perzyna 1966] P. Perzyna, "Fundamental problems in viscoplasticity", pp. 243–377 in *Advances in applied mechanics*, vol. 9, edited by G. Kuerti, Academic Press, New York, 1966.

[Perzyna 1971] P. Perzyna, "Thermodynamic theory of plasticity", pp. 313–355 in *Advances in applied mechanics*, vol. 11, edited by C.-S. Yih, Academic Press, New York, 1971.

[Ponthot 2002] J. P. Ponthot, "Unified stress update algorithms for the numerical simulation of large deformation elasto-plastic and elasto-viscoplastic processes", *Int. J. Plast.* **18**:1 (2002), 91–126.

[Shao and Shah 1997] Y. Shao and S. P. Shah, "Mechanical properties of PVA fiber reinforced cement composites fabricated by extrusion processing", *ACI Mater. J.* **94**:6 (1997), 555–564.

[Shao et al. 1995] Y. Shao, S. Marikunte, and S. P. Shah, "Extruded fiber-reinforced composites", *Concr. Int.* **17**:4 (1995), 48–52.

[Simo and Hughes 1998] J. C. Simo and T. J. R. Hughes, *Computational inelasticity*, Interdisciplinary Applied Mathematics **7**, Springer, New York, 1998.

[Srinivasan et al. 1999] R. Srinivasan, D. DeFord, and S. P. Shah, "The use of extrusion rheometry in the development of extruded fiber-reinforced cement composites", *Concr. Sci. Eng.* **1**:1 (1999), 26–36.

[Stouffer and Dame 1996] D. C. Stouffer and L. T. Dame, *Inelastic deformation of metals: models, mechanical properties and metallurgy*, Wiley, New York, 1996.

[Wang et al. 1997] W. M. Wang, L. J. Sluys, and R. de Borst, "Viscoplasticity for instabilities due to strain softening and strain-rate softening", *Int. J. Numer. Methods Eng.* **40**:20 (1997), 3839–3864.

[Zhou 2004] X. Zhou, *Rheological behaviors of the fresh SFRCC extrudate: experimental, theoretical and numerical investigations*, Ph.D. thesis, Hong Kong University of Science and Technology, Hong Kong, 2004.

[Zhou and Li 2005a] X. Zhou and Z. Li, "Characterization of rheology of fresh fiber reinforced cementitious composites through ram extrusion", *Mater. Struct.* **38**:275 (2005), 17–24.

[Zhou and Li 2005b] X. Zhou and Z. Li, "Characterizing rheology of fresh short fiber reinforced cementitious composite through capillary extrusion", *J. Mater. Civ. Eng.* (*ASCE*) **17**:1 (2005), 28–35.

[Zhou and Li 2006] X. Zhou and Z. Li, "Upsetting tests of fresh cementitious composites for extrusion", *J. Eng. Mech.* (*ASCE*) **132**:2 (2006), 149–157.

[Zhou and Li 2007] X. Zhou and Z. Li, "Numerical simulations of upsetting process of the fresh fiber-cement paste", *J. Eng. Mech.* (*ASCE*) **133**:11 (2007), 1192–1199.

XIANGMING ZHOU: Xiangming.Zhou@brunel.ac.uk
Brunel University, School of Engineering and Design, Kingston Lane, Uxbridge UB8 3PH, Middlesex, United Kingdom

ZONGJIN LI: zongjin@ust.hk
Hong Kong University of Science and Technology, Department of Civil and Environmental Engineering, Clear Water Bay, Kowloon, Hong Kong

BENDING OF LAMINATED PLATES WITH MIXED BOUNDARY CONDITIONS BASED ON HIGHER-ORDER SHEAR DEFORMATION THEORY

MOJGAN YAGHOUBSHAHI AND HOSSEIN RAJAIE

The bending of laminated plates is considered using higher-order transverse shear deformation theory. The principle of virtual work is used to derive a new set of seven governing equations and corresponding boundary conditions. These equations, combined with eighteen relationships between the resultant stress and displacement components, compose a system of first-order partial differential equations that is solved by the generalized differential quadrature method. Numerical results for laminated plates with a variety of mixed boundary conditions are calculated using the proposed method, and good agreement is found with the corresponding solutions obtained using ANSYS.

1. Introduction

Fiber-reinforced laminated composite materials are widely used in a variety of engineering fields, such as aerospace, civil, marine, mechanical, nuclear, and petrochemical engineering. Such materials are popular for industrial applications due to high strength-to-weight ratios, long fatigue life, good stealth characteristics, and enhanced corrosion resistance. A number of theories describing laminated composite plates exist in the literature.

Classical plate theory is based on the Kirchhoff kinematic hypothesis that straight lines normal to the undeformed midsurface remain straight and normal to the middle surface after deformation and undergo no thickness stretching. Neglecting transverse shear effects, this theory produces unacceptable approximations in the analysis of even thin laminated plates and shells. Surveys of various classic shell theories can be found in [Naghdi 1956; Bert and Francis 1974; Bert and Chen 1978].

The development of plate theories with transverse shear effects has improved the accuracy of results considerably. The refined theories are of different orders, based on discretization of the transverse shear effects and the number of terms included in the assumed displacement field. Reissner [1945] was the first to develop a plate theory that included transverse shear deformation for static analysis. Mindlin [1951] then expanded Reissner's theory for dynamic analysis. Both approaches rely on first-order shear deformation theory (FSDT). Reissner's theory is stress-based, whereas Mindlin's is displacement-based. These theories do not satisfy the condition of zero transverse shear stress at the top and bottom surfaces of the plate, and consider a uniform transverse shear stress distribution across the thickness of the plate. Therefore they require the use of a shear correction factor to increase the precision of the results.

Later a set of theories, generally known as higher-order shear deformation theories (HSDT), has been developed by a number of researchers. Basset [1890] appears to have been the first researcher to suggest that displacement fields can be expanded in a power series of the thickness coordinate. The higher-order

theory presented by Reddy and Liu [1985] is based on a displacement field in which the displacements in the surface of the shell are expanded as a quadratic function of the thickness coordinate. Actually, the higher-order theories require additional computation with respect to the first-order theories.

Employing such theories results in systems of highly coupled partial differential equations. Several methods exist for obtaining solutions for such systems. Among those numerical studies, the differential quadrature (DQ) method, introduced by Bellman et al. [1972], is an efficient method for obtaining accurate numerical results using a few grid points. DQ approximates the spatial derivative of a function with respect to a given coordinate at a discrete point as the weighted linear sum of all functional values in the domain of that coordinate direction. Two methods were proposed by those authors for obtaining the weighting coefficients of the first-order derivative: the first method solves a system of algebraic equations to determine the weighting coefficients, and the second utilizes a simple algebraic formulation, provided that the coordinates of grid points are chosen to be the roots of the shifted Legendre polynomial. The first method is simpler to apply, but the second is more efficient. For the first method, in which the coordinates of grid points are arbitrarily chosen, Quan and Chang [1989] used Lagrange interpolation polynomials as test functions to develop explicit formulations for determining the weighting coefficients for the first- and second-order derivative discretization.

A generalized differential quadrature (GDQ) method was introduced in [Shu and Richards 1990; Shu 1991]. It generalized all current methods via analysis of a higher-order polynomial approximation and analysis of a linear vector space. In GDQ, the weighting coefficients of the first derivatives are determined by a simple algebraic formulation, and there is no restriction on the coordinates of the grid points. The weighting coefficients of the second and higher-order derivatives are determined by a recurrence relationship.

Bert et al. [1988] were the first to apply the DQ method to structural mechanics problems. Subsequently, a number of researchers utilized this method to solve a variety of structural problems relevant to thin plate theory [Striz et al. 1988; Bert et al. 1989; Sherbourne and Pandey 1991]. A bending analysis of thin/thick laminated plates with various boundary conditions based on first-order shear deformation theory was described in [Aghdam et al. 2006]. The DQ method was used in [Li and Cheng 2005; Tornabene and Viola 2008] to solve for the vibration of plates and shells. In [Malekzadeh and Setoodeh 2007], large deformation of laminated plates on a nonlinear elastic foundation was analyzed by the DQ method.

The present study deals with the bending analysis of thin/thick laminated plates with various boundary conditions based on the higher-order shear deformation theory, in which the displacement field presented by Reddy and Liu [1985] is considered. Introducing two new unknown functions w_i $(i = 1, 2)$ for computational purposes, a new set of seven governing equations and corresponding boundary conditions for each edge are derived. Applying the w_i allows the governing equations and boundary conditions to be easily obtained from the virtual work formulation. These equations, together with eighteen relationships between the resultant stress and displacement components, form a system of 25 first-order partial differential equations. Solving a set of 25 equations simultaneously enables one to apply boundary conditions in the HSDT more accurately and conveniently. In the HSDT of Reddy and Liu, the governing equations are second-order partial differential equations, and the boundary conditions are first-order partial differential relationships. By applying this technique, the governing equations convert first-order and boundary conditions into linear algebraic relationships. Application of linear algebraic relationships as boundary

conditions is much easier, and the number of grid points required for convergence in the GDQ method is reduced.

In this paper, plates with free edge and mixed boundary conditions are considered. The results are compared with those obtained ANSYS version 5.4. Numerical results are presented to understand the complex deformation behavior of symmetric and antisymmetric cross ply plates.

2. Formulation

A rectangular plate with different boundaries in the α_1 and α_2 directions is considered. The principle of virtual work for the equilibrium of a body with surface S and volume V requires satisfaction of

$$\int_V \sum_{i=1}^{3} \sum_{j=1}^{3} \sigma_{ij}\, \delta\varepsilon_{ij}\, dV - \int_S \delta W_{\text{ext}}\, ds = 0, \tag{1}$$

where σ_{ij} denotes the stress components, $\delta\varepsilon_{ij}$ the variation of virtual strain components caused by virtual displacements, and δW_{ext} the variation in virtual work performed by the external forces. Employing a higher-order shear deformation theory, the displacement components, in terms of functions specifying the deformation of the middle surface of the plate, may be approximated as [Reddy and Liu 1985]

$$U_i(\alpha_1, \alpha_2, \zeta) = u_i(\alpha_1, \alpha_2) + \zeta\varphi_i(\alpha_1, \alpha_2) + \zeta^2\psi_i(\alpha_1, \alpha_2) + \zeta^3\theta_i(\alpha_1, \alpha_2), \qquad i = 1, 2$$
$$W(\alpha_1, \alpha_2, \zeta) = w(\alpha_1, \alpha_2), \tag{2}$$

where, ζ, ranging from $-h/2$ to $h/2$, is the variable in the thickness direction.

Convention. Henceforth, unless otherwise stated, we use the subscript n to refer to the normal direction (i.e., $n = 3$) and i, j are distinct indices ranging over the in-plane directions (i.e., $i = 1, 2$ and $j = 3 - i$).

One may assume, without loss of generality, that shear stress is absent from the top and bottom surfaces of the plate. Therefore,

$$\tau_{in}\left(\alpha_1, \alpha_2, \pm\frac{h}{2}\right) = 0. \tag{3}$$

Hooke's law for a laminated plate composed of orthotropic layers implies that (3) is equivalent to

$$\gamma_{in}\left(\alpha_1, \alpha_2, \pm\frac{h}{2}\right) = 0. \tag{4}$$

The strain-displacement relationships in the principal coordinates of a plate are

$$\varepsilon_{ii} = \frac{\partial U_i}{\partial\alpha_i}, \qquad \varepsilon_{nn} = \frac{\partial W}{\partial\zeta}, \qquad \gamma_{ij} = \frac{\partial U_j}{\partial\alpha_i} + \frac{\partial U_i}{\partial\alpha_j}, \qquad \gamma_{in} = \frac{\partial W}{\partial\alpha_i} + \frac{\partial U_i}{\partial\zeta}. \tag{5}$$

Substitution of (2) into (5) yields

$$\gamma_{in} = \frac{\partial w}{\partial\alpha_i} + \varphi_i + 2\zeta\psi_i + 3\zeta^2\theta_i. \tag{6}$$

Application of (4) to (6) gives the four equations

$$\begin{cases} \partial w/\partial\alpha_i + \varphi_i + h\psi_i + \frac{3}{4}h^2\theta_i = 0 \\ \partial w/\partial\alpha_i + \varphi_i - h\psi_i + \frac{3}{4}h^2\theta_i = 0 \end{cases} \qquad i = 1, 2. \tag{7}$$

Solving the system of algebraic equations (7) yields

$$\psi_i = 0, \qquad \theta_i = -\frac{4}{3h^2}\left(\frac{\partial w}{\partial \alpha_i} + \varphi_i\right). \tag{8}$$

Substituting (8) into (2) gives the displacement components in the thickness direction in terms of displacements of the middle surface of the plate:

$$U_i(\alpha_1, \alpha_2, \zeta) = u_i + \zeta\varphi_i - \zeta^3 \frac{4}{3h^2}\left(\frac{\partial w}{\partial \alpha_i} + \varphi_i\right), \qquad W(\alpha_1, \alpha_2, \zeta) = w(\alpha_1, \alpha_2). \tag{9}$$

The strain-displacement equations (7), in view of (9), give

$$\begin{aligned}
\varepsilon_{ii} &= \varepsilon_i^0 + \zeta\kappa_i^0 + \zeta^3\kappa_i^2, & \gamma_{in} &= \lambda_i^0 + \zeta^2\eta_i^1, \\
\varepsilon_{nn} &= \frac{\partial w}{\partial \zeta}, & \gamma_{ij} &= \gamma_i^0 + \zeta\mu_i^0 + \zeta^3\mu_i^2 + \gamma_j^0 + \zeta\mu_j^0 + \zeta^3\mu_j^2,
\end{aligned} \tag{10}$$

where we have set

$$\begin{aligned}
\varepsilon_i^0 &= \frac{\partial u_i}{\partial \alpha_i}, & \kappa_i^0 &= \frac{\partial \varphi_i}{\partial \alpha_i}, & \kappa_i^2 &= -\frac{4}{3h^2}\frac{\partial}{\partial \alpha_i}(w_i + \varphi_i), & \lambda_i^0 &= \frac{\partial w}{\partial \alpha_i} + \varphi_i, \\
\gamma_i^0 &= \frac{\partial u_j}{\partial \alpha_i}, & \mu_i^0 &= \frac{\partial \varphi_j}{\partial \alpha_i}, & \mu_i^2 &= -\frac{4}{3h^2}\frac{\partial}{\partial \alpha_i}(w_j + \varphi_j), & \eta_i^1 &= -\frac{4}{h^2}(w_i + \varphi_i).
\end{aligned} \tag{11}$$

Here we have introduced two new unknown functions, $w_i = \dfrac{\partial w}{\partial \alpha_i}$. The stress resultants are defined as

$$\begin{bmatrix} N_i & N_{ij} & N_{in} & M_i & M_{ij} & M_{in} & P_i & P_{ij} & P_{in} & S_i & S_{ij} \end{bmatrix}^T$$
$$= \int_{-h/2}^{h/2} \begin{bmatrix} \sigma_{ii} & \tau_{ij} & \tau_{in} & \zeta\sigma_{ii} & \zeta\tau_{ij} & \zeta\tau_{in} & \zeta^2\sigma_{ii} & \zeta^2\tau_{ij} & \zeta^2\tau_{in} & \zeta^3\sigma_{ii} & \zeta^3\tau_{ij} \end{bmatrix}^T d\zeta, \tag{12}$$

where T is the transpose of a vector. The applied load per unit area of the middle surface of a plate is taken as $q = q_1 e_1 + q_2 e_2 - q_n e_n$, where e_1, e_2, and e_n are unit vectors in the directions of the principal axes (α_1, α_2) and thickness direction (n), respectively. Let $\bar{\sigma}_{ii}$, $\bar{\tau}_{ij}$, and $\bar{\tau}_{in}$ be the components of applied traction on the edges $\alpha_i = $ constant. The virtual work done by external loads on the plate is

$$\delta w_{\text{ext}} = \int_{\alpha_1}\int_{\alpha_2}(q_1\delta u_1 + q_2\delta u_2 - q_n\delta w)\,d\alpha_1\,d\alpha_2 + \oint_{\alpha_j}\int_{-h/2}^{h/2}(\bar{\sigma}_{ii}\delta U_i + \bar{\tau}_{ij}\delta U_j + \bar{\tau}_{in}\delta W)\,d\zeta\,d\alpha_j, \tag{13}$$

where the second integral should be taken across the boundary of the plate. Substituting (9) into (13) and (10) into (1), employing (12), setting $\sigma_n = 0$, and carrying out the required manipulations, leads to the overall variational equation in the box on the next page.

From the first four lines of the boxed equation we derive seven governing differential equations:

$$\begin{aligned}
\frac{\partial N_i}{\partial \alpha_i} + \frac{\partial N_{ij}}{\partial \alpha_j} + q_i &= 0, & \frac{\partial M_i}{\partial \alpha_i} + \frac{\partial M_{ij}}{\partial \alpha_j} - N_{in} &= 0, \\
\frac{\partial N_{in}}{\partial \alpha_i} + \frac{\partial N_{jn}}{\partial \alpha_j} - q_n &= 0, & \frac{\partial S_i}{\partial \alpha_i} + \frac{\partial S_{ij}}{\partial \alpha_j} - 3P_{in} &= 0.
\end{aligned} \tag{14}$$

The remaining terms in the boxed equation lead to the boundary conditions for a plate. The boundary data on each edge $\alpha_i = $ constant are prescribed by selecting one member of each of the following seven

$$\int_{\alpha_1}\int_{\alpha_2}\left[\left(\frac{\partial N_1}{\partial\alpha_1}+\frac{\partial N_{12}}{\partial\alpha_2}+q_1\right)\delta u_1+\left(\frac{\partial N_2}{\partial\alpha_2}+\frac{\partial N_{12}}{\partial\alpha_1}+q_2\right)\delta u_2+\left(\frac{\partial N_{1n}}{\partial\alpha_1}+\frac{\partial N_{2n}}{\partial\alpha_2}-q_n\right)\delta w\right.$$

$$+\left(\frac{\partial M_1}{\partial\alpha_1}-\frac{4}{3h^2}\frac{\partial S_1}{\partial\alpha_1}+\frac{\partial M_{12}}{\partial\alpha_2}-\frac{4}{3h^2}\frac{\partial S_{12}}{\partial\alpha_2}-N_{1n}+\frac{4}{h^2}P_{1n}\right)\delta\varphi_1$$

$$+\left(\frac{\partial M_2}{\partial\alpha_2}-\frac{4}{3h^2}\frac{\partial S_2}{\partial\alpha_2}+\frac{\partial M_{12}}{\partial\alpha_1}-\frac{4}{3h^2}\frac{\partial S_{12}}{\partial\alpha_1}-N_{2n}+\frac{4}{h^2}P_{2n}\right)\delta\varphi_2$$

$$+\left(-\frac{4}{3h^2}\frac{\partial S_1}{\partial\alpha_1}-\frac{4}{3h^2}\frac{\partial S_{12}}{\partial\alpha_2}+\frac{4}{h^2}P_{1n}\right)\delta w_1+\left(-\frac{4}{3h^2}\frac{\partial S_2}{\partial\alpha_2}-\frac{4}{3h^2}\frac{\partial S_{12}}{\partial\alpha_1}+\frac{4}{h^2}P_{2n}\right)\delta w_2\bigg]\,d\alpha_1\,d\alpha_2$$

$$+\oint_{\alpha_2}\left[[\bar{N}_1-N_1]\delta u_1+\left[\left(\bar{M}_1-\frac{4}{3h^2}\bar{S}_1\right)-\left(M_1-\frac{4}{3h^2}S_1\right)\right]\delta\varphi_1-\frac{4}{3h^2}[\bar{S}_1-S_1]\delta w_1+[\bar{N}_{12}-N_{12}]\delta u_2\right.$$

$$+\left[\left(\bar{M}_{12}-\frac{4}{3h^2}\bar{S}_{12}\right)-\left(M_{12}-\frac{4}{3h^2}S_{12}\right)\right]\delta\varphi_2+\left[\left(\bar{N}_{1n}+\frac{4}{3h^2}\frac{\partial\bar{S}_{12}}{\partial\alpha_2}\right)-\left(N_{1n}+\frac{4}{3h^2}\frac{\partial S_{12}}{\partial\alpha_2}\right)\right]\delta w\bigg]\,d\alpha_2$$

$$+\oint_{\alpha_1}\left[[\bar{N}_2-N_2]\delta u_2+\left[\left(\bar{M}_2-\frac{4}{3h^2}\bar{S}_2\right)-\left(M_2-\frac{4}{3h^2}S_2\right)\right]\delta\varphi_2-\frac{4}{3h^2}[\bar{S}_2-S_2]\delta w_2+[\bar{N}_{12}-N_{12}]\delta u_2\right.$$

$$+\left[\left(\bar{M}_{12}-\frac{4}{3h^2}\bar{S}_{12}\right)-\left(M_{12}-\frac{4}{3h^2}S_{12}\right)\right]\delta\varphi_1+\left[\left(\bar{N}_{2n}-\frac{4}{3h^2}\frac{\partial\bar{S}_{12}}{\partial\alpha_1}\right)-\left(N_{2n}-\frac{4}{3h^2}\frac{\partial S_{12}}{\partial\alpha_1}\right)\right]\delta w\bigg]\,d\alpha_1$$

$$=0.$$

pairs of variables as a known quantity:

$$(N_i,u_i),\quad\left(M_i-\frac{4}{3h^2}S_i,\varphi_i\right),\quad(S_i,w_i),\quad(N_{ij},u_j),\quad\left(M_{ij}-\frac{4}{3h^2}S_{ij},\varphi_j\right),\quad(S_{ij},w_j),\quad(N_{in},w),$$

The stress–strain relationship for a single orthotropic lamina on a plate is

$$\begin{Bmatrix}\sigma_{11}\\\sigma_{22}\\\tau_{2n}\\\tau_{1n}\\\tau_{12}\end{Bmatrix}=\begin{bmatrix}\bar{Q}_{11}&\bar{Q}_{12}&0&0&\bar{Q}_{16}\\\bar{Q}_{12}&\bar{Q}_{22}&0&0&\bar{Q}_{26}\\0&0&\bar{Q}_{44}&\bar{Q}_{45}&0\\0&0&\bar{Q}_{45}&\bar{Q}_{55}&0\\\bar{Q}_{16}&\bar{Q}_{26}&0&0&\bar{Q}_{66}\end{bmatrix}\begin{Bmatrix}\varepsilon_{11}\\\varepsilon_{22}\\\gamma_{2n}\\\gamma_{1n}\\\gamma_{12}\end{Bmatrix}.\tag{15}$$

The matrix components of material properties in (15) may be written in terms of the stiffness coefficients in the direction of the principal axis of material orthotropy as

$$\bar{Q}_{11}=Q_{11}m^4+2(Q_{12}+2Q_{66})m^2n^2+Q_{22}n^4,\quad\bar{Q}_{12}=(Q_{11}+Q_{22}-4Q_{66})m^2n^2+Q_{12}(m^4+n^4),$$

$$\bar{Q}_{22}=Q_{11}n^4+2(Q_{12}+2Q_{66})m^2n^2+Q_{22}m^4,\quad\bar{Q}_{45}=(Q_{55}-Q_{44})mn,$$

$$\bar{Q}_{16}=(Q_{11}-Q_{12}-2Q_{66})m^3n+(Q_{12}-Q_{22}+2Q_{66})mn^3,\tag{16}$$

$$\bar{Q}_{26}=(Q_{11}-Q_{12}-2Q_{66})mn^3+(Q_{12}-Q_{22}+2Q_{66})m^3n,$$

$$\bar{Q}_{44}=Q_{44}m^2+Q_{55}n^2,\quad\bar{Q}_{55}=Q_{44}n^2+Q_{55}m^2,\quad\bar{Q}_{66}=(Q_{11}+Q_{22}-2Q_{12})m^2n^2+Q_{66}(m^2-n^2)^2.$$

In the equations above, m and n are defined as $m=\cos\chi$ and $n=\sin\chi$, where χ accounts for the angle between the principal axis of material orthotropy and the α_1-axis. In fact, the principal coordinates

of a plate differ from the material principal axes. The material principal axes make an angle χ with the principal coordinates of the plate. In terms of engineering constants, the material properties in (16) are derived as

$$Q_{11} = \frac{E_{11}}{\Delta}, \quad Q_{12} = \frac{E_{11}\nu_{21}}{\Delta}, \quad Q_{22} = \frac{E_{22}}{\Delta}, \quad Q_{44} = G_{23}, \quad Q_{55} = G_{13}, \quad Q_{66} = G_{12}, \quad (17)$$

where $\Delta = 1 - \nu_{12}\nu_{21}$. However, if the equations in (10) are substituted into (15), the resultant equations are substituted into (12), and the integration in the thickness direction is carried out, we arrive at the following equations for the stress resultants:

$$\begin{Bmatrix} N_1 \\ N_{12} \\ N_2 \end{Bmatrix} = \begin{bmatrix} C_{11}^1 & C_{16}^1 & C_{12}^1 & C_{16}^1 \\ C_{16}^1 & C_{66}^1 & C_{26}^1 & C_{66}^1 \\ C_{12}^1 & C_{16}^1 & C_{22}^1 & C_{26}^1 \end{bmatrix} \begin{Bmatrix} \varepsilon_1^0 \\ \gamma_1^0 \\ \varepsilon_2^0 \\ \gamma_2^0 \end{Bmatrix} + \begin{bmatrix} C_{11}^2 & C_{16}^2 & C_{12}^2 & C_{16}^2 \\ C_{16}^2 & C_{66}^2 & C_{26}^2 & C_{66}^2 \\ C_{12}^2 & C_{16}^2 & C_{22}^2 & C_{26}^2 \end{bmatrix} \begin{Bmatrix} \kappa_1^0 \\ \mu_1^0 \\ \kappa_2^0 \\ \mu_2^0 \end{Bmatrix} + \begin{bmatrix} C_{11}^4 & C_{16}^4 & C_{12}^4 & C_{16}^4 \\ C_{16}^4 & C_{66}^4 & C_{26}^4 & C_{66}^4 \\ C_{12}^4 & C_{16}^4 & C_{22}^4 & C_{26}^4 \end{bmatrix} \begin{Bmatrix} \kappa_1^2 \\ \mu_1^2 \\ \kappa_2^2 \\ \mu_2^2 \end{Bmatrix},$$

$$\begin{Bmatrix} M_1 \\ M_{12} \\ M_2 \end{Bmatrix} = \begin{bmatrix} C_{11}^2 & C_{16}^2 & C_{12}^2 & C_{16}^2 \\ C_{16}^2 & C_{66}^2 & C_{26}^2 & C_{66}^2 \\ C_{12}^2 & C_{16}^2 & C_{22}^2 & C_{26}^2 \end{bmatrix} \begin{Bmatrix} \varepsilon_1^0 \\ \gamma_1^0 \\ \varepsilon_2^0 \\ \gamma_2^0 \end{Bmatrix} + \begin{bmatrix} C_{11}^3 & C_{16}^3 & C_{12}^3 & C_{16}^3 \\ C_{16}^3 & C_{66}^3 & C_{26}^3 & C_{66}^3 \\ C_{12}^3 & C_{16}^3 & C_{22}^3 & C_{26}^3 \end{bmatrix} \begin{Bmatrix} \kappa_1^0 \\ \mu_1^0 \\ \kappa_2^0 \\ \mu_2^0 \end{Bmatrix} + \begin{bmatrix} C_{11}^5 & C_{16}^5 & C_{12}^5 & C_{16}^5 \\ C_{16}^5 & C_{66}^5 & C_{26}^5 & C_{66}^5 \\ C_{12}^5 & C_{16}^5 & C_{22}^5 & C_{26}^5 \end{bmatrix} \begin{Bmatrix} \kappa_1^2 \\ \mu_1^2 \\ \kappa_2^2 \\ \mu_2^2 \end{Bmatrix},$$

$$\begin{Bmatrix} P_1 \\ P_{12} \\ P_2 \end{Bmatrix} = \begin{bmatrix} C_{11}^3 & C_{16}^3 & C_{12}^3 & C_{16}^3 \\ C_{16}^3 & C_{66}^3 & C_{26}^3 & C_{66}^3 \\ C_{12}^3 & C_{16}^3 & C_{22}^3 & C_{26}^3 \end{bmatrix} \begin{Bmatrix} \varepsilon_1^0 \\ \gamma_1^0 \\ \varepsilon_2^0 \\ \gamma_2^0 \end{Bmatrix} + \begin{bmatrix} C_{11}^4 & C_{16}^4 & C_{12}^4 & C_{16}^4 \\ C_{16}^4 & C_{66}^4 & C_{26}^4 & C_{66}^4 \\ C_{12}^4 & C_{16}^4 & C_{22}^4 & C_{26}^4 \end{bmatrix} \begin{Bmatrix} \kappa_1^0 \\ \mu_1^0 \\ \kappa_2^0 \\ \mu_2^0 \end{Bmatrix} + \begin{bmatrix} C_{11}^6 & C_{16}^6 & C_{12}^6 & C_{16}^6 \\ C_{16}^6 & C_{66}^6 & C_{26}^6 & C_{66}^6 \\ C_{12}^6 & C_{16}^6 & C_{22}^6 & C_{26}^6 \end{bmatrix} \begin{Bmatrix} \kappa_1^2 \\ \mu_1^2 \\ \kappa_2^2 \\ \mu_2^2 \end{Bmatrix},$$

$$\begin{Bmatrix} S_1 \\ S_{12} \\ S_2 \end{Bmatrix} = \begin{bmatrix} C_{11}^4 & C_{16}^4 & C_{12}^4 & C_{16}^4 \\ C_{16}^4 & C_{66}^4 & C_{26}^4 & C_{66}^4 \\ C_{12}^4 & C_{16}^4 & C_{22}^4 & C_{26}^4 \end{bmatrix} \begin{Bmatrix} \varepsilon_1^0 \\ \gamma_1^0 \\ \varepsilon_2^0 \\ \gamma_2^0 \end{Bmatrix} + \begin{bmatrix} C_{11}^5 & C_{16}^5 & C_{12}^5 & C_{16}^5 \\ C_{16}^5 & C_{66}^5 & C_{26}^5 & C_{66}^5 \\ C_{12}^5 & C_{16}^5 & C_{22}^5 & C_{26}^5 \end{bmatrix} \begin{Bmatrix} \kappa_1^0 \\ \mu_1^0 \\ \kappa_2^0 \\ \mu_2^0 \end{Bmatrix} + \begin{bmatrix} C_{11}^7 & C_{16}^7 & C_{12}^7 & C_{16}^7 \\ C_{16}^7 & C_{66}^7 & C_{26}^7 & C_{66}^7 \\ C_{12}^7 & C_{16}^7 & C_{22}^7 & C_{26}^7 \end{bmatrix} \begin{Bmatrix} \kappa_1^2 \\ \mu_1^2 \\ \kappa_2^2 \\ \mu_2^2 \end{Bmatrix},$$

$$\begin{Bmatrix} N_{1n} \\ N_{2n} \end{Bmatrix} = \begin{bmatrix} C_{55}^1 & C_{54}^1 \\ C_{45}^1 & C_{44}^1 \end{bmatrix} \begin{Bmatrix} \lambda_1^0 \\ \lambda_2^0 \end{Bmatrix} + \begin{bmatrix} C_{55}^3 & C_{54}^3 \\ C_{45}^3 & C_{44}^3 \end{bmatrix} \begin{Bmatrix} \eta_1^1 \\ \eta_2^1 \end{Bmatrix},$$

$$\begin{Bmatrix} M_{1n} \\ M_{2n} \end{Bmatrix} = \begin{bmatrix} C_{55}^2 & C_{54}^2 \\ C_{45}^2 & C_{44}^2 \end{bmatrix} \begin{Bmatrix} \lambda_1^0 \\ \lambda_2^0 \end{Bmatrix} + \begin{bmatrix} C_{55}^4 & C_{54}^4 \\ C_{45}^4 & C_{44}^4 \end{bmatrix} \begin{Bmatrix} \eta_1^1 \\ \eta_2^1 \end{Bmatrix},$$

$$\begin{Bmatrix} P_{1n} \\ P_{2n} \end{Bmatrix} = \begin{bmatrix} C_{55}^3 & C_{54}^3 \\ C_{45}^3 & C_{44}^3 \end{bmatrix} \begin{Bmatrix} \lambda_1^0 \\ \lambda_2^0 \end{Bmatrix} + \begin{bmatrix} C_{55}^5 & C_{54}^5 \\ C_{45}^5 & C_{44}^5 \end{bmatrix} \begin{Bmatrix} \eta_1^1 \\ \eta_2^1 \end{Bmatrix},$$

where

$$C_{ij}^p = \frac{1}{p} \sum_{k=1}^{N} (\bar{Q}_{ij})_k (h_k^p - h_{k-1}^p), \quad p \in \{1, 2, \ldots, 7\}, \quad (18)$$

and $h_k - h_{k-1}$ is the thickness of the k-th layer. Substitution of (11) into the equations on page 1776 yields the stress resultants in terms of the displacement components. These equations, combined with (14), form a system of 25 first-order partial differential equations for displacements and stress resultants:

$$[K]\{u_1, u_2, w, \varphi_1, \varphi_2, w_1, w_2, N_1, N_{12}, N_2, M_1, M_{12}, M_2,$$
$$P_1, P_{12}, P_2, S_1, S_{12}, S_2, N_{1n}, N_{2n}, M_{1n}, M_{2n}, P_{1n}, P_{2n}\}^T = \{-q_1, -q_2, q_n, 0, \ldots, 0\}^T. \quad (19)$$

The coefficients of the matrix K are given in the box below (19). A numerical solution for (19) can be achieved by means of the GDQ method. The method is detailed, for example, in [Shu 1991; Bert et al. 1988], and its application to first-order differential equations is summarized here. In the GDQ method,

---

Nonzero entries of K referenced by row and column

Rows 1 to 7:

$1,8: \dfrac{\partial}{\partial \alpha_1}$ $\quad 1,9: \dfrac{\partial}{\partial \alpha_2}$ $\quad 2,9: \dfrac{\partial}{\partial \alpha_1}$ $\quad 2,10: \dfrac{\partial}{\partial \alpha_2}$ $\quad 3,20: \dfrac{\partial}{\partial \alpha_1}$ $\quad 3,21: \dfrac{\partial}{\partial \alpha_2}$

$4,11: \dfrac{\partial}{\partial \alpha_1}$ $\quad 4,12: \dfrac{\partial}{\partial \alpha_2}$ $\quad 4,20: -1$ $\quad 5,13: \dfrac{\partial}{\partial \alpha_2}$ $\quad 5,12: \dfrac{\partial}{\partial \alpha_1}$ $\quad 5,21: -1$

$6,17: \dfrac{\partial}{\partial \alpha_1}$ $\quad 6,18: \dfrac{\partial}{\partial \alpha_2}$ $\quad 6,24: -3$ $\quad 7,19: \dfrac{\partial}{\partial \alpha_2}$ $\quad 7,18: \dfrac{\partial}{\partial \alpha_1}$ $\quad 7,25: -3$

Rows 8 to 19:

$$k,k: \quad -1$$

$k,1: A_1' \dfrac{\partial}{\partial \alpha_1} + C_1' \dfrac{\partial}{\partial \alpha_2}$ $\quad k,4: \left(A_2' - \dfrac{4}{3h^2} A_4'\right) \dfrac{\partial}{\partial \alpha_1} + \left(C_2' - \dfrac{4}{3h^2} C_4'\right) \dfrac{\partial}{\partial \alpha_2}$ $\quad k,6: -\dfrac{4}{3h^2} A_4' \dfrac{\partial}{\partial \alpha_1} - \dfrac{4}{3h^2} C_4' \dfrac{\partial}{\partial \alpha_2}$

$k,2: B_1' \dfrac{\partial}{\partial \alpha_2} + C_1' \dfrac{\partial}{\partial \alpha_1}$ $\quad k,5: \left(B_2' - \dfrac{4}{3h^2} B_4'\right) \dfrac{\partial}{\partial \alpha_2} + \left(C_2' - \dfrac{4}{3h^2} C_4'\right) \dfrac{\partial}{\partial \alpha_1}$ $\quad k,7: -\dfrac{4}{3h^2} B_4' \dfrac{\partial}{\partial \alpha_1} - \dfrac{4}{3h^2} C_4' \dfrac{\partial}{\partial \alpha_2}$

where

for $k \in \{8, 11, 14, 17\}$, $\quad n = \tfrac{1}{3}(k - 8)$, $\quad A_l' = C_{11}^{n+l}$, $\quad B_l' = C_{12}^{n+l}$, $\quad C_l' = C_{16}^{n+l}$;

for $k \in \{9, 12, 15, 18\}$, $\quad n = \tfrac{1}{3}(k - 9)$, $\quad A_l' = C_{16}^{n+l}$, $\quad B_l' = C_{26}^{n+l}$, $\quad C_l' = C_{66}^{n+l}$;

for $k \in \{10, 13, 16, 19\}$, $\quad n = \tfrac{1}{3}(k - 10)$, $\quad A_l' = C_{12}^{n+l}$, $\quad B_l' = C_{22}^{n+l}$, $\quad C_l' = C_{16}^{n+l}$,

Rows 20 to 25:

$k,k: \quad = -1$ $\qquad\qquad k,4: \quad = A_1' - \dfrac{4}{h^2} A_3'$ $\qquad\qquad k,6: \quad = -\dfrac{4}{h^2} A_3'$

$k,3: \quad = A_1' \dfrac{\partial}{\partial \alpha_1} + B_1' \dfrac{\partial}{\partial \alpha_2}$ $\qquad k,5: \quad = B_1' - \dfrac{4}{h^2} B_3'$ $\qquad\qquad k,7: \quad = -\dfrac{4}{3h^2} A_3'$

where

for $k \in \{20, 22, 24\}$, $\quad n = \tfrac{1}{2}(k - 20)$, $\quad A_l' = C_{55}^{n+l}$, $\quad B_l' = C_{45}^{n+l}$,

for $k \in \{21, 23, 25\}$, $\quad n = \tfrac{1}{2}(k - 21)$, $\quad A_l' = C_{45}^{n+l}$, $\quad B_l' = C_{44}^{n+l}$.

the derivative of a function at any discrete point in a given direction is approximated by the weighted linear sum of the function values at all sampling points in that direction,

$$\frac{dF(x_k)}{dx} = \sum_{l=1}^{N} C_{kl} F(x_l), \qquad k \in \{1, 2, \ldots, N\}, \tag{20}$$

where N denotes the number of sampling points selected in the x-direction and C_{kl} are the weighting coefficients of the first derivative with respect to the variable x. Taking the Lagrange interpolation polynomials as test functions, the coefficients in (20) result in

$$C_{kl} = \frac{M(x_k)}{(x_k - x_l)M(x_l)}, \qquad k, l = 1, 2, \ldots, N, \quad k \neq l,$$

$$C_{kk} = -\sum_{\substack{l=1 \\ l \neq k}}^{N} C_{kl}, \qquad k = 1, 2, \ldots, N, \tag{21}$$

where $M(x_k) = \prod_{\substack{l=1 \\ l \neq k}}^{N} (x_k - x_l)$. The sampling points are chosen in the form of a cosine distribution as

$$x_k = \frac{a}{2}\left[1 - \cos\left(\frac{k-1}{N-1}\pi\right)\right], \qquad k = 1, 2, \ldots, N, \tag{22}$$

where a is the length in x-direction. Differentiating (19) with respect to α_1 and α_2 and using (20) together with the boundary conditions (see page 1775) leads to an overdetermined system of algebraic equations for displacements and stress resultants at the sampling points. These equations are then solved using least-squares minimization methods.

3. Numerical results

To verify the methodology developed in this study, the bending of symmetric ([0/90/0] and [90/0/90]) and antisymmetric [0/90] cross ply square plates, subjected to uniformly distributed transverse loads, were considered. A material with the following properties was used in these numerical calculations:

$$\frac{E_1}{E_2} = 25, \qquad \frac{G_{12}}{E_2} = \frac{G_{13}}{E_2} = 0.5, \qquad \frac{G_{23}}{E_2} = 0.2, \qquad \nu_{12} = 0.25,$$

in which E_1 and E_2 are the in-plane Young's modulus in the α_1 and α_2 coordinate directions. G_{12} is the in-plane shear modulus, G_{13} and G_{23} are the transverse shear modulus in the $\alpha_1 - n$ and $\alpha_2 - n$ planes, respectively, whereas ν_{12} is the major Poisson's ratio in the α_1-α_2 plane. The quantities w^* and M_1^* are

$$w^* = -\frac{10^3 E_2 h^3}{q_n a^4} w, \qquad M_1^* = \frac{10^3 M_i}{q_n a^2}.$$

Here, 'a' is the length of the edges of the square, and q_n denotes the uniformly distributed transverse load. In this study, three models with various boundary conditions were considered. The first model, called (S-S-S-S), is a plate with an SS2-type simply supported boundary condition on all edges. The second model, called (S-S-S-SF), is a plate with SS2-type simply supported boundary condition on three edges, and the fourth edge, corresponding to the edge $\alpha_1 = a$, is a mixed boundary condition of free and
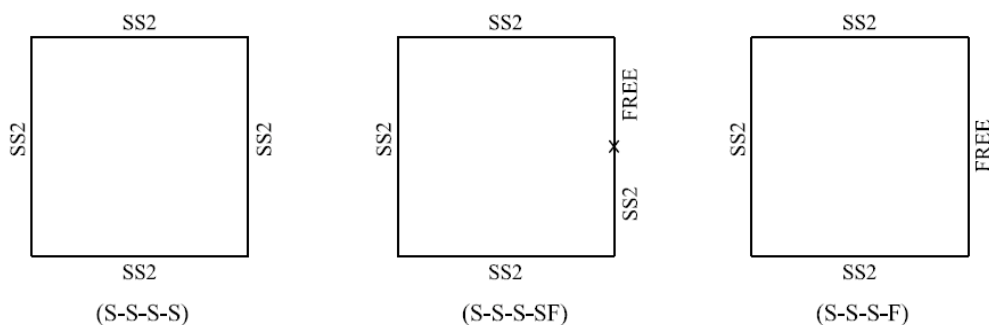
Figure 1. The models used in the present study with their various boundary conditions.

SS2-type simply supported boundary conditions, as shown in Figure 1. (S-S-S-F) is the last model and has three edges subjected to the SS2 boundary condition, and the edge corresponding to the edge $\alpha_1 = a$ is free.

The SS2-type simply supported boundary conditions and free edge defined on the edge $\alpha_i = \text{constant}$ are as follows:

SS2 type: $u_i = 0,$ $M_i = 0,$ $S_i = 0,$ $N_{ij} = 0,$ $\varphi_j = 0,$ $w_j = 0,$ $w = 0.$

Free edge: $N_i = 0,$ $M_i = 0,$ $S_i = 0,$ $N_{ij} = 0,$ $M_{ij} = 0,$ $S_{ij} = 0,$ $N_{in} = 0.$

In all models, the displacements and moments are computed at the center of the plate. Because the bending of a plate with mixed boundary conditions has not been extensively investigated, we compared the models to simulations performed with the ANSYS version 5.4 finite element software. The finite element mesh is composed of 400 SHELL99 elements with identical dimensions.

Table 1 compares the normalized central deflections of antisymmetric [0/90] and symmetric [0/90/0] and [90/0/90] cross ply square plates, characterized by four different a/h ratios, for the three models, computed using our approach versus ANSYS. In each direction, fifteen grid points are used for model (S-S-S-S), 17 for model (S-S-S-SF), and 19 for model (S-S-S-F). Table 2 shows the analogous compares for central moments.

The maximum w^* discrepancy between the two sets of results is observed for the (S-S-S-SF) model with a [0/90/0] lamination and $a/h = 10$. In comparing the results with FE, we mention that the boundary conditions used in the present approach are not identical to those in ANSYS. Therefore, we expect some discrepancies between the results. Nonetheless, discrepancies should not be more than 11%.

The discrepancies of the normalized central moments, M_1^*, between the two sets of results can be attributed to the fact that ANSYS calculates moments on grid points by extrapolating the moment calculated over the Gaussian points. Therefore, this method produces some approximations in the calculation of moments on grid points.

In the [90/0/90] lamination, the normalized central deflections of (S-S-S-SF) are larger than those of (S-S-S-F). A finite element analysis with 1600 elements ($a/h = 10$) was performed. The value of w^*, in the center of both (S-S-S-SF) and (S-S-S-F) models, is 11.73.

The first three rows of Figure 2 display the convergence (with $n_1 = n_2 = n$) of normalized transverse displacements w^* and normalized moments M_1^* for the (S-S-S-S), (S-S-S-SF), and (S-S-S-F) models
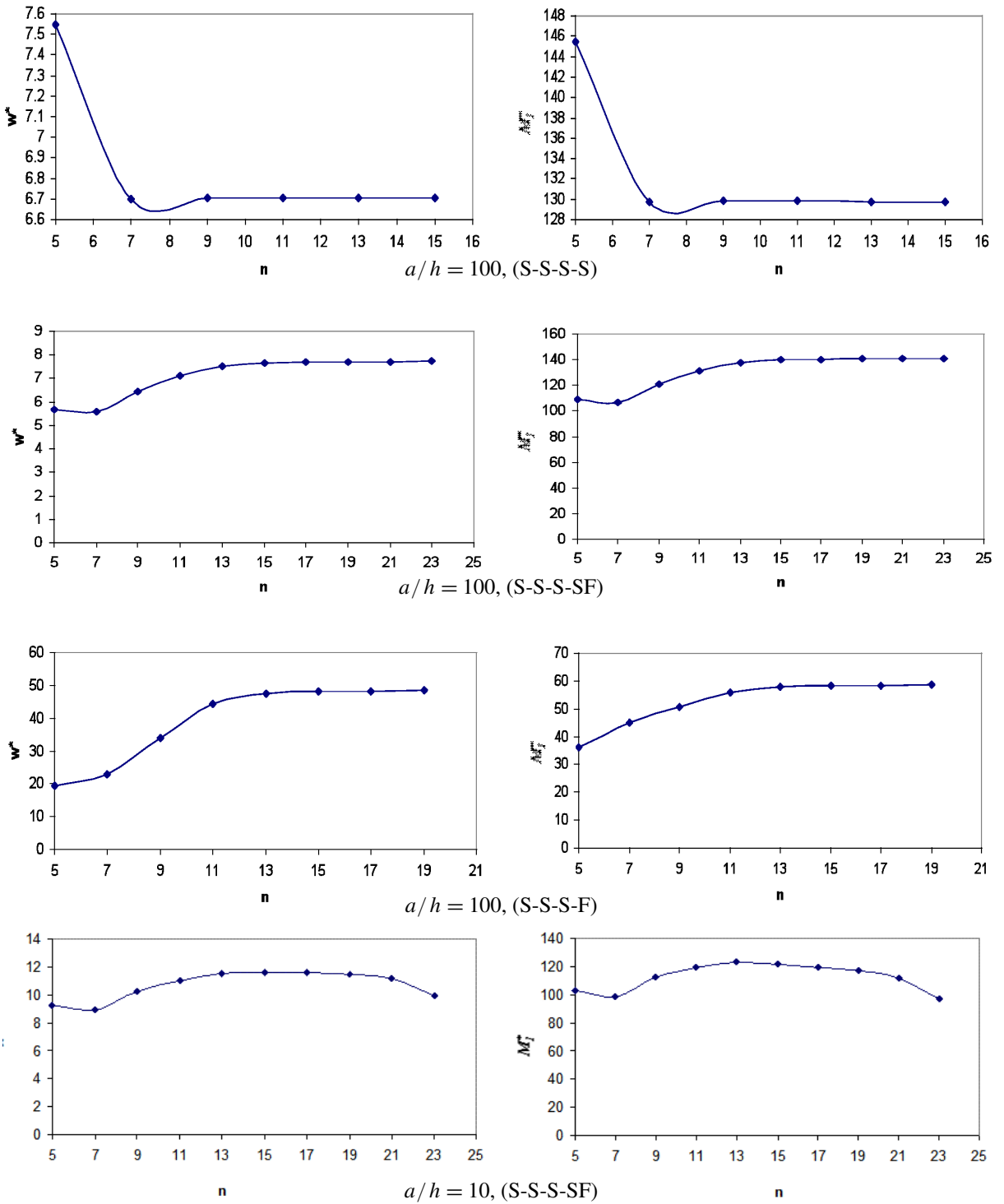
Figure 2. Convergence of the normalized central deflection w^* (left) and the normalized central moment M_1^* (right) of a symmetric cross ply [0/90/0] for the three models.

a/h		(S-S-S-S)		(S-S-S-SF)			(S-S-S-F)		
		[0/90]	[0/90/0]	[0/90]	[0/90/0]	[90/0/90]	[0/90]	[0/90/0]	[90/0/90]
10	present	11.73	10.98	11.65	11.60	11.41	17.88	52.79	10.97
	ANSYS	11.63	11.70	12.72	13.10	11.72	17.73	53.44	11.73
20	present	9.82	7.79	10.40	8.65	7.80	15.12	49.54	7.67
	ANSYS	9.72	7.96	10.58	9.34	7.96	14.98	49.64	7.85
50	present	9.23	6.84	9.76	7.87	6.84	14.27	48.54	6.72
	ANSYS	9.18	6.86	9.96	8.06	6.86	14.20	48.51	6.74
100	present	9.14	6.71	9.68	7.72	6.70	14.10	48.40	6.58
	ANSYS	9.11	6.73	9.87	7.83	6.73	14.09	48.55	6.61

Table 1. Normalized central deflections of square plates with different a/h ratios, cross ply patterns and models, calculated under the present approach and with ANSYS.

a/h		(S-S-S-S)		(S-S-S-SF)			(S-S-S-F)		
		[0/90]	[0/90/0]	[0/90]	[0/90/0]	[90/0/90]	[0/90]	[0/90/0]	[90/0/90]
10	present	69.42	122.88	63.19	116.55	14.94	23.14	53.90	7.26
	ANSYS	69.96	120.97	68.47	125.10	13.94	22.81	53.32	7.65
20	present	70.30	128.06	70.07	136.87	9.82	22.73	57.01	5.50
	ANSYS	70.67	128.20	69.08	141.03	9.80	22.66	56.89	5.61
50	present	70.64	129.57	73.75	140.15	8.58	22.57	58.21	4.92
	ANSYS	70.92	129.93	69.19	141.90	8.56	22.63	58.42	4.94
100	present	70.70	129.78	72.57	140.85	8.47	22.59	58.61	4.84
	ANSYS	70.97	130.17	69.18	142.02	8.39	22.63	58.82	4.84

Table 2. Normalized central moments of square plates with different a/h ratios, cross ply patterns and models, calculated under the present approach and with ANSYS.

describing symmetric cross ply [0/90/0] square plates with $a/h = 100$. Rapid convergence was observed for the (S-S-S-S) model, and convergence of the (S-S-S-SF) model was the slowest. The convergence of each model was similar for different a/h ratios, with the exception of model (S-S-S-SF), with $a/h = 10$, shown at the bottom in Figure 2. It is interesting to note that, as observed in this latter figure, the curve of convergence initially ascends, then descends at $n = 15$. The number 15 is reported as the convergence number for this case. Actually, convergence for the deflections and moments, for thicker plates, was accomplished with a smaller number of grid points. This characteristic was observed by Lanhe et al. [2005] in the vibration analysis of composite plates, by applying a least square GDQ method based on FSDT.

Figure 3, top left, compares the variation in central deflections w^* for three different laminations, including antisymmetric [0/90] and symmetric [0/90/0], [90/0/90], with respect to the a/h ratio, for the (S-S-S-S) model. It is seen in the figure that the normalized central deflections of two symmetric cross ply laminates are equal because the boundary conditions imposed on all edges are similar. However, the normalized central deflections, of the antisymmetric cross ply plate are considerably larger that their
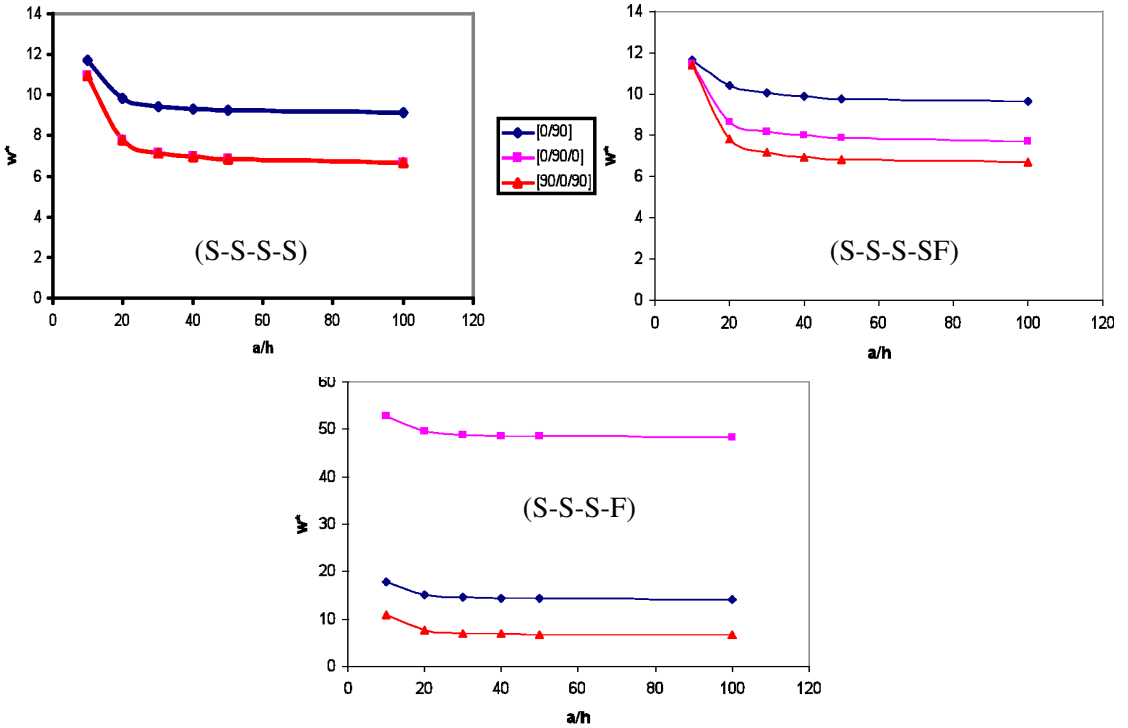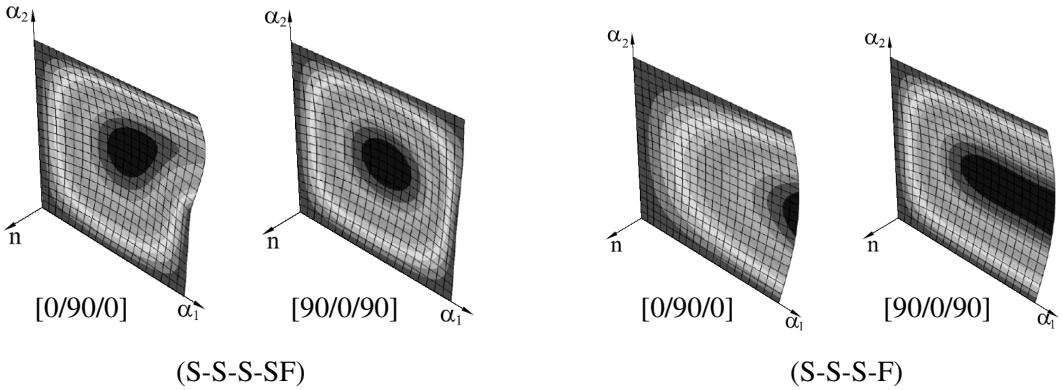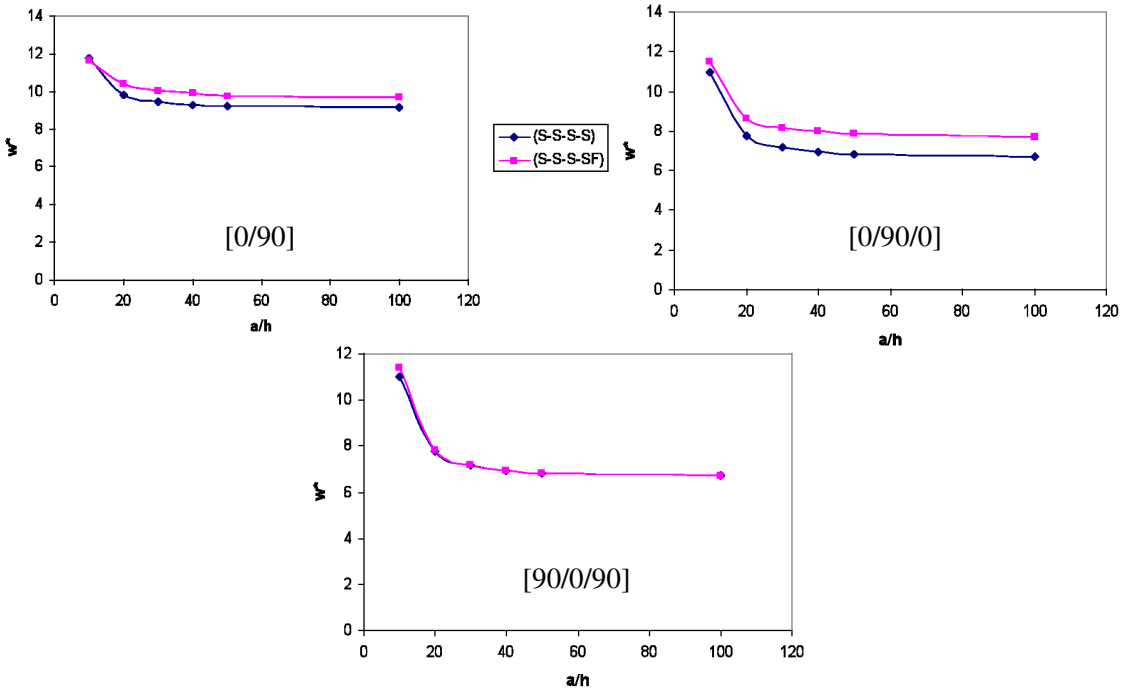
Figure 3. Variation in central deflection w^* with respect to the a/h ratio for [0/90], [0/90/0], and [90/0/90] laminations, in the three models.

symmetric counterparts. As the a/h ratio decreases from thin to moderately thick, the difference between symmetric and antisymmetric lamination decreases, and this decrease is much larger for moderately thick aspect ratios ($10 < a/h < 20$). This behavior is known as the "beam–column/tie bar" effect caused by the bending-stretching coupling present in the antisymmetric laminate.

Figure 3, top right, presents a comparison of the variation in central deflections w^* for three different laminations, including antisymmetric [0/90] and symmetric [0/90/0], as well as [90/0/90], with respect to the a/h ratio, for the (S-S-S-SF) model. As can be observed from the rule, the normalized central deflections of the two symmetric cross ply laminates are different, because the boundary conditions on the two edges $\alpha_1 = 0$ and $\alpha_1 = a$ are different. Therefore, in the [0/90/0] lamination, the orientation of most fibers of the laminate material is along to α_1 coordinate. This increases the deflection caused by the free part of the edge $\alpha_1 = a$. The difference between the behavior of the laminations [0/90/0] and [90/0/90] for the (S-S-S-SF) model is shown in the first two panels of Figure 4.

Figure 3, bottom, shows the comparison of the of the variation in the central deflections w^* for three different laminations, including antisymmetric [0/90] and symmetric [0/90/0], [90/0/90], with respect to the a/h ratio, for the (S-S-S-F) model. The figure highlights the differences between the laminations. In the [0/90/0] lamination, as was described for (S-S-S-SF), the direction of most fibers of the laminate material is along to α_1 axis. This contributes to an increase in the deflection of the plate. The difference between the behavior of laminations [0/90/0] and [90/0/90] is shown in Figure 4, right.

Figure 4. Displacement contours of a plate with laminations [0/90/0] and [90/0/90] for two of the models.

Figure 5 compares the central deflection of the (S-S-S-S) and (S-S-S-SF) models, for [0/90], [0/90/0], and [90/0/90] laminations. The maximum difference between (S-S-S-S) and (S-S-S-SF) is observed in the [0/90/0] lamination, and the minimum difference is observed in the [90/0/90] lamination. This effect can be understood from the explanation given for Figure 4, left.

Figure 5. Variation in central deflection w^* with respect to the a/h ratio for [0/90], [0/90/0], and [90/0/90] laminations, in the (S-S-S-S) and (S-S-S-SF) models.
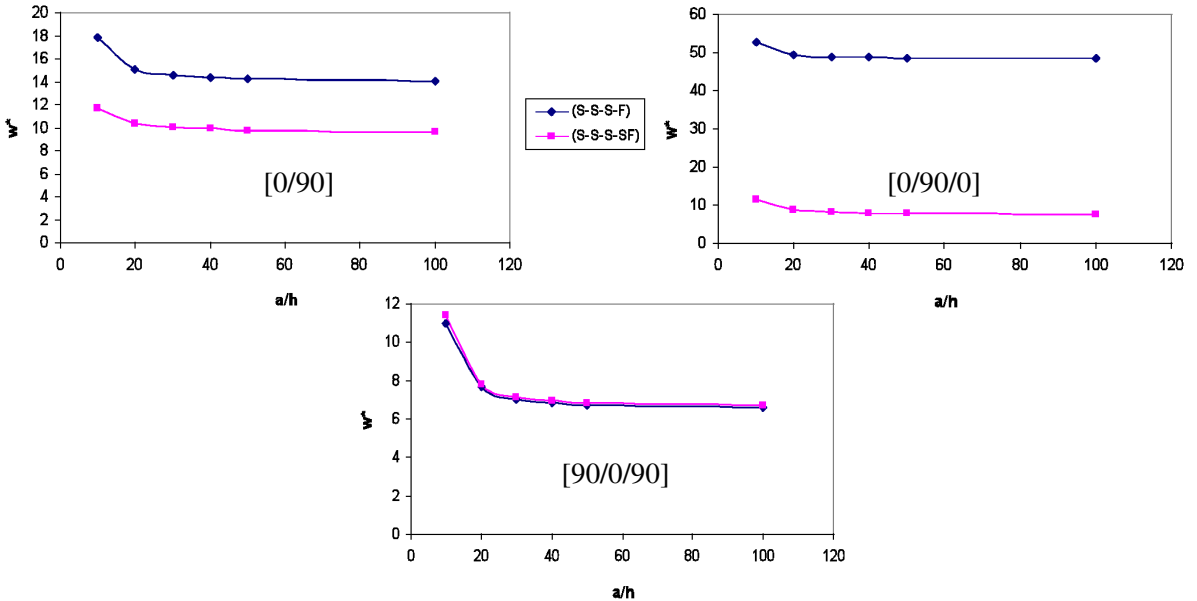
Figure 6. Variation in central deflection w^* with respect to the a/h ratio for [0/90], [0/90/0], and [90/0/90] laminations, in the (S-S-S-F) and (S-S-S-SF) models.

Figure 6 illustrates the comparison of central deflections, w^*, of the (S-S-S-SF) and (S-S-S-F) models for [0/90], [0/90/0], and [90/0/90] laminations. The maximum difference between (S-S-S-S) and (S-S-S-SF) is observed in the [0/90/0] lamination, and the minimum difference is in the [90/0/90] lamination. Although the boundary condition, SF, is much stronger than the boundary condition, F, in the [90/0/90] lamination, most of the normalized central deflections in the model (S-S-S-SF) are larger than those of (S-S-S-F). In the case of an isotropic material, it is always expected that the normalized central deflections of (S-S-S-F) are larger than those of (S-S-S-SF). However, when using composite materials, the behavior of the structure is more complex. We come to the conclusion that, in addition to the boundary conditions, the direction of the lamination contributes to the behavior of the structure.

4. Conclusion

A new formulation, based on higher-order shear deformation theory, is presented to solve the problem of laminated plates with mixed boundary conditions. Using the principle of virtual work, the governing equations, together with the required boundary conditions for higher-order shear deformation, are formulated. The equations are solved numerically by means of the generalized differential quadrature method. Three models differing in their boundary conditions on one edge are considered. The results are compared against solutions obtained using ANSYS, and reasonable agreement is observed. Numerical results presented here for cross ply plates demonstrate a reasonably fast convergence for the (S-S-S-S) model and slow convergence for the (S-S-S-SF) model.

When an isotropic material is used, it is usually expected that, because the constraint on SF is much stronger than the constraint on F, the normalized central deflections of (S-S-S-F) are larger than those of (S-S-S-SF). According to the tables, for the lamination [90/0/90], normalized central deflections of

(S-S-S-SF) are larger than those of (S-S-S-F). This result illustrates that when a composite material is used, the behavior of the structure is more complex, and we can come to the conclusion that, in addition to the boundary conditions, the direction of the lamination contributes to the behavior of the structures.

The direction of fibers in the [0/90/0] and [90/0/90] laminations has a significant effect, especially for models (S-S-S-SF) and (S-S-S-F). When the direction of most of the fibers is perpendicular to the free edge, the central deflections of the plates are larger than when it's parallel. The effect of the transverse shear deformation is described by the conceptual bending-stretching coupling effect, a characteristic of antisymmetric laminates. This characteristic is obvious in the model (S-S-S-S).

References

[Aghdam et al. 2006] M. M. Aghdam, M. R. N. Farahani, M. Dashty, and S. M. Rezaei Niya, "Application of generalized differential quadrature method to the bending of thick laminated plates with various boundary conditions", *Appl. Mech. Mater.* **5–6** (2006), 407–414.

[Basset 1890] A. B. Basset, "On the extension and flexure of cylindrical and spherical thin elastic shells", *Phil. Trans. R. Soc. A* **181** (1890), 433–480.

[Bellman et al. 1972] R. Bellman, B. G. Kashef, and J. Casti, "Differential quadrature: a technique for the rapid solution of nonlinear partial differential equations", *J. Comput. Phys.* **10**:1 (1972), 40–52.

[Bert and Chen 1978] C. W. Bert and T. L. C. Chen, "Effect of shear deformation on vibration of antisymmetric angle-ply laminated rectangular plates", *Int. J. Solids Struct.* **14**:6 (1978), 465–473.

[Bert and Francis 1974] C. W. Bert and P. H. Francis, "Composite material mechanics: structural mechanics", *AIAA J.* **12**:9 (1974), 1173–1186.

[Bert et al. 1988] C. W. Bert, S. K. Jang, and A. G. Striz, "Two new approximate methods for analyzing free vibration of structural components", *AIAA J.* **26**:5 (1988), 612–618.

[Bert et al. 1989] C. W. Bert, S. K. Jang, and A. G. Striz, "Nonlinear bending analysis of orthotropic rectangular plates by the method of differential quadrature", *Comput. Mech.* **5**:2–3 (1989), 217–226.

[Lanhe et al. 2005] W. Lanhe, L. Hua, and D. Wang, "Vibration analysis of generally laminated composite plates by the moving least squares differential quadrature method", *Compos. Struct.* **68**:3 (2005), 319–330.

[Li and Cheng 2005] J.-J. Li and C.-J. Cheng, "Differential quadrature method for nonlinear vibration of orthotropic plates with finite deformation and transverse shear effect", *J. Sound Vib.* **281**:1–2 (2005), 295–309.

[Malekzadeh and Setoodeh 2007] P. Malekzadeh and A. R. Setoodeh, "Large deformation analysis of moderately thick laminated plates on nonlinear elastic foundations by DQM", *Compos. Struct.* **80**:4 (2007), 569–579.

[Mindlin 1951] R. D. Mindlin, "Influence of rotatory inertia and shear on flexural motions of isotropic, elastic plates", *J. Appl. Mech.* (*ASME*) **18**:1 (1951), 31–38.

[Naghdi 1956] P. M. Naghdi, "A survey of recent progress in theory of elastic shells", *Appl. Mech. Rev.* (*ASME*) **9**:9 (1956), 365–388.

[Quan and Chang 1989] J. R. Quan and C. T. Chang, "New insights in solving distributed system equations by the quadrature methods, I: Analysis", *Comput. Chem. Eng.* **13**:7 (1989), 779–788.

[Reddy and Liu 1985] J. N. Reddy and C. F. Liu, "A higher-order shear deformation theory of laminated elastic shells", *Int. J. Eng. Sci.* **23**:3 (1985), 319–330.

[Reissner 1945] E. Reissner, "The effect of transverse shear deformation on the bending of elastic plates", *J. Appl. Mech.* (*ASME*) **12**:2 (1945), 69–77.

[Sherbourne and Pandey 1991] A. N. Sherbourne and M. D. Pandey, "Differential quadrature method in the buckling analysis of beams and composite plates", *Comput. Struct.* **40**:4 (1991), 903–913.

[Shu 1991] C. Shu, *Generalized differential quadrature integral quadrature and application to the simulation of incompressible viscous flows including parallel computation*, Ph.D. thesis, University of Glasgow, 1991.

[Shu and Richards 1990] C. Shu and B. E. Richards, "High resolution of natural convection in a square cavity by general-ized differential quadrature", pp. 978–985 in *Numerical methods in engineering: theory and appreciations* (*NUMETA 90*) (Swansea, 1990), vol. 2, edited by G. N. Pande and J. Middleton, Elsevier, London, 1990.

[Striz et al. 1988] A. G. Striz, S. K. Jang, and C. W. Bert, "Nonlinear bending analysis of thin circular plates by differential quadrature", *Thin-Walled Struct.* **6**:1 (1988), 51–62.

[Tornabene and Viola 2008] F. Tornabene and E. Viola, "2-D solution for free vibrations of parabolic shells using generalized differential quadrature method", *Eur. J. Mech. A Solids* **27**:6 (2008), 1001–1025.

MOJGAN YAGHOUBSHAHI: moyaeng@gmail.com
Department of Civil and Environmental Engineering, Amirkabir University of Technology, 424 Hafez Avenue, Tehran 15914, Iran

HOSSEIN RAJAIE: rajaieh@aut.ac.ir
Department of Civil and Environmental Engineering, Amirkabir University of Technology, 424 Hafez Avenue, Tehran 15914, Iran
http://www.aut.ac.ir/official/main.asp?uid=rajaieh

AXIAL COMPRESSION STABILITY OF A CRISSCROSS SECTION COLUMN COMPOSED OF CONCRETE-FILLED SQUARE STEEL TUBES

CHEN ZHI-HUA, RONG BIN AND APOSTOLOS FAFITIS

A crisscross section column composed of concrete-filled square steel tubes was tested in axial loading up to failure. The column was analyzed by the finite element method and the ultimate load as well as the failure mode were in agreement with the experimental findings. An analytical method was also proposed which when applied to the tested column gave an estimate of the ultimate load about 4% different from the experimental. The analytical method also predicted the mode of failure correctly.

1. Introduction

Special-shaped columns have found applications in many structures, especially residential buildings. Compared with regular columns, special-shaped columns have the distinguishing characteristic of flexible sections such as L-shaped, T-shaped, and crisscross sections. The use of special-shaped columns in residential buildings can give more indoor space than regular rectangular or square columns.

The behavior of special-shaped reinforced concrete columns has been the subject of investigation and many experimental and analytical studies have been published. Ramamurthy and Hafeez Khan [1983] have proposed a method to determine the theoretical ultimate loads of L-shaped concrete columns based on the concept of an equivalent square or rectangular column. Hsu [1985; 1989] has presented theoretical and experimental results for L-shaped and T-shaped reinforced concrete sections. Mallikarjuna and Mahadevappa [1992; 1994] have carried out numerical investigations on the strength of L-shaped and T-shaped short reinforced concrete columns that have been subjected to combined axial loading and bending in order to provide design aids for structural engineers. Tsao and Hsu [1993; 1994] have presented an experimental and analytical investigation of the strength and deformation behavior of biaxially loaded slender and tied columns with L-shaped cross sections. Dundar et al. [2008; Dundar and Sahin 1993] have studied reinforced concrete L-shaped sections under biaxial bending and axial loads. Demagh et al. [2005] have carried out numerical investigations for the analysis and the design of L-shaped short reinforced concrete columns subjected to combined axial loads and bending based on the fiber method. Tokgoz and Dundar [2008] have studied the behavior of concrete-encased composite columns with L-shaped sections under short-term axial loads and biaxial bending by means of both experiment and theoretical analysis. For determination of the behavior of eccentrically loaded short and slender composite columns, a theoretical procedure considering the nonlinear behavior of the materials has been proposed.
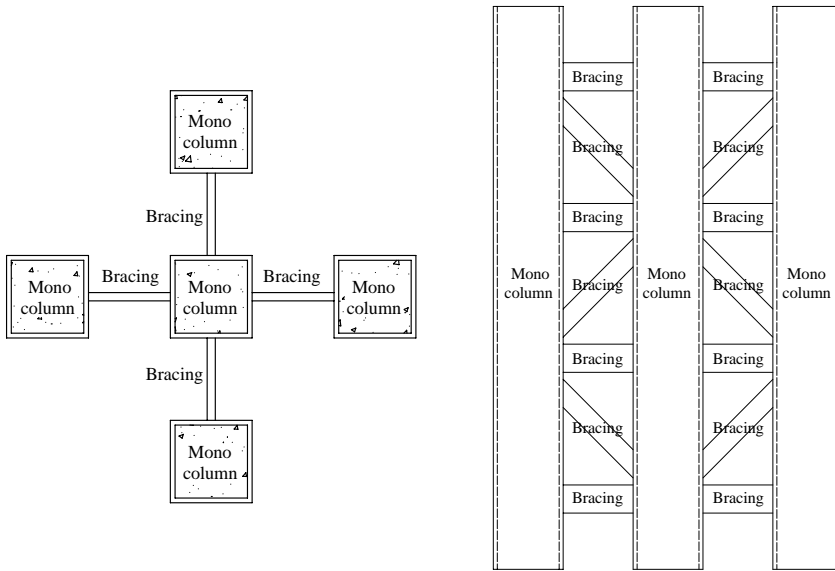
Figure 1. Schematic of a XCFST column.

In recent years, concrete-filled square steel tubular (CFST) columns have been widely used in the construction of buildings due to their excellent static and earthquake-resistant properties, such as high strength, high ductility, and large energy dissipation capacity. A large number of studies have been carried out on CFST columns. Several surveys on CFST structures have also been published [Han 2002; Tsai et al. 2003; Sakino et al. 2004; Fujimoto et al. 2004; Han et al. 2008]. By contrast, special-shaped columns consisting of CFST columns have not been studied. The focus of this investigation is a new type of crisscross section column composed of concrete-filled square steel tubes (XCFST) made up of five CFST columns with steel bracing connections as shown in Figure 1. Since each monocolumn is a CFST column, the whole XCFST column also has better static, earthquake, and fire resistance behavior.

Compared to regular columns, as shown in Figure 2, each monocolumn of an XCFST column has a smaller section. Therefore, in residential buildings, they can be embedded in walls so as to avoid convex corners indoors and to enlarge the usable interior area.
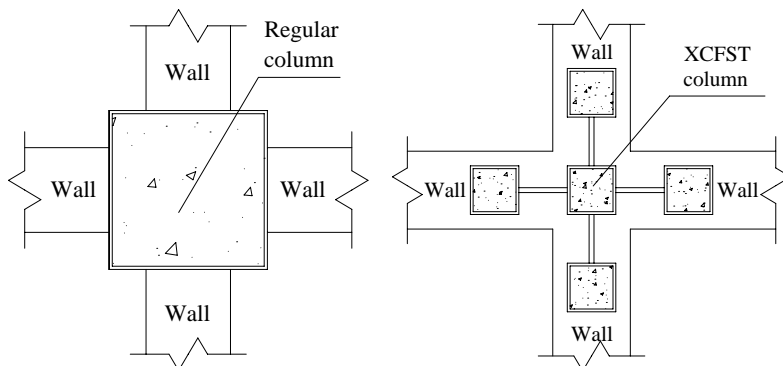
Figure 2. Applications of a regular column and an XCFST column.

The objectives of this study are to determine the maximum load-bearing capacity of an XCFST column subjected to axial compression and to investigate the failure pattern up to the ultimate load. We adopted a three-pronged approach: experiment, analytical study, and finite element simulation. Specifically, we report the experimental test results of an XCFST column under axial compression, use finite element modeling to analyze the process, and develop a method for calculating the maximum load-bearing capacity of an XCFST column under axial compression. All three approaches were applied to the same model, which we describe in the next section.

2. Experimental work

The specimen. The specimen in the experimental study was an XCFST column that was two meters long with square steel tubes of $100 \, \text{mm} \times 100 \, \text{mm} \times 5.75 \, \text{mm}$. The horizontal bracings were $100 \, \text{mm} \times 40 \, \text{mm} \times 10 \, \text{mm}$, and the diagonal bracings were $142 \, \text{mm} \times 28 \, \text{mm} \times 10 \, \text{mm}$ at $45°$.

The manufacturing process of the specimen was as follows. The tubes were all manufactured from steel plates, with the plates being tack welded into a square shape. After this, the square steel tubes and bracings were cut and welded together. A 10 mm thick steel plate was welded on the bottom of the specimen. Concrete was cast and consolidated in the square steel tubes tightly. After curing, a layer of cement mortar was used as a cap so that the concrete surface was flush with the steel tube at the top. Finally another 10 mm thick steel plate was welded at the top of the specimen. The specimen is shown in Figure 3, left.

Material properties. To determine the steel properties of the square tubes and the bracings, tension coupons were cut and tested in tension. For the square tubes, the average yield strength was 229 MPa, the ultimate strength 429 MPa, and the modulus of elasticity 1.89×10^5 MPa. For the bracings, the average yield strength was 274 MPa, the ultimate strength 415 MPa, and the modulus of elasticity 4.11×10^5 MPa.
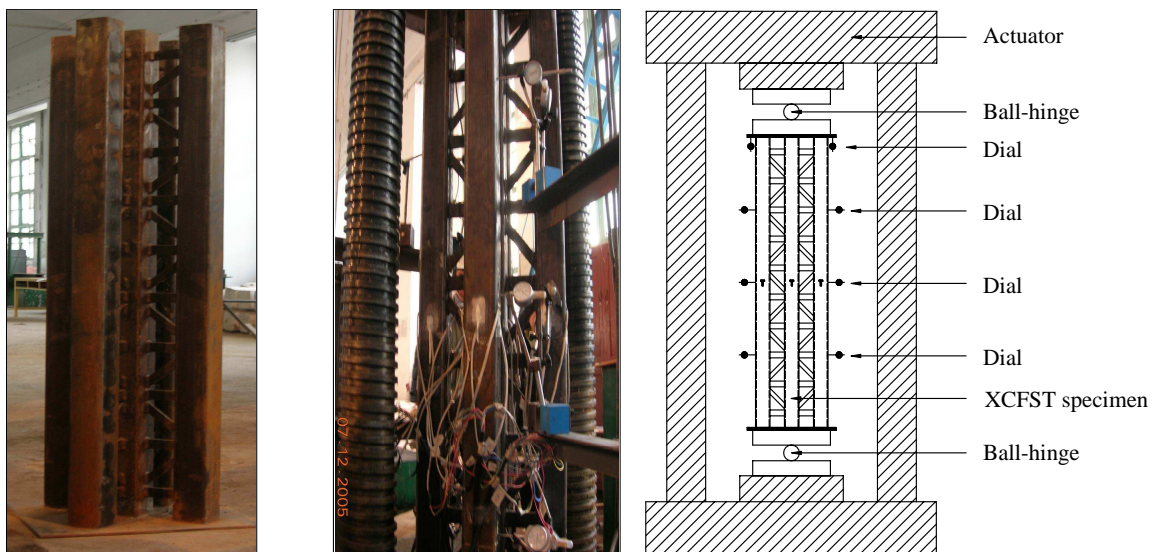
Figure 3. Left: The XCFST specimen. Middle and right: Test setup for the specimen.

To determine the concrete material properties, three $150 \times 150 \times 150$ mm cubes were cast and cured in conditions similar to that of the experiment. The mix proportions of concrete were cement 353 kg/m^3, water 175 kg/m^3, sand 696 kg/m^3, and coarse aggregate 1088 kg/m^3. The average crushing strength of these concrete cubes after 28 days was 49.7 MPa and the modulus of elasticity was 4.33×10^4 MPa.

Test procedure. The XCFST specimen was tested with pinned conditions at both ends using a 5000 kN capacity axial actuator. The testing setup for the XCFST specimen is shown in Figure 3, middle and right.

The specimen was loaded until it reached the failure point. A load interval of about one tenth of the estimated carrying load capacity was used. Each load interval was maintained for about 2–3 minutes. The progress of deformation, the mode of failure, and the maximum load taken by the specimen were recorded continuously.

During the test, the load level was controlled by the actuator. The lateral dials monitored the deflection of the monocolumns. The vertical dials recorded the displacement of the XCFST column. The location of the instrumentation is shown in Figure 4, left. The labels 1, 4, 7, and 10 indicate the lateral dials attached at 1.5 m from the ground plate; 2, 5, 8, and 11 indicate the lateral dials at 1.0 m, which is the middle height of each monocolumn; 3, 6, 9, and 12 indicate the lateral dials at 0.5 m; and 13 and 14 indicate the vertical dials in the top plate of the XCFST column.

Test results. The test was stopped when the XCFST column reached the ultimate bearing capacity. The deformation of failure was very small. Figure 4, right, shows the failure mode of the XCFST column, and as shown there were small deformations of each monocolumn.

Load versus axial shortening. The load versus shortening curve provides information on the ultimate carrying capacity of the XCFST column specimen.
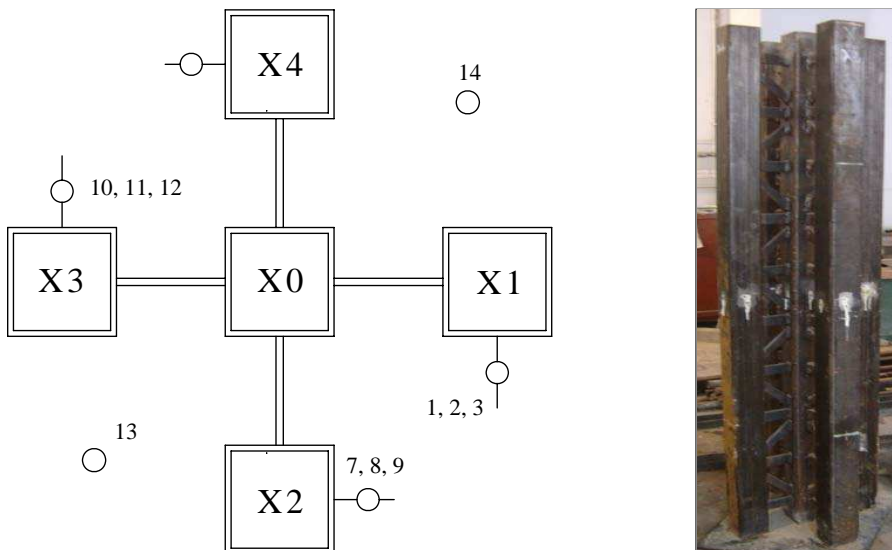
Figure 4. Left: positions of dial indicators. Right: Deformation of the XCFST specimen.
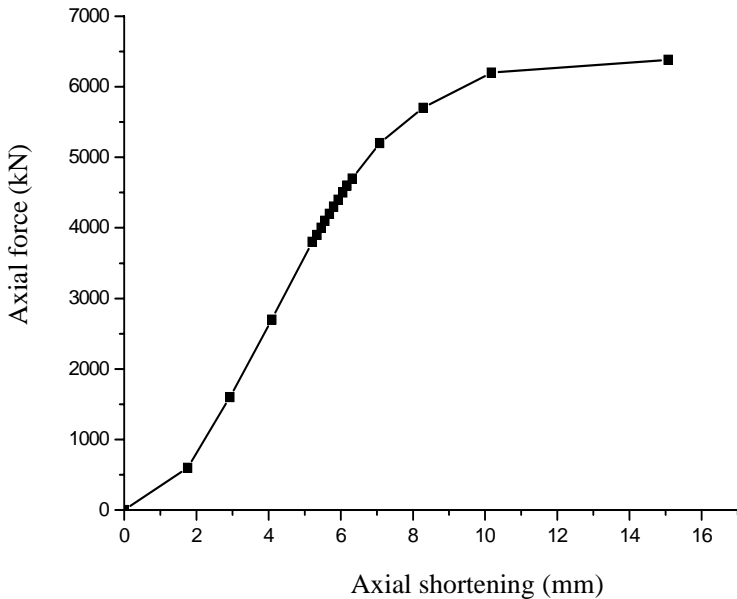
Figure 5. Axial load versus shortening curve of the XCFST specimen.

Figure 5 shows the relation of the axial force and axial shortening of the XCFST specimen. Note that up to about 6100 kN, the behavior was almost linear. Beyond this load, the XCFST column entered the bulking stage. Finally at a load of 6390 kN, the shortening was 15.2 mm and the test was stopped.

Deflection of monocolumn. Figure 6 shows the deformation history of each monocolumn. The number in parenthesis identifies the dials (for example, 1, 2, and 3). The load level designation from 600 kN to 6390 kN is shown in the box next to the profile of the column.

According to Figure 6, at the failure load of 6390 kN, the deflection of monocolumn X3 was the largest of the four monocolumns. The failure process was initiated by the buckling of monocolumn X3.

Discussions of experimental behavior of specimen. From the load-deformation curve, it is apparent that for a load less than about 6100 kN the XCFST column remains in the elastic range. This is true for the monocolumns X2, X3, and X4. For a load above 6100 kN the column enters gradually into the buckling stage and the load-deformation curve deviates from linearity. At a load of 6390 kN, the XCFST column has reached its ultimate capacity. Finally it appears that the failure process is initiated by the buckling of monocolumn X3.

3. Finite element analysis

General. The commercial finite element software ANSYS has been used to simulate the axial compression experiment of the XCFST specimen as described before. There are three main components that need to be modeled in order to simulate the behavior of the XCFST column. These are the steel tubes and bracings, the infilled concrete, and the interface between the concrete and the steel tube. In addition, the choice of the element type, the mesh size, the initial geometric deformation, the boundary conditions, and the load application are also important in simulating the special-shaped column.
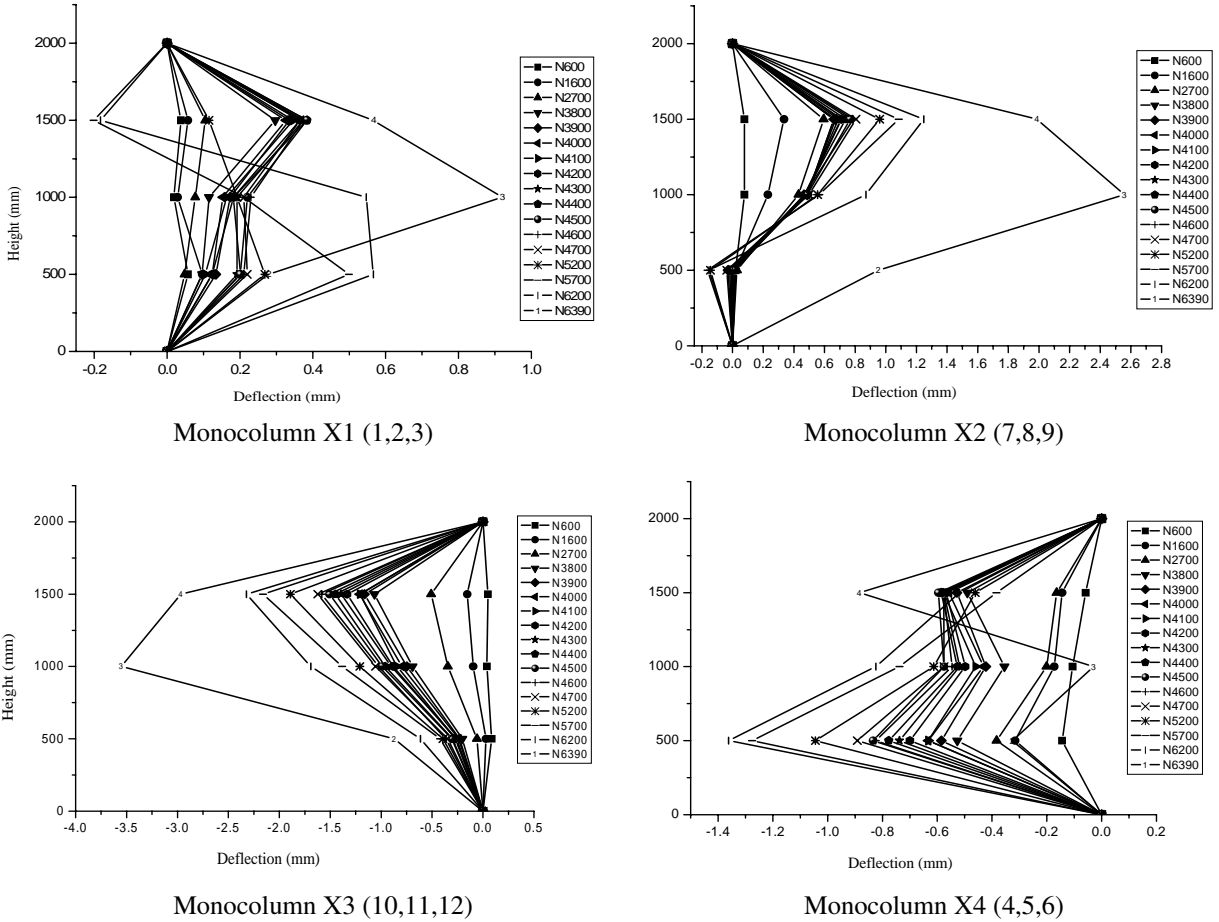
Figure 6. Deflection of single concrete-filled square steel tubes.

Modeling of the steel tubes and bracings. In this simulation, the element SHELL 181 was used to model the steel tubes and bracings. SHELL 181 is a 4-node doubly curved shell element which has six degrees of freedom per node. This element's capacity for transverse shear deformation provides adequate accuracy in simulating the buckling behavior of the steel tubes.

The constitutive law of steel tubes and bracings [GB50017 2003] was assumed elastoplastic with yielding strain equal to f_y/E_s. The strain hardening was ignored and the Poisson's ratio was equal to 0.3. The idealized stress-strain curve used in the numerical analysis is shown in Figure 7, left.

Modeling of the concrete. The three-dimensional 8-node element SOLID 65 was adopted to model the infilled concrete. Each node of the element has three degrees of freedom. This element is capable of cracking, crushing, and plastic deformation and can achieve accurate results in simulating the behavior of concrete in axial loads.

The ratio of the thickness of the tube plates to the overall size of the tube cross section was not adequate to provide confinement. Therefore, the uniaxial stress-strain curve was adopted [Ellobody and Young 2006]. The constitutive law of concrete has two branches. The ascending branch was assumed to
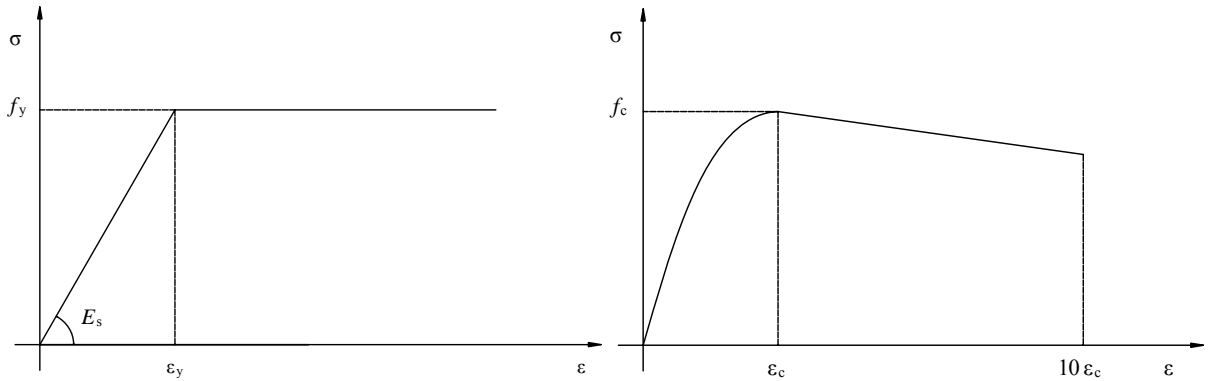
Figure 7. Left: constitutive law of steel tubes and bracings. Right: constitutive law of concrete.

be parabolic up to a strain equal to 0.003 and the descending branch was linear, as shown on the graph on the right in Figure 7.

Modeling of the concrete-steel tube interface. The contact action between the steel tube and the concrete was modeled by the contact elements TARGE 170 and CONTA 173. These surface-to-surface contact elements consist of two matching contact faces of the steel tube and concrete elements. The friction between the two faces is maintained as long as the surfaces remain in contact. The coefficient of friction between the two faces was taken as 0.25 in the analysis. These contact elements allow the surfaces to separate under the influence of tensile force. However, the contact elements are not allowed to penetrate each other.

Mesh size and initial geometrical deformation. Different mesh sizes have been tried to choose a reasonable mesh that can provide both accurate results and reasonable computational time. It was found that a mesh size of approximately 1:1:2 (length:width:depth) for solid elements and 1:1 (length:width) for shell elements can achieve accurate results. The coincident nodes between steel tubes and bracings were merged after all elements were meshed in order to ensure that the deformations of the steel tubes and bracings in such places were identical.

In practice, there are initial geometrical deformations in the XCFST specimen. Therefore the influence of initial geometrical deformation was considered in this simulation. For this purpose, a 1‰ initial deformation resembling the first-order buckling mode was introduced to the finite element modeling.

Boundary conditions and load application. Pinned boundary conditions were assumed. The top and bottom surfaces of the XCFST column were restrained in all translational degrees of freedom except for the displacement of the top plate in the direction of the applied load.

The load was applied as a static uniform load using the displacement control at each node of the loaded top surface, and the displacements were applied in incremental steps, which were identical to the steps of the experimental investigation.

The finite element model is shown in Figure 8.

Procedure verification. In order to validate the finite element analysis, recent axial compression experimental results on 42 concrete-filled square steel tubes conducted by Li et al. [1998] were compared with
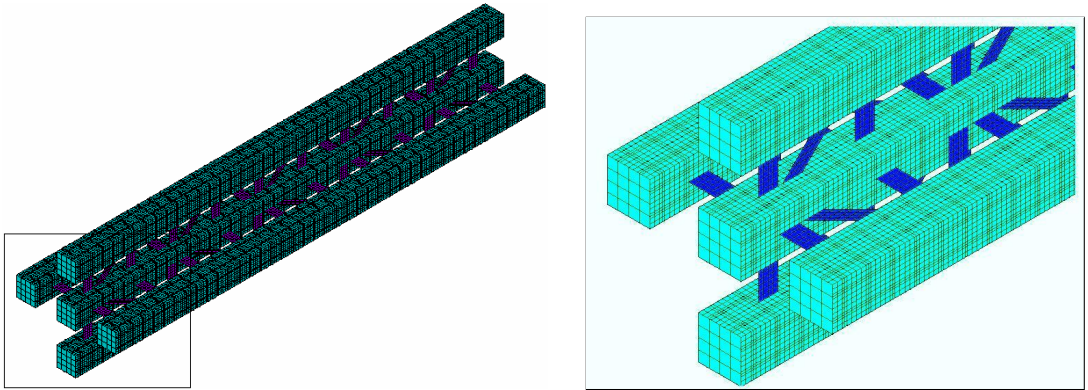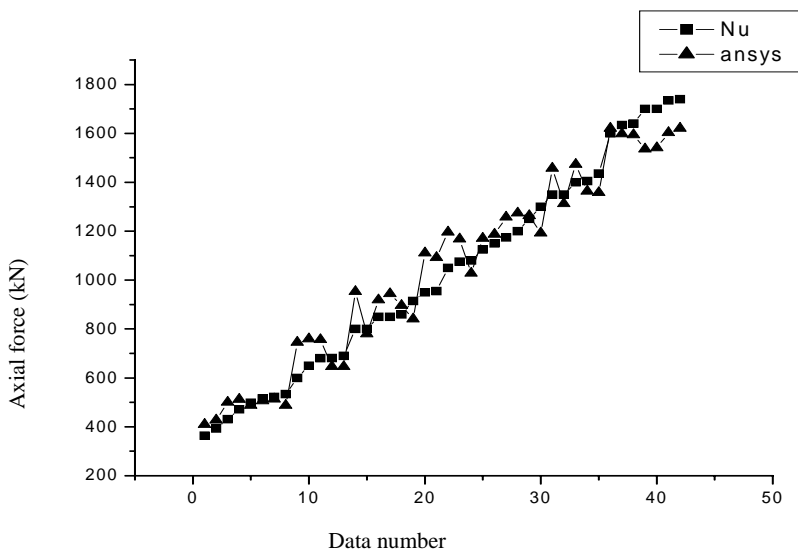
Figure 8. Finite element model.

the results of the finite element model in this study. The mean difference between the experiment data and the simulated results, shown in Figure 9, was less than 5%.

Comparison of results. The force-deformation curve obtained by finite element analysis is shown in Figure 10. The ultimate capacity is 5929 kN. The failure mode is shown in Figure 11. It was found that the deformation of the monocolumns was in the flexure mode whereas the deformation mode of the XCFST column was very small.

Note that the experimentally obtained failure load (6390 kN) compares well with the value predicted by finite element analysis (5929 kN), with a difference of 7.2%. Also the experimentally observed deformation models of the monocolumns and the XCFST column were the same as the ones predicted by finite element analysis.

Figure 9. Comparison between testing data and calculated data by ANSYS.
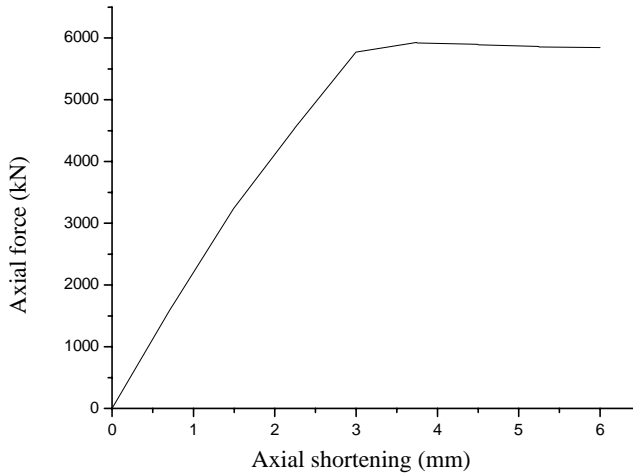
Figure 10. Load versus axial shortening curve.
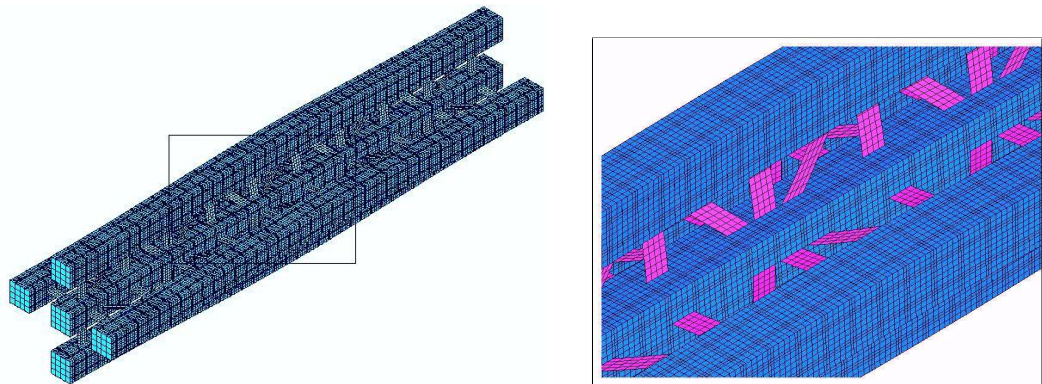
Figure 11. Failure mode of finite element model.

4. Analytical evaluation of the axial capacity

General. According to the Design Code for Steel Structures [GB50017 2003], the ultimate bearing capacity N_u, the sum of the capacities of the steel and the concrete, and the design capacity N are given by

$$N_u = \lambda \cdot f_y \cdot A_s + f_c \cdot A_c, \qquad N \leq N_u, \tag{1}$$

where λ is the stability factor, f_y is the yield stress of the steel, f_c is the axial strength of the concrete, A_c is the cross sectional area of the concrete, and A_s is the cross sectional area of the steel tube.

The slenderness ratio (λ_o). In an XCFST, the shear stiffness of the bracings among the monocolumns is weak so that buckling may happen under axial compression and the calculation of the slenderness ratio of the XCFST is the key component in the superposition theory.

The formula for λ_o is derived based on the following assumptions: All three monocolumns have the same size and material properties for steel and concrete. The horizontal and diagonal bracings have the same size. The spatial truss model is employed for the analysis.

The slenderness ratio of a truss with pinned supporting condition is given by the theory of elastic stability [Leonard and George 2005]:

$$\lambda_o = \sqrt{\lambda_1^2 + \pi^2 \gamma_1 \sum_{i=1}^{n} (E_s A_{si} + E_c A_{ci})}, \tag{2}$$

where λ_o is the slenderness ratio of the XCFST column, λ_1 is the slenderness ratio of the unbraced columns for the x-x or y-y axis as shown in Figure 12, γ_1 is the angle of unit shear as explained later (see (4)), n is the number of monocolumns, E_s is the steel modulus of elasticity, A_s is the cross sectional area of the steel tubes, E_c is the concrete modulus of elasticity, and A_c is the cross sectional area of the concrete.

The derivation of the slenderness ratio for buckling is based on Figure 13. One half of the structure is shown in Figure 13c because of symmetry.

From Figure 13b and c, it can be seen that the axial force of the diagonal bracing N_d is $N_d = \dfrac{1}{2 \sin \theta}$, where θ is the angle between the steel tube and the diagonal bracing.

The axial deformation of the diagonal bracing Δ_d is:

$$\Delta_d = \frac{N_d l_d}{E_s A_1} = \frac{a}{2 E_s A_1 \sin \theta \cos \theta}, \tag{3}$$

where l_d is the length of the diagonal bracing, a is the length of vertical projection for the diagonal bracing, and A_1 is the cross sectional area of the diagonal bracing.

Therefore, the angle of the unit shear is:

$$\gamma_1 \approx \frac{\Delta}{a} = \frac{\Delta_d}{a \sin \theta} = \frac{1}{2 E_s A_1 \sin^2 \theta \cos \theta}, \tag{4}$$

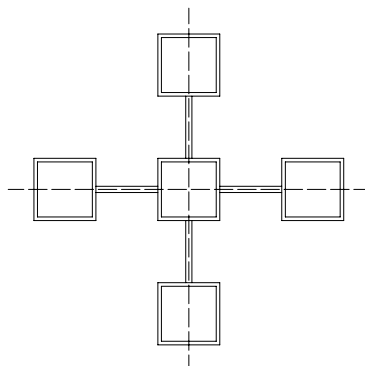where Δ is the length of horizontal projection of axial deformation for the diagonal bracing Δ_d.

Figure 12. XCFST section inertia axis.

Substituting γ_1 from (4) into (2), the equivalent slenderness ratio becomes:

$$\lambda_o = \sqrt{\lambda_1^2 + \frac{5\pi^2(E_s A_s + E_c A_c)}{2E_s A_1 \sin^2\theta \cos\theta}}. \tag{5}$$

Application of the analytical method. The method explained in the previous paragraph will be applied to compute the ultimate axial capacity of the tested XCFST column.

With reference to the previous two subsections, the values of the structural parameters involved in Equations (1)–(5) are the following:

$$n = 5, \quad A_s = 2167.75\,\text{mm}^2, \quad A_c = 7832.25\,\text{mm}^2, \quad A_1 = 280\,\text{mm}^2, \quad I = 189526605\,\text{mm}^4,$$

$$\theta = 45°, \quad f_y = 429\,\text{N/mm}^2, \quad f_c = 39.6\,\text{N/mm}^2, \quad E_c = 43300\,\text{N/mm}^2, \quad E_s = 189000\,\text{N/mm}^2.$$

The length of the column is 2 m. The size of the horizontal bracing is $100 \times 40 \times 10$ mm, and the diagonal bracing $142 \times 28 \times 10$ mm.

The slenderness ratios for the x-x and y-y axes respectively are

$$i = \sqrt{\frac{I}{5A_s}} = 132\,\text{mm}, \qquad \lambda_1 = \frac{l}{i} = \frac{2000}{132} = 15.$$

With these values, the slenderness ratio in bending buckling is given by (5):

$$\lambda_o = \sqrt{\lambda_1^2 + \frac{5\pi^2(E_s A_s + E_c A_c)}{2E_s A_1 \sin^2\theta \cos\theta}} = 35.$$

Based on the slenderness ratio $\lambda_o = 35$, the stability factor λ in (1) given as 0.918 in [GB50017 2003]. Therefore the ultimate capacity is

$$N_u = 5\lambda f_y A_s + 5 f_c A_c = 5820\,\text{kN}.$$
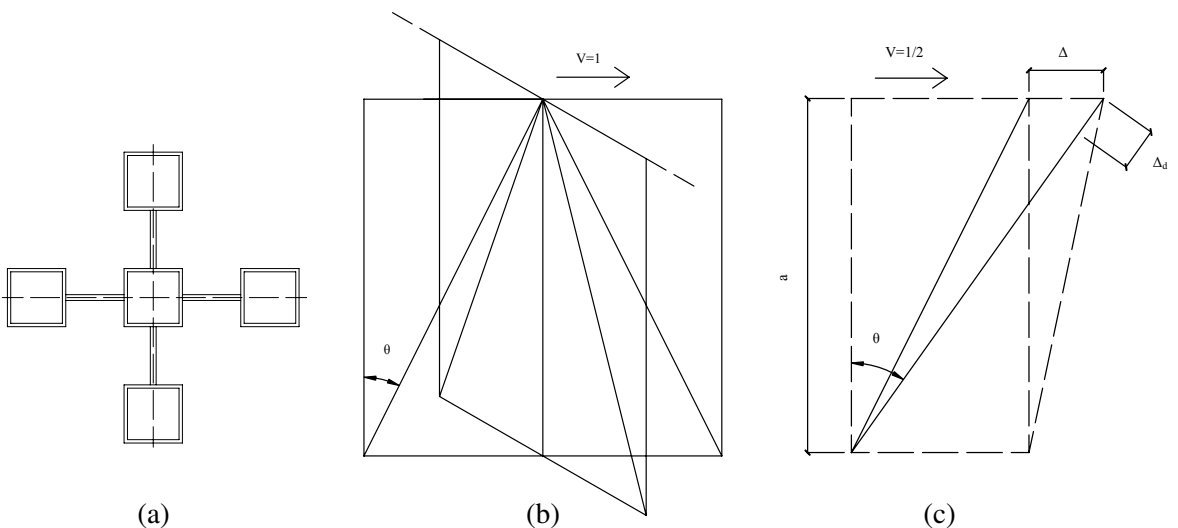
Figure 13. Calculation model of buckling.

5. Conclusions

The ultimate capacity of a crisscross section column composed of concrete-filled square steel tubes (XCFST) was determined experimentally by finite element analysis and by the analytical method explained in this paper. It was found that the results are in agreement.

More specifically, the ultimate capacity of the XCFST specimen was found experimentally to be equal to 6390 kN. By finite element analysis, the ultimate capacity was evaluated to be equal to 5959 kN, a difference of 7.2%. The value of the ultimate capacity predicted by the analytical method was 5820 kN, an 8.9% difference from the experimentally obtained value.

Based on the evidence presented in this paper, the analytical method predicts the ultimate capacity with adequate accuracy. The axial compression stability of an XCFST was studied, and the results of the analytical method and finite element analysis all show that the failure process of the XCFST specimen was initiated by the buckling of the monocolumn.

References

[Demagh et al. 2005] K. Demagh, H. Chabil, and L. Hamzaoui, "Analysis of reinforced concrete columns subjected to biaxial loads", pp. 433–440 in *Concrete for transportation infrastructure* (Dundee, 2005), edited by R. K. Dhir et al., Thomas Telford, London, 2005.

[Dundar and Sahin 1993] C. Dundar and B. Sahin, "Arbitrarily shaped reinforced concrete members subject to biaxial bending and axial load", *Comput. Struct.* **49**:4 (1993), 643–662.

[Dundar et al. 2008] C. Dundar, S. Tokgoz, A. K. Tanrikulu, and T. Baran, "Behaviour of reinforced and concrete-encased composite columns subjected to biaxial bending and axial load", *Build. Environ.* **43**:6 (2008), 1109–1120.

[Ellobody and Young 2006] E. Ellobody and B. Young, "Nonlinear analysis of concrete-filled steel SHS and RHS columns", *Thin-Walled Struct.* **44**:8 (2006), 919–930.

[Fujimoto et al. 2004] T. Fujimoto, A. Mukai, I. Nishiyama, and K. Sakino, "Behavior of eccentrically loaded concrete-filled steel tubular columns", *J. Struct. Eng.* (*ASCE*) **130**:2 (2004), 203–212.

[GB50017 2003] *Design code for steel structures*, GB50017, China Planning Press, Beijing, 2003. In Chinese.

[Han 2002] L.-H. Han, "Tests on stub columns of concrete-filled RHS sections", *J. Constr. Steel Res.* **58**:3 (2002), 353–372.

[Han et al. 2008] L.-H. Han, W. Liu, and Y.-F. Yang, "Behaviour of concrete-filled steel tubular stub columns subjected to axially local compression", *J. Constr. Steel Res.* **64**:4 (2008), 377–387.

[Hsu 1985] C.-T. T. Hsu, "Biaxially loaded L-shaped reinforced concrete columns", *J. Struct. Eng.* (*ASCE*) **111**:12 (1985), 2576–2595.

[Hsu 1989] C.-T. T. Hsu, "T-shaped reinforced concrete members under biaxial bending and axial compression", *ACI Struct. J.* **86**:4 (1989), 460–468.

[Leonard and George 2005] S. Leonard and F. George, *Appied structural steel design*, Tsinghua University Press, Beijing, 2005.

[Li et al. 1998] S. P. Li, H. D., Q. Wang, Y. C. Guo, and Y. Y. Huang, "Calculation for the ultimate bearing capacity of concrete filled steel tube columns under eccentric compression", *J. Build. Struct.* **19**:1 (1998), 41–51. In Chinese.

[Mallikarjuna and Mahadevappa 1992] Mallikarjuna and P. Mahadevappa, "Computer aided analysis of reinforced concrete columns subjected to axial compression and bending, I: L-shaped sections", *Comput. Struct.* **44**:5 (1992), 1121–1138.

[Mallikarjuna and Mahadevappa 1994] Mallikarjuna and P. Mahadevappa, "Computer aided analysis of reinforced concrete columns subjected to axial compression and bending, II: T-shaped sections", *Comput. Struct.* **53**:6 (1994), 1317–1356.

[Ramamurthy and Hafeez Khan 1983] L. N. Ramamurthy and T. A. Hafeez Khan, "L-shaped column design for biaxial eccentricity", *J. Struct. Eng.* (*ASCE*) **109**:8 (1983), 1903–1917.

[Sakino et al. 2004] K. Sakino, H. Nakahara, S. Morino, and I. Nishiyama, "Behavior of centrally loaded concrete-filled steel-tube short columns", *J. Struct. Eng.* (*ASCE*) **130**:2 (2004), 180–188.

[Tokgoz and Dundar 2008] S. Tokgoz and C. Dundar, "Experimental tests on biaxially loaded concrete-encased composite columns", *Steel Compos. Struct.* **8**:5 (2008), 423–438.

[Tsai et al. 2003] K.-C. Tsai, Y.-T. Weng, M.-L. Lin, C.-H. Chen, J.-W. Lai, and P.-C. Hsiao, "Pseudo dynamic tests of a full scale CFT/BRB composite frame: displacement based seismic design and response evaluations", pp. 165–176 in *Proceedings of the International Workshop on Steel and Concrete Composite Construction* (*IWSCCC-2003*) (Taipei, 2003), edited by K.-C. Tsai and G.-Y. Liu, National Center for Research on Earthquake Engineering, Taipei, 2003. Report NCREE-03-026.

[Tsao and Hsu 1993] W. H. Tsao and C.-T. T. Hsu, "A nonlinear computer analysis of biaxially loaded L-shaped slender reinforced concrete columns", *Comput. Struct.* **49**:4 (1993), 579–588.

[Tsao and Hsu 1994] W. H. Tsao and C.-T. T. Hsu, "Behaviour of biaxially loaded square and L-shaped slender reinforced concrete columns", *Mag. Concr. Res.* **46**:169 (1994), 257–267.

CHEN ZHI-HUA: zhchen@tju.edu.cn
College of Civil Engineering, Tianjin University, Tianjin 300072, China
http://www2.tju.edu.cn/colleges/civil/list.php?cid=23

RONG BIN: tjerobincn@hotmail.com
College of Civil Engineering, Tianjin University, Tianjin 300072, China

APOSTOLOS FAFITIS: fafitis@asu.edu
Department of Civil and Environmental Engineering, Arizona State University, Tempe, AZ 85287, United States
http://engineering.asu.edu/people/35093

SUBMISSION GUIDELINES

ORIGINALITY
Authors may submit manuscripts in PDF format on-line. Submission of a manuscript acknowledges that the manuscript is *original and has neither previously, nor simultaneously, in whole or in part, been submitted elsewhere.* Information regarding the preparation of manuscripts is provided below. Correspondence by email is requested for convenience and speed. For further information, consult the web site at http://www.jomms.org or write to

jomms.steele@stanford.edu

LANGUAGE
Manuscripts must be in English. A brief abstract of about 150 words or less must be included. The abstract should be self-contained and not make any reference to the bibliography. Also required are keywords and subject classification for the article, and, for each author, postal address, affiliation (if appropriate), and email address if available. A home-page URL is optional.

FORMAT
Authors are encouraged to use LaTeX and the standard article class, but submissions in other varieties of TeX, and, exceptionally in other formats, are acceptable. Electronic submissions are strongly encouraged in PDF format only; after the refereeing process we will ask you to submit all source material.

REFERENCES
Bibliographical references should be listed alphabetically at the end of the paper and include the title of the article. All references in the bibliography should be cited in the text. The use of BibTeX is preferred but not required. Tags will be converted to the house format (see a current issue for examples), however, in the manuscript, the citation should be by first author's last name and year of publication, e.g. "as shown by Kramer, et al. (1994)". Links will be provided to all literature with known web locations and authors are encoraged to provide their own links on top of the ones provided by the editorial process.

FIGURES
Figures prepared electronically should be submitted in Encapsulated PostScript (EPS) or in a form that can be converted to EPS, such as GnuPlot, Maple, or Mathematica. Many drawing tools such as Adobe Illustrator and Aldus FreeHand can produce EPS output. Figures containing bitmaps should be generated at the highest possible resolution. If there is doubt whether a particular figure is in an acceptable format, the authors should check with production by sending an email to

production@mathscipub.org

Each figure should be captioned and numbered so that it can float. Small figures occupying no more than three lines of vertical space can be kept in the text ("the curve looks like this:"). It is acceptable to submit a manuscript with all figures at the end, if their placement is specified in the text by comments such as "Place Figure 1 here". The same considerations apply to tables.

WHITE SPACE
Forced line breaks or page breaks should not be inserted in the document. There is no point in your trying to optimize line and page breaks in the original manuscript. The manuscript will be reformatted to use the journal's preferred fonts and layout.

PROOFS
Page proofs will be made available to authors (or to the designated corresponding author) at a web site in PDF format. Failure to acknowledge the receipt of proofs or to return corrections within the requested deadline may cause publication to be postponed.